

AD624097

Proceedings of the
FLUID AMPLIFICATION SYMPOSIUM

October 1965

VOLUME IV

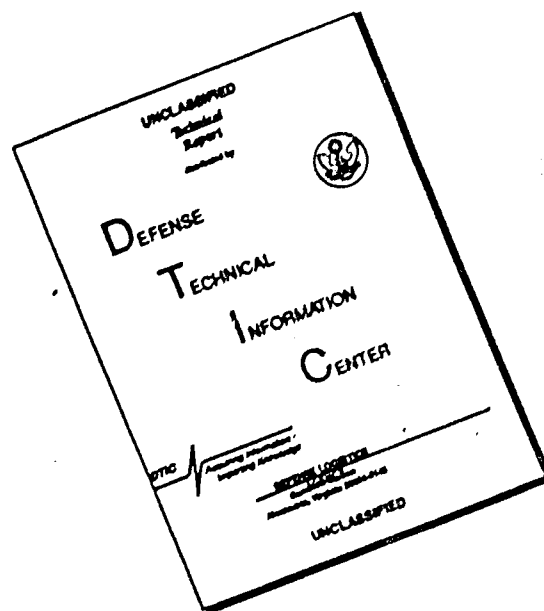
CLEARINGHOUSE FOR FEDERAL SCIENTIFIC AND TECHNICAL INFORMATION		
Hardcopy	Microfiche	
\$6.00	\$1.25	292 rp
ARCHIVE COPY		

Circle 1



U.S. ARMY MATERIEL COMMAND
HARRY DIAMOND LABORATORIES
WASHINGTON, D.C. 20438

DISCLAIMER NOTICE



THIS DOCUMENT IS BEST QUALITY AVAILABLE. THE COPY FURNISHED TO DTIC CONTAINED A SIGNIFICANT NUMBER OF PAGES WHICH DO NOT REPRODUCE LEGIBLY.

Proceedings of the
FLUID AMPLIFICATION SYMPOSIUM

Sponsored by the
HARRY DIAMOND LABORATORIES

26, 27, and 28 October 1965

VOLUME IV



U.S. ARMY MATERIEL COMMAND
HARRY DIAMOND LABORATORIES
WASHINGTON, D.C. 20438

CONTENTS

	<u>Page</u>
1. THE ANALYSIS OF SUBMERGED JET FLOW FIELDS BY A NUMERICAL FIELD COMPUTATION METHOD, Glen W. Zumwalt and William F. Walker, Oklahoma State University . . .	5-15
2. SCHLIEREN OBSERVATIONS OF THE EFFECT OF SOUND INJECTED INTO THE POWER NOZZLE OF A HELIUM-INTO-AIR JET, Jonathan Fine, Harry Diamond Laboratories	17-27
3. THE EFFECT OF SOUND ON A REATTACHING JET AT LOW REYNOLDS NUMBERS, Sanford D. Weinger, Harry Diamond Laboratories	29-46
4. TRANSITION TO TURBULENCE AND WALL ATTACHMENT OF MINIATURE JETS, E. F. Richards and S. D. Graber, Martin/Orlando	47-70
5. AN EXPERIMENTAL STUDY OF THE STATIC INTERACTION OF AN AXISYMMETRICAL FLUID JET AND A SINGLE RECEIVER- DIFFUSER, Karl N. Reid, Jr., Oklahoma State University	71-107
6. DYNAMIC INTERACTION OF A FLUID JET AND A RECEIVER LOAD SYSTEM, Karl N. Reid, Jr., Oklahoma State University	109-142
7. TRANSIENT THEORY OF SWITCHING IN A BISTABLE VALVE, D. W. Harvey, Missile and Space Systems Division, Douglas Aircraft Co., Inc.	143-149
8. FLUERIC PRESSURE REGULATION USING A RESISTANCE SET POINT, Captain Harry N. White, Harry Diamond Laboratories	151-163
9. A FLUERIC INDUCTION AND GATE, Elmer L. Swartz, Harry Diamond Laboratories	165-179
10. MECHANICALLY ENTRAINED FLUIDIC OSCILLATOR, W. J. Westerman, Jr., Martin Company, Orlando, Florida.	181-203
11. STEADY FLOW IN A PURE FLUID VALVE TVC SYSTEM, D. W. Harvey and R. P. McRae, Douglas Aircraft Co., Inc.	205-216

CONTENTS (Cont'd)

	<u>Page</u>
12. EXPERIMENTAL STUDY OF FLUID CONTROLLED VALVES, D. W. Harvey and P. P. McRae, Douglas Aircraft Co., Inc.	217-254
13. EXPERIMENTAL INVESTIGATION OF THE PERFORMANCE CHARACTERISTICS OF A FLOW-INSTABILITY SENSING DEVICE, E. F. Schroeder, Cornell Aeronautical Laboratory, Inc.	255-298

THE ANALYSIS OF SUBMERGED JET
FLOW FIELDS BY A NUMERICAL
FIELD COMPUTATION METHOD

by

Glen W. Zumwalt and William F. Walker
School of Mechanical Engineering
Oklahoma State University

THE DILEMMA

The fluid mechanics of fluid amplifiers has proven to be discouragingly difficult to analyze. Some special solutions have been obtained and insight has been gained by these into the phenomena involved, but generally, the flows and geometries are too complex to calculate. This is not surprising. Typical fluid control devices contain separated and reattaching flows, turbulent boundary layers and mixing regions, cross-moving streams, complex wall geometries, and all this inside bounding walls and receivers which impose pressure gradients in all directions.

To these difficulties we generally bring the methods developed in boundary layer studies. Since such a wealth of background work exists in the analysis of boundary layers (both guided and separated), it was natural that fluid amplifier studies should attempt to draw upon this fund. However, one does not work long at this before severe limitations in conventional fluid dynamics approaches are seen:

- (1) The flow models generally call for a large potential flow region to impress a pressure field upon the viscous regions. The pressure field is first solved, ignoring the viscous effects, and then the viscous regions are superimposed on the walls or separated boundary streamlines. But in fluid amplifier elements, the viscous flows often predominate and themselves determine the pressure field. This same difficulty has been faced in ejector and ducted-rocket analyses.
- (2) Small aspect ratios turn most problems into three-dimensional ones. These are almost beyond the formulation of flow models, and few solutions exist for even inviscid flows. Even the method of characteristics becomes hopelessly complex for bounded inviscid gases when the third dimension is introduced.
- (3) The non-linearity of the equations forces one to seek overall-effects type solutions by integral methods. For devices designed to operate

near the limits of the stable flow condition - and thus be "switchable" - the accuracy of results may be quite unacceptable. Also, details of flow patterns which are instinctive to the designer are often lacking.

The alternative to conventional fluid dynamic methods has been numerical methods. These have been used most widely and successfully in solving supersonic flow fields where the "method of characteristics" can apply. Unfortunately, the presence of viscosity destroys the mathematical simplicity which makes the method of characteristics useful. In jet mixing work, the inviscid jet boundary has provided the flow model upon which the laminar or turbulent jet mixing is superimposed. The method becomes useless, however, as mentioned above, when bounding walls severely restrict the extent of the frictionless flow. Thus, this numerical method offers little promise for the problem at hand.

SUGGESTED SOLUTION

A second type of numerical method has been recently successfully applied to transient flow problems. This differs from the method of characteristics in that the space co-ordinates are not unknowns to be solved for in the analysis. Rather, the field is divided into equal-sized cells, or represented by a grid of mesh points. At these points - or in these cells - all the basic equations are solved in difference equation form, based on the values of flow properties at surrounding points at previous times. Most of the mathematical development in the literature has been concerned with wave motion in fluids or solids, where the dissipating effects of viscosity were ignored. Further, the emphasis has been on the solution of moving shock wave problems, where wave diffraction and reflection complexities were well beyond all methods except difference-form computerized techniques.

It is the thesis of this paper that the numerical mesh-point methods offer the best - and perhaps the only - hope for truly analysing the completely-bounded jets of fluid amplifiers.

THE PRESENT STATUS

In dealing with problems involving the reflection and diffraction of moving shock waves, the classical methods of finite difference analysis were found unable to handle the occurrence of large, local variations of the dependent variables. The discontinuities associated with shock waves cause instabilities in the computation techniques quite similar to instabilities in a servo-mechanism. New methods were needed to allow computations to proceed through regions where surfaces of discontinuities existed. The basis for these methods was provided in 1950 by von Neumann

and Richtmyer (1) who suggested that the inviscid flow equations be altered so that discontinuities would be "blurred" into regions where all flow variables would be continuous, but rapidly varying. This was accomplished by adding to the equations terms often called "artificial viscosity" because they tend to dissipate the flow properties as viscosity would. This was followed by work, mainly at the Courant Institute for Applied Mathematics, on improving the accuracy of the computations and defining the stability requirements (2)(3)(4)(5). Lax and Wendroff (7) formalized the difference techniques to be applied to a set of conservation laws and thus be applicable to several types of physical problems.

In Russia in 1959 Godunov (8)(9) improved upon the von Neumann and Richtmyer and the Lax works with particular application to hydrodynamics. A more recent, and little known, work by Rusanov (10) draws together many of the best features of these previous papers. Rusanov made the coefficients in the artificial viscosity terms dependent upon the properties at the point being calculated, rather than using constant coefficients as did Lax. This considerably reduces the tendency to diffuse the gradients. At Oklahoma State University work has been underway for the past year to extend the approach of Rusanov to problems involving laminar or turbulent viscosity. It is this which will be presented in the following section.

A somewhat parallel line of work is being carried on at the Los Alamos Scientific Laboratory in a combination Lagrangian-Eulerian computation system known as the Particle-In-Cell (PIC) method. This permits the presence of more than one species of fluid, as in a plasma. Various modifications of this have been made for specific problems with very remarkable results; (11)(12)(13). The LASL work has, however, not yet appeared in a form which lends itself to the general viscous flow problem here considered, although there seems to be little doubt that the fluid mechanics research group at Los Alamos is without peer in this area of work.

THE BASIC EQUATION FORMS

The physical equations for the conservation of mass, momentum, and energy can all be written in a common form:

$$\frac{\partial f}{\partial x} + \frac{\partial F^x}{\partial x} + \frac{\partial F^y}{\partial y} = 0 \quad [1]$$

For the familiar frictionless, plane flow equations, the terms are expressible as vectors:

$$f = \begin{bmatrix} \rho \\ \rho u \\ \rho v \\ e \end{bmatrix} \quad F^x = \begin{bmatrix} \rho u \\ \rho + \rho u^2 \\ \rho uv \\ (e + p)u \end{bmatrix} \quad [2]$$

$$F^y = \begin{bmatrix} \rho v \\ \rho uv \\ \rho + \rho v^2 \\ (e + p)v \end{bmatrix}$$

If the upper term is substituted, the continuity equation is formed. The second and third terms give momentum equations in the x and y directions, respectively. The lower terms give the energy equation.

For numerical computations, the right side of the equation cannot be zero, or numerical instabilities occur in which property values diverge with successive iterations. Artificial viscosity terms are added which are essentially the sums of the second derivatives of f in each direction, weighted according to the magnitudes of the property.

If the conservation equations are derived for a turbulent jet flow, using order of magnitude arguments to eliminate some of the perturbation terms, as is commonly done in boundary layer analysis, the vectors to be inserted in equation [1] have been derived by W. F. Walker as:

$$\begin{aligned}
 f &= \begin{bmatrix} \bar{p} \\ \bar{p}\bar{u} \\ \bar{p}\bar{v} \\ \bar{p}\bar{e} \end{bmatrix} \\
 F^x &= \begin{bmatrix} \bar{p}\bar{u} \\ \bar{p} + \bar{p}\bar{u}\bar{u} - \zeta \frac{\partial \bar{u}}{\partial x} \\ \bar{p}\bar{u}\bar{v} - \zeta \frac{\partial \bar{v}}{\partial x} \\ (\bar{e} + \bar{p})\bar{u} - \frac{\zeta}{2} \left(\bar{u} \frac{\partial \bar{u}}{\partial x} + \bar{v} \frac{\partial \bar{u}}{\partial y} \right) \end{bmatrix} \\
 F^y &= \begin{bmatrix} \bar{p}\bar{v} \\ \bar{p}\bar{u}\bar{v} - \zeta \frac{\partial \bar{u}}{\partial y} \\ \bar{p} + \bar{p}\bar{v}\bar{v} - \zeta \frac{\partial \bar{v}}{\partial y} \\ (\bar{e} + \bar{p})\bar{v} - \frac{\zeta}{2} \left(\bar{u} \frac{\partial \bar{v}}{\partial x} + \bar{v} \frac{\partial \bar{v}}{\partial y} \right) \end{bmatrix}
 \end{aligned} \tag{3}$$

Here the "bars" indicate time-average values in a turbulent region, and

$$\zeta = \frac{U_a}{2\bar{V}^2} \rho X_j.$$

ζ represents the turbulent transport mechanism, and is derived from Goertler's functional representation of turbulent (eddy) viscosity. X_j is here the distance from the start of the jet mixing, U_a is the velocity of the flow adjacent to the mixing region, and \bar{V} is the experimentally determined jet spreading rate parameter. For subsonic flows, \bar{V} has been well established to be between 11 and 12. Thus

$$\zeta \cong 0.004 U_a \rho X_j$$

THE DIFFERENCE EQUATION FORMS

Following the approach of Rusanov, the differential equations [1], with [3] inserted were written in difference form, using central differences in space and forward differences in time. Let the superscript N indicate a particular time plane, and $N + 1$ the next successive calculation in time. The properties at any point at time $N + 1$ can then be computed based on the properties at time N at that point and the four adjacent points. The location of the point being computed will be given by the subscripts: m indicates the mesh location in the x -direction and l in the y -direction. Thus, $(m - 1, l)$ if the point is to the left, $(m, l + 1)$ is the point above, etc.

$$f_{m,l}^{N+1} = f_{m,l}^N - \frac{K_1}{2} [F_{m+1,l}^N - F_{m-1,l}^N] - \frac{K_2}{2} [F_{m,l+1}^N - F_{m,l-1}^N] + \frac{1}{2} [\phi_{m+\frac{1}{2},l}^N - \phi_{m-\frac{1}{2},l}^N + \phi_{m,l+\frac{1}{2}}^N - \phi_{m,l-\frac{1}{2}}^N]. \quad [4]$$

The second line of [4] contains the artificial viscosity terms. The details of these will be omitted here, but are available in references (14) and (15), or in the translation of Rusanov's paper (10). The actual dissipation terms (turbulent viscosity) perform the same stabilizing function as the artificial diffusion terms. Therefore, these fictional terms can be greatly reduced in magnitude when computing fields with viscosity included.

The axi-symmetric form of equations [1] through [4] can be readily derived and involves only the addition of a term to [1], increasing the computing complexity by about 40 per cent.

Boundaries of two types can be formulated to set the size of the field to be computed. Solid walls are represented by setting the velocity component normal to the wall equal to zero. Any fluid flow plane along which conditions are known can be used as an open boundary by simply inserting values at every time plane.

For a steady flow problem, initial conditions are inserted at every point which are reasonable approximations of the actual flow. The computations then are programmed to proceed point-by-point from the boundaries to cover the field, advance to a later time and again compute all points in the field. The steady state is reached asymptotically. The better the initial representation, the shorter the time required. The size of each time step is proscribed by stability requirements.

For non-steady flows, the open boundary conditions can be varied with time.

EXAMPLE

In connection with the Ph.D. thesis of William F. Walker, a computation of a turbulent jet issuing from a slit nozzle at a Mach number of 2.0 into a symmetrical cavity has been made. The initial field representation was purposely made poorly. The pressure was taken as equal to that of the exit plane of the nozzle, and the velocity profile of the nozzle exit plane was extended down the centerline unchanged.

Computations on an IBM 7094 solved the four basic equations at 90 points per second at a cost of \$0.15. The field contained 800 points in the half plane. (Only half of the field was required due to the symmetry.) Thus, each time plane was computed for \$1.35. To insure that the asymptotic limit had been closely approached, 1000 time planes were computed.

The results are shown in Figures 1 and 2. The final velocity profile closely corresponds to the Gaussian profile, which has been verified experimentally. Jet spreading rates are not easy to check in this case, due to the pressure gradients. The pressure field is shown in Figure 3. The pressure values have been normalized with respect to the nozzle exit plane pressure. It can be seen that the jet experiences a rapid expansion to about 70 per cent of the nozzle exit pressure. The pressure field is, of course, dependent on the proximity of the bounding walls. In this case, the downstream pressure was adjusted to avoid an opposing back pressure.

It is felt that the physical features of the flow field are well represented. Use can be made of intuition in the initial conditions, and the method can be extended to include multiple jets, receivers, and non-steady problems. Work is in progress at Oklahoma State University to put the equations in a simplified form for incompressible flows, for laminar boundary layer computations, and for shock-boundary layer interactions.

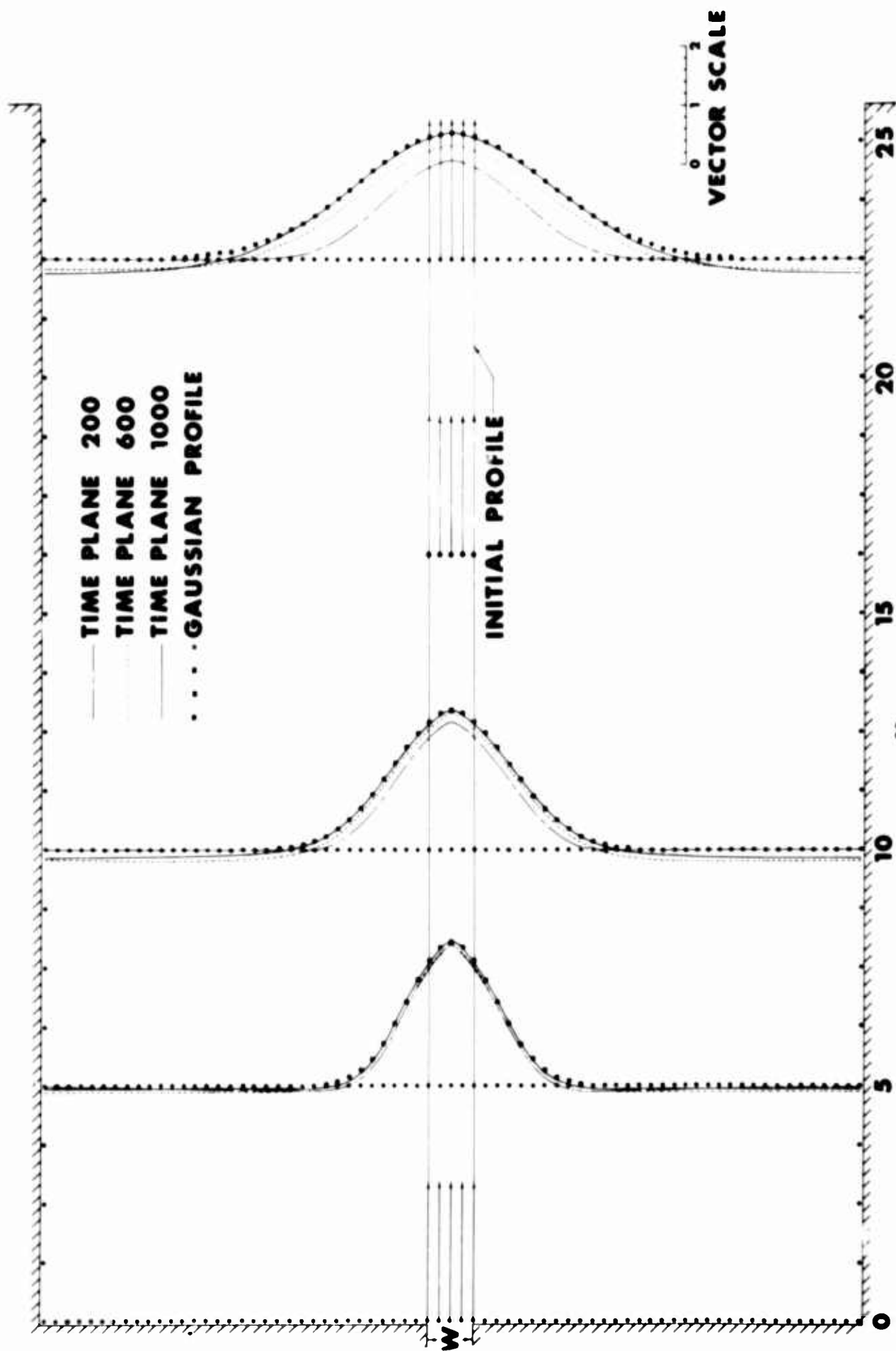


FIGURE 1

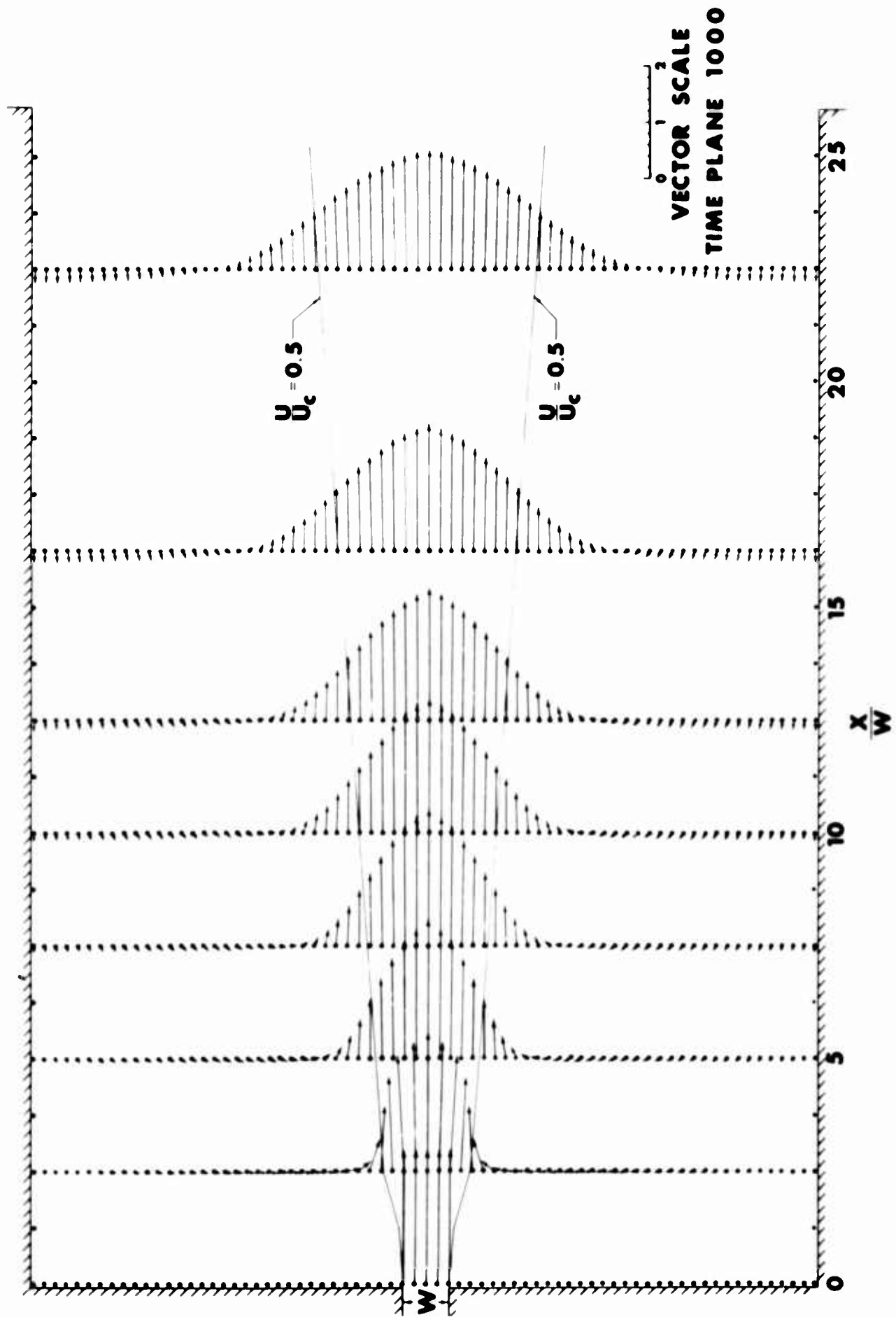


FIGURE 2
FULLY DEVELOPED VELOCITY PROFILES

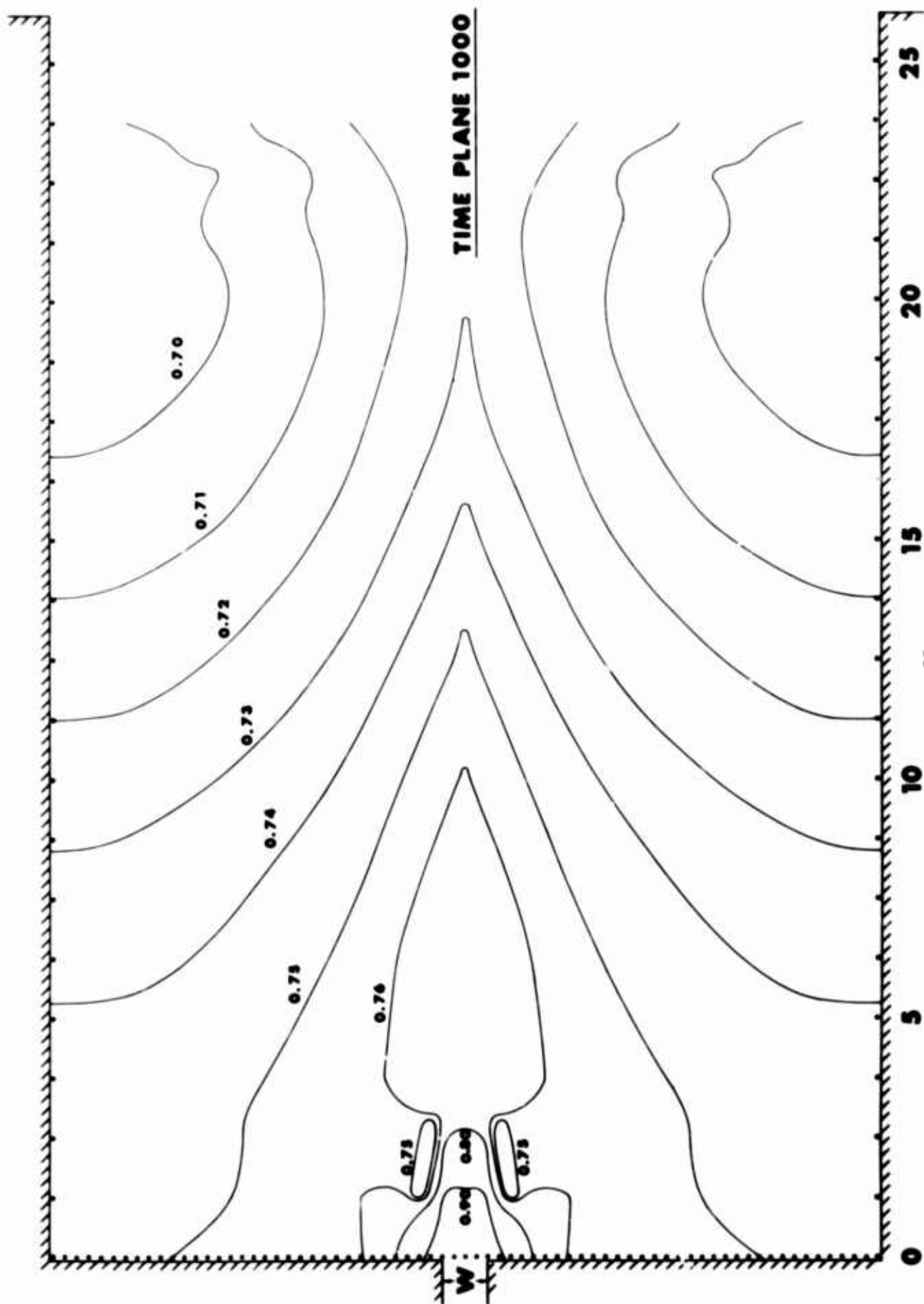


FIGURE 3

PRESSURE MAP OF FULLY DEVELOPED FIELD

REFERENCES

1. Von Neumann, J., and R. D. Richtmyer, "A Method for the Numerical Calculation of Hydrodynamic Shocks," J. Appl. Physics, Vol. 21, 1950, p. 232.
2. Courant, R., E. Isaacson, and M. Rees, "On the Solution of Nonlinear Hyperbolic Differential Equations by Finite Differences," Comm. Pur and Appl. Math., Vol. V, 1952, p. 243.
3. Lax, P., "On Discontinuous Initial Value Problems for Nonlinear Equations and Finite Difference Schemes," LAMS-1332, 1953.
4. Lax, P., "Weak Solutions of Nonlinear Hyperbolic Equations and Their Numerical Computation," Comm. Pure and Appl. Math., Vol. VII, 1954, p. 159.
5. Ludloff, H. F., and M. B. Friedman, "Difference Solution of Shock Diffraction Problem," J. Aero. Sci., Vol. 22, 1955, p. 139.
6. Payne, R. B., "A Numerical Method for a Converging Cylindrical Shock," J. Fluid Mech., Vol. II, 1957, p. 185.
7. Lax, P., and B. Wendroff, "Systems of Conservation Laws," Comm. Pure and Appl. Math., Vol. XIII, 1960, p. 217.
8. Godunov, S. K., "A Difference Method for the Numerical Calculation of Discontinuous Solutions of Hydrodynamic Equations," Matematicheskii Sbornik, Vol. 47, No. 3, 1959, p. 271.
9. Godunov, S. K., "The Problem of a Generalized Solution in the Theory of Quasilinear Equations and in Gas Dynamics," Russian Mathematical Surveys, Vol. 17, No. 3, 1962, p. 145.
10. Rusanov, V. V., "The Calculation of the Interaction of Non-Stationary Shock Waves and Obstacles," National Research Council of Canada Library, Ottawa, Canada, Tech. Translation 1027 by D. A. Sinclair, 1962. Translated From: Zhurnal Tekhnicheskoi Fiziki, (Akademiya Nauk, SSSR 1, Vol. 1, No. 7, 1961, p. 257.
11. Harlow, F. H., "The Particle-In-Cell Method for Numerical Solution of Problems in Fluid Dynamics," Proc. Symposia In Applied Math., Vol. XV, 1963, p. 269.
12. Hirt, C. W., "Multidimensional Fluid Dynamics Calculations With High Speed Computers." AIAA Paper 65-3, 1965.
13. Butler, T. D., "Numerical Calculations of the Transient Loading of Blunt Cylinders by Shocks in Air." AIAA Paper 65-4, 1965.

14. Jackomis, W. N., "Transient Flow Field Analysis of a Plane Blast Wave Intercepting a Stationary Cone at Zero Angle of Attack," Ph.D. Thesis, Oklahoma State University, May, 1965.
15. Tyler, L. D., "Numerical Solutions of the Flow Field Produced by a Plane Shock Wave Emerging into a Cross Flow," Ph.d. Thesis, Oklahoma State University, May, 1965.

HARRY DIAMOND LABORATORIES
Washington, D.C. 20438

SCHLIEREN OBSERVATIONS OF THE EFFECT OF SOUND INJECTED
INTO THE POWER NOZZLE OF A HELIUM-INTO-AIR JET

by

JONATHAN E. FINE

U.S. ARMY MATERIEL COMMAND

DEPARTMENT OF THE ARMY

ABSTRACT

The effect of sound on a jet of helium exhausting into air at ambient pressure and room temperature was investigated on the HDL Schlieren apparatus.

Acoustic signals from 50 to 4000 cps injected into a tank upstream of the nozzle caused a laminar jet to break up into turbulence or the transition region of a turbulent jet to move upstream.

The results indicate that the region of jet sensitivity is within the region of jet instability as described by Chanaud and Powell.

ACKNOWLEDGEMENTS

This paper describes a portion of the work sponsored under MIPR No. 33-657-2-R&D-105 by the Air Force Propulsion Laboratory of the Aeronautical Systems Division at Wright-Patterson Air Force Base (WPAFB) Ohio, and investigated by the Harry Diamond Laboratories. The general objective of this work is to provide basic technology in the control of advanced turbo-compressor jet engines with pneumatic (or fluid) techniques using no moving parts.

The cooperation of J. Keto and K. Toda in making the Schlieren system available is appreciated.

1. INTRODUCTION

The effect of a sinusoidal acoustical disturbance on the stability of a jet of helium exhausting into air at ambient pressure and room temperature has been investigated by the use of the HDL Schlieren apparatus.

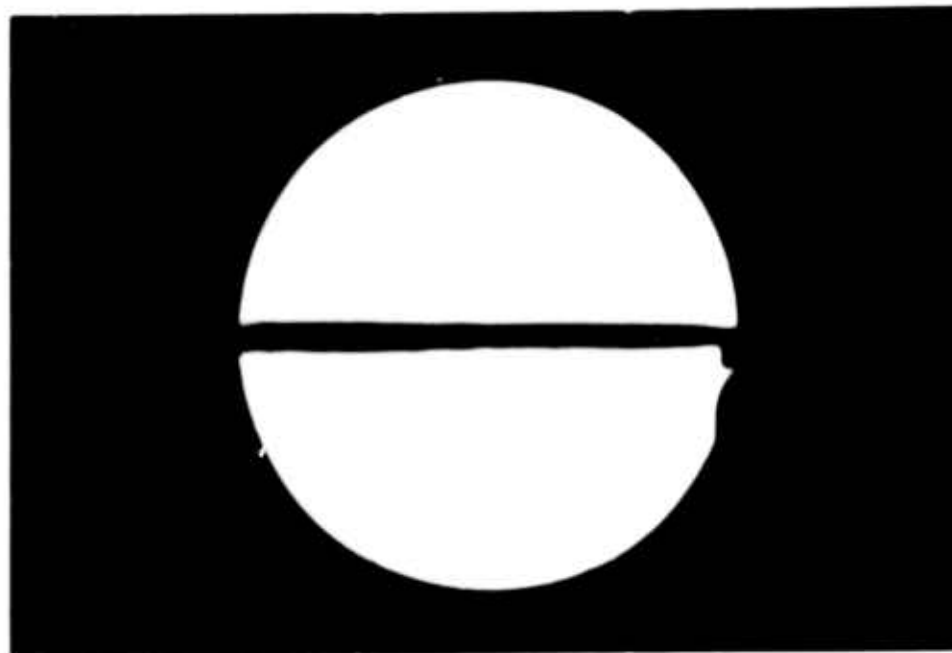
The Schlieren equipment (ref 1) produces an optical image whose intensity varies with the density gradient of fluid in a test section. It is thus possible to observe the changes of density gradient associated with the onset of turbulence in the section.

As an example, figure 1 shows a photograph of the jet in the test section before and after the jet is exposed to a sound field. The turbulence and increased spreading of the jet, absent in figure 1(a), are clearly visible in figure 1(b). Helium was used in the experiment to enhance visualization.

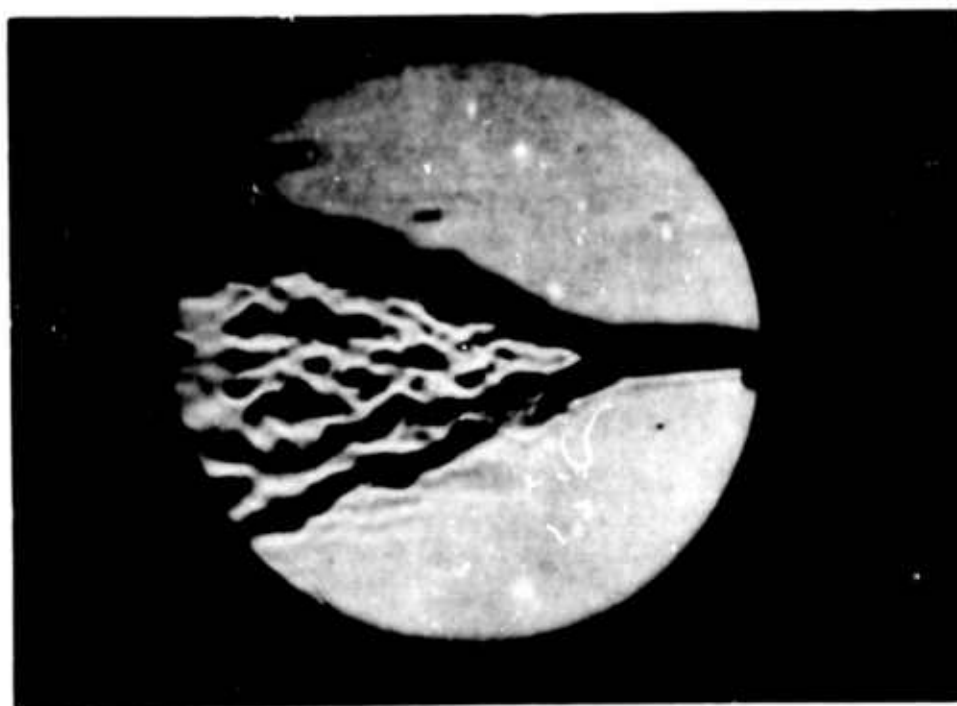
The power jet pressure P_0 is increased sufficiently above ambient pressure P_∞ so that in the absence of sound the point of transition from laminar to turbulent flow occurs at the center of the test section, as in figure 1(b). The application of sound causes the transition region to move closer to the nozzle. Removal of the sound allows the jet to return to its undisturbed condition.

Measurements were taken of power jet pressure and the frequency of sound to break up the jet for two configurations. One was a circular nozzle without cover plates and the other was a rectangular nozzle with cover plates. The Reynolds number and Strouhal number were calculated for both jets from the above data, the kinematic viscosity of the helium and the geometry of the nozzles.

The experimental procedure is described and the results are compared with the work of Chanaud and Powell (ref 2 and 3).



(a) No sound



(b) $f = 1,000$ cycles/second

$P_0 - P_{\infty} = 62 \text{ n/m}^2$

2210-64
Figure 1. Effect of injecting sound into the power nozzle of a jet of helium exhausting into air.

2. EXPERIMENTAL PROCEDURE

Circular Nozzle

A diagram of the experimental setup for the circular nozzle without cover plates is shown in figure 2. The power jet pressure was adjusted to 62 N/m^2 above ambient. The Reynolds number ($R = U_0 D/\nu$) was 910, where U_0 is the mean velocity of fluid at the nozzle exit in m/sec, D is the nozzle diameter in m, and ν is the kinematic viscosity of helium in m^2/sec . A 1-kc acoustic signal was generated by the acoustic driver, which fed into a tank upstream of the power jet nozzle. The amplitude was increased until the transition point moved from the window edge to about the center of the window, as shown in figure 1(b). This was repeated for various other frequencies.

The same procedure was utilized when the power jet pressure was reduced to $31 \frac{\text{N}}{\text{m}^2}$, giving a Reynolds number of 640.

Rectangular Nozzle

For studying the rectangular nozzle with cover plates, another apparatus was used (fig. 3). The nozzle, which was sandwiched between the cover plates of the test section, was fed from a cylindrical tank, which had inputs for the sound, helium flow, tank static pressure, and a pressure transducer. The same sound-producing arrangement was used in both experimental configurations. The pressure transducer was used to observe the waveform in the tank.

Power jet pressures of 98 N/m^2 and 30 N/m^2 were used, yielding Reynolds numbers ($R = U_0 d/\nu$) of 357 and 195, respectively, where d is the nozzle width in m.

3. EXPERIMENTAL RESULTS

Both the circular jet and rectangular jet were sensitive to sound over the frequency range from 50 to 4000 cps. Applying the sound caused the

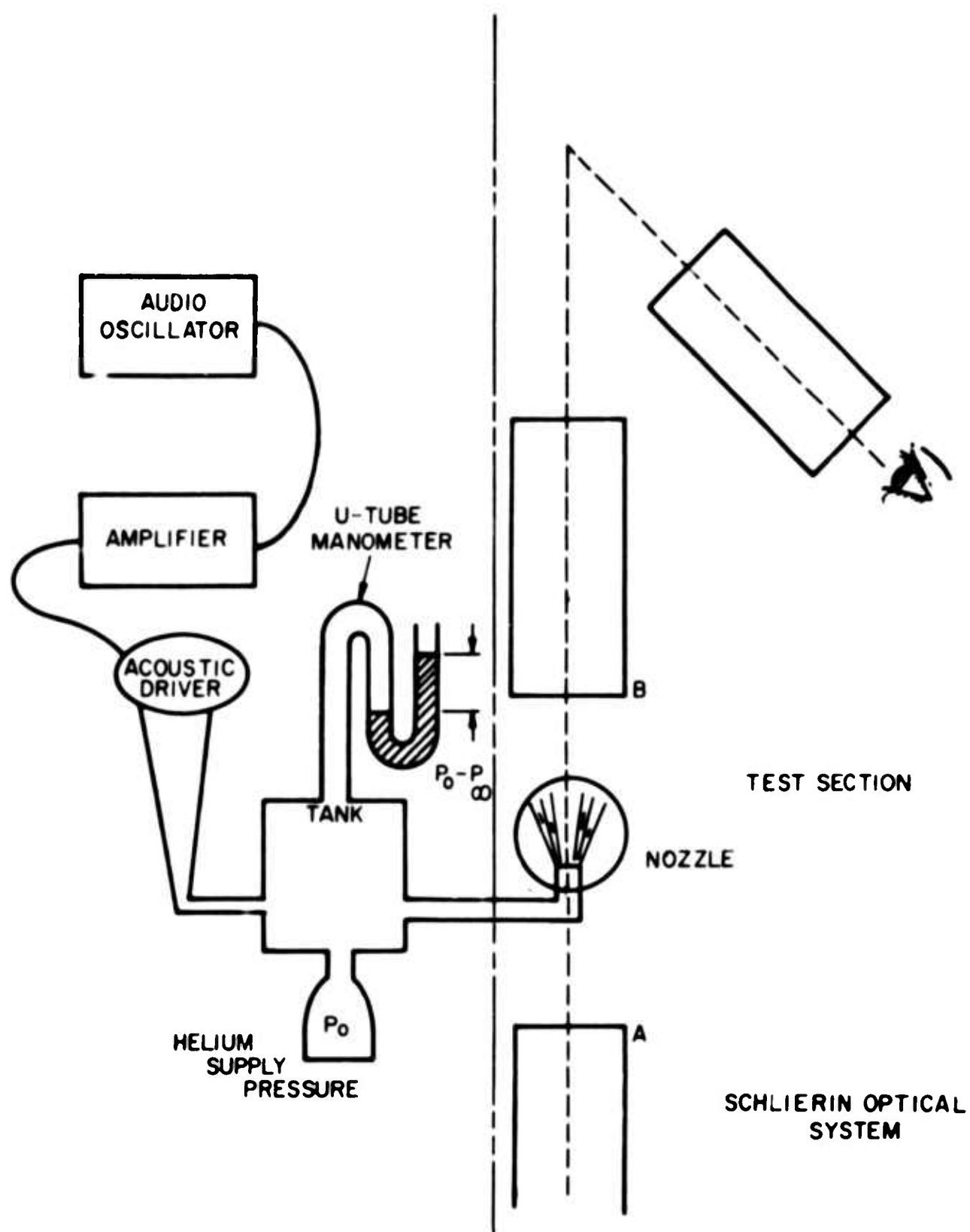


Figure 2. Experimental Apparatus for Studying the Circular Nozzle in the Schlieren System.

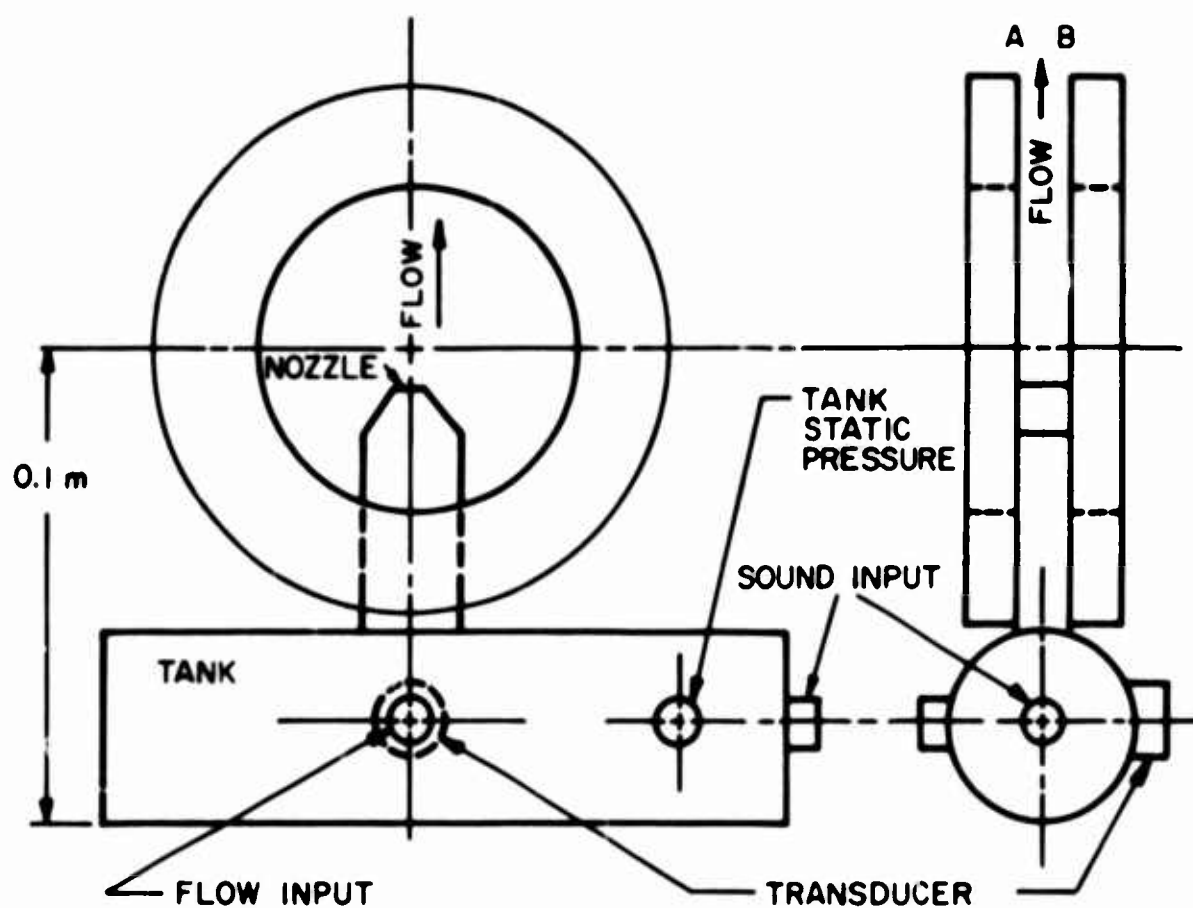


Figure 3. Apparatus for Studying the Rectangular Nozzle in the Schlieren System

laminar jet to break up into turbulence and caused the transition region of the turbulent jet to move closer to the nozzle. Removing the sound signal allowed the jet to revert to the undisturbed state.

The results obtained can be compared with the work of R. C. Chanaud and A. Powell in references 2 and 3. They found that for a free jet of air exhausting into air, the significant parameters are:

1. Reynolds number at the nozzle exit ($U_0 \delta / \nu$)
2. Strouhal number $S = (f \delta / U_0)$, where f is the disturbance frequency in cycles/second, δ is a characteristic length, and U_0 is a characteristic velocity
3. The nondimensionalized disturbance amplitude, and
4. Velocity profile of the jet.

To avoid investigating the fourth parameter, they attempted to maintain a parabolic velocity profile.

In figure 4 the Schlieren experimental points are plotted in a Reynolds-Strouhal diagram (ref 2, p. 914). The Strouhal numbers were calculated from the formula $S = \frac{fD}{U_0}$ for the circular jet and $S = \frac{fd}{U_0}$ for the rectangular jet, where the symbols have their previous meaning. The theoretical curve of neutral stability for a free jet shown in this figure is a curve above which the flow is stable and below which the flow is unstable and easily broken up by sound. The dashed curves labelled A_1 , A_2 , A_3 , and A_4 denote theoretical curves of constant sensitivity; that is, the intensity (power per unit area) of sound to break up the jet is the same for all values of R and S along one of these curves. The sound intensity is less for R and S values toward the center of the diagram, which means that curve A_2 represents points of the jet that are more sensitive than A_1 , etc.

The Schlieren data points for the circular free jet fall in the sensitive region of figure 4. The data points for the rectangular confined jet have also been plotted in figure 4. They, too, fall within the

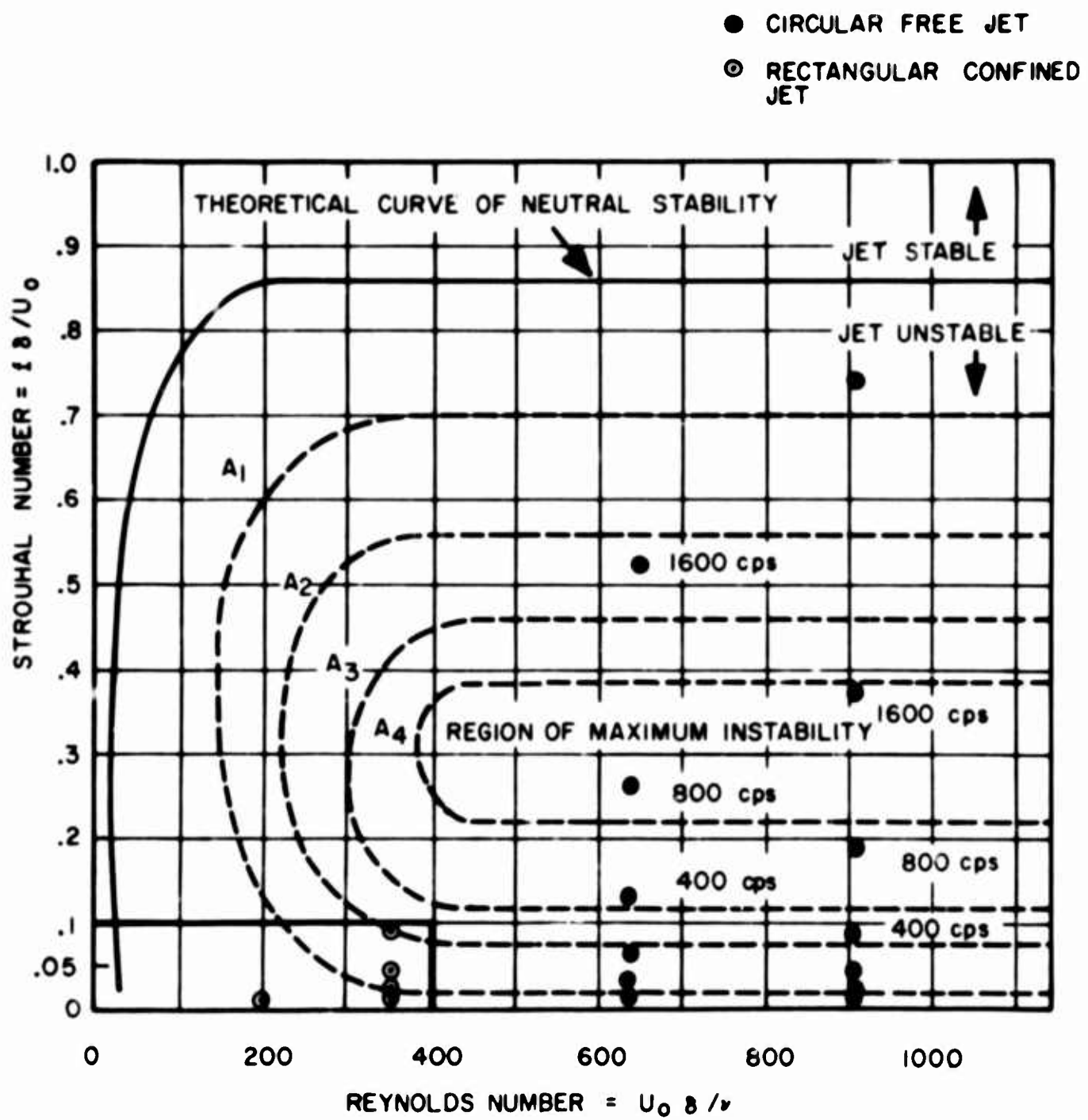


Figure 4. Comparison of Data with Theory

sensitive range of the jet but are displaced to the region of low Reynolds numbers and low Strouhal numbers. The effect of the top and bottom plate probably was the major cause of this displacement.

CONCLUSIONS

The laminar jet is sensitive to acoustical disturbances injected into the flow upstream of the nozzle. The sensitive region of the jet is from 50 to 4000 cps.

It was shown that the region of jet sensitivity is in the region of jet instability, as described in the literature. The confined rectangular jet is sensitive to sound frequencies yielding Reynolds and Strouhal numbers somewhat below the values predicted for a free jet.

REFERENCES

1. Keto, J. R., "Flow Visualization - Compressible Fluids," HDL Report TR-1041, 20 Aug 1962.
2. Chanaud, R. C., and Powell, A., "Experiments Concerning the Sound-Sensitive Jet," Journal of the Acoustical Society of America, Vol. 34, No. 7, July 1962, pp. 907-915.
3. Powell, A., "On the Edgetone," Journal of the Acoustical Society of America, Vol. 33, No. 4, Apr 1961, pp. 395-409.

HARRY DIAMOND LABORATORIES
Washington, D.C. 20438

THE EFFECT OF SOUND ON A REATTACHING
JET AT LOW REYNOLDS NUMBERS

by

SANFORD DALE WEINGER

U.S. ARMY MATERIEL COMMAND

DEPARTMENT OF THE ARMY

ABSTRACT

An explanation is given for the effect of sound on the reattachment point of a jet to an offset wall. The explanation depends on combining the movement of the reattachment point with jet Reynolds number and the effect of sound on the transition region of a jet from laminar to turbulent flow. The movement of the reattachment point with sound amplitude is found to be due to changing the location of the transition region. Typical experimental results are described.

INTRODUCTION

There has been a belief at HDL that sound could move the reattachment point of a jet. Experimental observations have justified this belief. However, there was no explanation for this phenomenon. The following explanation is given as to why the reattachment of a jet to an offset wall should be affected by sound. The explanation involves a discussion of the Coanda effect, jet stability, and finally a combination of the two. Finally, a series of experiments are discussed which confirm the expected results.

DISCUSSION

A. The Effect of Reynolds Number on Wall Attachment

The reattachment of a jet to an adjacent wall, due to the Coanda effect, has been discussed by numerous authors. It has been reported that the reattachment point varies with the Reynolds number in the following manner (references 1, 2, and 3): Firstly, there is a minimum Reynolds number below which the jet will not attach to the wall. This minimum Reynolds number is a function of the aspect ratio of the nozzle and levels off at a value of approximately 200 at high aspect ratios. Two hundred is the value often used for the transition Reynolds number for laminar to turbulent flow in a two-dimensional jet. The variation of minimum Reynolds number with aspect ratio for a double sided element is shown in Figure 1*. Secondly, there is a maximum Reynolds number of approximately 10^4 above which the reattachment point is independent of the Reynolds number. Between these two limits the reattachment point varies with Reynolds number.

It was observed in water table jets that after the minimum Reynolds number is reached and the jet attaches to the wall a further increase in the Reynolds number moves the transition region of the jet nearer the nozzle and moves the reattachment point upstream. This effect continues until the transition point is at the exit of the nozzle. This corresponds to the maximum Reynolds number mentioned earlier.

*Figures appear on pages 37 through 46.

This effect was investigated by Chapman et al (reference 4).

The importance of the location of the transition region is shown in Figure 2 where P_d is the pressure in the separation bubble and P' is the pressure after reattachment. The condition for equilibrium to exist is that the flow reversed into the bubble must equal the flow entrained out of the bubble by the jet. When the transition region moves from A to B, the entrained flow increases because more of the jet is turbulent and the reverse flow decreases because the increased turbulent mixing has given more of the jet a sufficient velocity to overcome the pressure rise at reattachment. The two mass flow curves now intersect at a new equilibrium point. This represents the new reattachment point.

B. The Effect of Sound on a Free Jet

The effect of sound on a free jet is included in the subject of hydrodynamic stability. A good discussion of this is given by A. Powell (reference 5). Further understanding has come from studies on the HDL Schlieren system. In short, it is well established that a jet of Reynolds number less than about 3000 is sensitive to sound. For a given Reynolds number in this range, there corresponds a sound frequency to which the jet is most sensitive. A microscopic input of sound will appear as a macroscopic change in the jet. Sound will cause a laminar jet to break up into turbulence in a much shorter distance than with no sound. If the amplitude of the sound is then increased (at this sensitive frequency), the transition region from laminar to turbulent flow will move toward the jet orifice. Finally, the amplitude can be increased to a value sufficient to move the transition point to the nozzle exit.

C. The Effect of Sound on Wall Attachment

By combining the effect of sound on a sensitive jet and the effect of the transition region of a separated jet on its reattachment point, the effect of sound on an attaching jet can be explained. Starting with an attached jet, a sensitive frequency of very small amplitude will disturb the jet. Increasing the sound amplitude will move the reattachment

point toward the nozzle by causing the transition region to move toward the nozzle. This will continue until the transition region of the jet is at the nozzle exit at which time the reattachment point has reached its maximum upstream position.

The movement of the reattachment point caused by a sound input in the power nozzle is shown in Figure 3. In the first photograph [3(a)], the attached jet is shown without a sound input. In succeeding photographs [3(b) to 3(f)], the sound amplitude is continuously increased. Figure 3(f) is the maximum upstream position. While taking these pictures, it was noted that increasing the sound amplitude beyond that needed to move the reattachment point to its maximum upstream position caused the reattachment point to move downstream. This movement is not predicted by the previous explanation and will be investigated in the experiments which will obtain quantitative values of both the upstream and downstream motion of the reattachment point.

THE EXPERIMENT

A. Experimental Apparatus

The tests were conducted with an adjustable wall and a nozzle with an aspect ratio of 8. The unit had top and bottom cover plates. The setback (SB) of the wall could be varied from zero to seven nozzle widths and the wall angle (α) could be varied from zero to twenty-five degrees. There were forty-eight static pressure probes along the wall spaced one nozzle width (.7" mm) apart.

The pressure distribution along the wall was measured with a Scanivalve using a variable reluctance transducer and a carrier amplifier. The pressure distribution was plotted on an X-Y recorder.

The velocity at the nozzle exit was measured with a constant temperature hot-wire anemometer using a platinum-coated tungsten wire (.005-mm D).

The sound was generated by an audio oscillator and amplified by a 40 Watt audio amplifier which drove a hi-fi speaker. The sound was introduced into the unit by a transmission line terminating opposite the wall.

The sound was measured with a microphone placed in the top cover plate. The output of the microphone was sent through a preamplifier and an amplifier and displayed on a storage oscilloscope.

B. Test Procedure

The wall angle, setback, and velocity were set at the desired values. The pressure distribution along the wall was recorded with no sound input. At this point, the sound was turned on at the desired frequency. The initial amplitude was barely audible. The pressure distribution was recorded for this amplitude. The amplitude was then increased gradually and the pressure distribution was recorded for each value of sound amplitude.

C. Experimental Results

Figure 4 shows the typical wall pressure distributions which were obtained. With a sound input of small amplitude, the pressure in the separation bubble decreased and the point of maximum pressure moved upstream. As the point of maximum pressure occurs slightly downstream of the point of reattachment, the change in its position can be considered a good approximation of the change in the position of the reattachment point. Figures 5 and 6 illustrate the movement of the point of maximum pressure with increasing sound amplitudes. Significant upstream movements are obtained with extremely small sound inputs. These results are precisely what was predicted by the qualitative analysis. The downstream movement was also observed at much higher sound amplitudes.

Although it was not the purpose of the experiment, interesting and significant results were obtained from the curves taken with no sound input. These results are shown in Figures 7 and 8. These figures show that the reattachment point is a function of the Reynolds number at Reynolds numbers of less than 1000 for an aspect ratio of 8. This is approximately five times the minimum Reynolds number for this aspect ratio.

CONCLUSIONS

1. For low Reynolds numbers, frequencies within the sound-sensitive range will affect the location of the reattachment point.

2. The upstream movement of the reattachment point with low amplitude sound inputs is caused by a corresponding upstream movement of the transition region of the jet.

3. Very high amplitude inputs (compared with those for the upstream movement) will move the reattachment point downstream of its maximum upstream location.

4. The location of the reattachment point cannot be assumed to be independent of the Reynolds number for Reynolds numbers less than five times the minimum Reynolds number.

ACKNOWLEDGEMENTS

The author wishes to acknowledge the valuable assistance of J. Fine, E. Flester, and E. Hastie in conducting his experiments. K. Toda and R. Berry took the excellent Schlieren photographs.

A portion of this work was supported by the Air Propulsion Laboratory of the Aeronautical Systems Division.

REFERENCES

1. Comparin, R. A., Glaettli, H. H., Mitchell, A. E., and Mueller, H. R., "On the Limitations and Special Effects in Fluid Jet Amplifiers," ASME Symposium on Fluid Jet Control Devices, Nov 1962.
2. Olson, R. E., "Reattachment of a Two-Dimensional Compressible Jet to an Adjacent Plate," ASME Symposium on Fluid Jet Control Devices, Nov 1962.
3. Mitchell, A. E., Discussion following reference 2.
4. Chapman, D. R., Kuehn, D. M., and Larson, H. K., "Investigation of Separated Flows in Supersonic and Subsonic Streams with Emphasis on the Effect of Transition," NACA TN 3869, Mar 1957.
5. Powell, A., "On the Edgetone," Journal of the Acoustical Society of America, Vol. 33, Apr 1961.

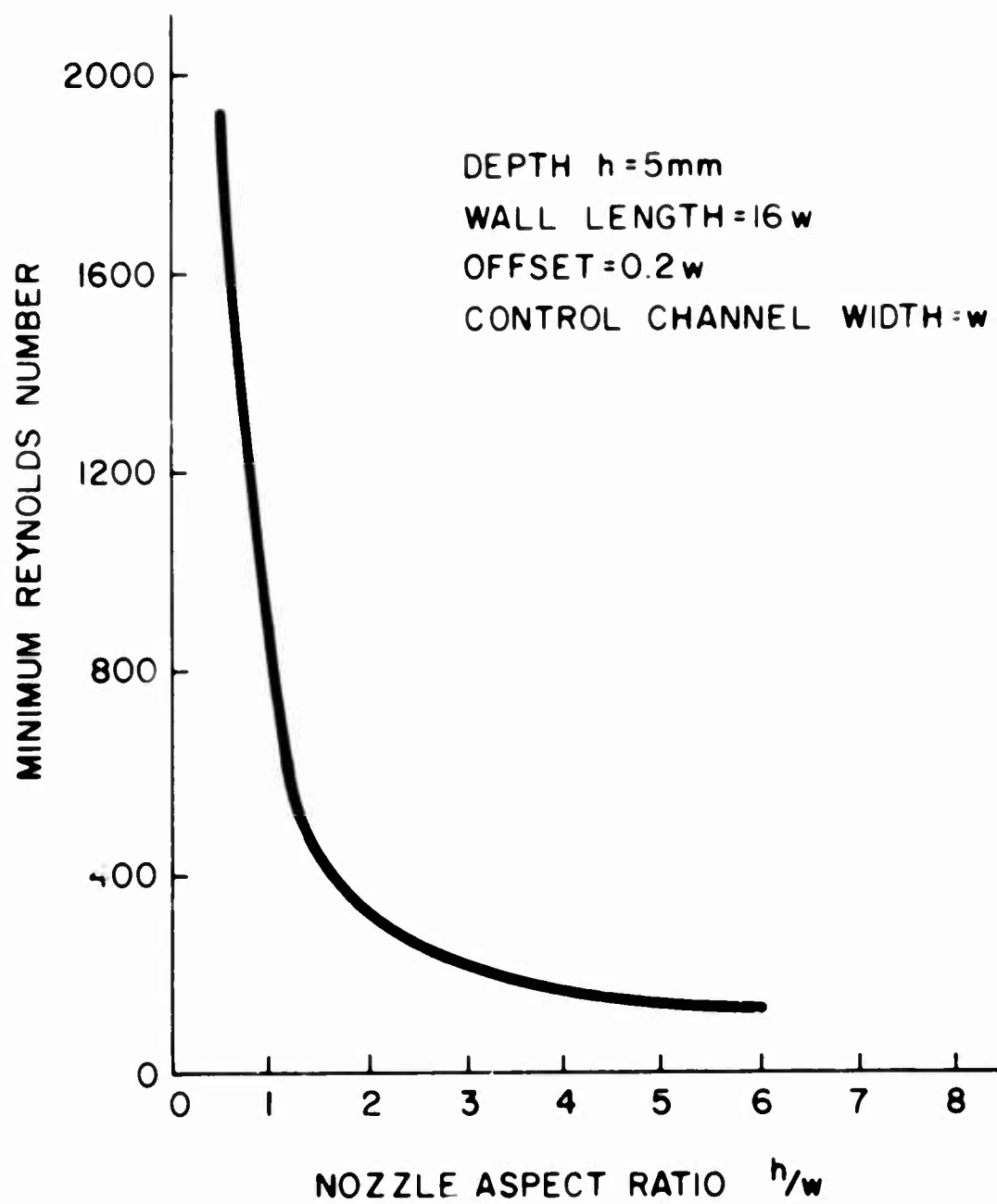


Figure 1. The effect of aspect ratio on the minimum Reynolds number.

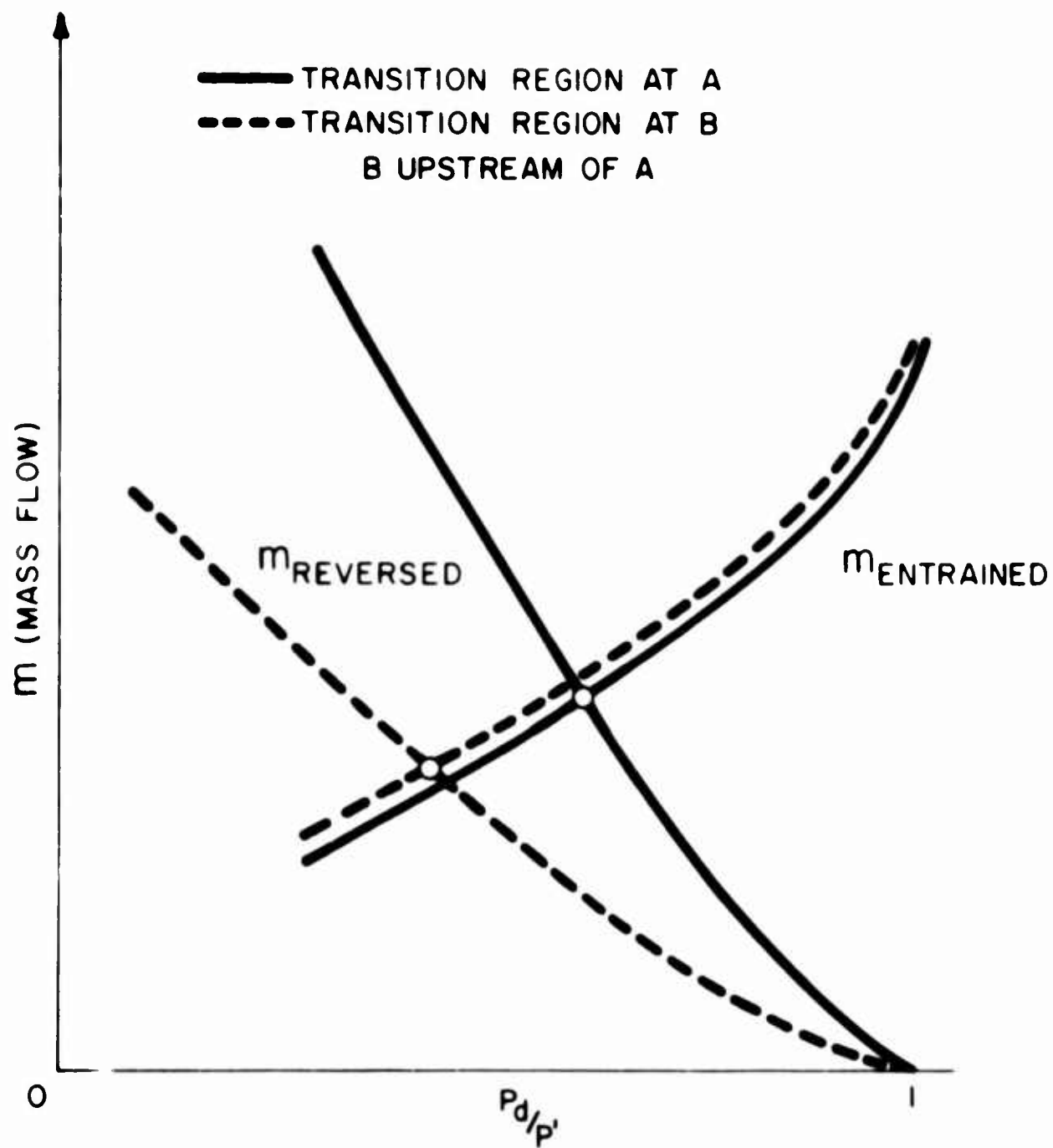


Figure 2. Movement of the reattachment point with a varying jet transition point.



(a)



(b)

Figure 3. The effect of sound on a jet reattaching to an offset wall.

999-65



(c)



(d)

1000-65

Figure 3. The effect of sound on a jet reattaching to an offset wall.



(e)



(f)

Figure 3. The effect of sound on a jet reattaching to an offset wall.

1001-65

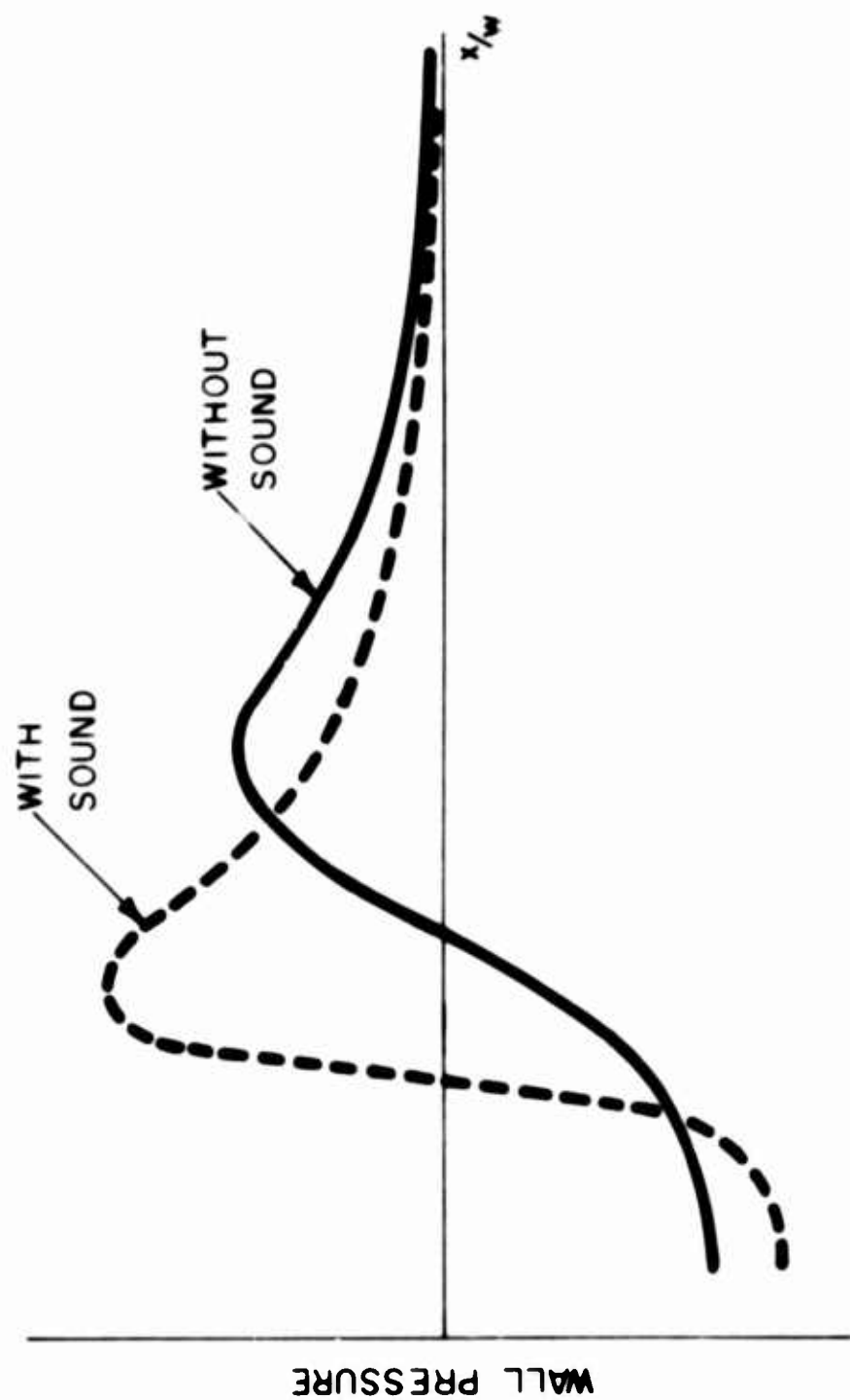


Figure 4. Typical wall pressure profiles .

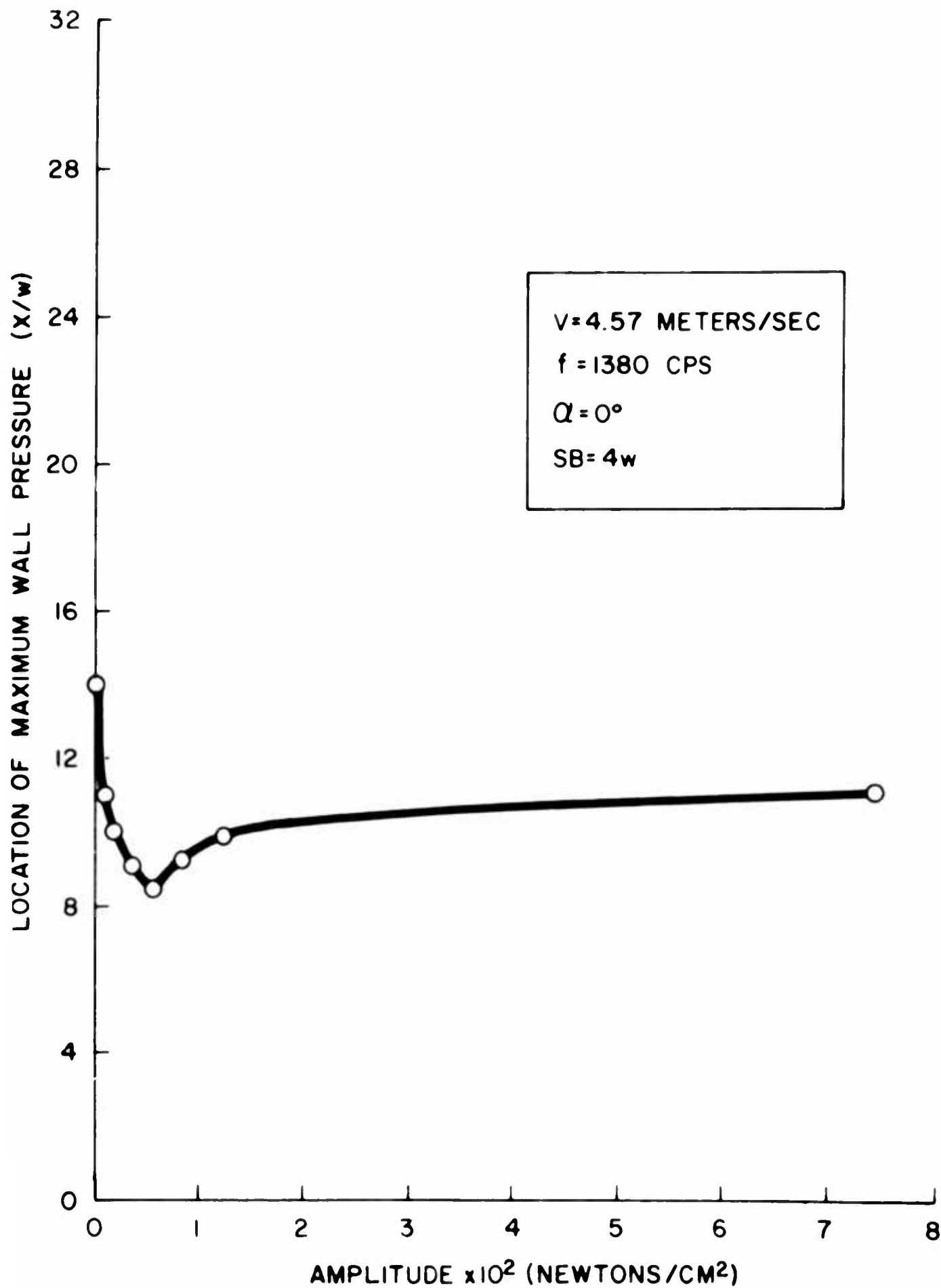


Figure 5. Movement of the location of the maximum wall pressure with varying sound amplitude.

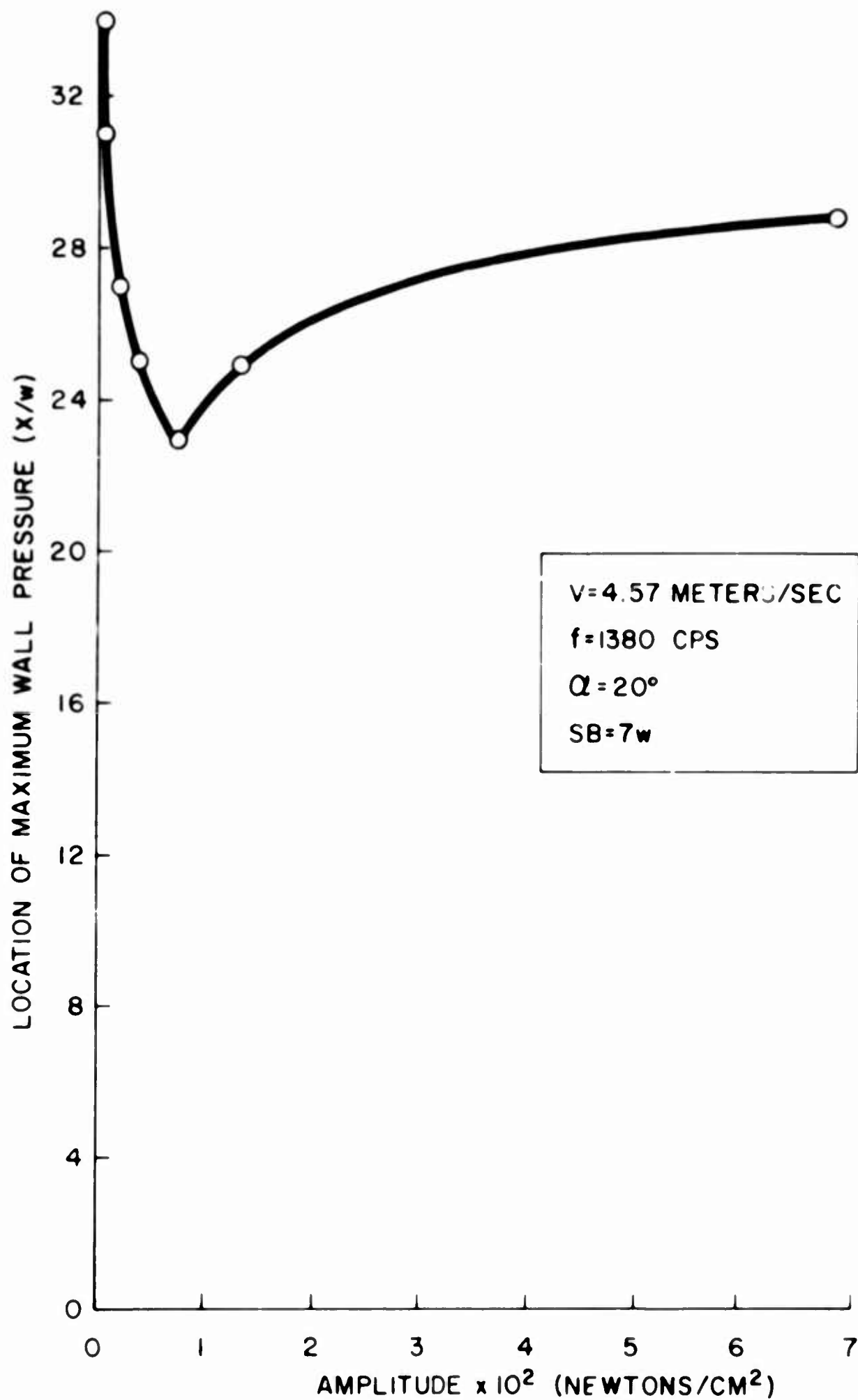


Figure 6. Movement of the location of the maximum wall pressure with varying sound amplitude.

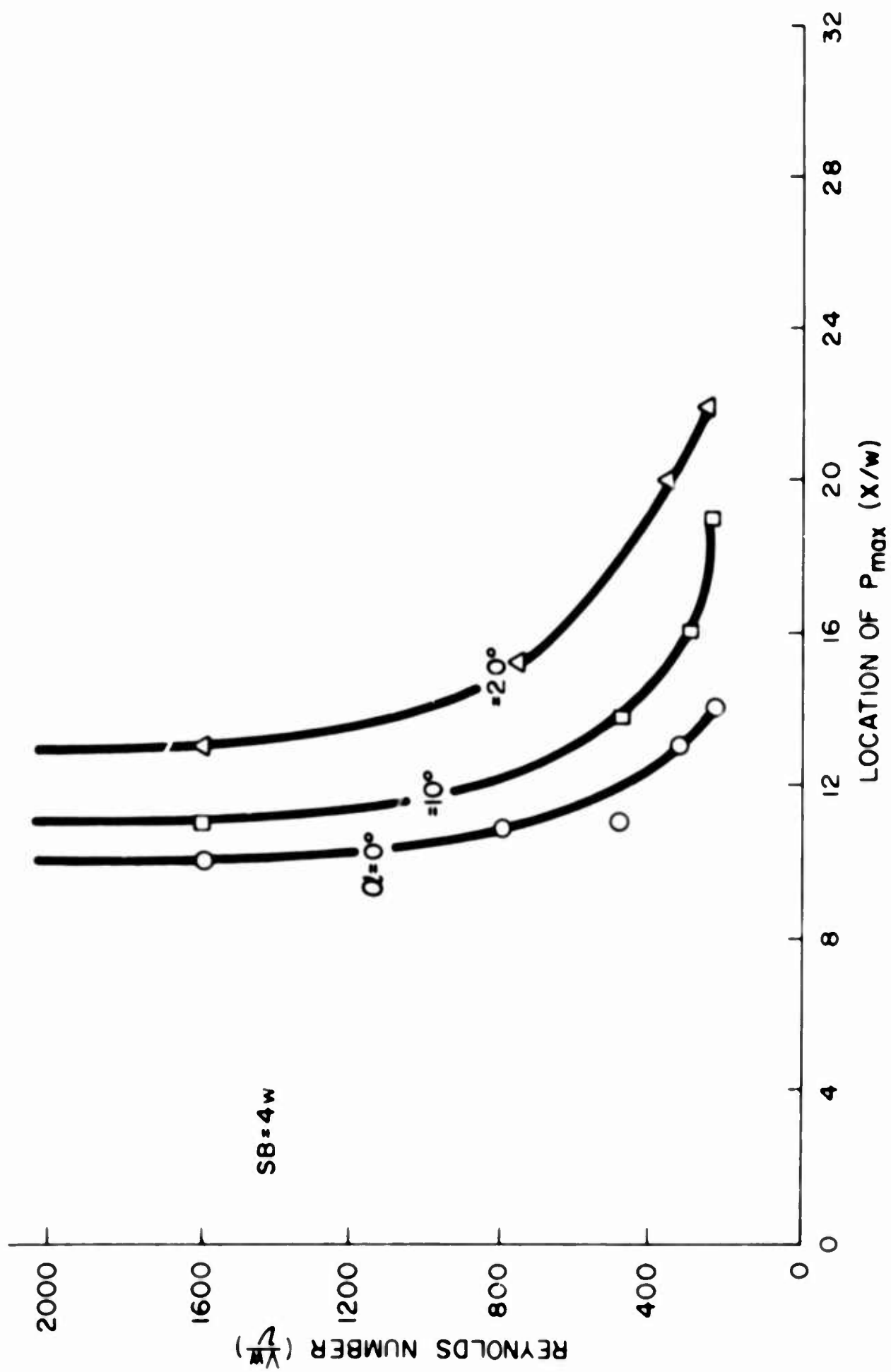


Figure 7. The effect of Reynolds number and wall angle on the location of the maximum wall pressure.

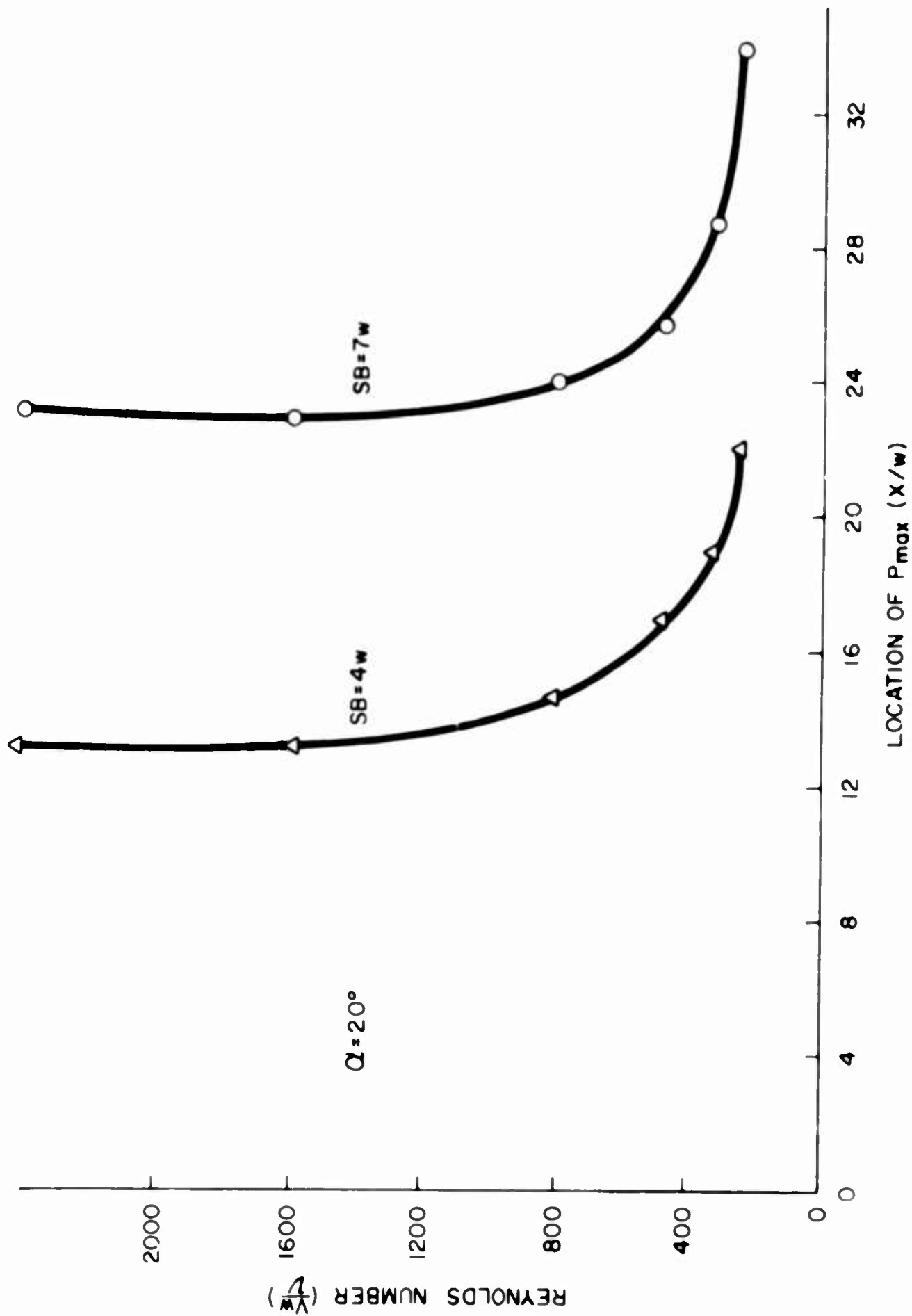


Figure 8. The effect of Reynolds number and setback on the location of the maximum wall pressure.

by E.F. Richards and S.D. Graber of Martin/Orlando

INTRODUCTION

Fluidic digital techniques, as did their electronic predecessors, yield precise unambiguous output information even though component parameters drift, or there is a very low signal to noise ratio. Unfortunately binary representations of fairly simple functions often require thousands of discrete logic elements; each element must respond just enough that the overall rate is suitable for practical use. For example; a digital mechanization using only a few levels of logic requires element operating rates of about 20 micro seconds to interface with a 3 cps control system.

Since operating rates are limited by element size and interconnecting line length, size reduction provides a compound improvement. Miniaturization also decreases volume, weight, power requirement, and enhances dynamic stability since the resonant frequency of the short passages is usually greater than the elements' response. Unfortunately as the size of a fluid jet is reduced it becomes progressively more difficult to sustain or induce the turbulence necessary for efficient fluidic elements.

This paper discusses the phenomenon of transition to turbulence and wall attachment in miniature jet devices. Appropriate analytical procedures are developed, a computerized solution discussed, and a visualization technique for correlating results is described.

TRANSITION TO TURBULENCE IN NOZZLES AND JETS

In order to obtain a turbulent flow pattern an appropriately defined critical Reynolds number must be exceeded. For a fluid jet with a sufficient aspect ratio and converging nozzle this parameter is conveniently taken as

$$R = \frac{\rho_o V_o b_o}{\mu_o}$$

where ρ = density, V = mean velocity, b = jet width, μ = viscosity, and the subscript "o" denotes conditions at the nozzle exit. If the nozzle width is decreased at a constant pressure level the efflux velocity V_o decreases due increased viscous action in the nozzle. This may cause a small change in ρ_o if the operating fluid is a gas and the pressure level is sufficiently high. For the most part, however, the Reynolds number decreases in proportion to b_o . Eventually the Reynolds number becomes too small and the jet will no longer be fully turbulent. Similar effects are observed if the aspect ratio of the nozzle is decreased.

Ideally, the flow should be turbulent in the nozzle section in which case the jet flow, being less stable, would be fully turbulent. However, if the nozzle flow is laminar, the jet's turbulent transition point affects the required element configuration. An analysis of transition in nozzles and a discussion of transition in jets follows.

NOZZLES

At typical values of R the shear layer develops very little in the convergent portion of the nozzle. The flow structure in the parallel wall portion of the nozzle is thus the same as that of the laminar inlet problem; see figure 1.*

The flow is assumed to enter the channel with a uniform velocity V_0 . Turbulence is often intense in the potential core, the latter having in effect an infinite Reynolds number. It is the stability of the shear layer that determines the gross characteristics of the flow.

Schlichting (1:168) obtained a series solution to the laminar inlet problem. His results, depicted in figure 2a indicate that the fully developed parabolic profile exists at $x/aR_e \approx 0.16$, where $R_e = V_0 a / \nu$. Results of an approximate momentum integral solution due to Sparrow (2, 3:43) are shown in figure 2b. His solution, based on assumed velocity profile of the form

$$\frac{u}{V_1} = 2\eta - \eta^2, \quad \eta = \frac{y}{\delta(x)} \quad (1)$$

agrees well with that of Schlichting. For the potential core velocity and boundary layer thickness he obtains

$$\delta \bar{x} = \frac{3(\bar{v}-1)(9\bar{v}-7)}{10\bar{v}^2} \delta \bar{v} \quad (2)$$

$$\bar{\delta} = 3(1 - 1/\bar{v}) \quad (3)$$

where $\bar{x} = x/aR_e$
 $\bar{v} = V_1/V_0$
 $\bar{\delta} = \delta/a$ (4)

Eq. (2) integrates to

$$\bar{x} = \frac{3}{10} (9\bar{v} - 16 \ln \bar{v} - 7/\bar{v} - 2) \quad (5)$$

The shear layers join at $\frac{x_1}{aR_e} = 0.103$ according to Sparrow's solution.

*Figures appear on pages 60 through 70.

To determine the stability of the Karman-Pohlhausen velocity profile given by eq. (1) we employ results due to Schlichting and Ulrich (1:414). The latter have obtained the curve shown in figure 3 for the critical Reynolds number based on the momentum thickness of the boundary layer vs. a shape factor Λ defined by

$$\Lambda = \frac{\int_0^{\delta} u^2 dy}{\int_0^{\delta} u dy}$$

From equations (3) and (4) we obtain

$$\Lambda = 9 \left(1 - \frac{1}{\bar{v}}\right) \frac{d\bar{v}}{dx}$$

which, using equation (2), becomes

$$\Lambda = \frac{30(\bar{v} - 1)}{9\bar{v} - 7} \quad (6)$$

Applying the definition of the momentum thickness to the profile of eq. (1) we obtain

$$\delta^* = \int_{y=0}^{\infty} \left(1 - \frac{u}{V_1}\right) dy = \frac{1}{3}$$

Then from equations (3) and (4)

$$\delta^* = \frac{1}{3} \delta = a \left(1 - \frac{1}{\bar{v}}\right)$$

Hence

$$R_{\delta^*} = \frac{V_1 \delta^*}{\nu} = \frac{V_1 a}{\nu} \left(1 - \frac{1}{\bar{v}}\right) = R_a \left(1 - \frac{1}{\bar{v}}\right) \quad (7)$$

\bar{v} lies in the domain $1.4 \leq \bar{v} \leq 1.5$ (see figure 2) which by equation (6) gives for the range of Λ

$$0 < \Lambda < 2.3$$

We see from the semi-log plot of figure 3 that for the range of Λ of interest we may approximate the curve by

$$(R_{s*})_{crit} = 645 \exp(0.568\Lambda) \quad (8)$$

Then setting R_{s*} in equation (7) equal to $(R_{s*})_{crit}$ in equation (8) we obtain

$$R_a(1 - 1/\bar{v}) = 645 \exp(0.568\Lambda) \quad (9)$$

For values of \bar{v} between 1.0 and 1.5 we may obtain Λ from equation (6) and x from equation (5). Then equation (9) may be solved for R_a as a function of x . The computed results of this procedure up to $R_a = 18,000$ are plotted in Figure 4. The loci of points at which the boundary layers join and then become fully developed are plotted as two straight lines in the figure. For R_a less than 7,177 transition will not occur before the boundary layers coalesce. C.C. Lin (1:399) calculated the laminar stability of the fully developed parabolic profile, obtaining $R = 3,544$ as shown in the figure. The assumed connection in the region between the end of the potential core and the existence of the fully developed profile (which strictly speaking is approached asymptotically) is shown as a dashed line. The plot of figure 4 includes the Reynolds numbers generally found in small amplifiers. Representative values of the above solution at higher Reynolds numbers are given as follows:

19,178	15.5
22,385	11.4
27,738	7.85
38,461	4.77
70,679	2.16

With a channel of reasonable length, say 10 channel widths, a Reynolds number greater than 23,000 is required to obtain turbulence within the channel section. With the Reynolds number encountered in miniature amplifiers (typically 10,000 or less) and typical nozzle lengths, transition will not occur in the nozzle section.

FREE JETS

The results of the previous section indicate that for most turbulent jets encountered in small fluid amplifiers turbulence must be initiated in the jet itself. The first successful prediction of a critical Reynolds number for two-dimensional jet flow was made by Curle (4), in 1957. He obtained the expression

$$R_b \left\{ 1 + \frac{x}{0.656 R_b} \right\}^{1/3} = 3.843 \quad (10)$$

where R_0 is the critical Reynolds based on the mean efflux velocity and nozzle width and x is the distance from the nozzle exit at which transition occurs. To determine the Reynolds number for a fully developed jet we set $x = 0$ and obtain $R_0 = 4$.

Tatsumi and Kakutani (5), in 1958, obtained a neutral stability curve which they considered to be more accurate in shape than Curle's but which predicts essentially the same critical Reynolds number. Curle had stated that this value seems quite low but referred to experiments by Andrade (6) that indicate that transition occurs in jets with R_0 in the neighborhood of 10. Schlichting (1:168) quotes the critical value of 30 from Andrade's experiments. In Andrade's experiments however turbulence usually wasn't indicated until some 50 or more nozzle widths from the exit. For any value of R_0 we would expect transition at some point downstream so the statement is not actually justified.

Chanaud and Powell (7) and Sato and Sakao (8) have experimentally investigated transition in two-dimensional jets. Neither pair of authors verifies nor conclusively discounts the theoretical predictions.

In order to predict the critical Reynolds number the linearized Navier-Stokes equations are reduced to the Orr-Sommerfeld equation by the assumption of parallel flow. Calculations by Sato and Sakao demonstrate the doubtful validity of the mathematical consequences of this assumption at the low Reynolds number of 4.

These studies of laminar jet stability assume a fully developed jet profile. However a parabolic profile is not usually attained in the nozzle and the fully developed jet profile would not exist until some distance beyond the nozzle exit. Thus a stability analysis ignoring the transition zone would not be completely adequate.

The distance between the points of instability and transition depend to a marked degree on the intensity of turbulence in the potential core. A highly turbulent potential core can be instrumental in facilitating transition in the jet. Hence, a shorter nozzle, less capable of damping the turbulent fluctuations, may sometimes be preferable. A short nozzle also is preferable from the standpoint of predictability, since a nearly uniform velocity profile at the exit results in simple initial conditions facilitating the analysis of the turbulent jet as performed in the next section.

GEOMETRIC REQUIREMENTS FOR BISTABLE OPERATION

Having established turbulence the problem becomes that of determining a minimum sized geometry that will insure bistable operation. Brown (9) recognized that attachment is caused by a static instability of the jet in its center position. He obtained a mathematical criterion based on flow equilibrium which required experimental load-flow curves for implementation. Recently an analysis by Simson (10) was coupled with a stability criterion based on force equilibrium to obtain a theory requiring little or no experimental data (11). The results were shown to be derivable from either the

flow or force equilibrium criterion. This analysis has since been extended at Martin/Orlando to include low Mach number compressible jets (essentially subsonic and perfectly expanded sonic jets).

The nomenclature used in the following analysis is depicted in figure 5 and the associated list.

For small deflections the centerline of the jet deflects as a circular arc. The lateral component of the jet reaction can be expressed as:

$$F_M = J_0 \sin \theta \cong J_0 \theta = \frac{2J_0}{x_0} y_1 \quad (11)$$

The force due to the unbalanced pressure acting on the jet is given by

$$F_P = (P_2 - P_1) x_0 \tau \quad (12)$$

The mass flow coming into the control region from the environment is

$$W_{a1} = C_d \gamma y_{a1} \tau \sqrt{2\rho_s (-P_1)} \quad (13)$$

where C_d is an experimentally determined coefficient with possible values $0 \leq C_d \leq 1$ ($C_d = 1$ for inviscid flow) and γ is an expansion coefficient ($\gamma = 1$ for incompressible flow). Noting that $w_{e1} = w_{a1}$, in the absence of control lines, we obtain from Eq. (13)

$$P_1 = - \frac{1}{2\rho_s} \left(\frac{w_{e1}}{C_d \gamma y_{a1} \tau} \right)^2 \quad (14)$$

We will assume that the entrained flow changes negligibly with curvature and hence $w_{e1} = w_{e2} = w_e = \text{const.}$ (It is shown in reference 11 that changes in w_e have very little effect on center position stability.) Writing the relation analogous to Eq. (14) for side 2, subtracting the two equations and substituting into Eq. (12) gives

$$F_P = \frac{w_e^2 x_0}{8\rho_s (C_d \gamma)^2 \tau} \left[\frac{1}{y_{a1}^2} - \frac{1}{y_{a2}^2} \right]$$

From the geometry of the jet we have

$$\begin{aligned} y_{a1} &= D - y_1 \\ y_{a2} &= D + y_1 \end{aligned} \quad , \quad D = y_0 - \frac{b_x}{2}$$

where b_0 is the width of the jet at $x = x_0$.

Therefore,

$$F_p = \frac{x_0}{8\rho_s \lambda} \left[\frac{w_e^2}{(C_d Y)^2} \left\{ \frac{1}{(D-y_1)^2} - \frac{1}{(D+y_1)^2} \right\} \right] \quad (15)$$

The criterion for center-position stability is

$$\left(\frac{\partial F_M}{\partial y_1} \right)_{y_1=0} \geq \left(\frac{\partial F_p}{\partial y_1} \right)_{y_1=0}$$

Assuming C_d and Y remain constant for small deflections, application of the above criterion to equations (11) and (15) gives

$$\left(y_0 - \frac{b_0}{2} \right) \geq \left(\frac{x_0}{2C_d Y} \right)^{2/3} \frac{w_e^{2/3}}{(\rho_s \lambda J_0)^{1/3}} \quad (16)$$

It now is necessary to determine w_e and $\frac{b_0}{2}$ for the compressible jet. Here we will restrict ourselves to low mach number flows for which the following assumptions should provide reasonable accuracy:

1. The velocity profile and half width of the jet remain the same as for the incompressible case.
2. Adiabatic (isoenergetic) mixing occurs in the jet.
3. The nozzle flow is perfectly expanded.
4. Perfect gas.

Subject to these assumptions, we have

$$\left(\frac{p}{p_0} \right) = \left(\frac{T}{T_0} \right)^{\gamma} \quad (17)$$

where the subscript "0" denotes static conditions at the nozzle exit. From the energy eq. for adiabatic flow

$$C_p T + \frac{1}{2} u^2 = C_p T_0 + \frac{1}{2} u_0^2$$

which gives

$$\frac{T}{T_0} = 1 + \frac{\frac{1}{2} u_0^2}{C_p T_0} \left[1 - \left(\frac{u}{u_0} \right)^2 \right]$$

From the definition of Mach number we obtain

$$\frac{T}{T_0} = 1 + \frac{\gamma-1}{2} M_0^2 \left[1 - \left(\frac{u}{u_0} \right)^2 \right] \quad (18)$$

Combining Eqs. (17) and (18) gives

$$\frac{\rho}{\rho_0} = \left\{ 1 + \frac{\gamma-1}{2} M_0^2 \left[1 - \left(\frac{u}{u_0} \right)^2 \right] \right\}^{-1} \quad (19)$$

The jet mass flow rate at station x is given by

$$W = \int_{-b/2}^{+b/2} \rho u dy = \rho_0 u_0 \int_{-b/2}^{+b/2} \frac{\rho}{\rho_0} \frac{u}{u_0} dy$$

From eq. (10) and the symmetry of the integrand

$$\frac{W}{W_0} = \frac{2}{b_0} \int_0^{b/2} \frac{u/u_0}{\left\{ 1 + \frac{\gamma-1}{2} M_0^2 \left[1 - \left(\frac{u}{u_0} \right)^2 \right] \right\}} dy \quad (20)$$

rearranging

$$\frac{W}{W_0} = \frac{4}{(\gamma-1) b_0 M_0^2} \int_0^{b/2} \frac{u/u_0}{\xi - \left(u/u_0 \right)^2} dy$$

$$\xi = 1 + \frac{2}{(\gamma-1) M_0^2}$$

The results of Simson (10) are now employed to express the velocity profile as a function of x and y in the zone of developing ($x \leq x_0$) and developed ($x \geq x_0$) flow.

$$x \leq x_0: \quad \frac{u}{u_0} = \begin{cases} 1 & |y| < \frac{b_0}{2} \left(1 - \frac{x}{x_0} \right) \quad (\text{potential core}) \\ [1 - \eta^2]^{1/2} & -1 < \eta < +1 \quad (\text{shear layer}) \end{cases}$$

$$x \geq x_c: \frac{u}{u_0} = \sqrt{\frac{x_c}{x}} \left[1 - \eta^{3/4} \right]^2, \quad -1 < \eta < +1 \quad (21)$$

$$\text{where } \eta = \frac{x_c}{1.378 b_0 x}$$

Substituting from eq. (21) into eq. (20) gives

$$\frac{w}{w_0} = \left(1 - \frac{x}{x_c} \right) + \frac{1.378}{\frac{(\gamma-1)}{2} M_0^2} \frac{x}{x_c} \phi(\xi) \quad x \leq x_c \quad (22)$$

$$\frac{w}{w_0} = \frac{1.378}{\frac{(\gamma-1)}{2} M_0^2} \left(\frac{x}{x_c} \right)^{3/2} \phi\left(\xi \frac{x}{x_c}\right) \quad x \geq x_c$$

$$\phi(u) = 2 \int_0^1 \frac{(1 - \eta^{3/4})^2}{u - (1 - \eta^{3/4})^4} d\eta$$

A numerical evaluation of the integral of eq. (22) is presented in Table 1.

For $\gamma = 1.4$ (air, nitrogen, etc.), eqs. (22) becomes

$$\frac{w}{w_0} = 1 + \frac{x}{x_c} \left[6.89 \frac{\phi(\xi)}{M_0^2} - 1 \right] \quad x \leq x_c$$

$$\frac{w}{w_0} = 6.89 \left(\frac{x}{x_c} \right)^{3/2} \frac{\phi\left(\xi \frac{x}{x_c}\right)}{M_0^2} \quad x \geq x_c$$

$$\xi = 1 + \frac{5}{M_0^2}$$

Noting that the entrained flow is given by $w_e = w - w_0$, we obtain

$$\frac{w_e}{w_0} = \left[6.89 \frac{\phi(\xi)}{M_0^2} - 1 \right] \frac{x}{x_c} \quad x \leq x_c$$

$$\frac{w_e}{w_0} = 6.89 \left(\frac{x}{x_c} \right)^{3/2} \frac{\phi\left(\xi \frac{x}{x_c}\right)}{M_0^2} - 1 \quad x \geq x_c \quad (23)$$

The term in brackets of eq. (23a) is plotted vs. Mach number in figure 6. As $M_0 \rightarrow 0$, $\frac{w_e}{w_0} \rightarrow 0.364 \frac{x}{x_c}$ as obtained by Simson (10) for an incompressible jet. Substituting eq. 23 into eq. 16 and using the values for $b_{1/2}$ for the incompressible jet from reference 10, we obtain the geometrical requirements for stability;

$$x_0 \leq \bar{x} : \\ y' \geq 0.878 \frac{x'_0}{\bar{x}} + 0.5 + \left(\frac{\rho_0}{\rho_s}\right)^{1/3} \left\{ \left[\frac{6.89}{M_0^2} \Phi(\xi) - 1 \right] \left(\frac{x'_0}{2\bar{x}C_dY} \right) \right\}^{2/3}$$

$$x_0 \geq \bar{x} :$$

$$y' \geq 1.378 \frac{x'_0}{\bar{x}} + \left(\frac{\rho_0}{\rho_s}\right)^{1/3} \left\{ \frac{6.89}{M_0^2} \left(\frac{x'_0}{\bar{x}} \right)^{3/2} \Phi\left(\xi \frac{x'_0}{\bar{x}}\right) - 1 \right\} \left(\frac{\bar{x}}{2C_dY} \right)^{2/3}$$

where primes denote nondimensionalization with respect to b_0 .

For the geometry of figure 5 we relate the critical value of y_0 to the critical value of ϕ by

$$\phi = \tan^{-1} \left[\frac{y'_0 - (a' + \frac{1}{2})}{x'_0} \right]$$

Thus, the geometry for marginal bistability is a function of \bar{x} , $\frac{\rho_0}{\rho_s}$, M_0 , C_d and Y . Experiments with axisymmetrical jets indicate that the potential core length, \bar{x} , is a function of both Reynolds and Mach numbers (12 - discussion by Baines, 13). It appears that with $M_0 \leq 1.0$, Mach number effects are unimportant. Until further data on two-dimensional jets is available, $\bar{x} = 5.2 b_0$, based on data taken at pipe Reynolds numbers between approximately 4,000 and 10,000 (12 - fig. 9) is recommended.

Except with large x_0 and w_0 , compressibility effects in the atmospheric flow w_a should be negligible so that $Y \approx 1.0$. If not, Y may be determined from compressible flow theory. ρ_0/ρ_s and M_0 may also be determined from compressible flow theory. This requires a determination of the control port pressure which may be accomplished by assuming $C_d = 1.0$ or, if accuracy warrants it, lower values based on experimental data may be used. Calculations based on $C_d Y = 1.0$ include a factor of safety in the prediction of bistability since frictional and compressibility effects in w_a (resulting in $C_d Y < 1.0$) enhance center-position instability. Agreement with experimental data has been obtained with values of C_d between 0.5 and 0.7.

The above analysis has been extended (in the incompressible case) to include control flow into the control port region (which has a stabilizing effect) and may be used to predict line resistances for bistability (reference 11).

From the analysis we may obtain design charts such as that of figure 7 which plots the wall angle for marginal center position stability vs. amplifier length x_0 and offset a (here for the case of incompressible flow and $C_d = 1.0$).

Several techniques have been employed to indicate the onset of turbulence in fluid flows. Common methods include hot wire anemometry, the use of pitot tubes to detect a sudden drop in dynamic pressure, and optical methods. The latter provides less quantitative data but provides useful information concerning the flow structure and influences that might otherwise go undetected. Chanaud and Powell obtained useful information concerning jet stability by means of a dye-marking technique. In small fluid amplifiers dye marking is rather cumbersome. Injectors cannot be conveniently placed in the nozzle of miniature devices and if the entire jet flow is dyed the tests cannot be run continuously without eventually dyeing the control region as well and making the flow field difficult to observe.

A birefringent flow visualization technique has proven extremely useful in facilitating direct observation of the flow structure existing in laboratory test elements. Some water-dye solutions will behave in a manner analogous to stress sensitive solids and provide a vivid display of lines of constant shear in a flowing liquid. A beautiful display of laminar flow regimes and a clearly defined point of transition may be observed. The location of a turbulent jet can be readily determined.

In figures 8 through 13, photographs of birefringent flow studies in an element with a 0.031 inch nozzle and an aspect ratio of 1 are presented. Unfortunately, the black and white reproduction has lost much of the detail.

Figure 8 shows the element operating at 2.5 psi. For this figure and the next four figures the control ports are closed and the output legs are vented to a recirculatory system. At 2.5 psi the flow throughout the element appears to be laminar and no attachment occurs.

Figure 9 shows the element operating at 5 psi. The jet is going turbulent just upstream of the splitter tip, but still attachment does not occur.

Figure 10 was taken with an operating pressure of 5 psi. The jet is going turbulent in the control port region but still does not attach.

Figures 11 and 12 show the jet attached to the left and right sides respectively. Both were taken at an operating pressure of 11 psi. The jet is going turbulent shortly after it enters the "Vee" shaped control zone. Although it is difficult to tell from the photographs, the point of attachment is upstream of the control inputs. This is easier to verify by direct observation of the device.

Figure 13 was taken with an operating pressure of 2 psi with both control ports vented to the return system. The return pressure existing in the left port is slightly higher than that in the right and the jet is deflected so that most of the flow is traveling down the right output. The

flow is laminar throughout and no attachment occurs. The entire flow structure is vividly defined.

In order to compare data taken with the birefringent flow setup a small milling machine has been fitted with 0.1 mil dial indicators on all three axis and a tiny probe soft soldered to a slip-on tube fitting and placed in the cutting tool mount of the machine (figure 14). This enables accurate locating of the jet centerline in small elements enabling the determination of regimes of bistable flow, switching characteristics, etc.

SUMMARY AND CONCLUSIONS

A study of transition to turbulence in nozzles has been undertaken with useful predictions resulting. To the right of the vertical line and above the curved lines of figure 4 the nozzle flow is potentially turbulent. The results should be used with a realization of their approximate nature as they are based on an approximate analysis of the laminar flow problem. It should also be realized that the limit of stability for the fully developed flow which lies at $R_e = 3,544$ exceeds the experimentally observed transition Reynolds number contradicting the theory of small disturbances on which Lin's analysis is based (1:451).

Both theoretical and experimental work in transition to turbulence in jets is needed. The effects of aspect ratio as well as Reynolds number needs to be investigated. The birefringent visualization technique appears to be well adapted to such experimentation.

It has been possible to predict the geometrical requirements for bi-stability in symmetrical elements operating with subsonic and perfectly expanded sonic jets. Limited verification of the theory has been completed in the incompressible case. All trends appear to be well represented.

References

1. Schlichting, Hermann, Boundary Layer Theory, McGraw Hill Book Co., Inc. New York, 1962.
2. Sparrow, E., NACA TN 3331, Jan. 1955.
3. Rohsenow, W. M., and Choi, H. Y., Heat Mass and Momentum Transfer, Prentice-Hall Inc., Anglewood Cliffs, N.J., 1963.
4. Curle, N., "On Hydrodynamic Stability in Unlimited Fields of Viscous Flow," Proc. Roy. Soc. London, A238, 1957.
5. Tatsumi, T. and Kakutani, T., "The Stability of a Two-dimensional Laminar Jet," Journal of Fluid Mechanics, Vol. 4, 1958, P. 261.
6. Andrade, E. N., "The Velocity Distribution in a Liquid Into Liquid Jet, Part 2: The Plane Jet," Proc. Phys. Soc. London, Vol. 51, 1931.
7. Chanaud, R. C. and Powell, A., "Experiments Concerning the Sound-Sensitive Jet," Journal of the Acoustical Society of America, July 1962.
8. Sato, H. and Sakao, F., "Instability of a Two-dimensional Jet," Journal of Fluids Mechanics, Vol. 20, March 1964.
9. Brown, F. T., "Pneumatic Pulse Transmission with Bistable-Jet-Relay Reception and Amplification," Sc.D. Thesis, Dept. of Mech. Engr., Mass. Inst. of Tech., May 1962.
10. Brown, F. T. and Simson, A. K., "Research in Pressure-Controlled Fluid Jet Amplifiers," Report #9213-1 prepared for M.I.T. for U.S. Army, November 1963.
11. Graber, S.D., "Stability Problems in Fluid Jet Amplifier Components and Systems," S.M. Thesis, Dept. of Mech. Engr., Mass. Inst. of Tech., May 1965.
12. Albertson, M.L., et.al., "The Diffusion of Submerged Jets," Transactions of American Society of Civil Engineers, Vol. 115, 1950. Discussed by Baines, W.D., et.al.
13. Anderson, A.R. and Johns, F.R., "Characteristics of Free Supersonic Jets Exhausting Into quiescent Air," Jet Propulsion, Vol. 25, 1955, No. 1.

TABLE I

<u>μ</u>	<u>$\phi(\mu)/2$</u>
2.0	0.3720
3	.2099
4	.1469
5	.1131
6	.09200
7	.07755
8	.06702
9	.05902
10	.05272
11	.04764
12	.04346
13	.03995
14	.03696
15	.03439
16	.03216
17	.03019
18	.02846
19	.02691
20	.02552
25	.02029
30	.01684
35	.01439
40	.01256
45	.01115
50	.01002
60	.008333
70	.007132
80	.006234
90	.005537
100	.004979
200	.002482
300	.001653
400	.001193
500	.0009411
600	.0008257
700	.0007077
800	.0006192
900	.0005503
1000	.0004952
1500	.0003301
2000	.0002676

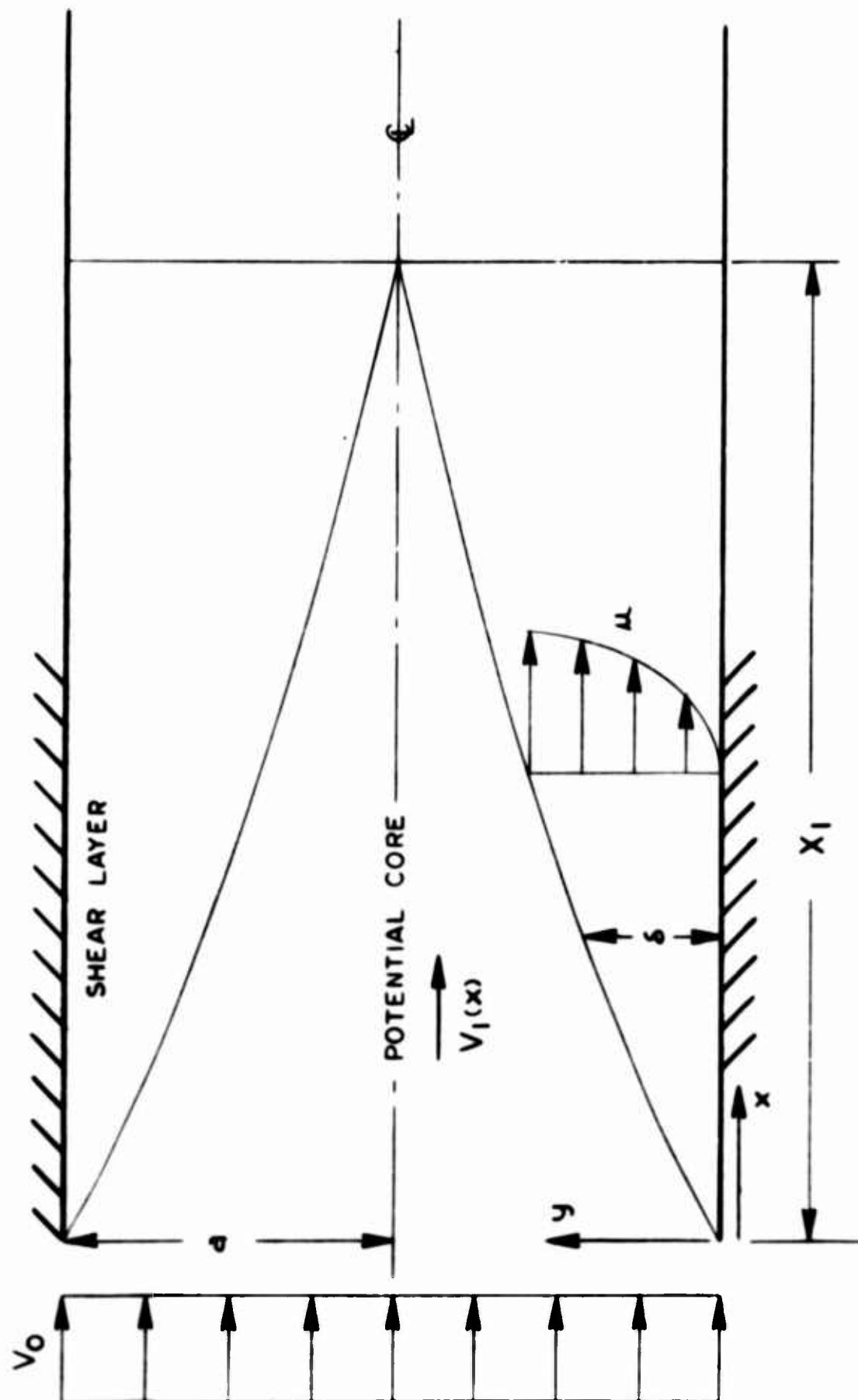
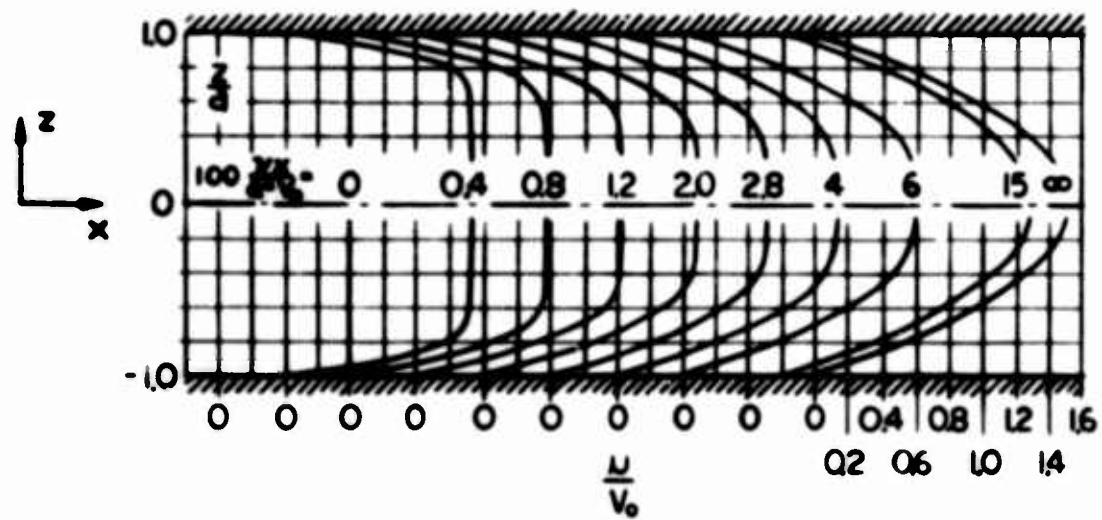
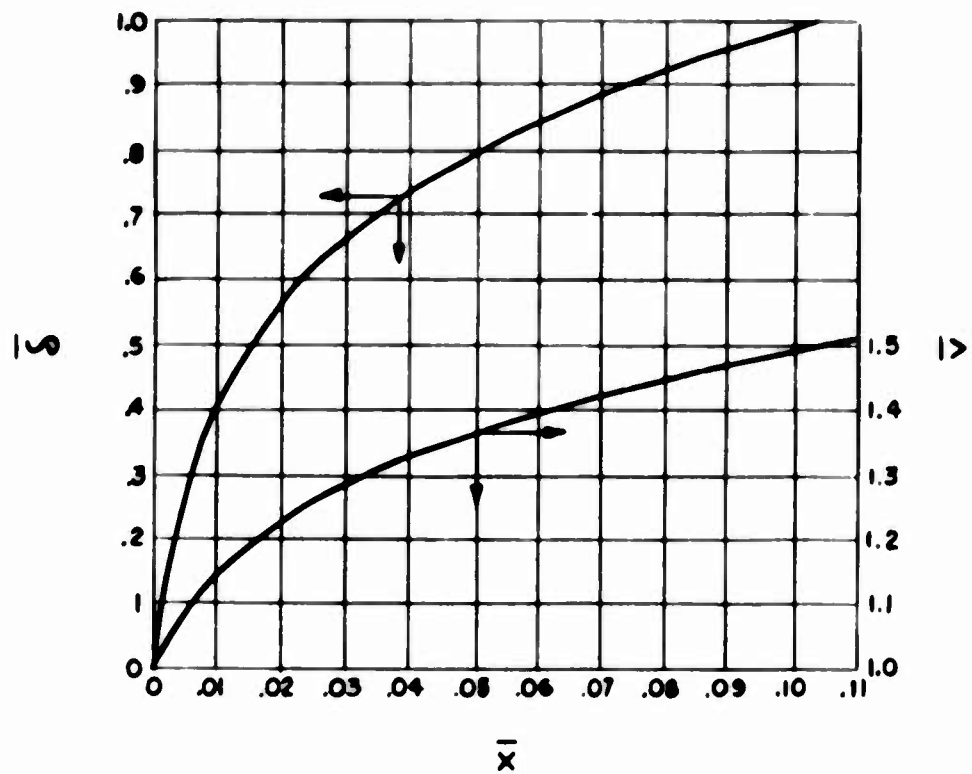


FIGURE 1 TWO-DIMENSIONAL LAMINAR INLET FLOW



(a)



(b)

Fig. 2. Laminar flow in inlet section between parallel plates. (a) Results of series solution (Schlichting). (b) Results of integral solution (Sparrow).

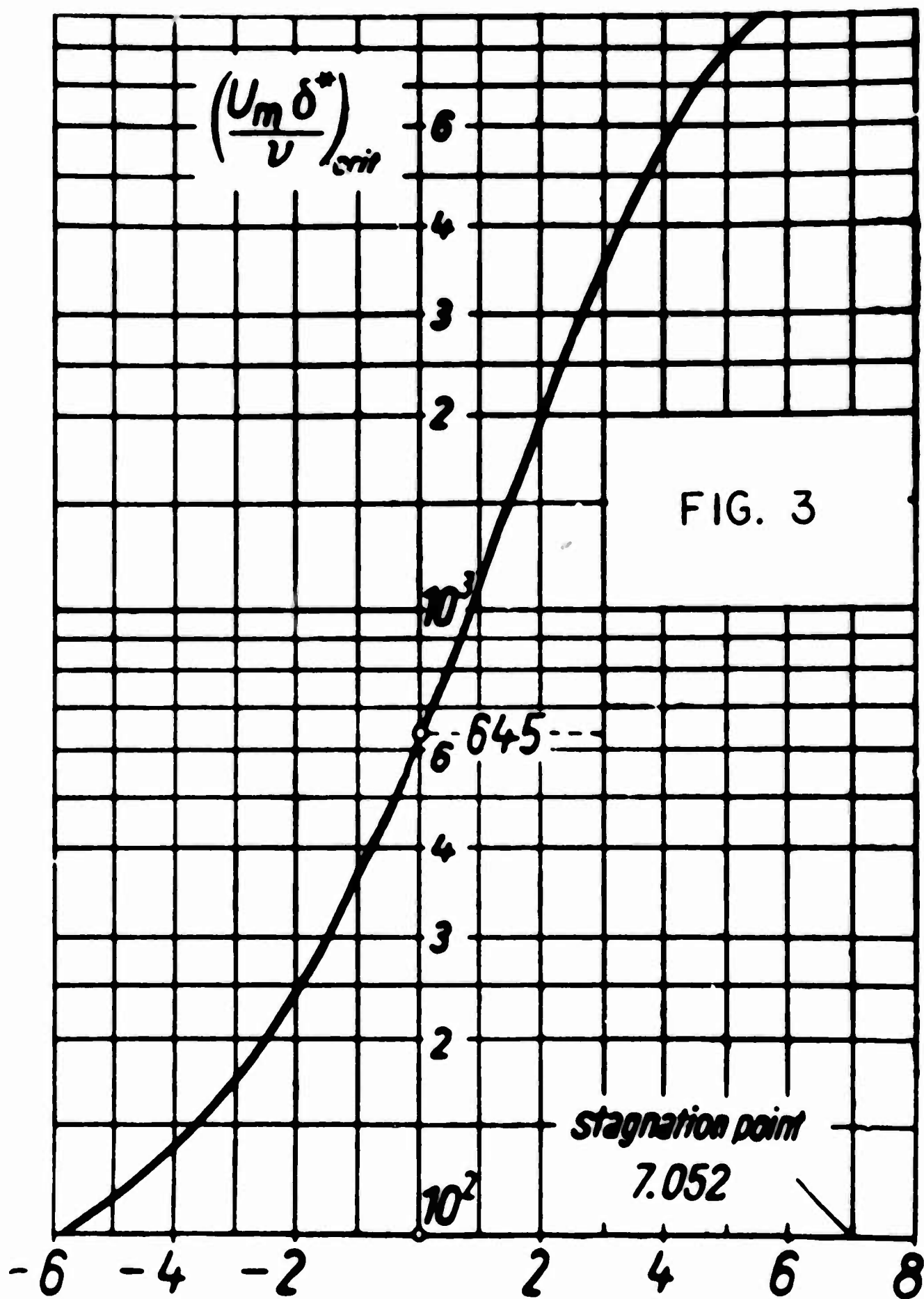


FIG. 3

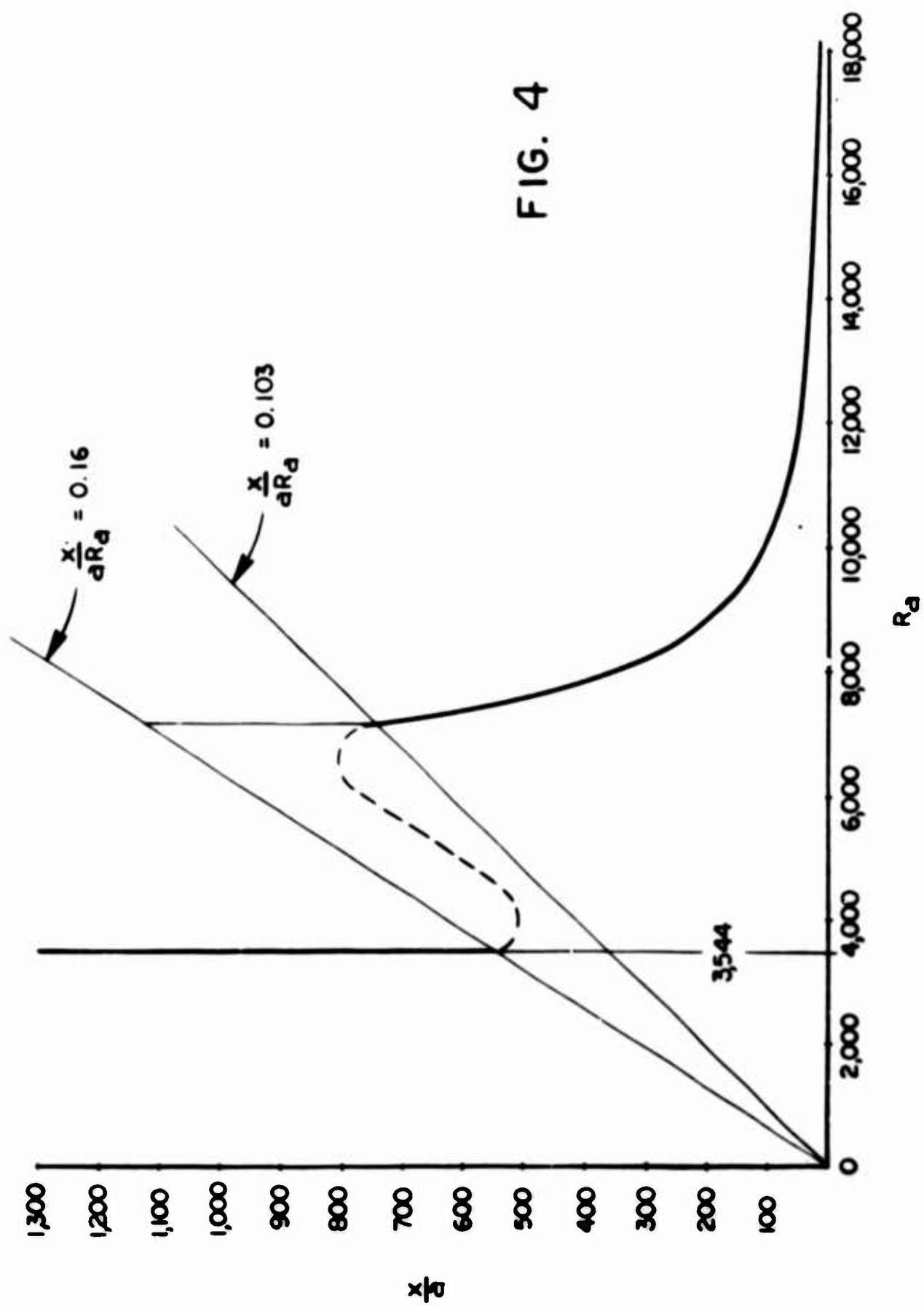
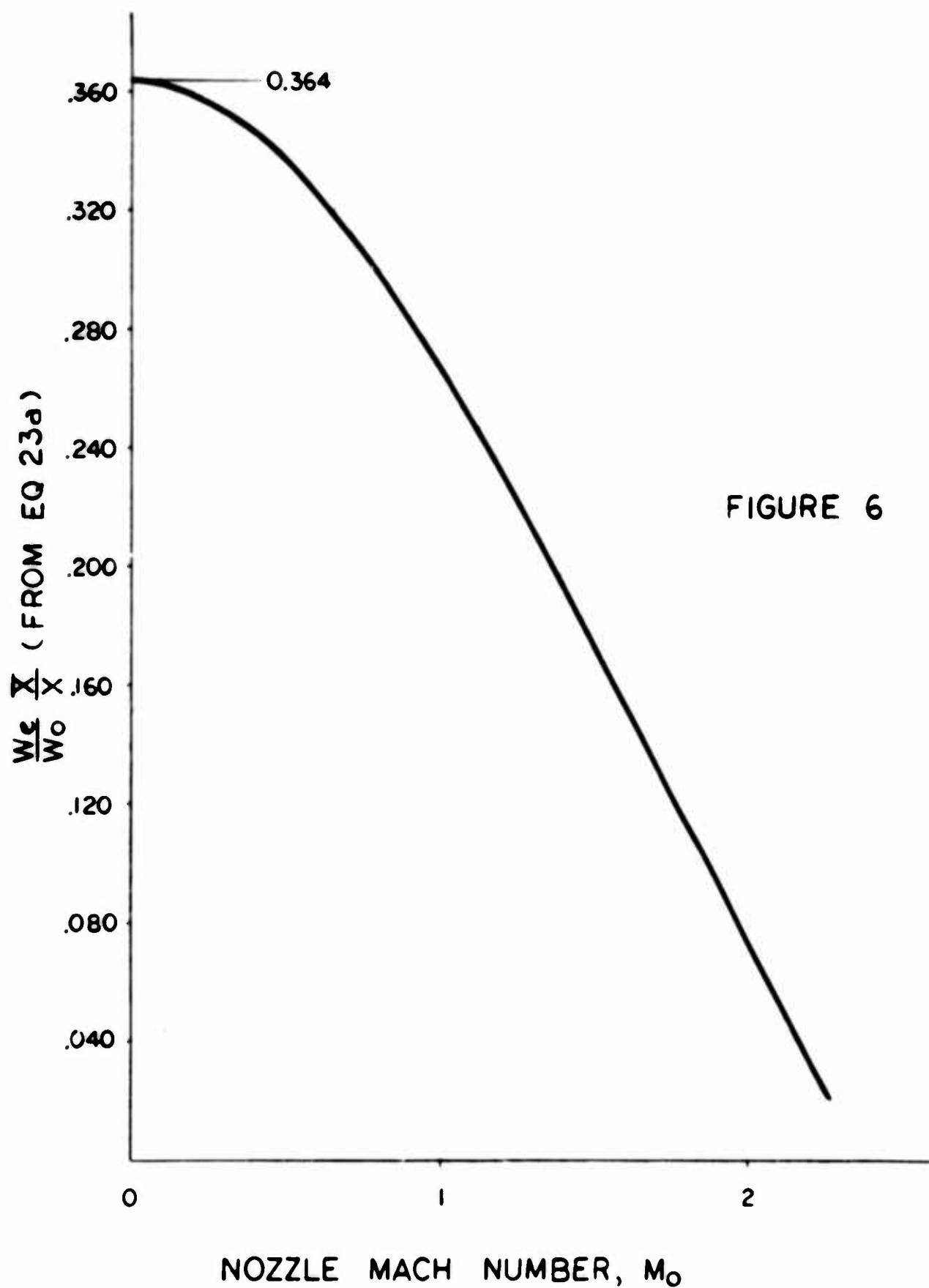


FIG. 4



FULLY TURBULENT JET

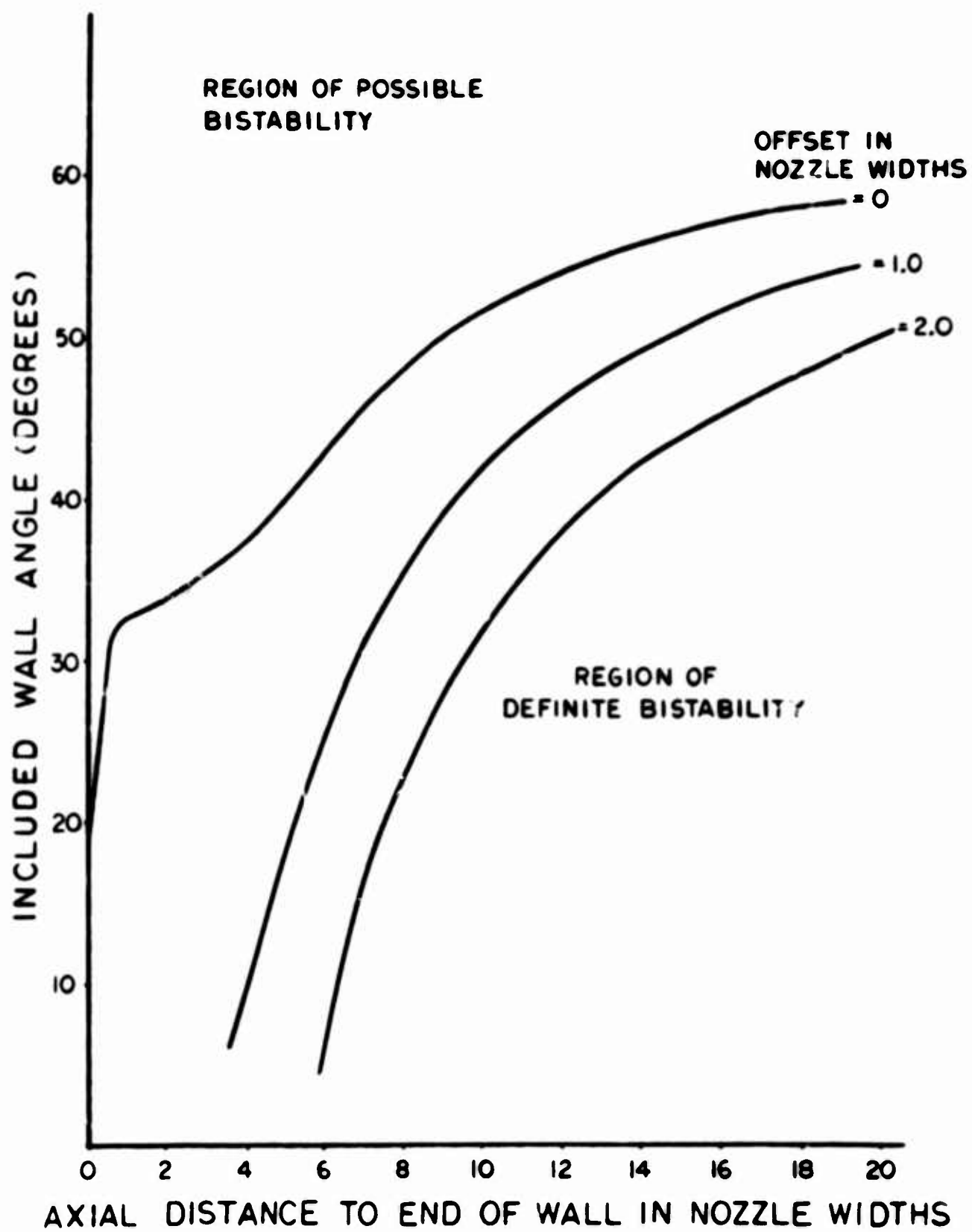


FIG. 7

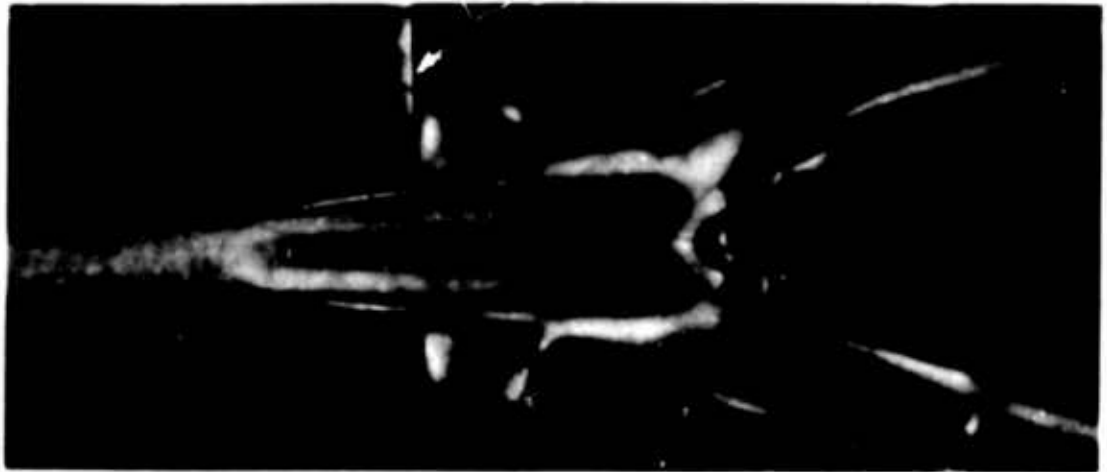


FIG. 8
10x



FIG. 9
10x



FIG. 10
10x

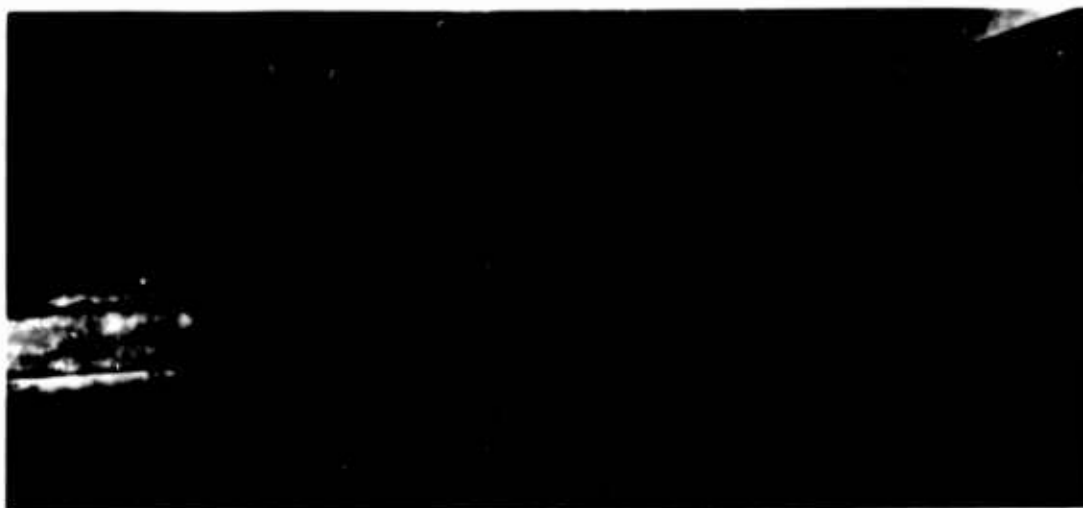


FIG. 11
10 X

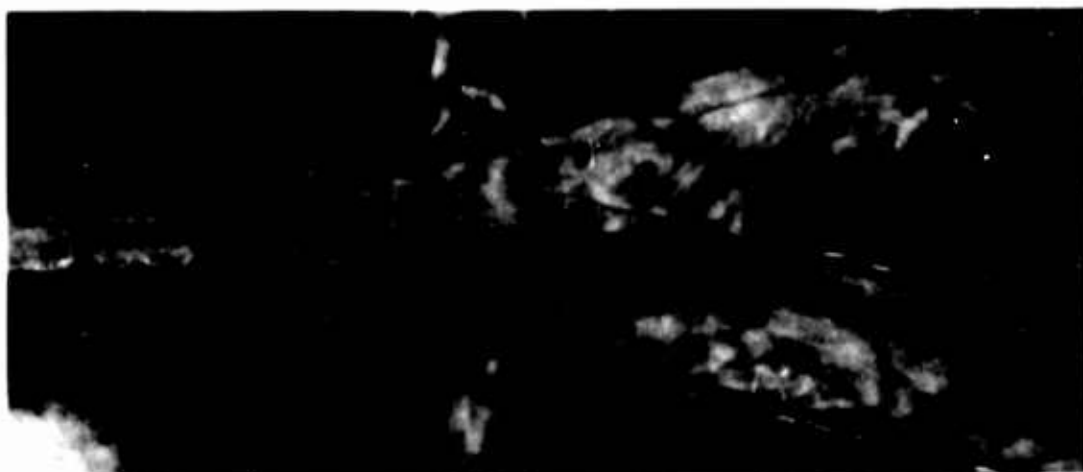


FIG. 12
10 X

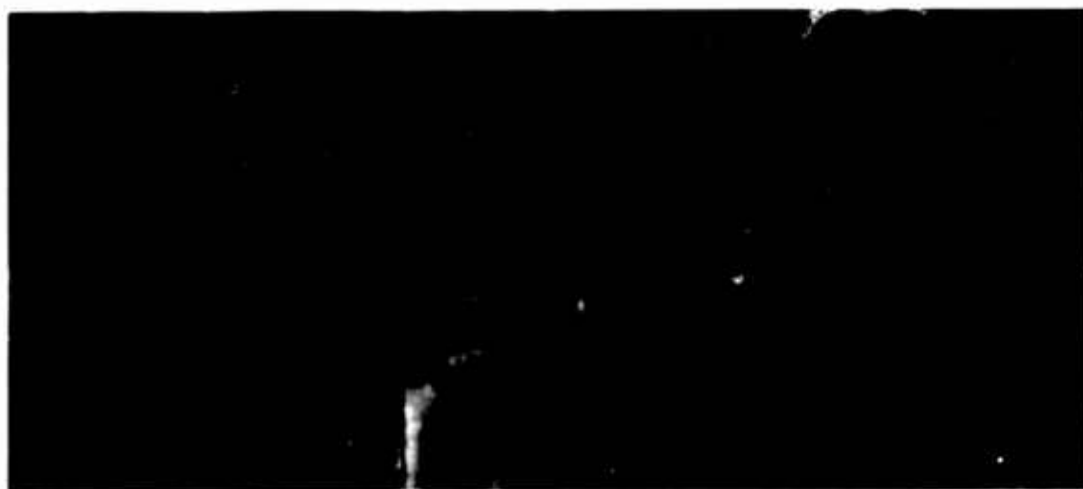
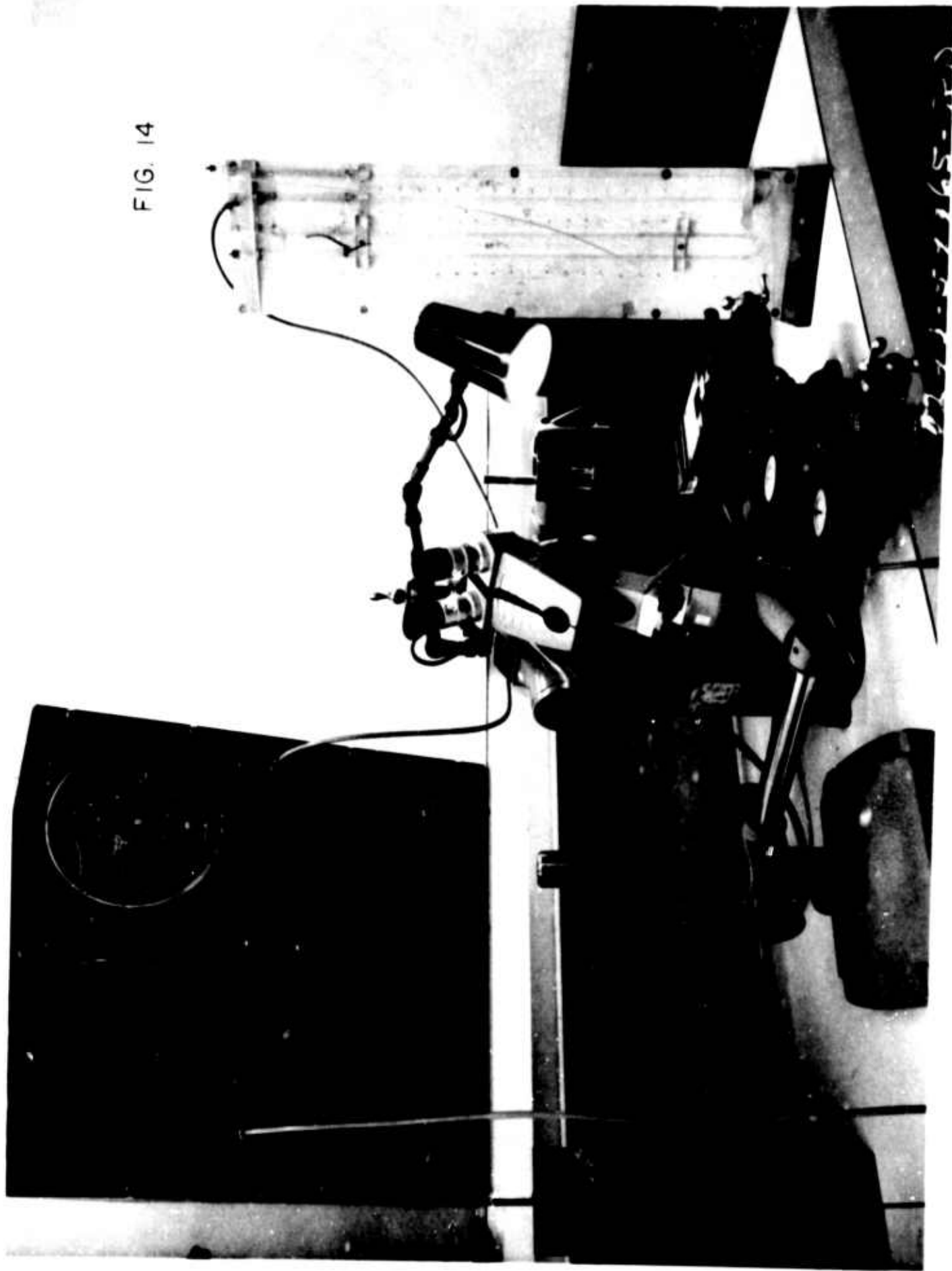


FIG. 13
10 X

FIG. 14



AN EXPERIMENTAL STUDY OF THE STATIC INTERACTION OF AN AXISYMMETRICAL FLUID JET AND A SINGLE RECEIVER-DIFFUSER

Karl N. Reid, Jr., Assistant Professor
School of Mechanical Engineering
Oklahoma State University
Stillwater, Oklahoma

ABSTRACT

Results are presented from studies of several fundamental hydrodynamic processes typically encountered in fluid-jet modulator systems. Measured velocity profiles are presented for the flow establishment, transition, and established flow regions of an axisymmetrical, free, submerged, turbulent air jet. Improved velocity profile correlation and prediction techniques are suggested.

Studies have been conducted to elucidate the details of internal diffusion of the nonuniform stream resulting from direct impingement of a submerged jet on the mouth of a receiver-diffuser system comprised of a constant-area mixing section followed by an area-change diffuser. Results are presented from measurements of transverse profiles of the axial velocity and wall static pressure taken at various stations along the receiver-diffuser system. Velocity profile uniformity factor correlations are presented which permit rapid computation of the static pressure increase or decrease as a function of length of the constant-area mixing section. Judgements and decisions may be made as to the "optimum" length of the constant-area mixing section of a receiver-diffuser in order to maximize over-all diffusion efficiency.

A set of measured pressure-flow characteristics is presented for the case of an axially aligned, axisymmetric jet-receiver-diffuser system. It is demonstrated that previously used methods of predicting blocked-load pressure recovery and open-load flow recovery based on free-jet velocity profile integrations, may result in significant errors.

Introduction

The establishment of an analytical basis for predicting the static and dynamic performance characteristics of fluid jet modulators has long eluded investigators. To date most practical jet modulator designs have evolved through successive trial and error means, with almost total dependence on experimentally derived performance characteristics. Efficient design to satisfy particular performance requirements would be enhanced greatly by the development of analytical means for predicting jet modulator performance.

Previous attempts at predicting over-all static performance have been hampered generally by a lack of sufficient understanding of the fundamental physical processes involved. It has become apparent that one cannot hope to formulate a truly successful theory describing the performance of jet modulators without first examining in some detail the fundamental hydrodynamic processes which are related to the over-all complex problem.

Included herein is a discussion of an experimental study of the fundamental processes involved in the static interaction of a fluid jet and a single receiver-load system. This discussion summarizes a portion of the author's Doctoral Thesis [Ref. 1].

The Static Performance Problem

In order to provide a basis for discussing the fundamental hydrodynamic problems associated with a fluid-jet modulator, it is convenient to reduce the modulator to the simplified geometrical representation of Figure 1. A modulator with two receiving apertures is depicted. For simplicity, these apertures are not drawn side-by-side as they might appear in an actual device.

The nozzle serves to convert the available energy of the fluid supply into kinetic energy of a jet. In most practical cases the jet is "submerged" since it issues from the nozzle into like fluid [e.g., air into air, water into water, etc.]. In the case of a jet-pipe valve, actual motion of the nozzle provides the means of directing the jet such that it has the desired alignment relative to the receiver-diffuser. For a modulator with no moving mechanical parts, the nozzle is stationary and the relative alignment of the jet with the receiver-diffuser is effected by controlling the pressure distribution across the jet [e.g., a "momentum" or a "pressure" control amplifier]. Means of controlling the pressure distribution across the jet and therefore jet deflection, as required in the latter case, are not shown in Figure 1 and are not considered herein.

The receiver-diffuser functions to convert some of the kinetic energy of the submerged jet into controllable potential energy. Experience with jet pumps and ejectors indicates that the receiver-diffuser should take the form of a "mixing section" and a "diffuser section." The desirable extent of the receiver diffusion process depends on the particular application whereas the efficiency of the process depends on certain geometrical factors. The geometrical extremes which one might expect to be of importance for the "mixing section" are a constant-area passage and a constant-pressure passage (converging). Practical considerations favor the constant-area passage, especially where two receivers are situated side-by-side. In Figure 1 the mixing section is depicted as a constant-area passage, the axis of which is considered to be parallel to the nozzle axis.

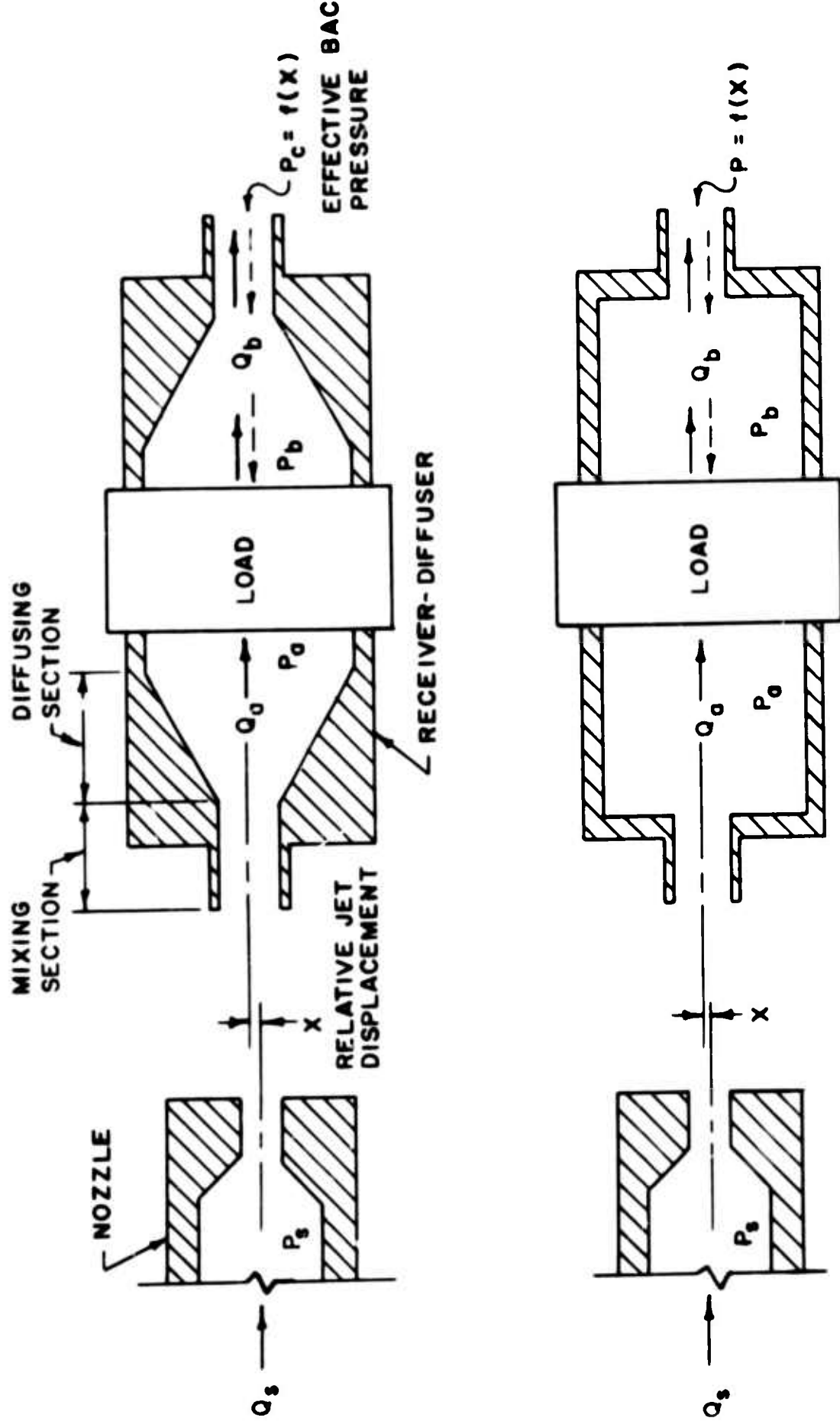


FIG. 1 SIMPLIFIED GEOMETRICAL REPRESENTATION OF A JET MODULATOR

It is hard to imagine any diffuser section geometry that could be more efficient than a section with a $5-7^\circ$ included angle. In cases where simplicity of construction is of more concern than efficiency, a sudden-expansion diffuser section may be preferable. The receiver-diffuser design problem and therefore the basis for analytical treatment becomes one of predicting the geometrical conditions necessary to achieve the desired performance, e.g., maximum efficiency, good linearity, etc.

Following the recovery and subsequent diffusion of flow which enters the receiver-diffuser most nearly aligned with the jet axis (upstream receiver aperture, a), a pressure P_a and a flow rate Q_a are available to drive the load. Very often the nature of the load depends on whether the modulator is a signal processing or power control device. The load may be a dynamic machine such as a full or partial admission turbine, reaction-jet turbine, etc., or it may be a positive displacement machine such as an equal or unequal area piston-cylinder arrangement. Usually, but not always, a jet modulator being used as a signal processing device has a load which consists of one or more fixed resistances [e.g., orifices or capillary tubes).

It is obvious that the over-all static performance problem can be separated conceptually into several related fundamental hydrodynamic problems. Here it is appropriate to consider the following problems: flow through orifices and nozzles (not to be discussed herein), flow of a submerged jet in a confined region, diffusion of a nonuniform turbulent stream in a constant-area passage, and conversion of kinetic to potential energy in "slow-expansion" and "sudden-expansion" diffusers. Once each of these fundamental problems is sufficiently well understood, it ideally would be possible to formulate a theory for predicting over-all performance. Unfortunately, such a level of understanding does not exist at present. There is, however, a substantial body of literature which treats certain aspects of each of the above mentioned problems.

The adequacy and limitations of the available literature in providing a basis for prediction of the static performance of a fluid jet modulator are discussed in detail in the author's Doctoral Thesis [Ref. 1 - Chapter 3] ; a brief summary follows.

SOME CONSIDERATIONS RELATED TO STATIC PERFORMANCE PREDICTION

Submerged Jets

Many solutions and considerable experimental data exist for various aspects of the free submerged jet problem [Refs. 2, 3, 4, 5, 6 and 7]. Both time-average and turbulent fluctuation properties of jets have been studied. A summary of common incompressible jet theories and correlations for the time-average transverse velocity profile is presented in Table 1.

Table 1 Summary of Common Incompressible Free Submerged Jet Theories and Correlations

INVESTIGATOR	ZONE	GENERAL FORM OF RADIAL DISTRIBUTION OF AXIAL VELOCITY	REMARKS
Geortler (Ref. 15) (Modified for finite source)	Established Flow, Two Dimensional	$v = \sqrt{\frac{36Q}{\pi(z + \frac{z_0}{2})}} \left[\operatorname{sech}^2 \left(\frac{QY}{z + \frac{z_0}{2}} \right) \right]$ Where $z_0 = 7.67$ (experimental-Batchelor)	$z = \int_{-\infty}^{\infty} v^2 dY$ - Generally plotted in form $\frac{z}{z_0} = f \left(\frac{Y}{z_0} \right)$, where $z_0 = \frac{36Q}{v_0}$ Y_0 = value of Y when $v = \frac{1}{2}v_0$
Tollmien (Ref. 15) (Modified for finite source)	Established Flow; Axisymmetric	$v = \frac{36Q}{\pi(z + \frac{z_0}{2})} \left(1 + \frac{1}{2} \frac{Y^2}{(z + \frac{z_0}{2})^2} \right)^{-2}$ Where $z_0 = \frac{1}{2} \sqrt{\frac{36Q}{v_0}} \left(\frac{Y}{z_0} \right)$; $z = \frac{1}{2} \sqrt{\frac{36Q}{v_0}}$ And $z_0 = 0.0461 \sqrt{Q}$ (experimental - Batchelor)	$z = \int_{-\infty}^{\infty} v^2 dY$ Generally plotted in form $\frac{z}{z_0} = f \left(\frac{Y}{z_0} \right)$
Taylor, Grinter, and Cummings (Ref. 59)	Established Flow; Axisymmetric	$v = v_0 \left(\frac{z}{z_0} \right)^{-2} \exp \left[-0.695 \left(\frac{Y}{z_0} \right)^2 \right]$ $\frac{z_0}{D_0} = 0.175 \frac{1}{D_0} \quad (\text{experimental-Taylor, et.al.})$	z_0 = Radius where $v = \frac{1}{2}v_0$ and $v_0 = v_0 \left(\frac{z}{z_0} \right)^{-2}$ The constant in expression for z_0 seems too low, Albertson & Bold find 0.190
Albertson, Bai, Jensen, and Rouse (Ref. 10)	Established Flow; Two Dimensional	$v = v_0 \sqrt{\frac{z}{z_0}} \exp \left[-\frac{1}{2} \left(\frac{Y}{z_0} \right)^2 \left(\frac{z}{z_0} \right) \right]$	Valid for $z \geq z_0$ and all R $v_0 = v_0 \sqrt{\frac{z}{z_0}}$
	Established Flow; Axisymmetric	$v = v_0 \left(\frac{z}{z_0} \right)^{-2} \exp \left[-\frac{1}{2} \left(\frac{Y}{z_0} \right)^2 \left(\frac{z}{z_0} \right) \right]$	Valid for $z \geq z_0$ and all R $v_0 = v_0 \left(\frac{z}{z_0} \right)^{-2}$
	Flow Establishment; Two Dimensional	$v = v_0 \exp \left[-\frac{1}{2} \left(\frac{Y}{z_0} \right)^2 \left(\frac{z}{z_0} + \frac{1}{2} \left(\frac{z}{z_0} - 1 \right) \right) \right]$	Valid for diffusion region outside potential core, i.e., for $v > \frac{1}{2}v_0 \left(1 - \frac{z}{z_0} \right)$ Inside potential core $v = v_0$
	Flow Establishment; Axisymmetric	$v = v_0 \exp \left[-\frac{1}{2} \left(\frac{Y}{z_0} \right)^2 \left(\frac{z}{z_0} + \frac{1}{2} \left(\frac{z}{z_0} - 1 \right) \right) \right]$	Valid for diffusion region outside potential core, i.e., for $z > \frac{1}{2}z_0 \left(1 - \frac{z}{z_0} \right)$ Inside potential core $v = v_0$
Salemson and Sankhara (Ref. 21)	Flow Establishment; Axisymmetric	$v = v_0 \left[1 - 7.9 \left(\frac{R - \frac{1}{2}D_0}{z} \right)^2 \right]^2$ Where $D = D_0 (1 - 0.2 \frac{z}{z_0})$	Valid for diffusion region outside potential core, i.e., for $z > \frac{1}{2}z_0$. Inside potential core, $v = v_0$. Based on experimental data giving $z_0 = 5D_0$.
	Established Flow; Axisymmetric	$v = v_0 \left\{ \frac{1 - 2.85 \left(\frac{R - \frac{1}{2}D_0}{z} \right)^2}{0.5 + 0.14 \frac{z}{z_0}} \right\}^2$	Valid for $z \geq z_0$ and all R . Based on experimental data giving $z_0 = 5D_0$.
Simon (Ref. 11)	Flow Establishment; Two Dimensional	$v = v_0 \left[1 - \left(\frac{Y - \frac{1}{2}Y_{\max}}{Y_{\max} - \frac{1}{2}Y_{\max}} \right)^2 \right]^2$ where $D = D_0 \left(1 - \frac{z}{z_0} \right)$; $Y_{\max} = 1.570 D_0 \left(\frac{z}{z_0} \right)$	Valid for diffusion region outside potential core, i.e., $Y_{\max} < Y < 2Y_{\max}$.
	Established Flow; Two Dimensional	$v = v_0 \sqrt{\frac{z}{z_0}} \left[1 - \left(\frac{Y}{Y_{\max}} \right)^2 \right]^2$ where $Y_{\max} = 1.570 D_0 \frac{z}{z_0}$	Valid for $z \geq z_0$ and $Y < Y_{\max}$ $v_0 = v_0 \sqrt{\frac{z}{z_0}}$
DEFINITIONS OF PARAMETERS			
TWO-DIMENSIONAL JET		AXISYMMETRIC JET	
NOTE: $D \neq D_0$			

The main question concerning these free jet theories, is their applicability in the prediction of jet-receiver static performance. It has been assumed by several investigators in the past that the total pressure distribution which exists at the inlet section of a receiver is the same as would exist in the jet at the same section with the receiver removed. The validity of this assumption is discussed in the last section of this paper.

Characteristics of Diffusion Processes

Diffusion of a stream in internal flow, in the sense of increasing static pressure, is accomplished by means of velocity profile "smoothing" and/or simple area change. Although it is well known that diffusion takes place in a diverging passage due to the area change itself, it is often forgotten that changes in the velocity profile also affect the diffusion process, i.e., the ability of a passage to transform energy from kinetic to potential. Equally important, but less well known, is the fact that diffusion may take place in a constant-area passage due to the effect of velocity profile smoothing.

The process of constant-area diffusion is best understood by considering the uniformity of a fluid stream. Uniformity refers to the closeness to which the transverse profile of the longitudinal velocity approaches a "rectangular" profile. A convenient quantitative measure of the uniformity of a velocity profile is the momentum coefficient defined as follows:

$$\alpha = \frac{\text{true momentum of the stream}}{\text{momentum based on the continuity average velocity}}$$

$$\text{Thus } \alpha = \frac{\int V^2 dA}{(\bar{V})^2 A} \quad [1]$$

Considering now the constant-area passage shown in Figure 2, the law of conservation of momentum requires that

$$\bar{P}_2 - \bar{P}_1 = \rho(\bar{V}_1)^2(\alpha_1 - \alpha_2) - \frac{4\tau_w L}{D} \quad [2]$$

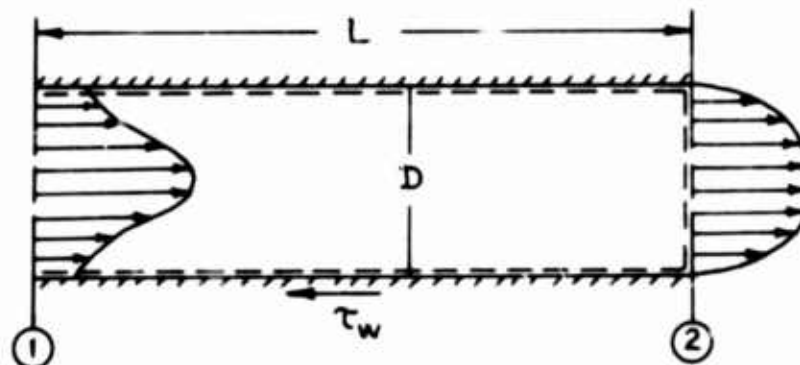


Figure 2 Velocity Profile Smoothing
In A Constant-Area Passage

where

\bar{P}_1 = average static pressure at station 1

\bar{P}_2 = average static pressure at station 2

V = axial velocity at a point

$\bar{V}_1 = \bar{V}_2$ = continuity average velocity

α_1, α_2 = momentum coefficients; $\alpha=1$ for uniform profiles;
 $\alpha > 1$ for nonuniform profiles

τ_w = wall shear stress

ρ = fluid mass density

D = passage diameter

The velocity profile of the flow in a constant-area passage tends to stabilize along the passage, i.e., asymptotically approach a "fully-developed" profile. The "fully-developed" velocity profile effectively may be approached from either of two directions, either from a more or less uniform profile. Generally speaking, the mechanism governing the stabilization process is different for the two cases. The first case is typical of the common "entry length" problem, wherein the growth of the wall boundary layer is the dominant effect in the process. The second case may result in a turbulent flow due to the action of turbulent or "apparent" shear stresses and corresponding transfer of momentum between transverse layers in the flow.

If the profile at a station in the passage is highly nonuniform [α is much greater than the corresponding fully developed value], then Equation [2] shows that an increase in profile uniformity may cause an increase in static pressure which outweighs the decrease due to wall shear. Of course if the passage is long enough, wall friction will eventually dominate.

In a passage whose area increases in the direction of flow, the "profile smoothing" form of diffusion is superimposed on the area-change form. Energy losses in area-change diffusers primarily result from velocity profile smoothing, wall shear, and separation. Experience indicates that a nonuniform velocity profile at the entrance to a "slow expansion" area-change diffuser, leads to a significantly larger over-all energy loss than would occur with a more uniform inlet profile. It is apparent on consideration of a free submerged jet that the receiver-diffuser inlet velocity profile will be nonuniform in character.

Figure 3 serves to illustrate schematically what might be expected to occur in constant-area diffusion in the constant-area mixing section of a receiver-diffuser. In cases a and b, it is assumed that the flow in the passage is turbulent and that the velocity profile is identical to the profile in the corresponding section of an unobstructed free

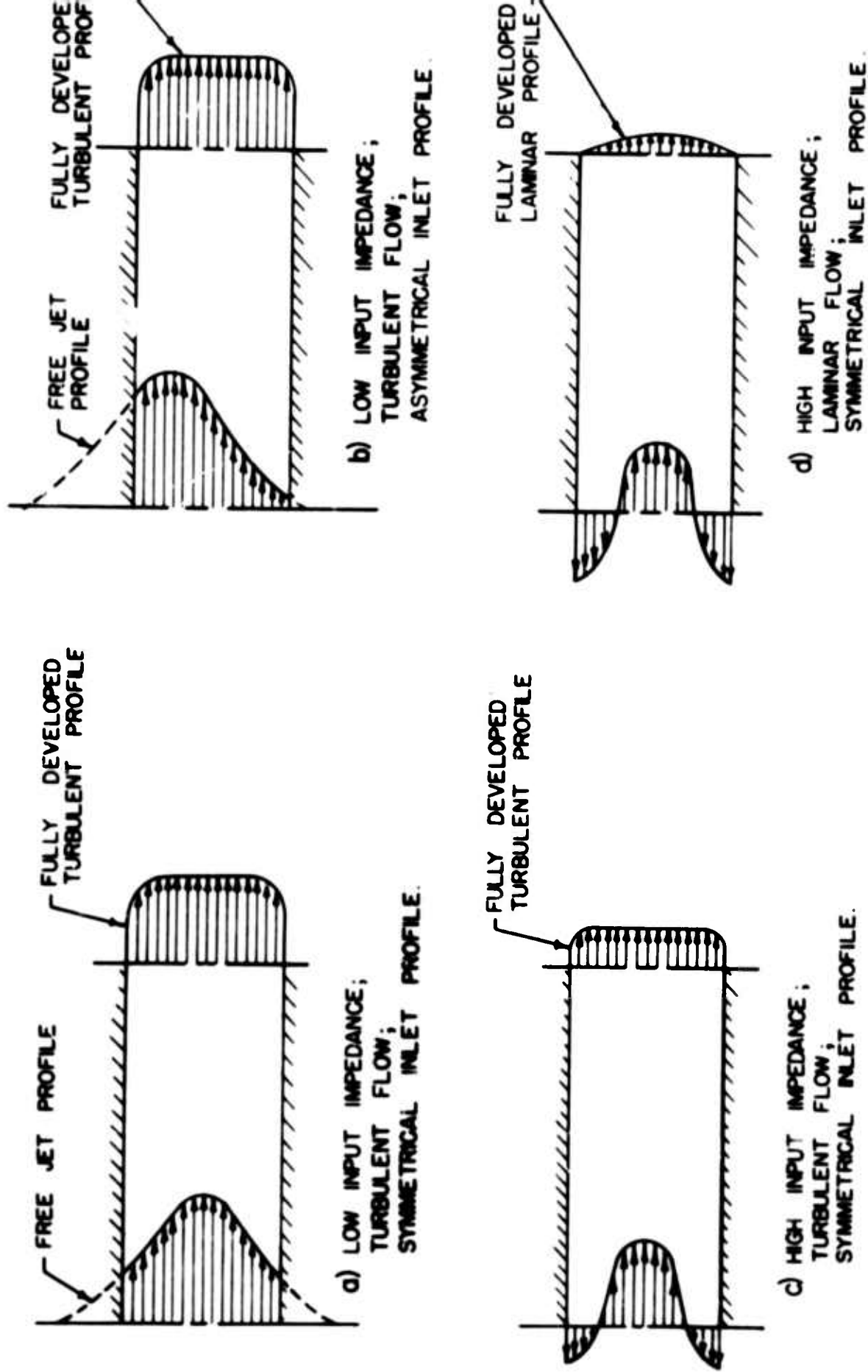


FIG 3 CONSTANT-AREA DIFFUSION OF NON-UNIFORM STREAMS.

submerged jet. These two cases represent one end of the spectrum of interest, i.e., the situation which should exist when no throttling takes place downstream of the diffuser [receiver input impedance is essentially zero]. When considerable throttling takes place [receiver input impedance becomes very large], the flow in the passage may be laminar rather than turbulent. Certainly as the receiver input impedance approaches infinity, the flow in the passage must proceed from turbulent to laminar. Cases c and d of Figure 3 illustrate cases of high, but not infinite, receiver input impedance [i.e., finite through flow]. In all cases, the corresponding fully-developed profile is approached. Up until the present investigation was conducted, very little beyond qualitative reasoning existed to substantiate the schematic representations of Figure 3.

Area-Change Diffusion

Although many basic problems remain unanswered, considerable experimental data are available on the "efficiency" of circular, square, and rectangular diffusers having various area ratios, divergence angles, inlet boundary layer conditions, and Reynolds numbers.

Of the various efficiencies used in the literature, the most common and probably the most useful in the majority of situations is the "static pressure efficiency", or as sometimes termed, the "energy-conversion efficiency". This efficiency is defined as the ratio of the rate at which energy is transformed to the rate at which energy is supplied for transformation. Consider a passage which expands from an initial area A_1 to a final area A_2 . Let P be the static pressure, ρ the fluid mass density, V the component of velocity parallel to the axis of the passage and W the absolute velocity at any point. If the flow is purely axial at sections 1 and 2, $W = V$ and P is a constant over the section [i.e., no streamline curvature]; the actual static pressure efficiency becomes

$$\eta_{sp} = \frac{(P_2 - P_1) \bar{V}_1 A}{\int_{A_1} \frac{1}{2} \rho V^3 dA - \int_{A_2} \frac{1}{2} \rho V^3 dA} \quad [3]$$

where \bar{V} is the continuity averaged velocity. Equation [3] can be simplified by defining a kinetic energy factor β as follows:

$$\beta = \frac{\int V^3 dA}{(\bar{V})^3 A}$$

The kinetic energy factor is analogous to [but not equal to] the momentum factor, α , in that it accounts for the nonuniformity of the velocity profile. Utilizing this definition and recognizing that continuity requires $V_1 A_1 = V_2 A_2$, the following expression is obtained:

$$\eta_{ep} = \frac{P_2 - P_1}{\frac{1}{2} \rho (\bar{V}_1)^2 \left[\beta_1 - \beta_2 \left(\frac{A_1}{A_2} \right)^2 \right]} \quad [4]$$

Many investigators have used a one-dimensional approximation to Equation [4] as follows:

$$\eta_p = \frac{P_2 - P_1}{\frac{1}{2} \rho (\bar{V}_1)^2 \left[1 - \left(\frac{A_1}{A_2} \right)^2 \right]} \quad [5]$$

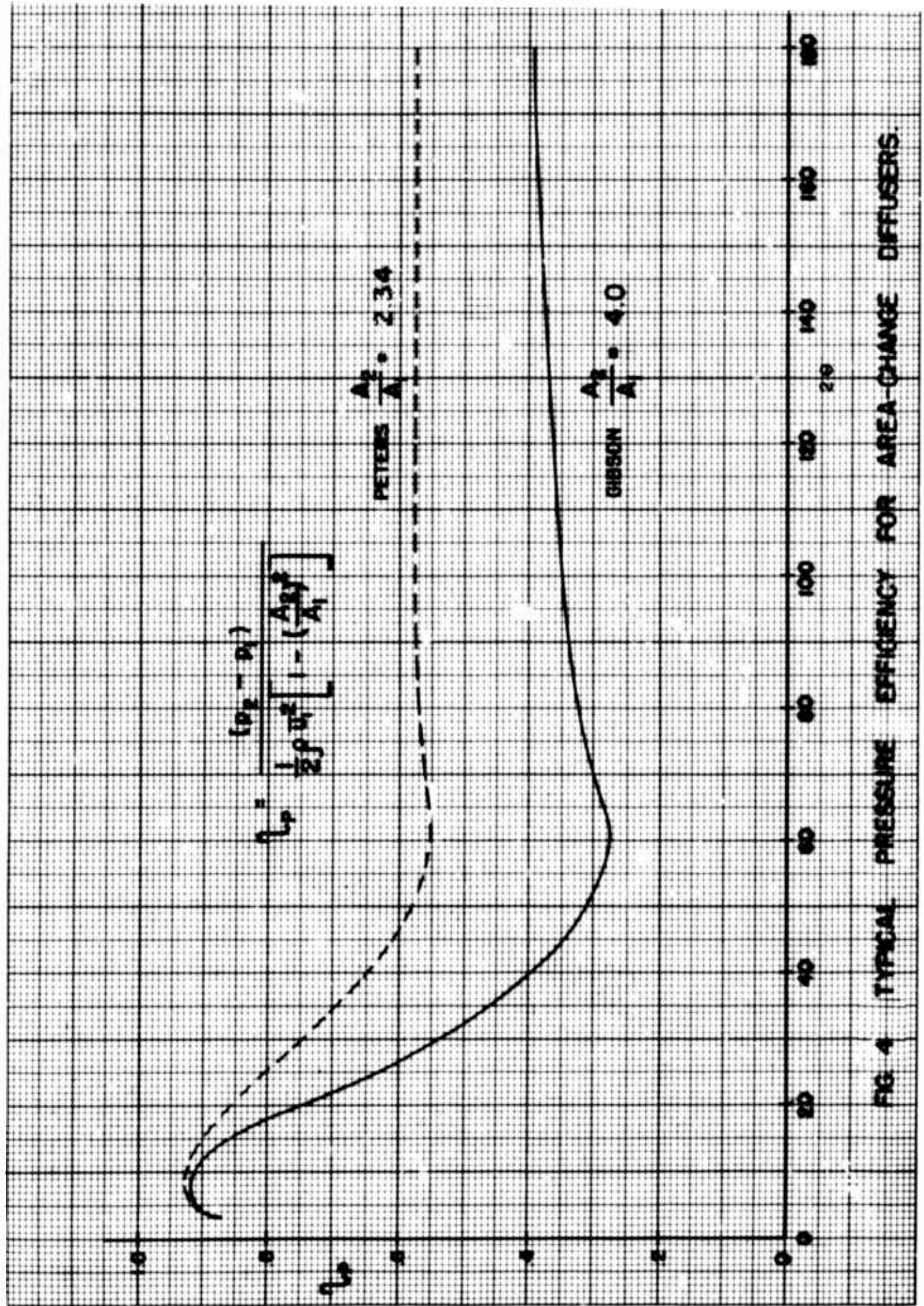
Equation [4] reduces to Equation [5] if it is assumed that the velocity profiles at the entrance and exit sections are uniform [i.e., $\beta_1 = \beta_2 = 1.0$].

The efficiency depends on many factors, the most important of which is the rate of expansion of the flow. Results of experiments on the flow between straight diverging walls [conical section] by Gibson [Ref. 8] and Peters [Ref. 9] are summarized in Figure 4. Efficiency, η_p , is plotted against 2θ , the included angle between the diverging walls. The [Borda] limiting condition [i.e., a sudden expansion diffuser] is derived from simple continuity and momentum considerations; the following expression results:

$$\eta_p = \frac{2}{1 + \frac{A_2}{A_1}} \quad [6]$$

The most important feature of the results of Figure 4 is that the efficiency reaches a peak value, which is quite high, in the vicinity of 6-8 degrees.

A factor which is often obscured in the presentation of diffuser performance data is the effect of inlet and exit velocity profile non-uniformity. Most investigators have not bothered to make the additional [and tedious] measurements necessary to establish β_1 and β_2 . A few investigators have studied the effect on diffuser efficiency of various inlet velocity profiles produced by using different lengths of constant diameter inlet pipe. The percentage difference between the efficiencies calculated from Equations [4] and [5] may be as small as a few percent or



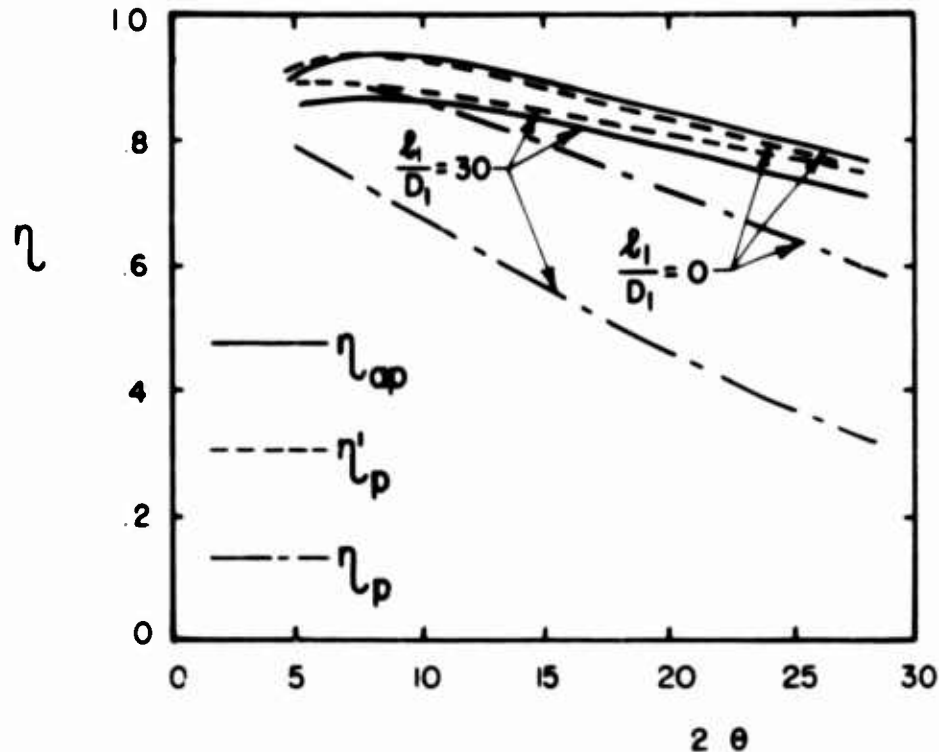


Fig. 5 Effect of Entrance and Exit
Section Length on Diffuser
Pressure Efficiency (Ref. 10)

as large as 10-15 percent. Even if the diffuser entrance profile is approximately uniform [i.e., $\beta_1 \approx 1.0$] the exit profile normally is quite nonuniform [$\beta_2 > 1.0$]. Figure 5 shows the effect of inlet and exit section length for the various methods of defining the pressure efficiency. The term l_1 , refers to the length of the constant area entry tube and η'_p refers to the efficiency of a diffuser with a 6 diameter constant-area tail section.

The discussion above gives only a sample of the factors which must be considered in the efficient design of area-change diffusers. Much remains to be done in properly evaluating and extending the existing diffuser performance data.

EXPERIMENTAL PROGRAM OBJECTIVES AND APPARATUS DESIGN

Objectives

An experimental program was carried out aimed at obtaining sufficiently detailed information about the basic flow processes involved in a jet-receiver-diffuser so that rational techniques for over-all performance prediction

could be explored and developed. Considerable attention was given to the basic problem of constant-area turbulent diffusion of a nonuniform stream because it is so little understood and has received virtually no discussion in the literature. Likewise, the important flow establishment region of the free jet was studied in some detail because of its relatively limited treatment in the literature.

Apparatus

As is the usual case, the apparatus design and instrumentation selection involved several compromises. Currently proposed fluid jet modulator fabrication techniques result in square or moderately rectangular passage sections, both of which exhibit extremely complicated flow fields. For simplicity, an axisymmetrical configuration was chosen for this initial investigation.

Work is now underway by the author at Oklahoma State University, to extend the work reported herein to plane passage configurations.

Figure 6 shows a schematic of the complete apparatus.

Air was supplied by a compressor capable of producing 400 SCFM at 1 psi. Output flow was varied by means of a simple butterfly throttle valve on the intake.

The settling chamber was comprised of six, rolled and butt welded 14 gauge sheet metal sections. All welded joints were ground smooth. A 30° [included angle], 6 inch to 12 inch conical diffuser was followed by 5 cylindrical sections, each 12 inches in diameter. The first cylindrical section included within, 8 - 1/2 inch pieces of Fiberglass, 3 - 1 inch thick pieces of rubberized packing material, approximately 5000 - 1/8 inch diameter paper soda straws, and a taut 30 mesh copper wire screen soldered to the front end. Three intermediate 5 inch long sections followed and each had a taut 30 mesh copper wire screen soldered to its front end. A final 24 inch long section bolted directly to the 1/2 inch thick aluminum mounting plate. Flanges 1-1/2" x 1-1/2" x 14 gauge were seam welded to the ends of each section.

A Cox Type 210 standard flow nozzle, 1.94 inches in diameter, was mounted in a 1/2 inch vertical plate. The nozzle upstream face was smooth and flush with the milled upstream face of the plate.

The receiver-diffuser assembly consisted of three parts [in order]:

- 1] a standard cast plastic tube -- 30 inches long, 3 inch inside diameter, 3-1/2 inch outside diameter;
- 2] a special cast plastic conical diffuser -- 3 inch inside diameter inlet, 6 inch inside diameter outlet, 10 degree included angle;

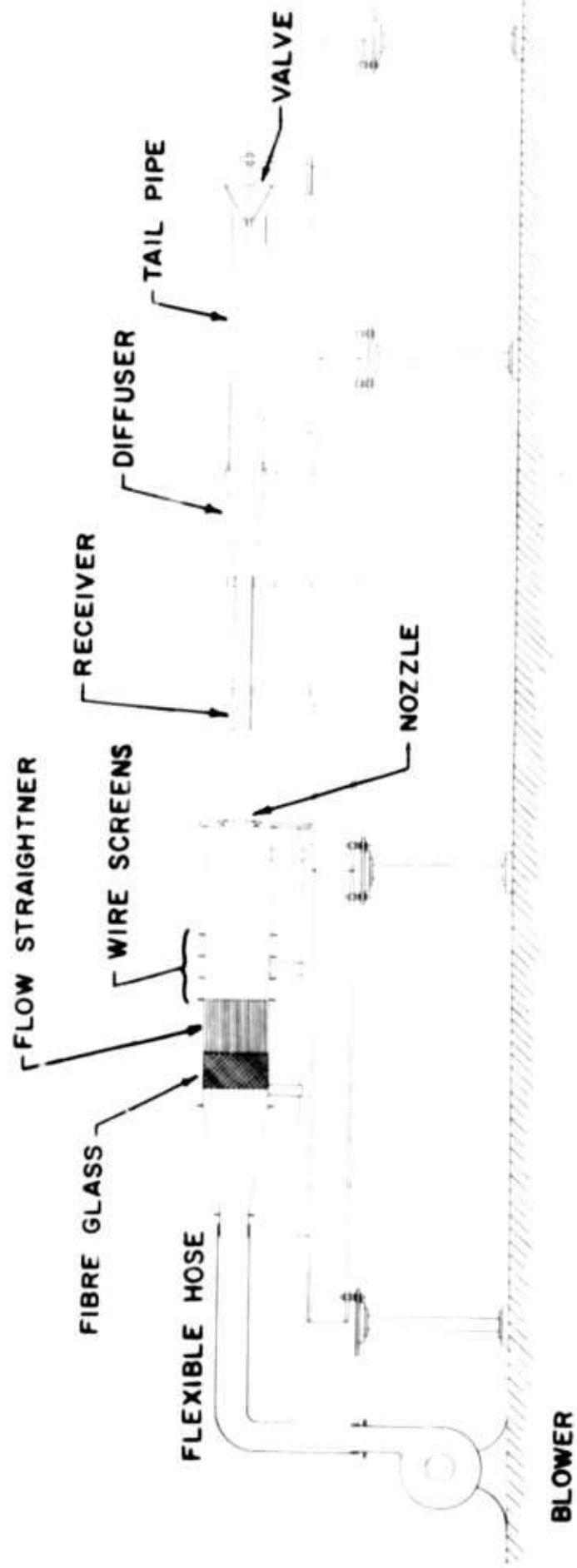


FIG. 6 SCHEMATIC OF TEST APPARATUS

- 3] a standard cast plastic tube -- 54 inches long, 6 inch inside diameter, 6-1/2 inch outside diameter.

Thirteen 3/8 inch diameter reamed holes were provided in the receiver tube wall for inserting total and static pressure probes. To provide a smooth wall, each hole was fitted with a plastic plug, having a tip machined with a radius to match the inside radius of the tube. Fourteen wall static pressure taps were provided on the wall diametrically opposite the probe holes. These taps were located so that they would allow wall static pressure measurement at the same axial location that total pressure readings were made with a probe. Velocity could be computed from these two readings.

The area-change diffuser was molded out of plastic and finish machined to have 10° included angle and a 4:1 area ratio; this was a compromise between performance and length. The area-change diffuser was provided with 8 - 3/8 inch diameter reamed holes for inserting pressure probes. To provide a smooth internal surface, each hole was fitted with a plastic plug, having a tip machined with a radius and angle to match the inside wall. Fourteen wall pressure taps were provided in the wall diametrically opposite the probe holes to facilitate velocity and wall static pressure measurements.

The entire apparatus was mounted on 3 sections of standard 8 x 4 inch, 25 lb. I-beam. The top surface of the center 8 ft. I-beam was planed and a 3/8 inch wide - 1/8 inch deep keyway was cut along the entire length on the centerline. The keyway provided an accurate reference for mounting and alignment of all remaining portions of the apparatus.

Throttling of the outlet tube of the receiver assembly was accomplished with a conical valve constructed from a standard funnel.

A three-axis probe traversing apparatus enabled a pressure probe to be accurately positioned at any desirable location within the field between the nozzle and the receiver entry.

Instrumentation

The primary instrumentation was that required for measurement of stream velocity. Since a static pressure gradient existed in the entry region of the receiver, the standard technique of inferring velocity from measurements of local total pressure and wall static pressure was inadequate. In the interests of minimizing probe interference and still limiting the tube size to a practical 3 inches I.D., two "matched" 0.031 inch O.D. "right angled" probes were constructed: a total pressure probe, and a static pressure probe. Both probes were essentially of the standard Prandtl type. The pressure measurements from these instruments were accomplished with standard draft gauges and vertical manometers. To facilitate accurate measurements, all wall static pressure taps in the receiver and diffuser sections were connected with plastic tubing to a 3/2 tube inclined manometer board, having a single adjustable reservoir.

DATA PRESENTATION, INTERPRETATION, AND CORRELATION

Introduction and Nomenclature

Presented and evaluated herein are results of experimental measurements of free-jet axial velocity profiles, receiver-diffuser internal flow characteristics, and jet-receiver-diffuser over-all static performance. Nomenclature used in the data presentation are summarized below for the convenience of the reader.

D_o	=	nozzle diameter
D_r	=	receiver diameter
P_{atmos}	=	atmospheric pressure
P_o	=	nozzle stagnation pressure
P_b	=	receiver back pressure [static]; measured six diameters [36 inches] downstream of area-change diffuser
P_{wall}	=	receiver-diffuser wall static pressure
Q	=	net volumetric rate of flow through receiver
Q_o	=	volumetric rate of flow through nozzle
R	=	radial distance measured from jet centerline
$R_{1/2}$	=	radial distance for which $V = 0.5 V_c$
R_o	=	nozzle radius
Re_D	=	Reynolds number based on nozzle diameter
V	=	axial velocity at radial distance R
V_o	=	ideal axial velocity at nozzle exit plane
V_c	=	jet centerline axial velocity
\bar{V}_2	=	continuity average velocity in constant-area passage
X	=	axial distance measured from nozzle exit plane
X_1	=	axial distance from nozzle exit plane to receiver entrance plane
X_s	=	axial distance from nozzle exit plane to receiver-diffuser section at which measurement is made
X_o	=	length of jet potential core
ρ	=	fluid mass density

Free-Jet Characteristics

Two types of data were obtained: 1] axial distribution of the centerline axial velocity, and 2] transverse profiles of the axial velocity. Typical centerline velocity distributions are presented in Figure 7. These data provide information necessary for the definition and determination of the so-called potential core length, X_0 . The intersection of the straight line asymptotes for small and large X/D_0 serves to define the value of X_0/D_0 or the "dimensionless" potential core length. These data agree well with data obtained at comparable Reynolds number by Albertson [Ref. 5], Taylor [Ref. 11], and Baines [Ref. 12].

A typical set of data representing the transverse profiles of the axial component of velocity is presented in Figure 8.

For convenience in correlating the experimental data, analytical expressions are reproduced [slightly rearranged] from Table 1 below.

Zone of flow establishment [Albertson]

$$\frac{V}{V_0} = \exp \left[-2 \left(\frac{X_0}{D_0} \right)^2 \left(\frac{R - \frac{D_0}{2}}{x} \right)^2 + \frac{1}{2} \left(\frac{D_0}{X_0} \right)^2 \right] \quad [7]$$

Zone of established flow [Albertson]

$$\frac{V}{V_c} = \exp \left[-2 \left(\frac{X_0}{D_0} \right)^2 \left(\frac{R}{x} \right)^2 \right] \quad [8]$$

and [Taylor]

$$\frac{V}{V_c} = \exp \left[-0.693 \left(\frac{R}{R_{1/2}} \right)^2 \right] \quad [9]$$

Generalized plots of the experimental data are presented in Figures 9 and 10 for the two zones of flow. For the zone of flow establishment, the data for various sections correlate well with each other. A single corresponding plot presented by Albertson, et. al., shows a significant amount more scatter. Equation [7] is plotted in Figure 9 for comparison. The correlation is not as good as might be desired. Better correlation is realized if the effective length of the potential core, as used in Equation [7], is shortened by 20% [see dashed curve in Figure 9]. Albertson arrived at the same conclusion. Lacking further experimental verification, it might be concluded that Equation [7] together with the Baines data for $X/D_0 = f[Re_D]$, provides an adequate correlation for the flow establishment region providing the 20% factor is included.

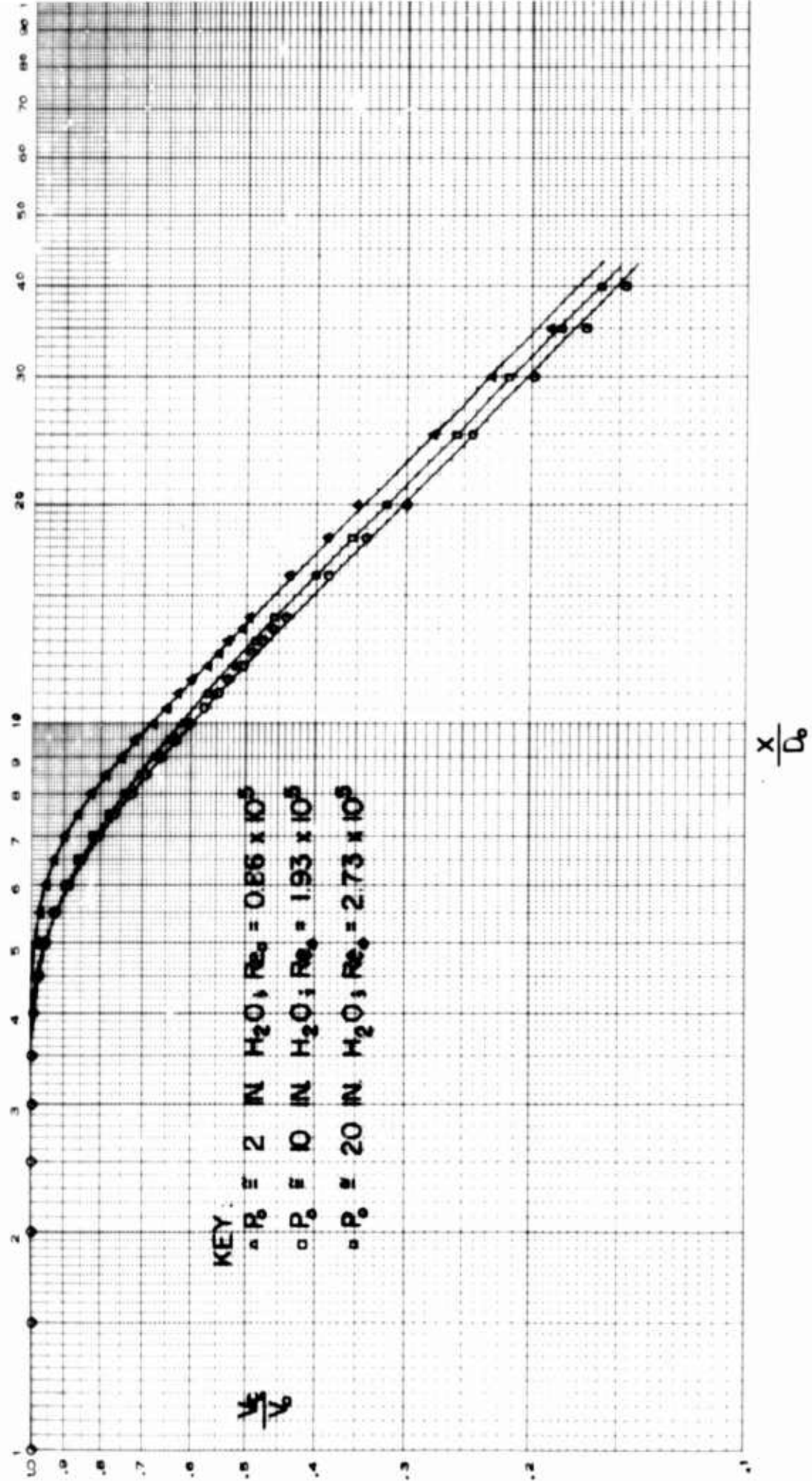


FIG. 7 MEASURED CENTERLINE VELOCITY DISTRIBUTIONS FOR AN AXI-SYMMETRIC SUBMERGED JET

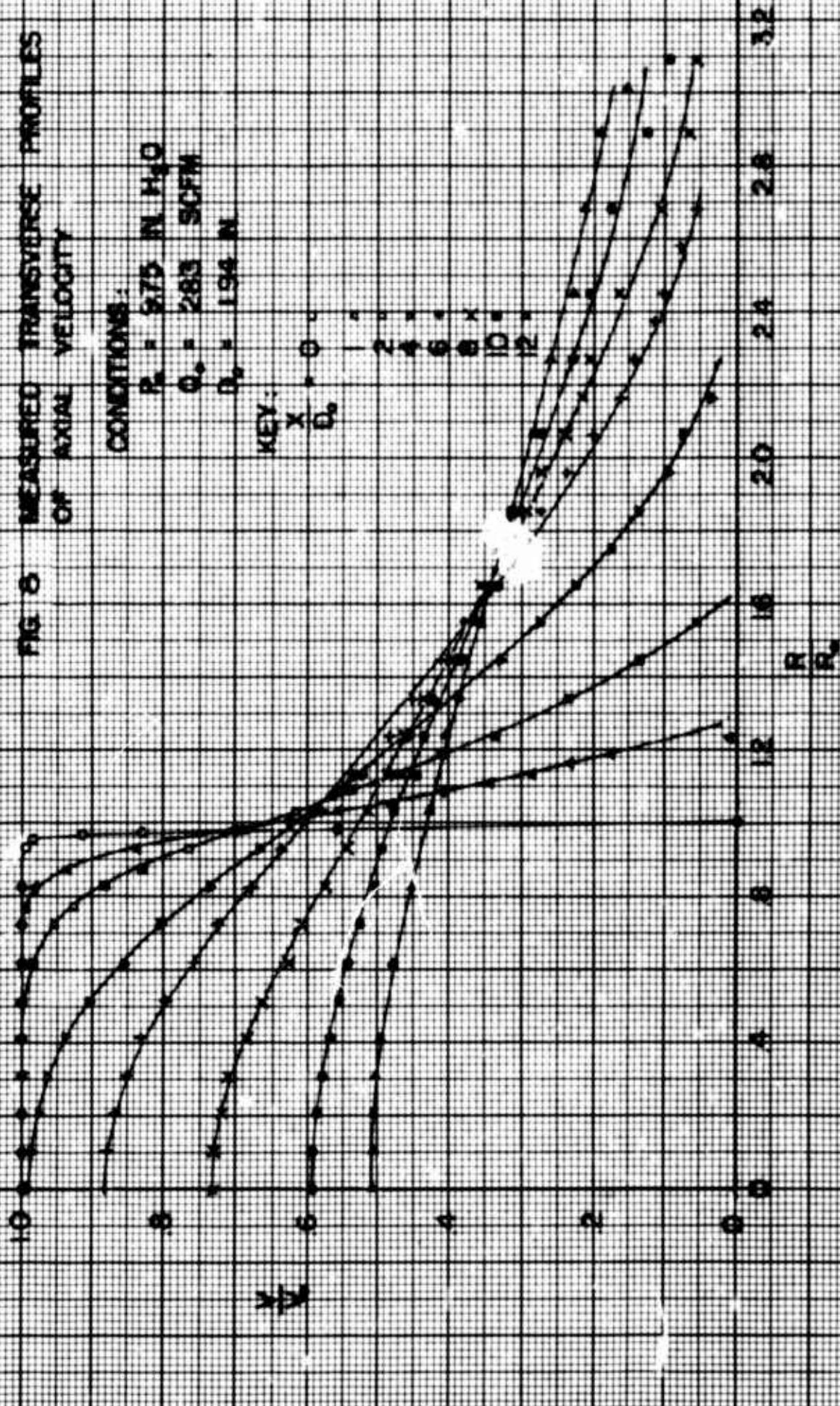
FIG. 8 MEASURED TRANSVERSE PROFILES
OF AXIAL VELOCITY

CONDITIONS:
 $P_s = 975$ IN H_2O
 $Q_s = 283$ SCFM
 $D_s = 1.94$ IN

KEY:

\times
 $\frac{x}{D_s}$

2 4 6 8 10 12



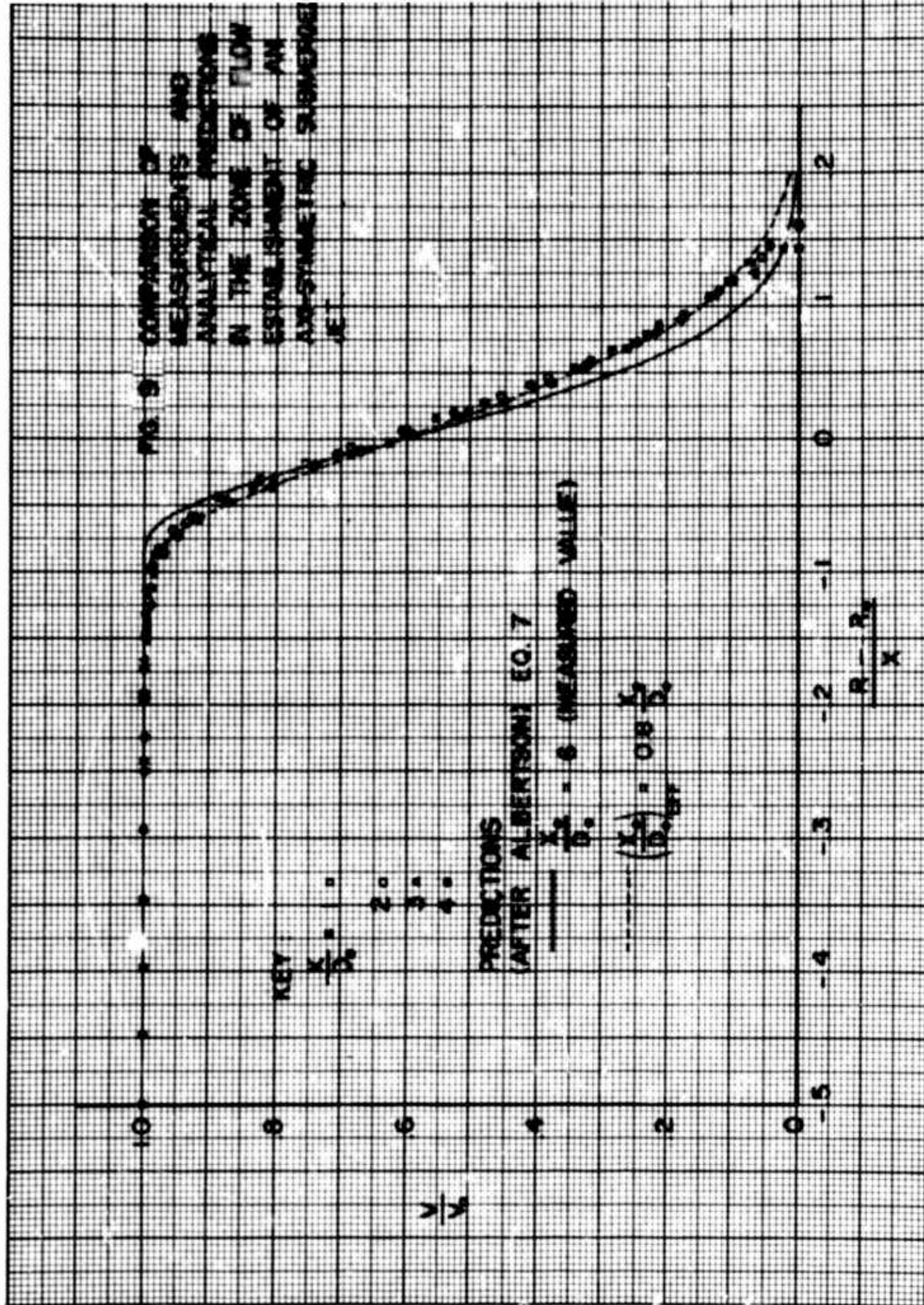
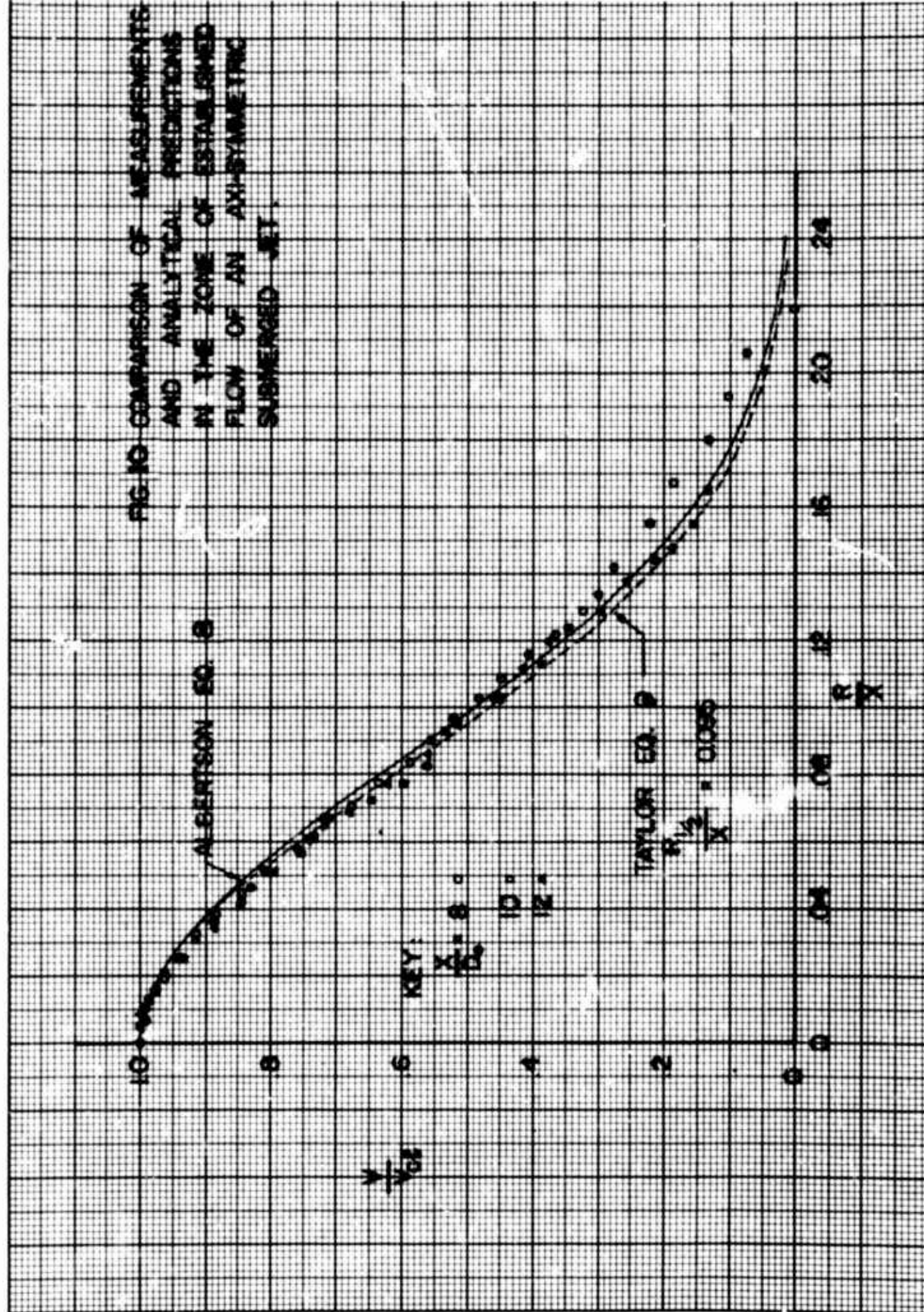


FIG. 10 COMPARISON OF MEASUREMENTS
AND ANALYTICAL PREDICTIONS
IN THE ZONE OF ESTABLISHED
FLOW OF AN AXI-SYMMETRIC
SUBMERGED JET.



Data taken in the zone of established flow [Figure 10] shows reasonably good correlation for the profiles at $X/D_0 = 10$ and 12. The profiles at $X/D_0 = 6$ and 8 do not correlate well with these methods of generalized plotting. This lack of correlation is to be expected and is indicative of the following:

- 1] that the profiles in this region are not similar, and
- 2] that an identifiable "transition" zone separates the end of the zone of flow establishment and the effective beginning of the zone of established flow.

The presence of a "transition" zone has been recognized by some of the previous investigators but, with the exception of Kuethe [Ref. 6] and Taylor, et. al., [Ref. 11], little attention has been given to this zone. In fact, none of the analytical correlations presented in the literature represent the data well in this region. Unfortunately, the transition region is of particular importance in the design of jet modulators.

Equation [8] [after Albertson] is plotted in Figure 11 to show the difficulty involved in using a correlation technique which works well in the zones of flow establishment and established flow, for the "transition" zone. Also shown is the analytical correlation [after Taylor] given by Equation [9]. Here the value of $R_{1/2}/X$ was determined from the plot of V/V_c vs R/X ; this result was then used in Equation [9]. This is, of course, an "after-the-fact" method of analytical correlation. To make this a practical method of computing velocity profiles in the transition region, a "law" or correlation is needed for $R_{1/2}$.

Values of $R_{1/2}$, as determined from the experimental data, are plotted in Figure 12. Using the correlation of Figure 12 and Equation [9], the velocity profiles in the transition region can be computed directly and the resulting profiles should be valid within a few percent over the range of conditions considered in the study.

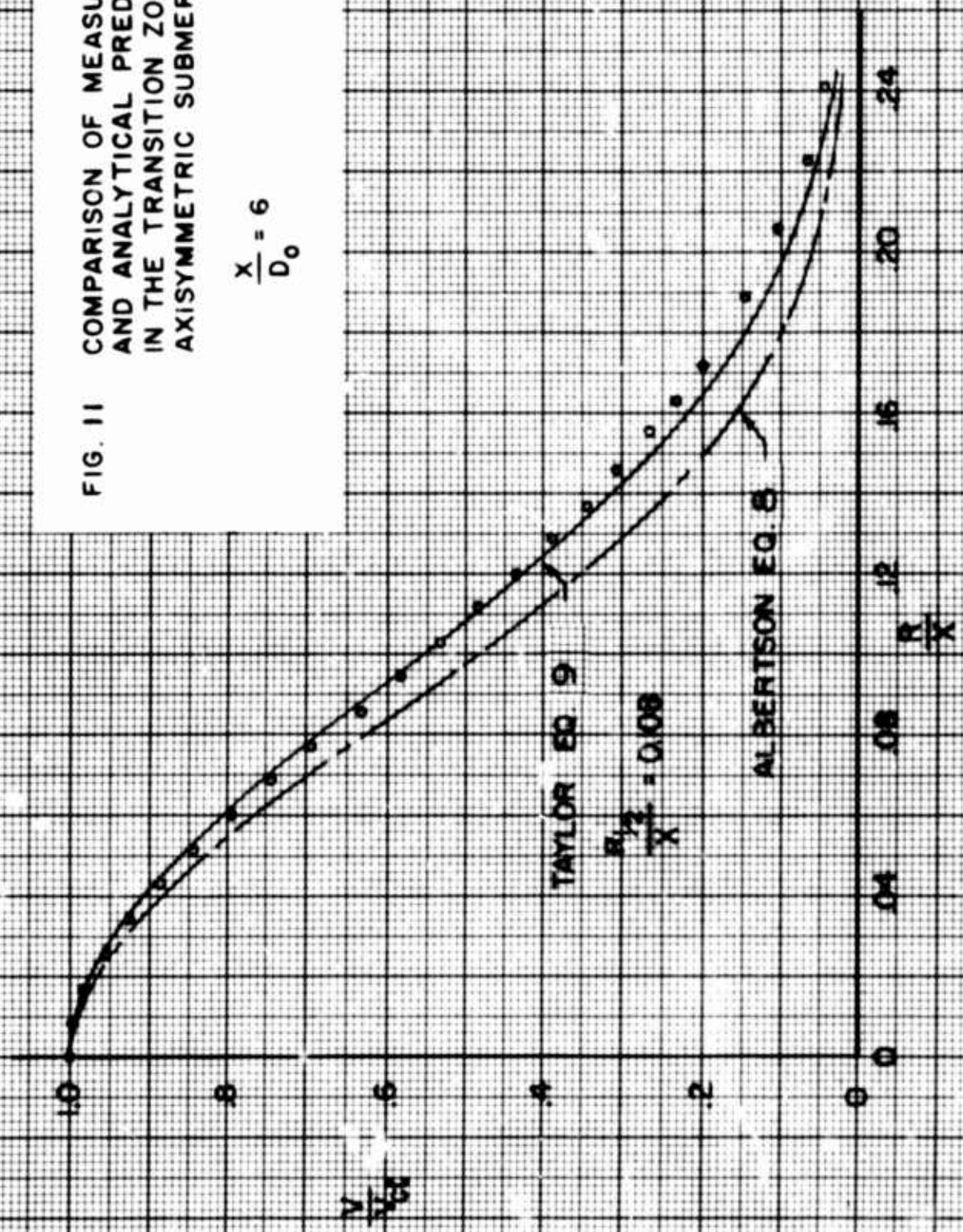
Constant-Area and Area-Change Diffusion

The receiver internal-flow mixing process constitutes the most important single problem in receiver-diffuser design. Data taken to elucidate the details of the mixing process were of two types: 1] transverse profiles of the axial velocity, and 2] wall static pressure distributions. These data were taken with a variety of downstream throttle conditions, nozzle-to-receiver spacings, and nozzle-receiver axial alignments. All measurements discussed herein were taken with a nozzle diameter of 1.74 inches, a receiver diameter of 3.0 inches, a receiver length of 30 inches, a diffuser included angle of 10° , a diffuser area ratio of 4, and a nozzle upstream stagnation pressure of 10 inches H_2O .

Typical axial velocity profiles for the aligned and non-aligned cases are shown in Figures 13 and 14 respectively. These data present a semi-quantitative "picture" of the over-all diffusion process as a function of

FIG. 11 COMPARISON OF MEASUREMENTS
AND ANALYTICAL PREDICTIONS
IN THE TRANSITION ZONE OF AN
AXISYMMETRIC SUBMERGED JET

$$\frac{x}{D_0} = 6$$



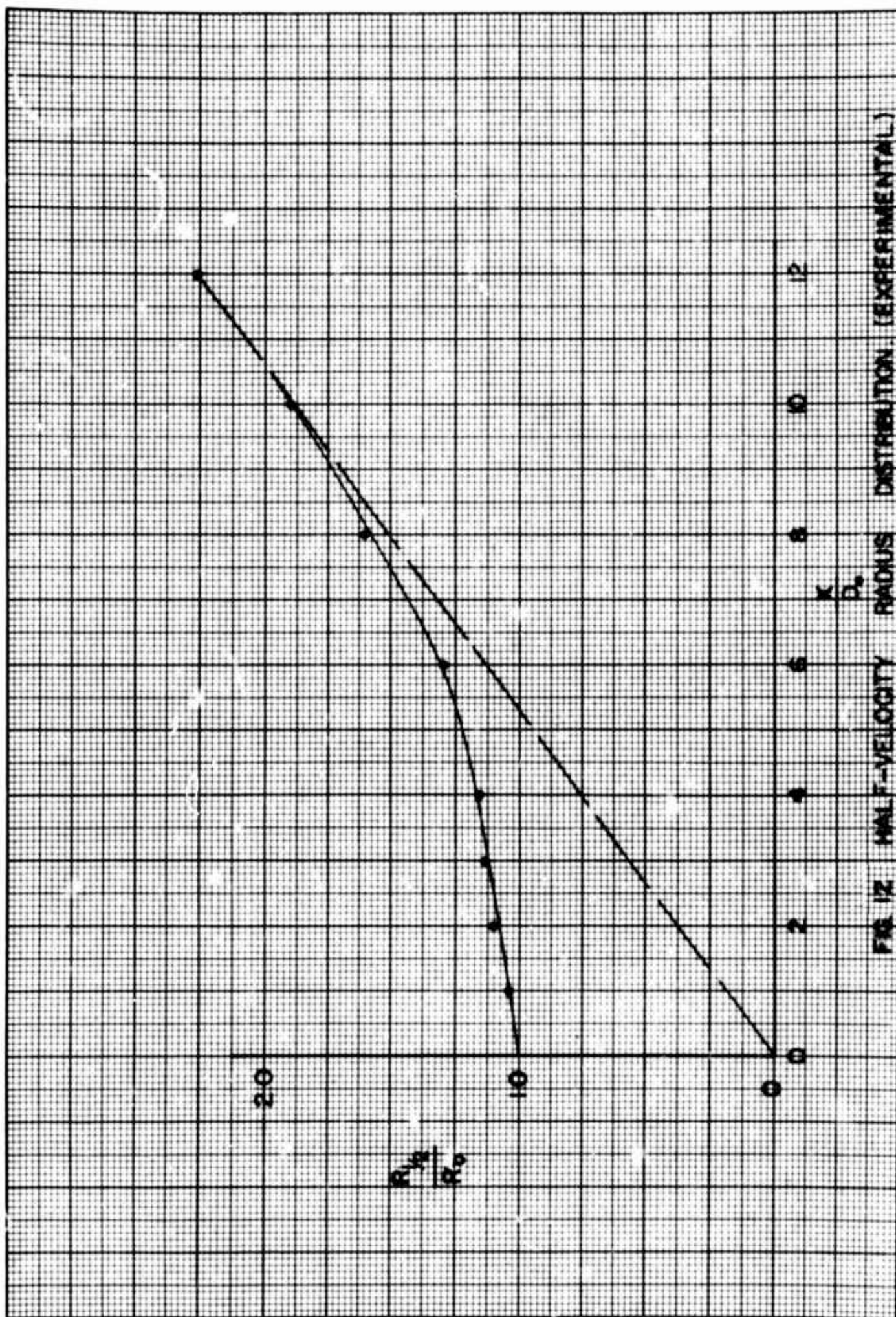


FIG. 12 HALF-VELOCITY RADIUS DISTRIBUTION (EXPERIMENTAL)

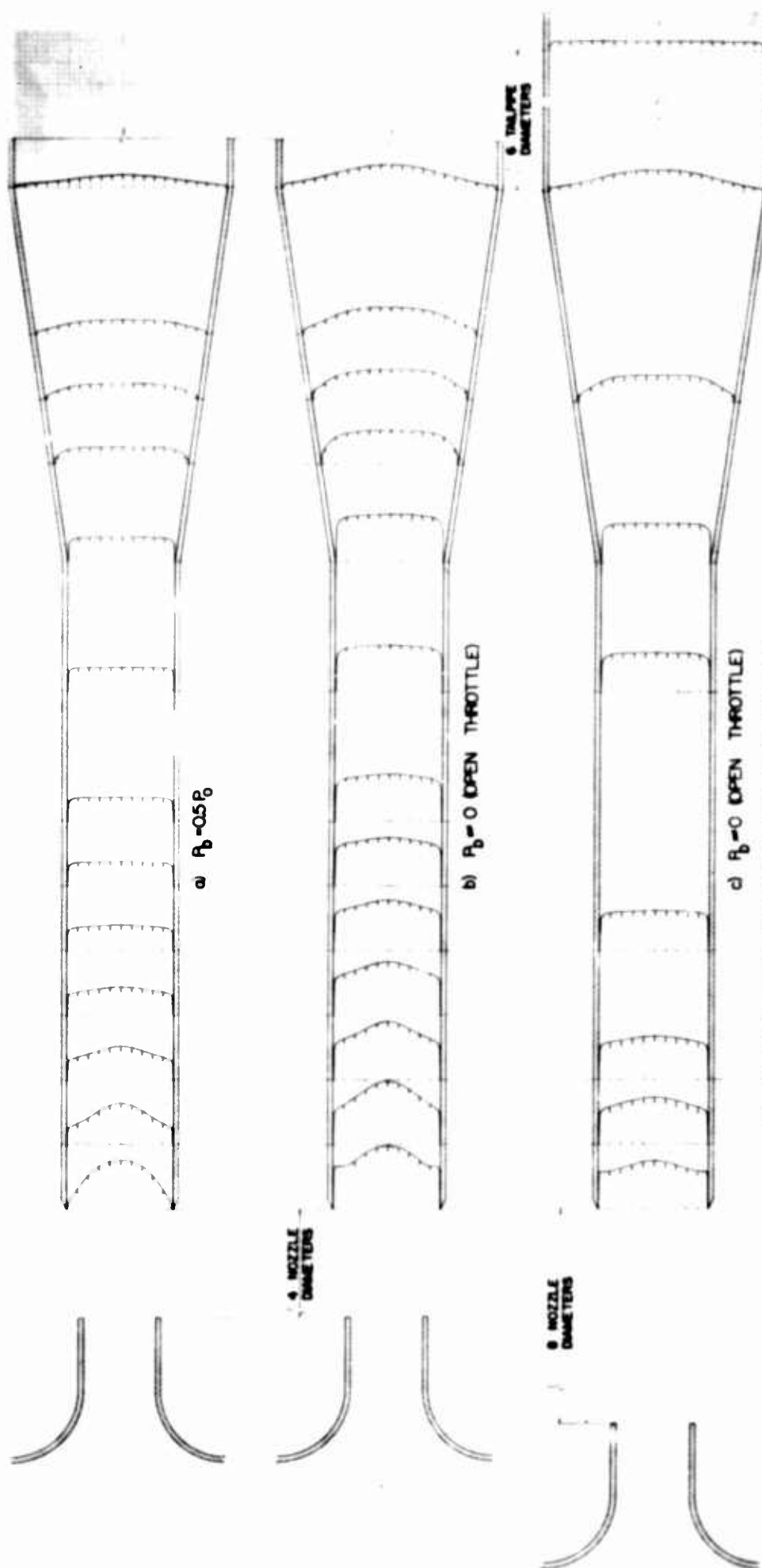


FIG. 19 FLOW DEVELOPMENT IN AN AXI-SYMMETRIC REGENERATIVE-FUSER WITH AN AXIALLY-ALIGNED NOZZLE.

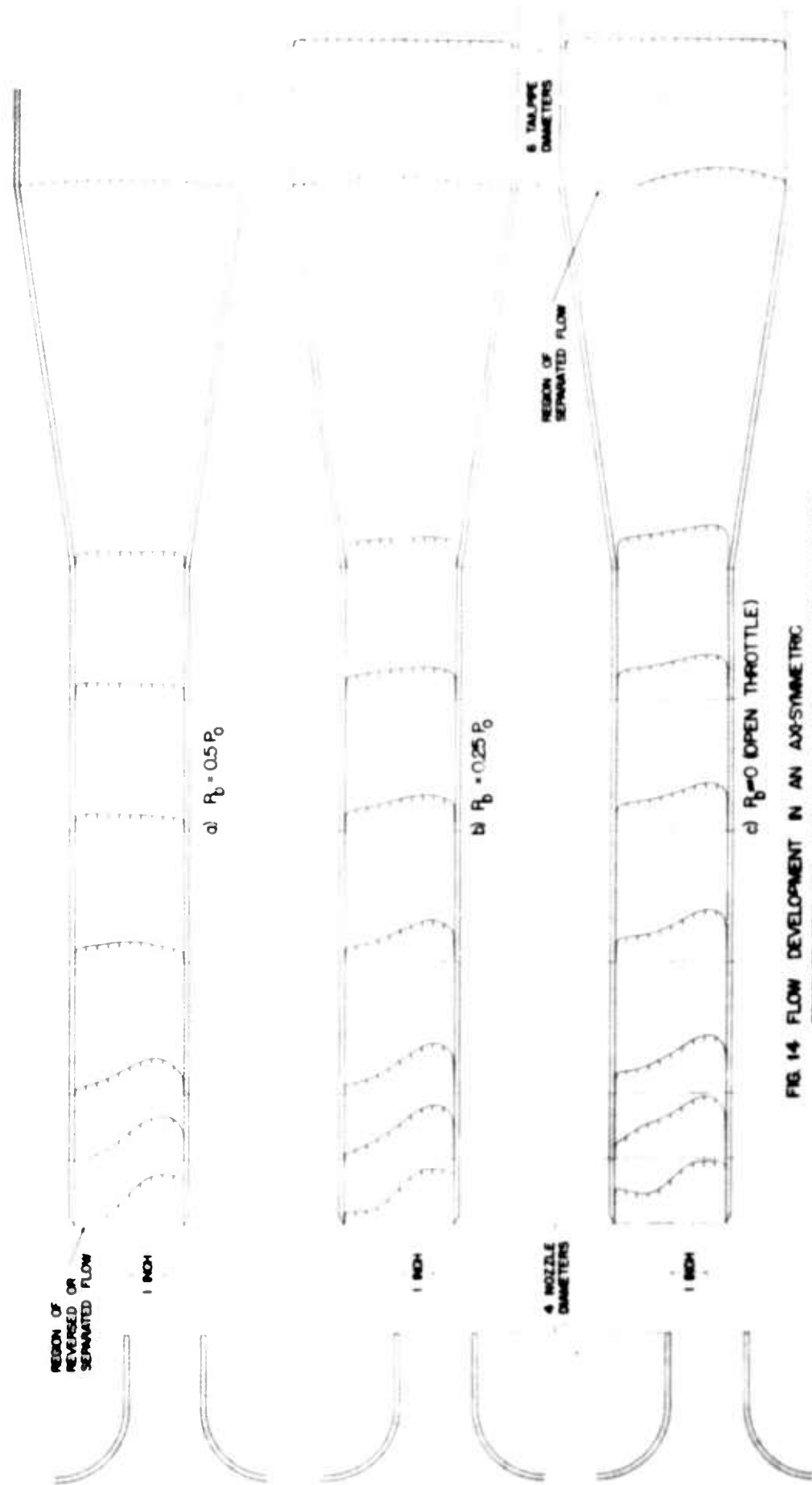


FIG. 14 FLOW DEVELOPMENT IN AN AXISYMMETRIC RECEIVER-OFFUSER WITH A NON-AXUALLY-ALIGNED NOZZLE.

critical geometrical and operational parameters. The constant-area mixing section provides a favorable geometry for rapid diffusion of a nonuniform flow. In all cases, the degree of nonuniformity at the receiver entry is significantly greater than that of "fully-developed" turbulent flow. As would be expected, the rapidity at which the profile approaches the fully developed profile in the constant-area section, depends on the nozzle-receiver axial spacing and alignment as well as the receiver back pressure P_b . The effect of increasing receiver back pressure is to hasten the velocity profile smoothing process.

In the axially-aligned cases of Figure 13, the velocity profile appears to resemble the "fully developed" turbulent flow profile in 4-6 receiver diameters, depending somewhat on geometry and back pressure.

The effect of profile skewness is vividly demonstrated in Figure 14[C]. Here, although considerable profile smoothing has taken place in the constant-area section, the profile at the entrance of the area-change section is still skewed. This skewness brings about early separation in the area-change section and results in a significant decrease in diffuser efficiency.

Also indicative of the character of the diffusion processes are the typical wall static pressure data of Figure 15.

The initial rise of static pressure in the receiver entry is, of course, due to the profile smoothing type of diffusion. For the lower back pressures the wall static pressure may be sub-atmospheric in the early portion of the receiver, or sometimes in the entire receiver-diffuser, because of inductive effects and separation at the leading edge. The presence of the wall static pressure maximum indicates that wall static pressure decrease due to wall shear has become important and eventually dominates the flow process. The static pressure rise in the area-change section follows the well known Bernoulli equation prediction.

A final indication of the character of the diffusion process in the constant-area section is given by the momentum coefficient $[\alpha]$ distributions in Figure 16. These factors were computed from the experimentally determined velocity profiles. It is seen, that although the momentum coefficient or "uniformity factor" is significantly greater than unity in the receiver entry, it very rapidly approaches a limiting value of about 1.02 in 2-3 diameters. Values of the momentum coefficients computed from the well known fully-developed pipe flow data of Nikuradse [Ref. 2] are very near 1.02 as well.

Typical values of pressure efficiency for the area-change diffuser as computed from wall static pressure and velocity profile measurements are given in Table 2. Comparison of these values with the data of Peters and Gibson is very good.

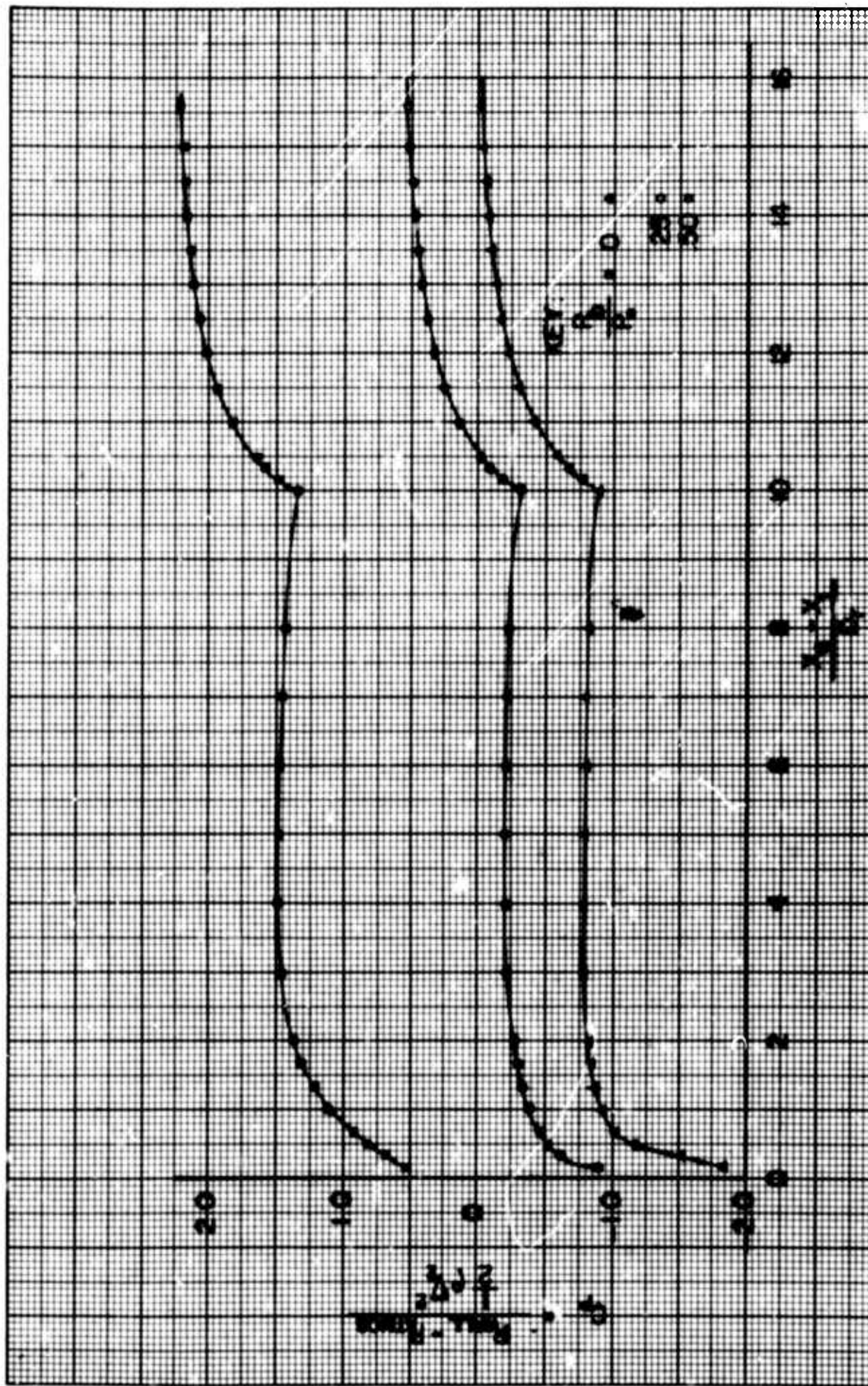


FIG. 15 MEASURED DIMENSIONLESS WALL STATIC PRESSURE DISTRIBUTION FOR $\frac{X_1}{D_0}$

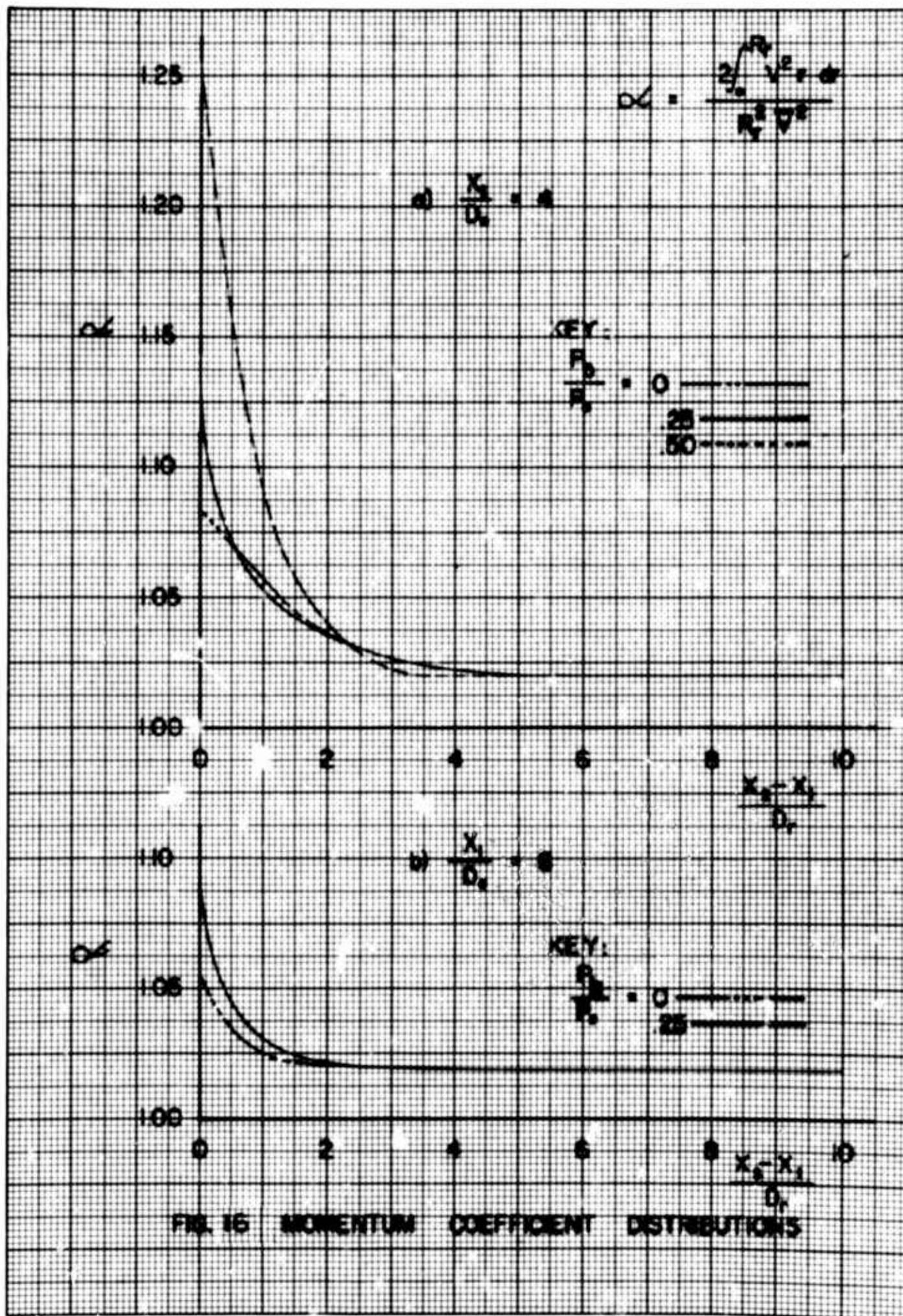


Table 2. Typical Values of Area-Change Diffuser Pressure Efficiency [Experimental]

X/D_o	4			6		8	
P_b/P_o	0	0.25	0.5	0	0.25	0	0.25
η_p	0.90	0.88	0.88	0.90	0.89	0.86	0.86
η_{ap}	0.90	0.89	0.89	—	—	0.90	0.88

Several important conclusions can be made concerning constant-area and area-change diffusion processes for the range of conditions considered.

1] The "rapidity" of the constant-area turbulent diffusion process is a function of receiver back pressure and receiver inlet profile uniformity and degree of skew.

2] For an axially-aligned nozzle-receiver system, the receiver axial velocity profile effectively reaches its fully-developed value in 2-4 diameters, depending to some extent on operational and geometrical conditions. The "optimum" length of constant-area mixing section for obtaining the highest degree of uniformity with the least over-all energy loss, is approximately equal to that length necessary for the profile to become effectively fully developed. Receivers with short constant-area mixing sections may involve large separation losses in the area-change section because of profile nonuniformity; likewise receivers which have long mixing sections may result in excessive wall shear losses. The uniformity factor, for stations three or more diameters downstream from the entry, may be estimated with good accuracy from fully-developed pipe flow data over a wide range of conditions; it is only required that the flow be turbulent.

3] For a non-aligned nozzle-receiver system, the "optimum" [as defined in 2 above] length of constant-area mixing section is significantly longer than in the axially-aligned case. Severe separation losses may occur in the area-change section for cases [generally the lower back pressure] where the profile has not effectively reached its fully-developed value.

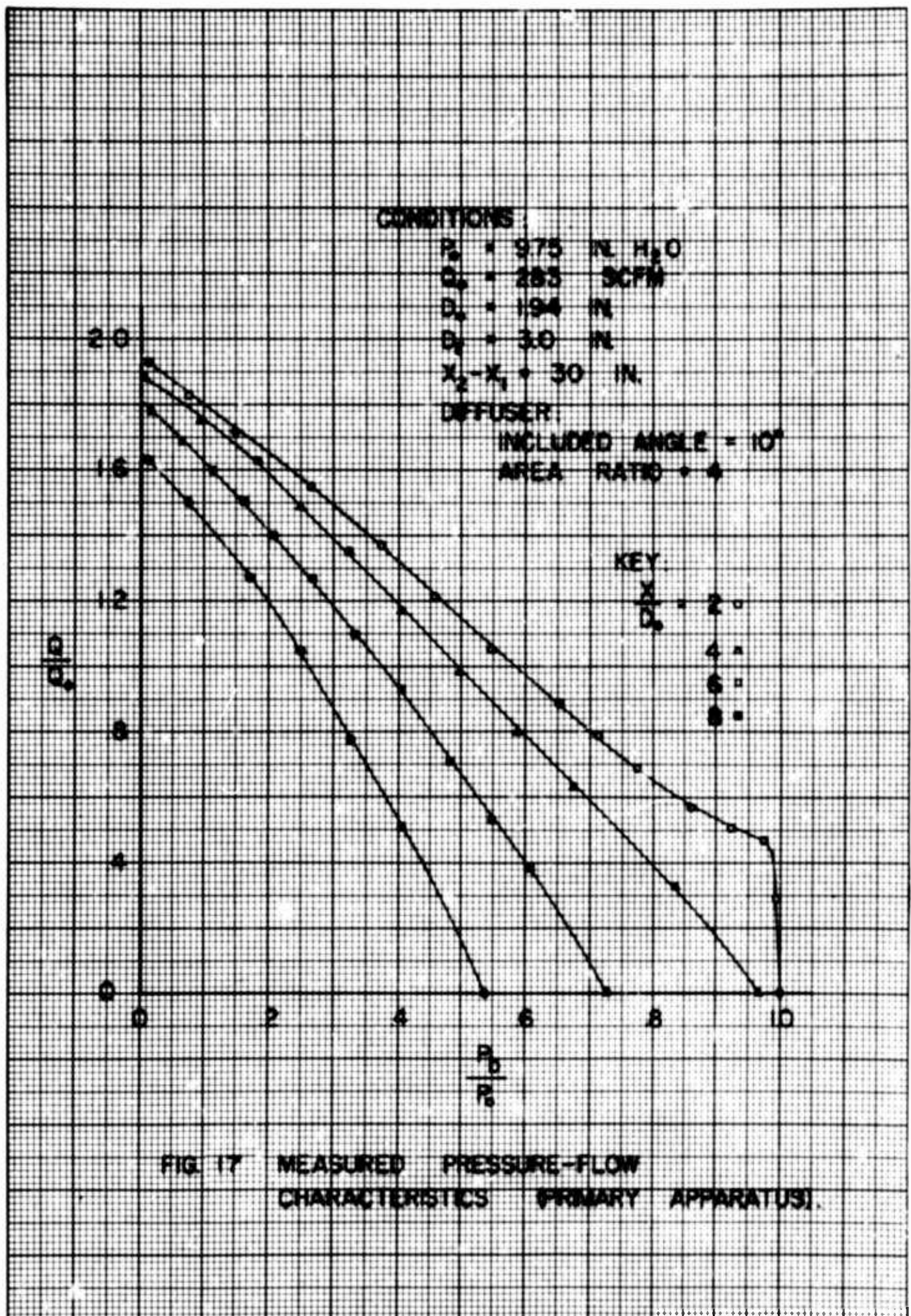
4] For systems employing area-change diffusers with "fully-developed" inlet velocity profiles, the data of Peters [Ref. 9] and Robertson [Ref. 13] and others, may be used to predict pressure efficiency with a reasonable degree of accuracy. Information is almost totally lacking in the literature, however, for cases involving other than fully-developed profiles and for Reynolds numbers below about 10^4 [range of particular interest in miniature jet modulators].

Pressure-Flow Characteristics

Over-all static performance is specified in terms of the relationship between receiver pressure and flow rate as downstream load conditions are varied. Typical measured pressure-flow characteristics are presented in Figure 17 for the axially-aligned jet-receiver-diffuser. The decrease in maximum or blocked-load pressure recovery [horizontal intercept] as the nozzle-to-receiver spacing is increased, is due primarily to the inherent spreading of the free jet and the resulting decrease in centerline total pressure. The corresponding decrease in open-load flow recovery [vertical intercept] as spacing is increased, is due also to the diffusion of the free jet. In that latter case, diffusion of the jet results in lower velocity gradients and, therefore, less favorable conditions for induction. It is significant that the characteristics presented in Figure 17 are all reasonably linear over the middle 60-70% of the curves.

Various techniques have been employed by other investigators to predict the two end points of the pressure-flow characteristic curves, i. e., the blocked-load pressure recovery and the open-load flow recovery. Blocked-load pressure recovery has often been estimated from an integration of the free jet total pressure. [See Refs. 7, 14 & 15]. The integral is evaluated over an area [$A = \pi R_f^2$] equal to the receiver entrance area and at an axial location [in the otherwise free jet] corresponding to the receiver entry location. Experimental justification for this approach has been lacking, however. It may be argued that the total pressure should be smaller than the actual blocked-load pressure; but how much smaller? It would seem that the jet centerline total pressure would necessarily be a good estimate of the blocked-load pressure. Indeed this is true, as demonstrated by the experimental measurements presented in Figure 18. A maximum error of about 6 % is incurred if the free-jet centerline total pressure is used to estimate the blocked-load recovery in the important region $x/D_0 \leq 10$. This is fortuitous, since the great body of information related to free submerged jets can be used to compute the blocked-load pressure recovery under a variety of operational and geometrical conditions. Also shown in Figure 18 for purposes of comparison, are results from integrating the total-pressure profiles. Obviously the total-pressure integral approach, for the particular geometrical conditions considered, is far from adequate. The large disparity indicated would, of course, be significantly reduced if the receiver were made smaller relative to the nozzle. In the case of plane or rectangular passages, the disparity probably would be smaller for comparable geometries because of the nature of the integral itself.

The open-load flow recovery point most often has been estimated from an integration of the flow in the otherwise free jet. [See Refs. 7, 14 & 15] Again, the integral is evaluated over an area equal to the receiver area and at an axial location corresponding to the receiver entrance. Previous investigators have assumed, without adequate experimental verification, that this flow integral approach is reasonably accurate. An exception is the interesting and thoughtful approach of Zalmanzon [Ref. 16] which utilizes a receiver inlet "discharge coefficient" estimated on the basis of experimental data. Such is not the case, as evidenced by the results of the



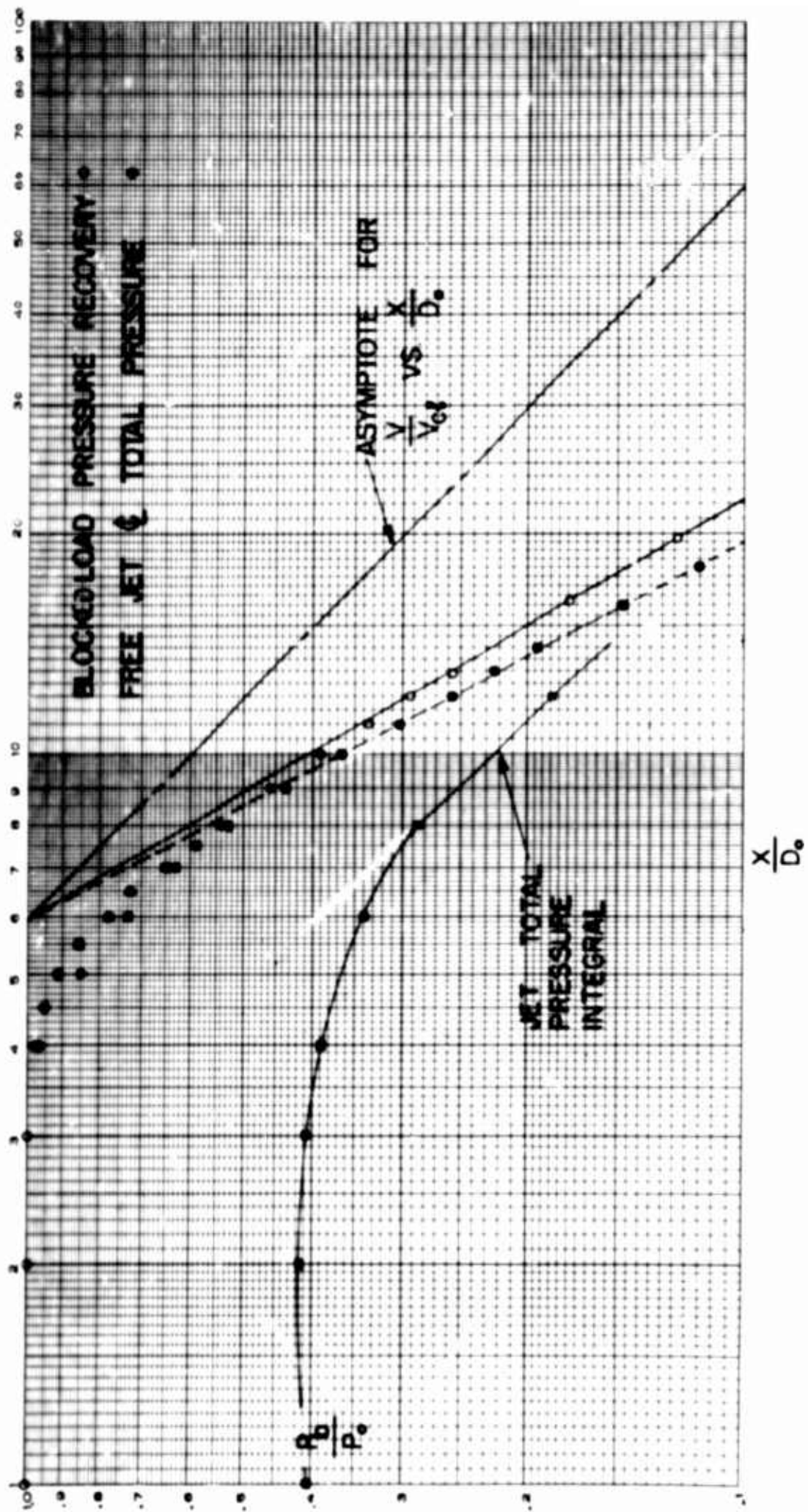


FIG. 18 CORRELATION OF MEASURED VALUES OF BLOCKED LOAD PRESSURE AND FREE JET CENTERLINE TOTAL PRESSURE.

present investigation. Because of the significant "jet-pump" or "induction" effects at the receiver entrance, significantly more flow is recovered than corresponds to the flow integrated over the receiver area.

A comparison of the maximum flow and maximum pressure points on the P-Q curves, as actually measured and as computed from the above mentioned integrals, is given in Table 3. It is obvious that for the range of geometrical and operational conditions considered, simple free jet integrations are inadequate to estimate the limiting points on the P-Q curves. Thus, it must be concluded that previously established analytical techniques for computing the entire P-Q curve, which are based on free jet integrations, are inadequate. This rather significant conclusion is indicative of the need for a more thoughtful approach to static performance prediction.

Table 3. Comparison of Measured and Computed Maximum Pressure and Flow Recoveries.

$\frac{x}{D_o}$	$\left(\frac{Q}{Q_o}\right)_c$	$\left(\frac{Q}{Q_o}\right)_e$	$\left(\frac{P_b}{P_o}\right)_c$	$\left(\frac{P_b}{P_o}\right)_e$
1	1.130	--	0.409	1.0
2	1.297	1.94	0.413	1.0
3	1.375	--	0.405	1.0
4	1.395	1.89	0.387	0.969
6	1.344	1.81	0.339	0.728
8	1.248	1.65	0.282	0.538
10	1.116	--	0.221	0.390
12	1.017	--	0.182	0.292

Subscripts:

c - Computed by integrating measured free jet (receiver removed) characteristics over area equal to receiver entrance area.

e - Experimentally measured with receiver in place.

Analytical techniques for predicting the over-all static performance of an aligned nozzle-receiver-diffuser system are explored in Ref. 1. Four simplified analyses are presented in order of their apparent applicability, adequacy, and degree of sophistication. The first two analyses assume one-dimensional flow and do not account for jet-mixing and internal flow energy losses. Energy losses are partially accounted for in the second two analyses by employing the momentum coefficient and pressure recovery correlations of Figures 16 and 18 respectively. Correlation of these analytical predictions with experimental results is surprisingly good for several important cases.

A more refined analytical prediction method, based on all of the pertinent details of the basic flow processes involved, is also presented in Ref. 1. The approach, as in the latter two simplified analyses, is based on a so-called "cow" streamline concept (often used in analyses of air breathing engines). In contrast to the simplified theories, this approach utilizes the characteristics of the free submerged jet. It is believed that the five analyses presented provide an important first step in the eventual development of a truly rational approach to jet modulator static performance prediction.

Conclusions

The experimental results presented herein illustrate the nature and complexity of some of the important flow processes involved in fluid jet devices. New insight has been gained concerning the rapidity of the diffusion process in constant-area mixing sections. Methods for utilizing free jet data in computations involving confined jets have not been adequately established. It has been demonstrated that predictions of steady-state pressure-flow characteristics of jet-receiver-load systems based on simple integrations of free jet axial velocity and total pressure profiles, may differ significantly from experimental measurements.

Acknowledgements

The guidance and advice of Professor F.T. Brown of M.I.T. is gratefully acknowledged.

This work was supported in part by the U.S. Air Force, ASD, under contract AF 33(657)-7535, the USAF, ASD, under contract AF 33(657)-8384, and the National Aeronautics and Space Administration under contract NASA 5208, and sponsored by the Division of Sponsored Research of the Massachusetts Institute of Technology. Current studies at Oklahoma State University are supported by the Harry Diamond Laboratories under contract DA-49-186-AMC-221(D).

REFERENCES

1. Reid, K. N., Jr., "Static and Dynamic Interaction of a Fluid Jet and a Receiver-Diffuser", Sc.D. Thesis, Department of Mechanical Engineering, Massachusetts Institute of Technology, Cambridge, Mass., September 1964.
2. Schlichting, H., Boundary Layer Theory, McGraw-Hill Book Co., Inc. New York, 1960.
3. Pai, S. I., Fluid Dynamics of Jets, Van Nostrand Co., 1954.
4. Berkoff, G. and Zarantonello, E. H., Jets, Wakes, and Cavities, Academic Press, New York, 1957.
5. Albertson, M. L., Dai, Y. B., Jensen, R. A., and Rouse, H., "Diffusion of Submerged Jets", Transactions ASCE, Vol. 115, 1950.
6. Kuethe, A. M., "Investigation of the Turbulent Mixing Regions Formed by Jets", Transactions ASME, Vol. 57, 1935.
7. Simson, A. K., "A Theoretical Study of Design Parameters of Subsonic Pressure Controlled, Fluid Jet Amplifiers", Ph.D. Thesis, Department of Mechanical Engineering, Massachusetts Institute of Technology, Cambridge, Mass., July, 1963.
8. Gibson, A. H., "On the Flow of Water Through Pipes and Passages Having Converging or Diverging Bow Laries", Proc. Roy. Soc., Series A, Vol. 83, 1910.
9. Peters, H., "Conversion of Energy in Cross-Sectional Divergences Under Different Conditions of Inflow", NACA TM 737, March, 1934.
10. Patterson, G. N., "Modern Diffuser Design", Aircraft Engineering, Vol. 10, 1938, pp. 267-273.
11. Taylor, J. R., Grimmett, H. L., and Comings, E. W., "Turbulent Mixing in an Isothermal Free Jet", University of Illinois Experiment Station, Technical Report No. 2, Contract N6-ori-71, Task Order XI, Office of Naval Research, November, 1948.
12. Baines, W. D., Discussion of Reference 5.
13. Robertson J. M., and Ross, D., "Effect of Entrance Conditions on Diffuser Flow", Transactions ASCE, Vol. 118, 1953, pp. 1063-1097.
14. Reilly, R. J. and Moynihan, F. A., "Notes on a Proportional Fluid Amplifier", Presented at the Symposium on Fluid Jet Control Devices, ASME Winter Annual Meeting, New York, November, 1962.

15. Peperone, S. J., Katz, S., and Goto, J. M., "Gain Analysis of the Proportional Fluid Amplifier", Presented at the Fluid Amplification Symposium, Harry Diamond Lab., October, 1962.
16. Zalmanzon, L. A., "Fundamentals of Theory and Calculations of Elements of Pneumo-Automatics", Proceedings of the First International Conference of the International Federation for Automatic Control, Moscow, June, 1960.

DYNAMIC INTERACTION OF A FLUID JET AND A RECEIVER LOAD SYSTEM

Karl N. Reid, Jr., Assistant Professor
School of Mechanical Engineering
Oklahoma State University
Stillwater, Oklahoma

ABSTRACT

One important class of jet-receiver-load dynamic interaction problems has been studied in detail. It is demonstrated that a static or dynamic instability may exist as a result of jet-receiver-load interaction. Methods are presented for characterizing the jet-receiver interaction region both statically and dynamically. Typical static pressure-flow characteristics for the interaction region are presented which exhibit an S-shaped character for certain geometrical configurations. It is demonstrated that the S-shaped characteristic leads to a static instability for high impedance loads. Analytical, graphical, and numerical computation techniques are presented which permit rapid and accurate prediction of relative and absolute stability for a jet-receiver-load system. Experimental measurements show good correlation with predictions of system limit cycle frequencies and amplitudes.

INTRODUCTION

The Dynamic Interaction Problem

Most persons who have dealt experimentally with fluid jet modulators have encountered some type of dynamic instability, evidenced by oscillations of the main jet and/or pressure fluctuations in the receiver passages. Although the sources of such instabilities are not well understood, it is most certain that jet-receiver interactions, including cross-coupling between receiver ports and/or load ports, and complicated by "jet noise" are the important influencing phenomena. The jet itself provides the necessary energy source to continually "feed" the instability, while the jet-receiver interactions and potential receiver cross-coupling provide the internal feedback required for instability.

Pressure oscillations may occur in jet modulators operating with an "incompressible" or "compressible" fluid. There is no truly incompressible fluid, and therefore wave motion effects can exist in any fluid modulator. It is convenient, however, to identify two classes of stability problems: 1) those associated with low-velocity gas flows (Mach number less than 0.3) and "incompressible" liquid flows; and 2) those associated with periodic jets from underexpanded sonic and supersonic nozzles (i.e., so-called resonance tubes). The sources of instability seem to be quite different for these two cases, whereas the resulting effects are much the same. Only the first stability problem will be discussed here. The discussion which follows is a condensation of one

portion of the author's Doctor of Science Thesis (Ref. 1).

Scope of Investigation

Several important limitations were imposed in the investigation so as to make the problem solution more tractable. The most important limitation was the restriction to a single receiver-load system, thereby ignoring all possible effects of cross-coupling between two or more receivers. However, since the investigation was aimed primarily at demonstrating techniques for studying jet-receiver dynamic interaction, the potential usefulness of the information presented should not be hindered significantly by this restriction. There are, in fact, a number of jet modulator designs which incorporate only a single receiver.

The investigation was conducted and is herein presented with the following primary goal in mind:

To conduct an exploratory study of dynamic interaction between a fluid jet and single receiver-load system, so as to establish techniques for measuring the interaction region static and dynamic characteristics and for utilizing this information in the direct analytical prediction of system absolute and relative stability.

STATIC AND DYNAMIC CHARACTERIZATION OF THE JET-RECEIVER INTERACTION REGION

Basis for Experimental Dynamic Characterization

The investigation was initiated with the following premise: if the jet-receiver interaction can be characterized dynamically, then it is possible to predict system dynamic stability* for a wide variety of load conditions by using conventional stability analyses. The dynamic characterization approach selected involves the determination of the effective "reflection coefficient" of the receiver looking upstream into the main jet. The experimental technique for measuring the "reflection coefficient" involves the generation of a pressure pulse at a location downstream of the receiver mouth, the dynamic measurement of the "incident" pressure wave as it passes a point between the pulse source and the receiver mouth, and the dynamic measurement of the wave as reflected from the receiver mouth. Of principal interest is whether the reflected waves can be characterized in terms of a simple "reflection coefficient" rather than a more complicated transfer function.

Figure 1 illustrates a simplified situation under which the appropriate measurements can be made. The jet-receiver interaction region is treated as a "black box" and termed the "source terminal." A transmission line connects the source terminal to be studied to the "load terminal." The transmission line merely provides a means of "separating" the incident and reflected waves in time.

* It will be seen later that there exist two types of dynamic stability and one type of static stability.

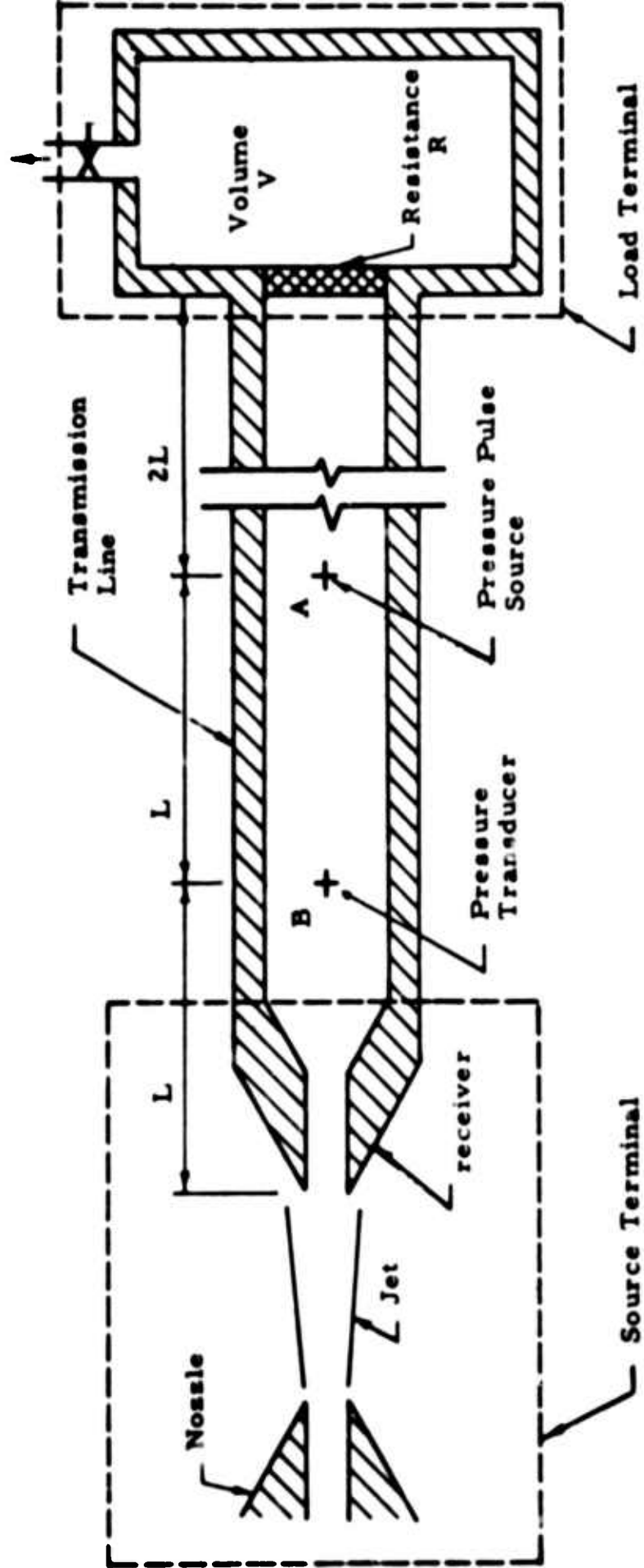


Fig. 1 Representation of Technique for Studying Jet-Receiver Dynamic Interaction

The "load terminal" functions to stabilize the receiver pressure under a blocked or partially blocked load condition. The information to be determined is contained in the relative shapes and amplitudes of the incident and reflected waves. The difficulties involved in implementing this method of source dynamic characterization are discussed in Ref. 1.

Axisymmetric Nozzle-Receiver-Transmission Line Apparatus

Initially, an attempt at source dynamic characterization was made using an instrumented proportional fluid jet modulator (less control jets) of rather conventional design (two receiver ports). It soon became apparent that several interactions were being studied simultaneously, and it was difficult to separate them. Consequently, a simple axisymmetric nozzle-receiver (like the schematic of Fig. 1) was built to eliminate all unnecessary boundaries in the vicinity of the nozzle, and all potential receiver cross-coupling effects. With this apparatus the influence of various types of nearby bounding surfaces could be studied.

The final apparatus was comprised of a $3/8$ in. diameter, long tube nozzle and a $1/2$ in. diameter receiver tube. A transmission line of $1/2$ in. diameter was attached to the receiver. The terminal load was a pneumatic R-L-C device specially designed to minimize reflections and still allow the possibility of a "blocked load". The resistance element was constructed with a resistance equal to the surge impedance of the transmission line. A pulse source was formed by blowing air through an appropriately slotted disk.

"Creation" of an Active Source

Before a meaningful study of the dynamic or static characteristics of the interaction region could be made, it was necessary to establish means for "creating" an active source, i.e., a source which "feeds" an impending oscillation. Certainly, past experience with jet modulators of various types is sufficient to give one confidence that a sustained pressure oscillation in the receiver can be produced.

The axisymmetric apparatus was arranged to have a source driving a transmission line blocked at its downstream end, since a sustained pressure oscillation is most likely to occur in such a system. Then, various solid boundaries were placed in the interaction region in an effort to create a "large" amplitude pressure oscillation in the line. The configurations, shown in Fig. 2, were found to produce the desired oscillation. Case (a) typifies the phenomena observed.

By proper placement of the wall in the jet, the jet is caused to attach and follow the wall until the point is reached where an adverse pressure gradient causes it to separate. Placement of the receiver mouth near the separation point results in a sustained pressure oscillation in the transmission line and a corresponding oscillation of the jet. The nature and cause of the oscillation in these particular cases can be explained qualitatively as follows: as the jet is "turned on,"

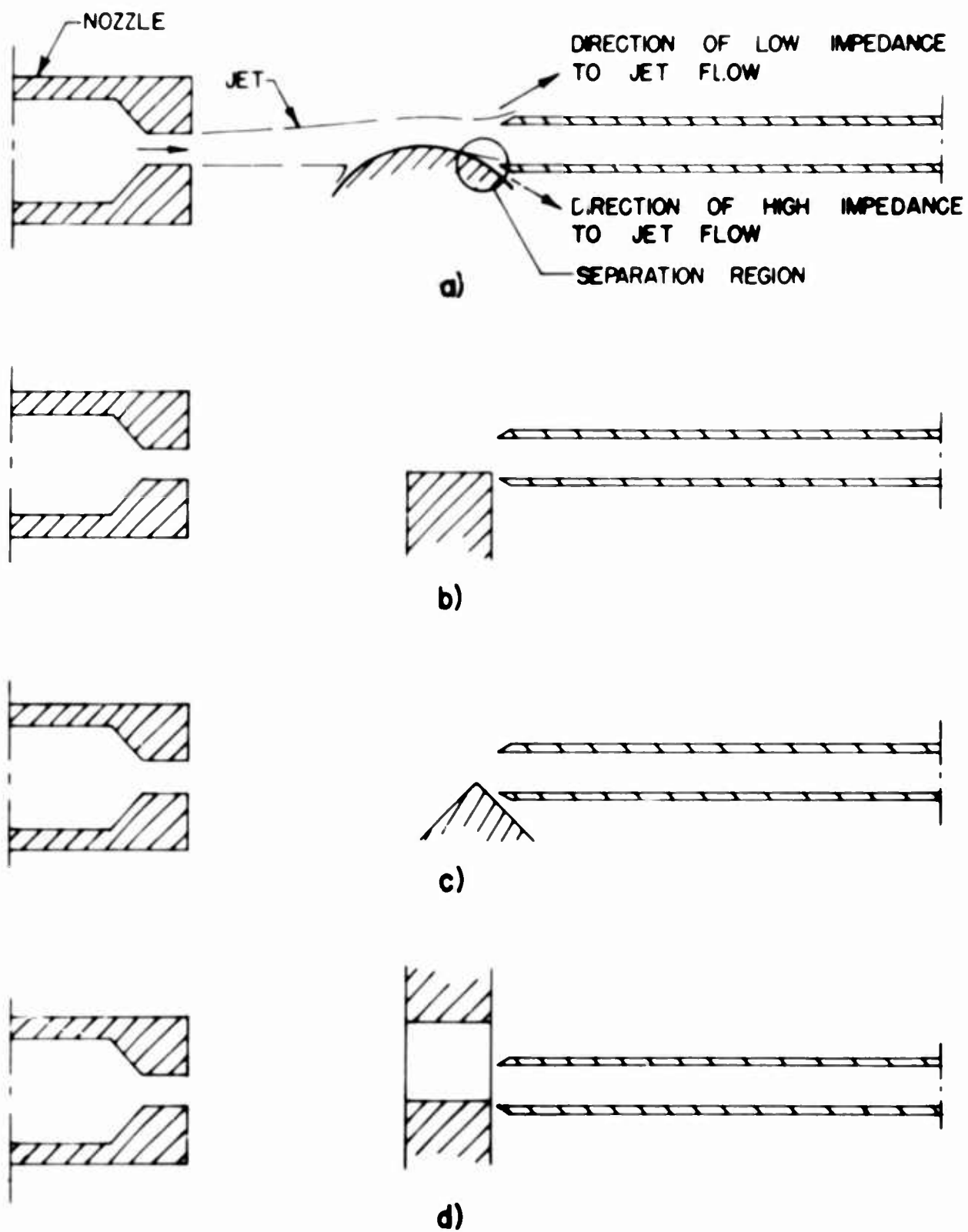


FIG. 2 DEMONSTRATED "ACTIVE" SOURCES.

the pressure begins to rise in the receiver as a result of simple charging of the associated capacitance; the pressure in the separation region also rises above its "equilibrium" value because of the high resistance to flow introduced by the wall-to-receiver mouth restriction; the pressure in the separation region finally becomes large enough (but not necessarily above atmospheric) so that the jet is caused to separate further up the wall and thus partially miss the receiver; the receiver and separation region pressures then tend to decrease until the original separation point is restored, at which point the process is repeated again and again. Of course, wave motion in the receiver line plays an important role in this phenomena. As the jet is turned on, a compression wave travels down the line and is reflected from the blocked end as a compression wave. When this wave returns to the receiver mouth, it causes the separation region pressure to increase rapidly and the jet to flip suddenly away from the wall. The motion of the jet causes a sudden decrease in the pressure at the receiver entry and, as a consequence, causes a rarefaction wave to travel down the line. This wave is reflected from the blocked end in like sense, and on its return to the receiver mouth, reduces the separation region pressure enough so that the jet can re-attach at the original point of attachment. The receiver pressure oscillation is very nearly triangular in shape.

It is not necessary to have a wave-like element (i.e., a transmission line) connected to the source in order to observe a sustained oscillation. If a tank (simple capacitance) is substituted for the transmission line, the tank pressure will oscillate as well. In this case, the oscillation is characterized by an exponential rise followed by an exponential decay, i.e., a direct result of the inherent RC characteristics of the receiver-tank combination. The charging and discharging time constants usually are different, the discharging time constant generally being the smaller of the two.

Recent experiments carried out by the author (at Oklahoma State University) using plane (rectangular) geometries, indicate that potentially unstable configurations can be "created" in the following ways: merely offsetting the receiver centerline from the nozzle centerline; placing a cylindrical "deflector" at a location approximately one third of the distance between the nozzle and receiver; enclosing one side of the interaction region as in a "one-sided" pressure-control amplifier. It also has been demonstrated experimentally that the pressure in a blocked-load system may oscillate if a cylindrical body is placed across the receiver mouth (transverse to the axis or flow direction). In this latter case oscillations are probably keyed to the frequency of vortex shedding from the cylinder. Research aimed at better understanding of these instability mechanisms is currently being carried out by the author.

Results of Experiment to Determine Source Dynamic Characteristics

Simple pulse response measurements were performed with the apparatus arranged as follows:

- 1) a 20 ft., 1/2 inch diameter line was connected to the 9 inch long, 1/2 inch diameter receiver;
- 2) the pulse source was placed at a T-junction located about 10 feet from the receiver mouth;
- 3) a Kistler quartz crystal pressure transducer was placed between the pulse source and the receiver mouth (about 5 feet from receiver mouth);
- 4) a curved boundary was placed in the interaction region so as to produce a large sustained oscillation for a blocked-load condition;
- 5) the blocked-load terminal was replaced by the specially designed RLC load so as to damp out the oscillation.

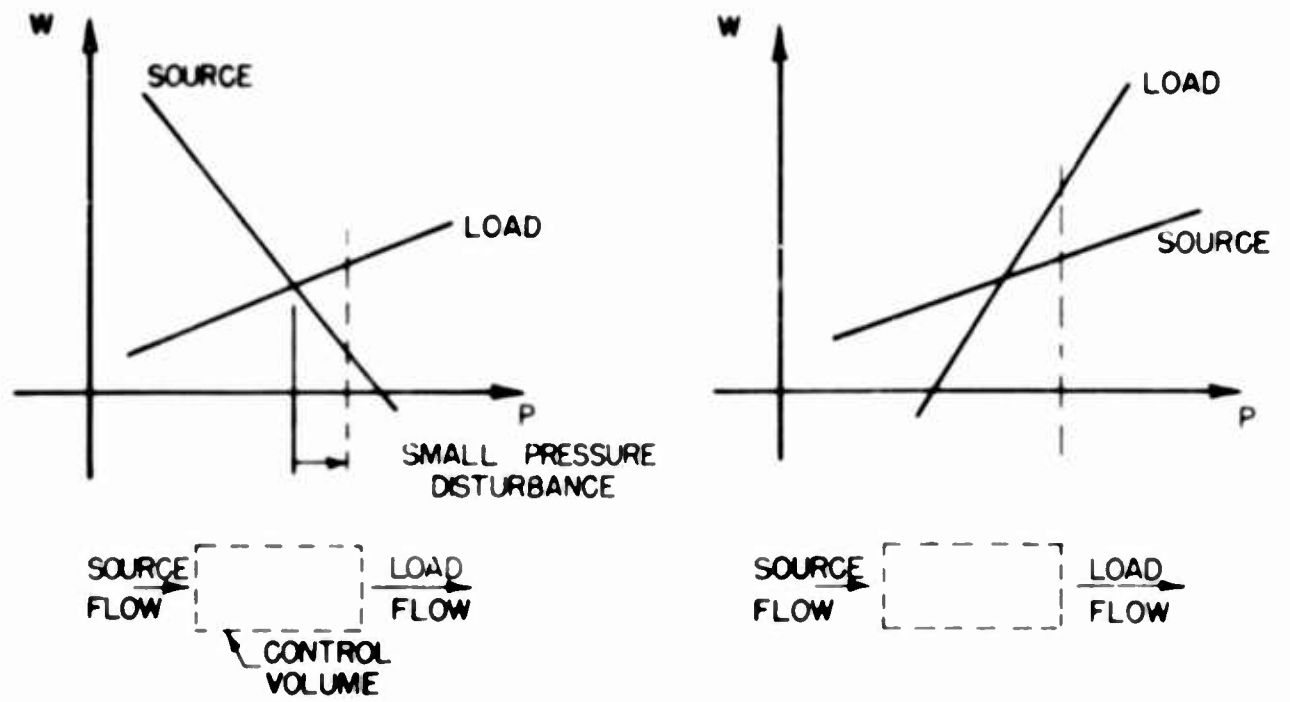
Although noise somewhat obscured the results of interest, it was concluded that for frequencies up to several thousand cycles per second, source dynamic phenomena are insignificant. It is reasonable to expect, in fact, that dynamic effects would involve time lags or delays of the same order as the fluid transport time from the nozzle to the receiver. It should be possible, therefore, to utilize a steady-state characterization of the interaction region. It was, in fact, on this basis that the remaining portion of the dynamic interaction study was carried out. Results of a recent M.I.T. Doctoral thesis by L. E. Johnston confirm these conclusions (Ref. 2).

Measurement of Steady-State Characteristics of an Active Source

Physical intuition and reasoning leads one to the conclusion that the steady-state pressure-flow characteristic for a potentially unstable source configuration (active source) is probably S-shaped, i.e., having both negative and positive slopes. Many dynamic systems which exhibit a tendency toward self-excited oscillations have an S-shaped characteristic curve.

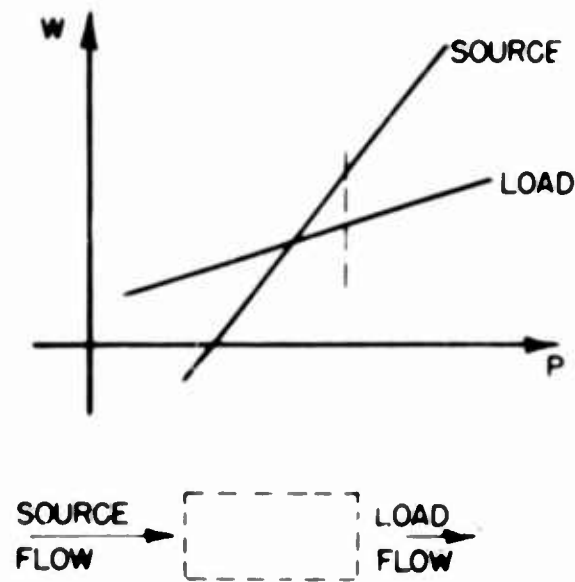
To better understand the relationship which must exist between load and source resistances in order to produce an instability, it is helpful to refer to Fig. 3. Three typical cases are shown for example only. This in no way presents a complete picture of system stability, as will become evident in the following section. In each of the cases shown in Fig. 3, only the region of intersection of the two characteristics is shown. Stability "in-the-small" may be determined by considering the consequences of a small positive pressure disturbance relative to the apparent equilibrium condition. Below each W vs P plot is a schematic of a small control volume supposed to be situated between the source and load. The source flow enters the control volume and the load flow leaves the control volume; equilibrium requires that these two flows be equal. The length of arrow is indicative of the relative magnitude of the corresponding flows entering and leaving as a result of the pressure disturbance.

Both cases (a) and (b) represent stable systems since a positive pressure disturbance leads to a load flow demand which is greater than the source can provide, thereby causing the pressure to decrease once again. In contrast, case (c) represents a situation where the positive pressure disturbance leads to a load flow demand which is smaller than the source supplies; i.e., the source must be "active." As a result, the pressure



a) STABLE

b) STABLE



c) UNSTABLE

FIG. 3 CONCEPT OF STATIC STABILITY "IN-THE-SMALL".

increases even further until eventually some mechanism places a limit on its magnitude. This is a static type of instability. It will be seen later that three types of instabilities can be identified, one of which is a static instability.

The conventional technique for measuring the portion of the pressure-flow characteristic curve in the first quadrant for a passive source involves varying the load resistance from zero (vertical line) to infinity (horizontal line), in such a way that the resistance is always positive. To measure the portion of the curve in the fourth quadrant, it is necessary to vary the load curve slope from a large negative value to a small negative value by supplying flow from an external source.

Obviously the technique employed to measure the characteristic of a passive source would lead to a static instability in the case of an active source (e.g., see Fig. 3 (c)). If, however, a family of load characteristic curves can be generated which all have a relatively low resistance (i.e., large change in flow for a small change in pressure) in the vicinity of their point of intersection with the source curve, stable operation can be achieved (e.g., see Fig. 3 (b)).

An experimental technique which can be used to obtain the active source characteristic curve is shown schematically in Fig. 4.

The flow rate to be determined, W_a , is equal to the total flow as indicated by the downstream rotameter minus the constant flow from the external source. In the first quadrant, W_a is positive and the rotameter flow is greater than the flow from the constant-flow source. In the fourth quadrant W_a is negative and the rotameter flow is less than the flow from the constant-flow source. If the flow from the constant-flow source is adjusted properly, the flow rate W_a can be made to undergo large changes while the metering pressure P_m undergoes only small changes. The progressive variation from one load characteristic curve to another is accomplished simply by varying the amount of downstream throttling.

Typical measured characteristics using the technique outlined above are plotted in dimensionless form as a function of nozzle supply pressure in Fig. 5. The source geometry was chosen such that, when coupled with a transmission line blocked at its downstream end, a high degree of instability existed. The shape of the curve is controlled primarily by the effective resistance to reversed flow (i.e., negative W_a). If the resistance to reversed flow is large, the source characteristic may not be S-shaped at all. Likewise, if the resistance to reversed flow is very small, the curve will not "turn back" with large $-W_a$.

It was the purpose of this experiment to demonstrate technique only. A systematic study of the effect of geometrical variations on the character of the source is presently being conducted at Oklahoma State.

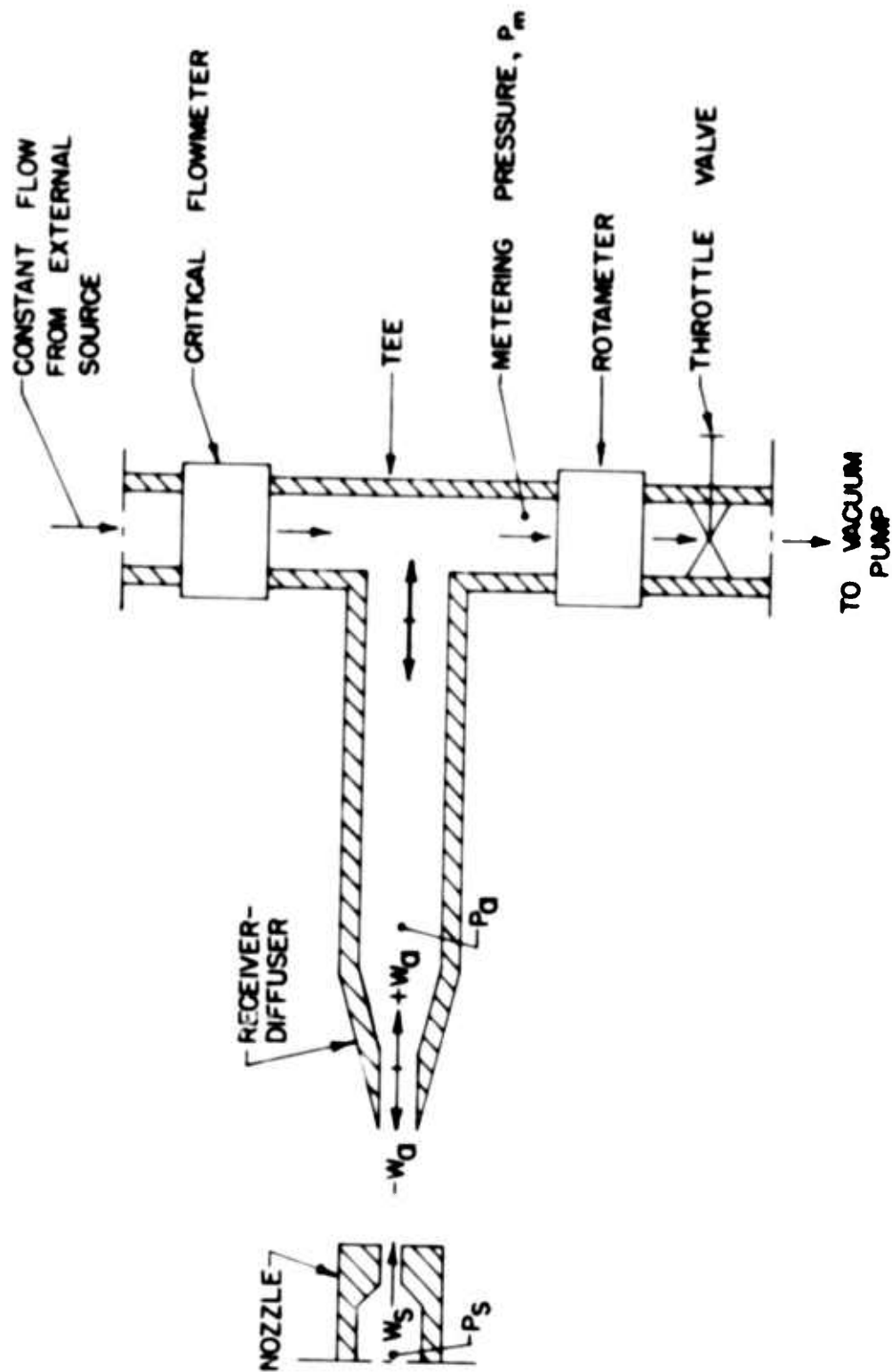
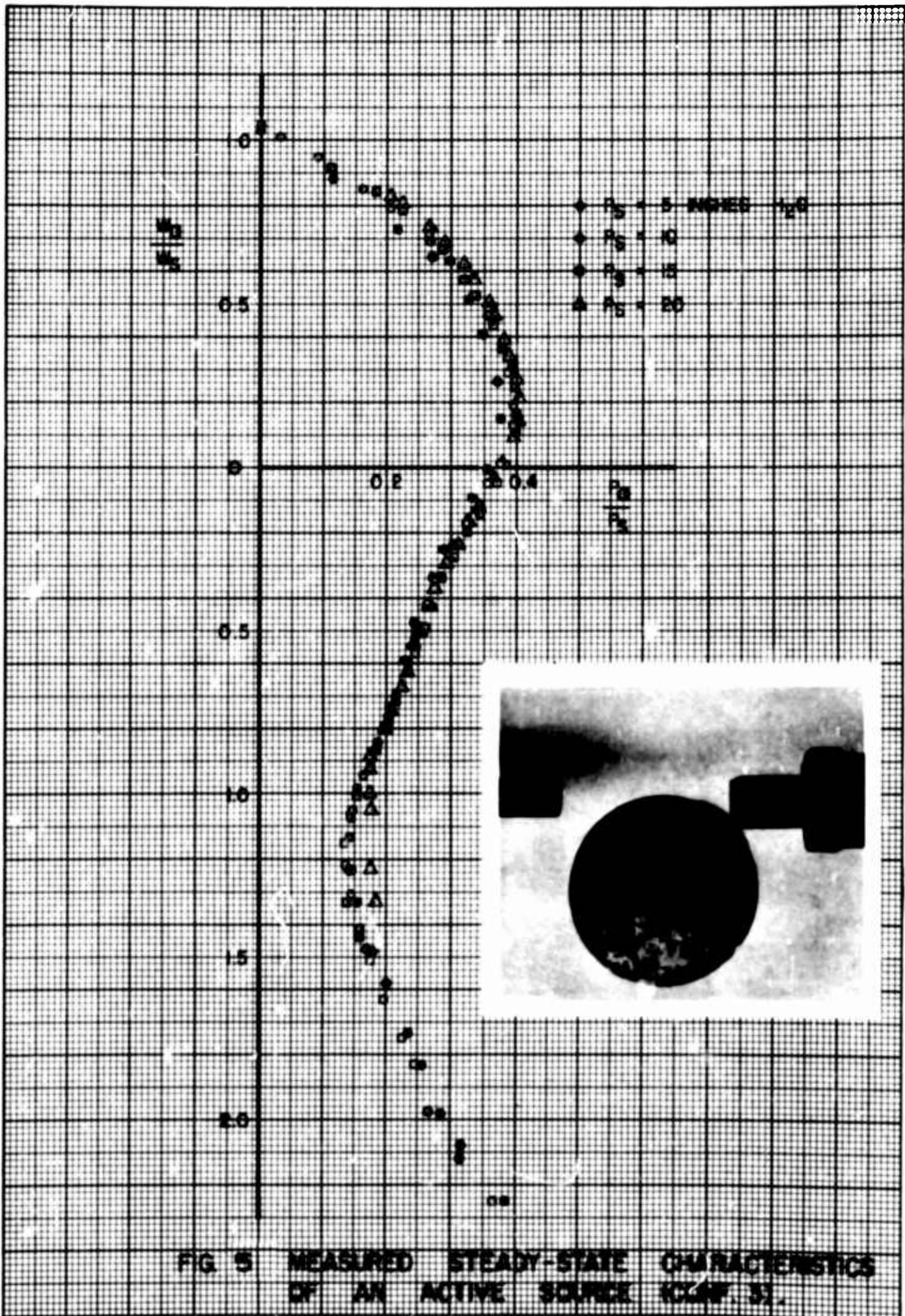


FIG. 4 EXPERIMENTAL TECHNIQUE FOR DETERMINING THE STATIC CHARACTERISTIC OF AN ACTIVE SOURCE.



SYSTEM STABILITY PREDICTION AND CORRELATION WITH EXPERIMENTAL RESULTS

Analytical Prediction of Absolute "Stability-in-the-Small"

Consider, as before, the single-receiver system consisting of an active source coupled to an active or passive load terminal by means of a simple transmission line. Such a system is interesting as well as practical in that it serves as a potential building block for more complicated systems.

The presence of the "wave-like" element (transmission line) in the system suggests that consideration be given to system dynamic stability as well as the static stability discussed in the previous section. Professor F.T. Brown of M.I.T. has suggested that the absolute stability "in-the-small" of such a system be classified according to the character of the load (Ref. 3). The following types of stability (or instability) are then identifiable: static, wave and surge. These three types of stability arise on considering the effect of the length of the transmission line coupling the source and load. Static stability is obviously associated with a system containing an extremely short line. Referring to the sketches in Fig. 3, it is possible to establish a simple criterion for static stability "in-the-small" (i.e., for small disturbances). The system is stable in the vicinity of the equilibrium point (i.e., point of intersection of the source and load curves) if the source impedance, Z_s , and the load impedance, Z_l , are related by the inequality,

$$\frac{1}{Z_s} + \frac{1}{Z_l} > 0 \quad . \quad (1)$$

Notice that a positive value of source impedance implies a negative slope on the W vs P plot, whereas a positive value of the load impedance implies a positive slope on the W vs P plot. This is merely a result of sign convention for the flow, i.e., positive flow is defined as flow from the source to the load.

If the source-to-load capacitance is very small, the static instability will result in a very high frequency oscillation. In such a case, the concept of static stability based on the measured steady-state pressure-flow characteristic for the source may lose its physical meaning because of the inadequacy of this characteristic at high frequencies. For this case, the source dynamic characteristics must be considered.

If the line attached to the source is very long, pressure waves take a considerable time to travel down the line and then return again. Over the period of the round-trip of a wave, the effective load impedance seen by the source is the "surge" or "characteristic" impedance of the line rather than the impedance of the load terminal. The idealized (i.e., neglecting wall shear) characteristic impedance of a line of cross-sectional area A, in terms of a ratio of pressure to mass-flow rate at a point in the line, is given simply by $Z_c = c/A$, where c is the speed of sound in the medium. The stability criterion given by Eq. (1) applies to this surge situation if Z_l is replaced simply by Z_c .

The system is surge-wise stable if the following inequality is satisfied:

$$-\frac{1}{Z_s} + \frac{1}{Z_c} > 0 \quad (2)$$

The oscillation frequency associated with a static or surge-type instability is characteristically quite high. The very high frequency noise associated with most jet-modulator systems is undoubtedly a manifestation of the surge-type instability.

Since the surge impedance only represents the true load impedance seen by the source for relatively short periods of time, it is necessary to consider wave motion effects if stability over longer periods of time is of interest (and it most often is of prime interest). Wave motion effects obviously have their greatest importance for intermediate line lengths. Here, consideration of the reflection of waves from both ends of the transmission line leads to the concept of "wave stability."

For a transmission line having a terminal impedance, Z_t , and a characteristic impedance, Z_c , the ratio of the reflected to the incident pressure waves is given by (Ref. 1):

$$r = \frac{Z_t - Z_c}{Z_t + Z_c} \quad (3)$$

where r is defined as the "reflection coefficient" and is, in general, frequency dependent. The reflection coefficient must be equal to or less than unity if the terminal is passive, and is unbounded if the termination is active.

Consider now a "lossless" transmission line having two terminals, a source and a load. For generality let the associated terminal impedances be denoted as Z_1 and Z_2 . If a wave reflects first off of one terminal and then the other, that is, undergoes one complete cycle returning to its initial position and direction of motion, its new amplitude is $r_1 r_2$ times its initial amplitude. The product $r_1 r_2$ may be positive or negative and equal to, less than, or greater than unity. If $|r_1 r_2| > 1$, then the wave has picked up energy (from an active source and/or load) and the system is unstable. One of two types of instabilities may exist. If $r_1 r_2 > +1$, the instability is exponential or non-oscillatory in-the-small; if $r_1 r_2 < -1$, the instability is oscillatory. The criterion for wave-type absolute stability in terms of the surge and two terminal impedances, is

$$|r_1 r_2| = \left| \frac{Z_1 - Z_c}{Z_1 + Z_c} \frac{Z_2 - Z_c}{Z_2 + Z_c} \right| < 1 \quad (4)$$

A summary of the stability types and criteria for all possible permutations of real terminal impedances (resistances) is given in Table 1. This summary was originally prepared by Professor F.T. Brown and is reproduced from Ref. 3. The reader interested in a detailed treatment of absolute stability in "two-line" systems, including coupling between receivers and/or loads, should refer to Professor Brown's development in Ref. 3.

Z ₁ and Z ₂			Wave Stability		Surge Stability $\frac{1}{Z} + \frac{1}{Z_c} > 0$	Static Stability $\frac{1}{Z_1} + \frac{1}{Z_2} > 0$
-Z _c	0	Z _c	Stable	Type		
✓			No	Non-oscillatory	Yes	No
✓	✓		No	Oscillatory	No	No
	✓		No	Non-oscillatory	No	No
✓		✓	when Z ₁ Z ₂ + Z _c ² < 0	Oscillatory	Yes	Yes
✓		✓	when Z ₁ + Z ₂ < 0	Non-oscillatory	Yes	when Z ₁ + Z ₂ ≤ 0
	✓	✓	when Z ₁ + Z ₂ > 0	Non-oscillatory	No	when Z ₁ + Z ₂ ≤ 0
✓	✓	✓	when Z ₁ Z ₂ + Z _c ² > 0	Oscillatory	No	No
		✓	Yes	--	Yes	Yes
		✓	Yes	--	Yes	Yes
		✓	Yes	--	Yes	Yes

Table 1 Summary of Stability Types and Criteria
for Source-Transmission Line-Load Systems

Graphical Techniques for Prediction of System Relative Stability

The stability criteria developed in the previous section are particularly useful when information concerning the absolute stability of a system is desired; that is, is the system stable or unstable "in-the-small?" Nothing can be inferred directly from these criteria concerning the relative stability of the system for small or large perturbations. In addition, these or similar criteria are difficult to apply in cases involving non-real terminal impedances. Very often, a knowledge of the frequency and amplitude of a pressure oscillation is required. For example, such information is vital in the design of oscillators. As another example, consider a system which exhibits an instability. The over-all performance of the system may not be impaired significantly providing the oscillation frequency is high enough and the amplitude is low enough; again a knowledge of the detailed character of the oscillation is required before its effect can be fully evaluated.

The suitability of graphical techniques such as the method of characteristics (Ref. 4) and slope-line integration (Ref. 5) for dealing with transient phenomena in systems incorporating simple nonlinearities, wave-like elements, and other simple active and passive elements, is well known. As will become evident in the discussion which follows, graphical techniques afford a reasonably accurate and rapid approach to the study of jet-receiver system relative stability. An example is discussed below to illustrate the utility of graphical analysis. The analysis is semi-empirical in that experimentally derived (or otherwise known) source and load pressure-flow characteristics are utilized. The solutions presented are, therefore, limited to the range of frequencies for which the steady-state source and load characteristics are valid. The basic equations describing system behavior are presented in finite difference form, since the graphical techniques involve a type of numerical step-by-step solution.

Consider, as an example, the system shown schematically in Fig. 6. Limiting cases of this example are considered in Ref. 1. The solution sought is as follows: given a small disturbance from "equilibrium" in the load-end pressure, P_b , what is the resulting variation of P with time, i.e., does the disturbance die out or does the presence of the active source lead to a dynamic instability? Further, the detailed nature of any limit cycle is to be determined.

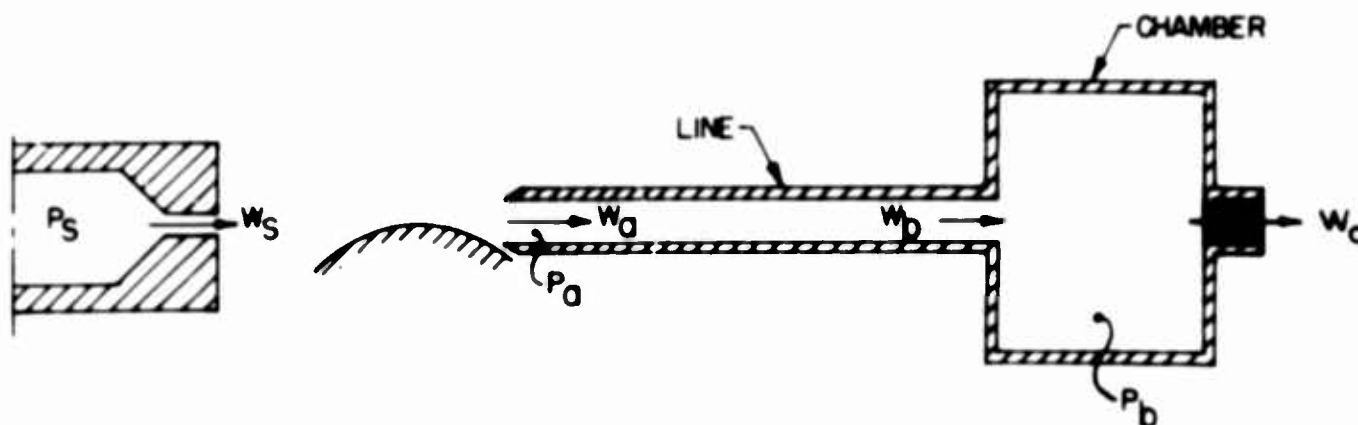


Fig. 6 Active Source Coupled to a Transmission Line Terminated by a Load Chamber

First, consider the transmission line portion of the system only. The line may be treated as a distributed parameter system.* It is assumed that the pressure waves are of small amplitude, the gross fluid velocity in the line is very small compared to the speed of sound in the medium, and wave dispersion effects are unimportant. These assumptions permit use of the well-known linearized form of the wave equations. Of the various forms of the solution, the most convenient is that given in terms of the conditions at the ends of the line as follows:

$$\begin{bmatrix} P_b \\ W_b \end{bmatrix} = \begin{bmatrix} \cosh \Gamma & -Z_c \sinh \Gamma \\ -\frac{1}{Z_c} \sinh \Gamma & \cosh \Gamma \end{bmatrix} \cdot \begin{bmatrix} P_a \\ W_a \end{bmatrix} \quad (5)$$

where Γ = propagation operator

Z_c = characteristic impedance of the line; defined as the complex ratio of the instantaneous pressure to the instantaneous flow rate at a given point in the line.

Both Γ and Z_c are, in general, frequency dependent properties. Brown (Ref. 6) has shown that, for the case of uniform attenuation (i.e., no dispersion), the propagation operator can be approximated as follows:

$$\Gamma \approx -\alpha + Ts \quad (6)$$

where

T = characteristic time of the line, s = Laplace operator,
 e^{α} = the attenuation factor; α is termed the attenuation constant.

For the special case of an ideal, lossless pneumatic line it follows that

$$\begin{aligned} \Gamma &= Ts \\ Z_c &= \frac{c_o}{A} \equiv Z_{co} \end{aligned}$$

where

c_o = acoustic speed of sound, and
 A = cross sectional area of the line.

Experiment and analysis shows, however, that line friction is important even in seemingly short lines. As will become evident later, reasonable correlation between theory and experiment requires consideration of at least the gross effects of line friction (and corresponding attenuation).

* Alternatively, a lumped model could be used to accurately model the line for frequencies which are small compared to the fundamental natural frequency of the line.

Two reasonably convenient techniques are available for determination of the characteristic parameters Γ and Z_c ; the constant R-L-C model and a more rigorous and exact model based on the direct solution of the continuity, momentum, and energy equations which describe the process. Although considerably more complex, the "exact" model is generally superior since it includes velocity profile and heat transfer effects. Nevertheless, in certain cases the two models yield very nearly the same results and the simpler R-L-C model is adequate. Brief summaries of the techniques available for computation of the characteristic parameters are given in Appendix A.

Having established means of computing Γ and Z_c it is necessary now to rewrite the line equations in a form suitable for step-by-step graphical or numerical solution. The method of solution requires that the equations be written in time-difference form. By noting that

$$\cosh \Gamma = \frac{e^{\Gamma} + e^{-\Gamma}}{2} ; \quad \sinh \Gamma = \frac{e^{\Gamma} - e^{-\Gamma}}{2}$$

and

$$e^{\Gamma} F(t) = F(t + T)$$

a combination of Eqs. (5) and (6) yields the appropriate time difference equations for the transmission line.

Referring to system schematic in Fig. 6, the following time difference equations may be written:

Source

$$\frac{W_a}{W_s} = f\left(\frac{P_a}{P_s}, \text{ geometry}\right) \quad (7)$$

Line (See Appendix B)

$$\frac{W_b(t + 2T)}{W_s} - e^{2\alpha} \frac{W_b(t)}{W_s} = \frac{1}{Z_c} \left[2e^{\alpha} \frac{P_a(t + T)}{P_s} - e^{2\alpha} \frac{P_b(t)}{P_s} - \frac{P_b(t + 2T)}{P_s} \right] \quad (8)$$

$$\frac{W_b(t + 2T)}{W_s} + e^{2\alpha} \frac{W_b(t)}{W_s} = 2e^{\alpha} \frac{W_a(t + T)}{W_s} - \frac{1}{Z_c} \left[\frac{P_b(t + 2T)}{P_s} - e^{2\alpha} \frac{P_b(t)}{P_s} \right] \quad (9)$$

Chamber (continuity equation)

$$\delta \left(\frac{P_b}{P_s} \right) \approx \delta \tau \left[\frac{W_b}{W_s} - \frac{W_c}{W_s} \right] \text{ AVE} \quad (10)$$

where

$$\tau = \frac{tW_s}{K_1 P_s} ; \quad K_1 = \frac{\rho V_c}{\beta}$$

Load Resistance

$$\frac{W_c}{W_s} = \frac{P_s}{R_l W_s} \frac{P_b}{P_s} \quad (11)$$

Nomenclature used above but not previously introduced, is defined below.

t = time variable,

$T = \frac{L}{C_o}$ = characteristic time of line,

L = transmission line length,

$\bar{Z}_c = \frac{Z_c P_s}{W_s}$ = dimensionless characteristic impedance of line,

δ = small change of a quantity,

ρ = fluid mass density,

β = bulk modulus of elasticity of fluid,

V_c = chamber volume.

The graphical technique involves a simultaneous solution of equations (7) through (11). In the present example, there are two coupled dynamic elements - the line and the chamber. Consequently, two graphical solutions must be carried on simultaneously, one for the line and one for the chamber, with the resulting "common point of intersection" being the "answer". A graphical interpretation of the technique is given in Fig. 7. Graphical interpretation of Eqs. (8) and (9) is complicated by the presence of the friction correction terms; more tractable equations are formulated in Appendix B. It is evident that events occur in increments of the characteristic time of the line, i.e., the time for a wave to travel from one end to the other. Therefore the minimum value allowed for $\delta\tau/2$ is $TW_s/K_1 P_s$.

A typical complete graphical solution for the lossless line case is shown in Fig. 8. For the particular conditions chosen, it is seen that a limit cycle instability exists.

The limit cycle or "surge" frequency can be determined directly from the plot by counting the number of time increments required to complete one encirclement on the phase plane plot, or more easily, by observing the period on the time plot. The parameters which determine the limit cycle frequency and amplitude for a given source characteristic are obviously the line length and characteristic impedance, the chamber volume, and the terminal impedance. The nature of the solution in normalized form reduces the "free" parameters to the following two ratios:

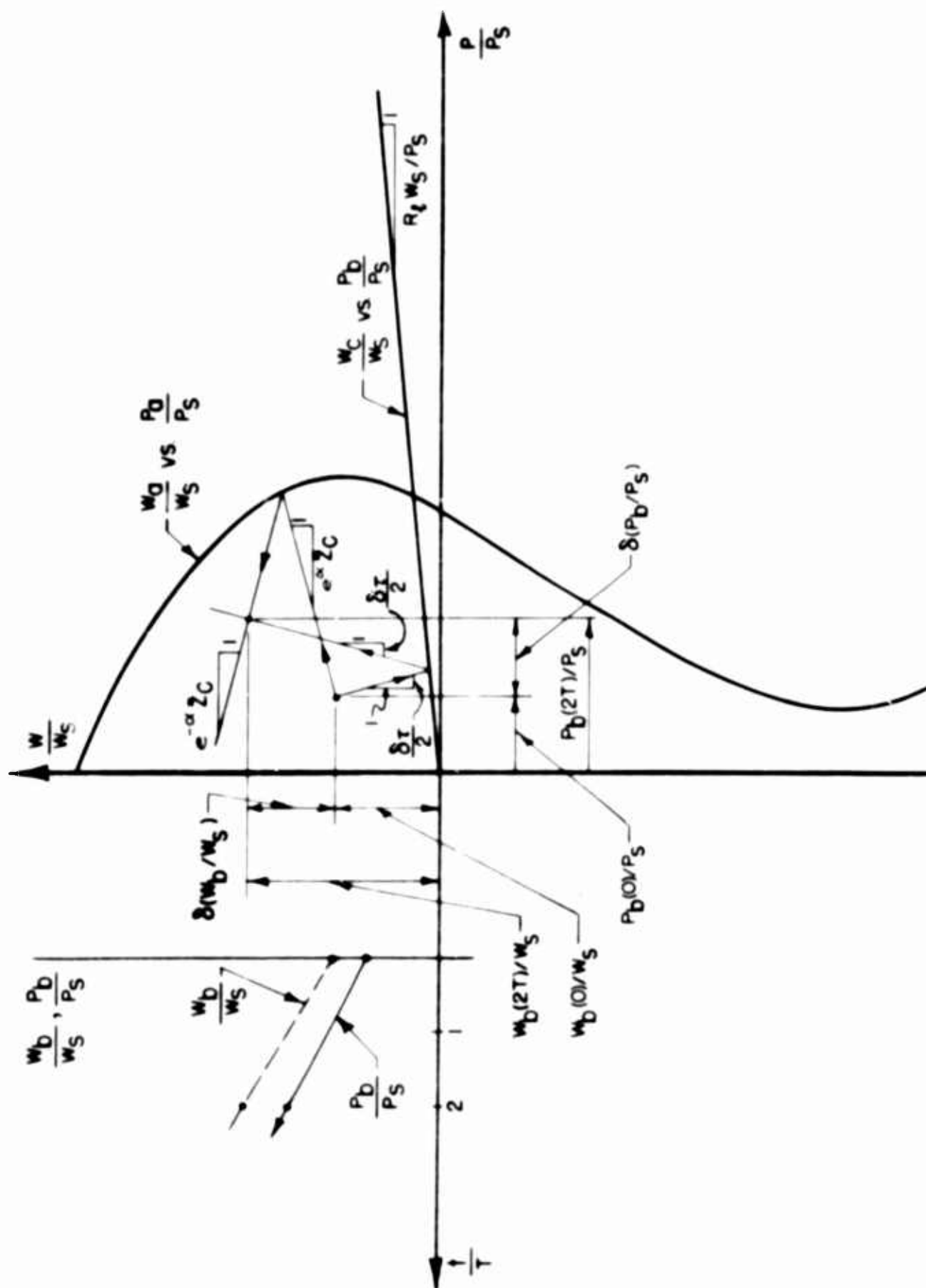


FIG. 7 GRAPHICAL INTERPRETATION OF EXAMPLE

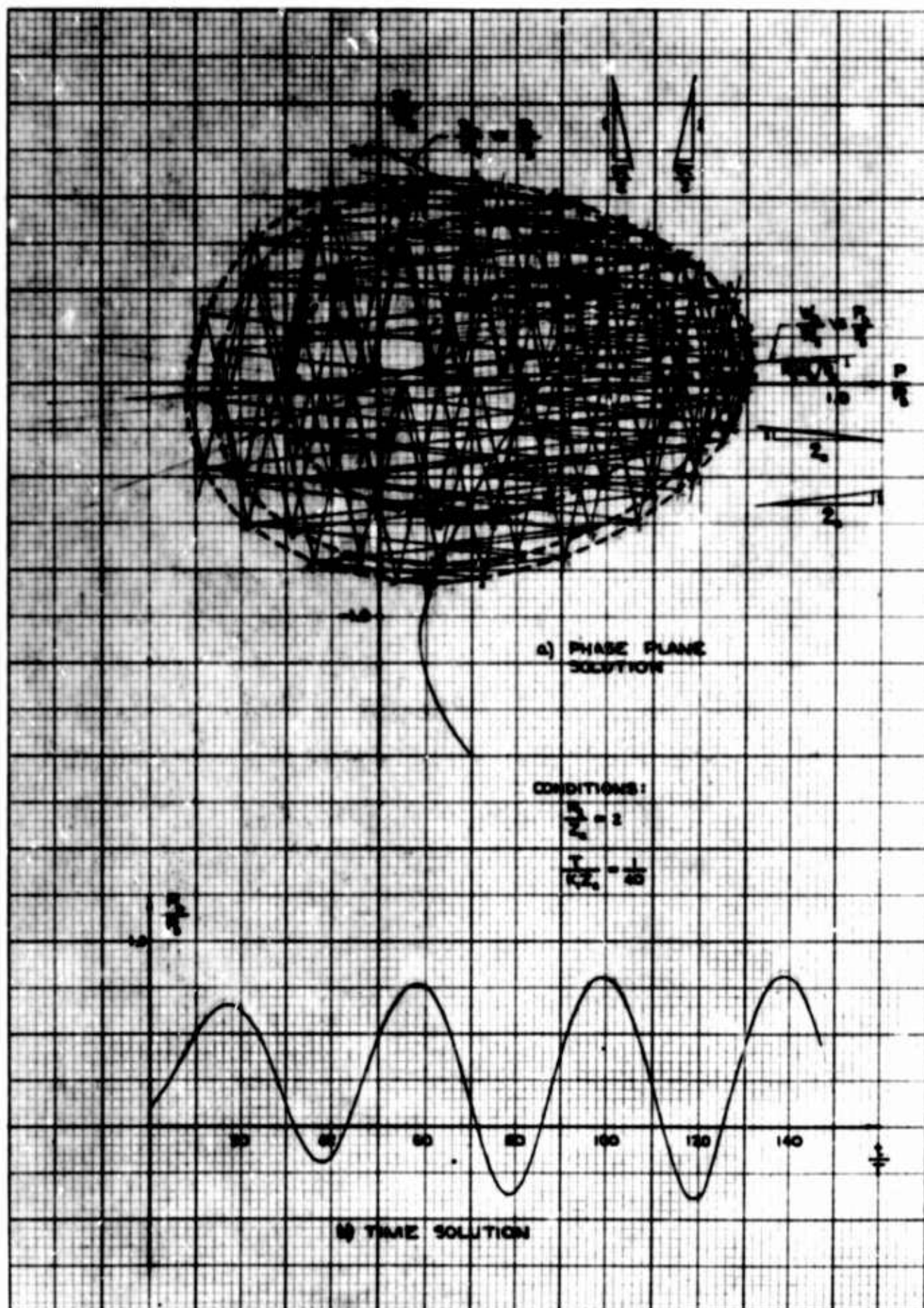


Fig. 8 Graphical Stability Analysis of an Active Source Coupled to a Lossless Transmission Line Terminated by a Load Chamber and Resistance

$$\frac{R_L}{Z_C} \quad \text{and} \quad \frac{V_L}{V_C}$$

where V_L = volume of transmission line. Simple analytical means for computing the "surge" or limit cycle frequency for the special case of $R_L = \infty$ are presented in Appendix C.

Unfortunately, accuracy of solution using this particular technique is not assured in all cases. Since the system contains a single delay element (i.e., the transmission line), computations yield results only at the points in actual time represented by $t = 2T, 4T, 6T, \dots$ etc. Good accuracy requires that the slope $1 : \delta\tau/2$ be large. However, there is an important constraint placed on the minimum size of $\delta\tau/2$ due to the presence of the line. Unless V_L/V_C is very small compared to unity, the slope $1 : \delta\tau/2$ may be too small (or $1 : Z_C$ may be too large) to assure adequate accuracy of solution.* Obviously, simple scaling manipulations on the abscissa and ordinate do not help. What actually is required is the introduction of an artifice that will effectively reduce the minimum relative value of $\delta\tau/2$. Such an artifice is achieved simply by dividing the uniform transmission line into n -sections, each having a length $L' = L/n$ and a characteristic time $T' = T/n$. The chamber "slope lines" are increased in number and slope by the factor n . Equations identical to Eqs. (8) and (9) except for obvious changes in subscripts, can be written for each section. The graphical analysis is demonstrated in Ref. 1.

Computer-Aided Numerical Prediction of System Relative Stability

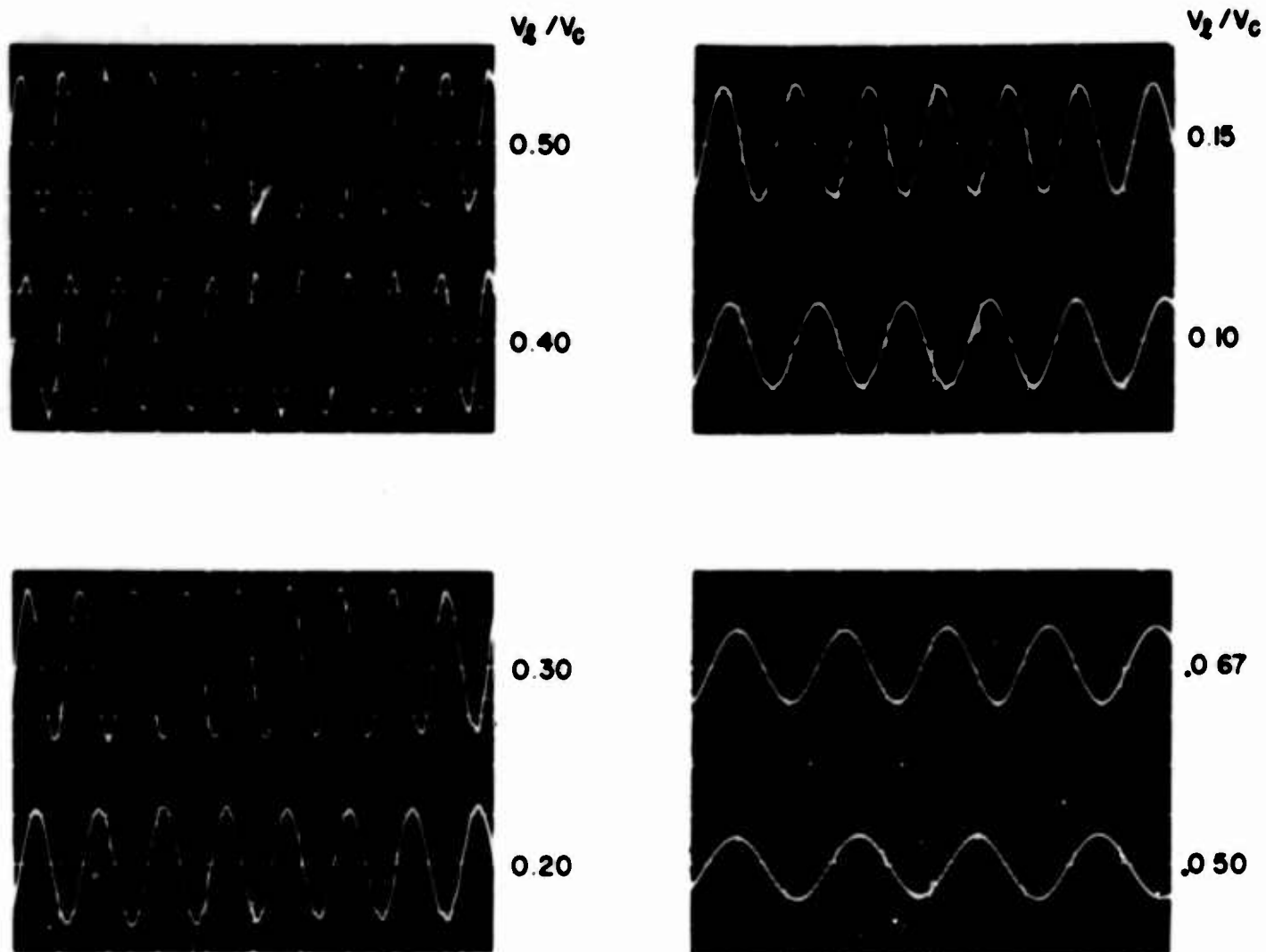
The elegance and general utility of the graphical techniques presented in the previous section are obvious. These techniques provide insight into problem formulation and solution which is exceedingly difficult to realize with other numerical methods. Nevertheless, for detailed design studies involving extensive computations, only machine computation affords the necessary speed and over-all flexibility. Techniques for solving the previous example problem numerically with the aid of a digital computer, are demonstrated in detail in Ref. 1. Equations (8) and (9), rather than their approximations, are utilized. In addition, the line may be artificially divided into a sufficient number of sections so that the desired accuracy is achieved. Results of actual computations are given in the following section.

Comparison of Empirical Predictions with Experimental Measurements

Results of a typical set of digital computer solutions and experimental measurements are presented below to demonstrate the validity of the numerical methods.

It was established earlier that the pertinent free parameters are V_L/V_C and R_L/Z_C . Only the infinite resistance case ($R_L = \infty$) is considered here. Figure 9 shows typical waveforms for various values of V_L/V_C . The chamber coupled to the line introduces a type of filtering

* An interesting exception is the case where $V_C = 0$ (See Ref. 1). In this case the solution is exact.



ALL PICTURES :

VERTICAL SCALE = 10.2 INCHES H_2O / DIVISION
 HORIZONTAL SCALE = 10 MILLISECONDS / DIVISION
 NOZZLE SUPPLY PRESSURE = 10 INCHES H_2O
 LINE LENGTH = 12 INCHES
 LINE DIAMETER = 0.518 INCH
 V_2/V_c = LINE-TO-CHAMBER VOLUME RATIO

**FIG.9 PRESSURE OSCILLATIONS IN A BLOCKED CHAMBER
COUPLED TO AN ACTIVE SOURCE (CONF. 3).**

effect, such that the higher harmonics do not generally appear as they do with the line alone (Ref. 1). As V_L/V_C becomes large, higher harmonics make the waveforms less sinusoidal. A comparison of measured and theoretical (See Appendix C) limit cycle frequencies is given in Fig. 10. The comparison is remarkably good even for such short lines, thereby showing the validity of the mathematical formulation for the range of conditions considered.

Oscillation amplitude measurements were carried out using a true RMS voltmeter. The RMS value and the amplitude of the fundamental were assumed to be the same. A typical comparison of predicted and measured results is shown in Fig. 11. The correlation is remarkably good considering the difficulties of measurement and the sensitivity of the solution to the friction correction. Since the frequencies were low compared to the natural frequency of the line alone, the attenuation factor was computed from the lumped R-L-C model (See Appendix A). A minor improvement (in the favorable direction) could be achieved by using the more exact values. Typical values of the attenuation factor are: $e^{\alpha} = 0.9988$ for $L = 1$ ft. and $e^{\alpha} = 0.9953$ for $L = 4$ ft. Sensitivity to changes in the fourth digit are apparent.

Conclusions

It is believed that the experimental measurements conducted to date adequately demonstrate the importance, general usefulness, and limitations of the source characterization and the various prediction models. Certain refinements are needed in the models, but, for several practical cases considered, the predictions are in remarkably good agreement with the experiments. The techniques developed should provide added insight into jet modulator dynamic stability problems. In certain special but important situations these techniques should provide rapid and sufficiently accurate results for actual component and system design. Further work is needed to extend these techniques to fluid jet modulators of conventional design.

Acknowledgements

The guidance and advice of Professor F. T. Brown of M.I.T. is gratefully acknowledged.

This work was supported in part by the U.S. Air Force, ASD, under contract AF 33(657)-8384, the USAF, ASD, under contract AF 33(657)-7535, and the National Aeronautics and Space Administration under contract NASA 5208, and sponsored by the Division of Sponsored Research of the Massachusetts Institute of Technology. Current research being carried out at Oklahoma State University is supported in part by the Harry Diamond Laboratories under contract DA-49-186-AMC-221(D).

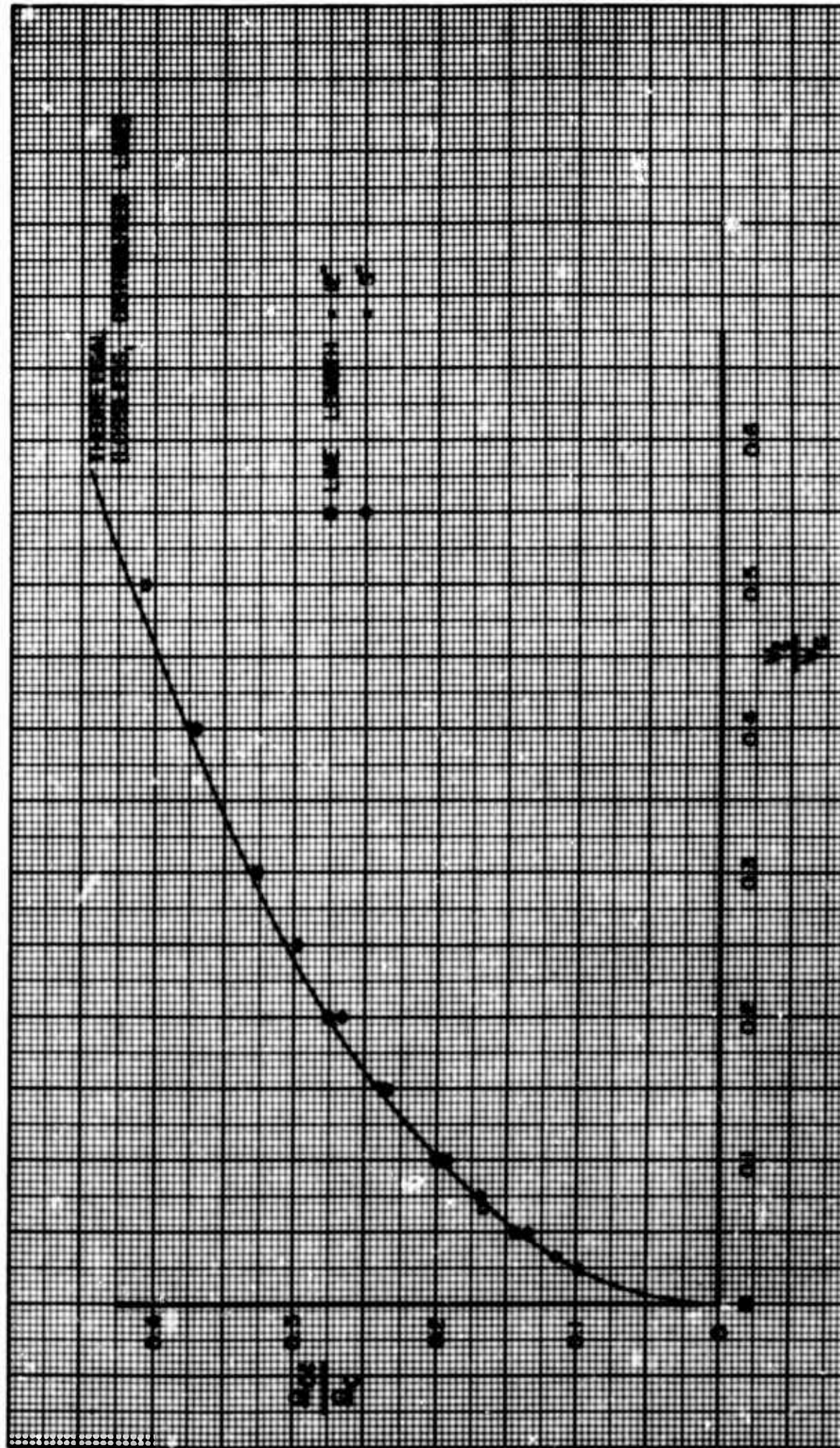


FIG. 10 COMPARISON OF MEASURED AND PREDICTED SURGE FREQUENCIES OF A TRANSMISSION LINE TERMINATED BY A SIMPLE CHAMBER

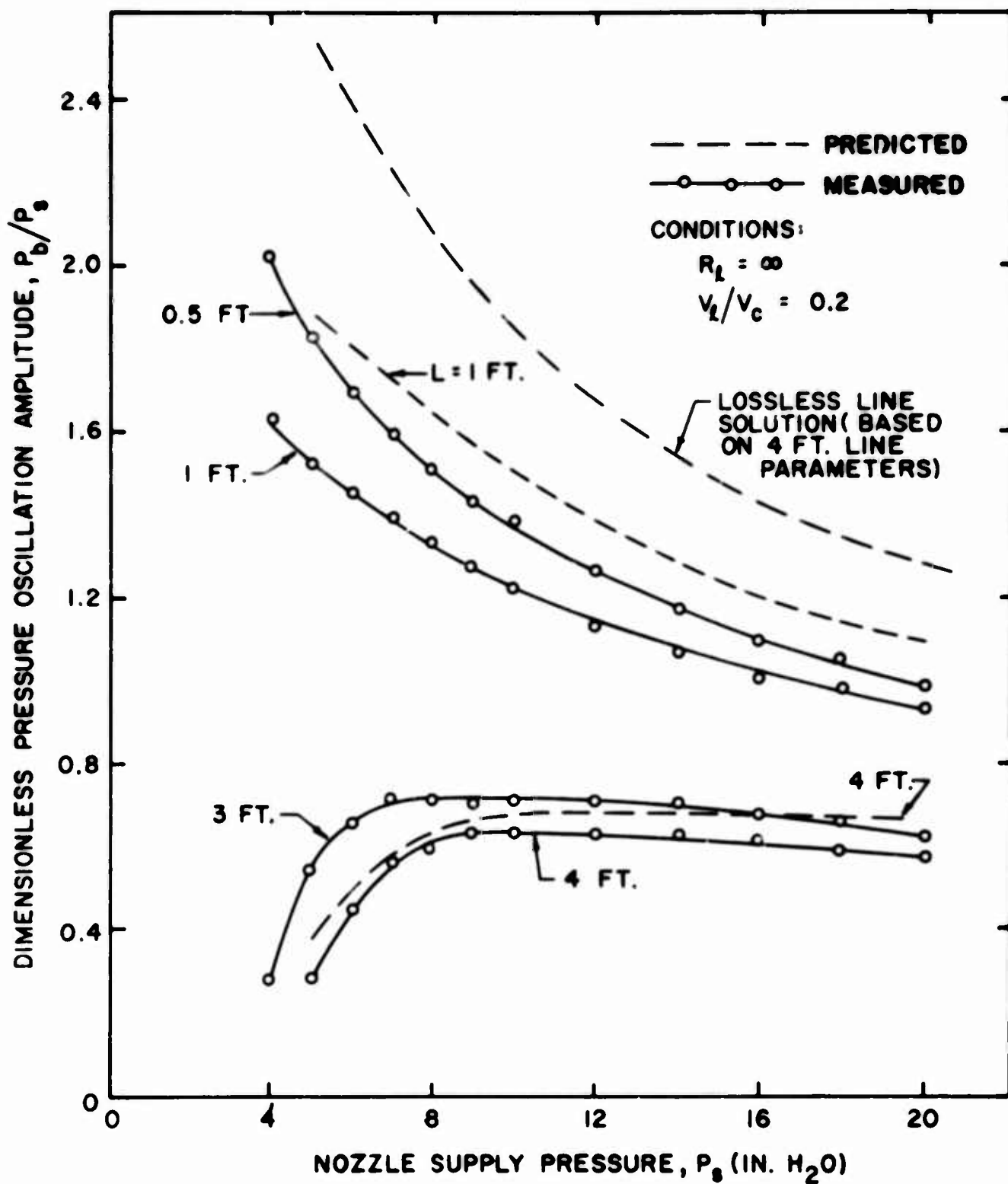


FIG. II COMPARISON OF MEASURED AND PREDICTED PRESSURE OSCILLATION AMPLITUDES FOR AN ACTIVE SOURCE COUPLED TO A TRANSMISSION LINE TERMINATED BY A CHAMBER

REFERENCES

1. Reid, K. N. Jr., "Static and Dynamic Interaction of a Fluid Jet and a Receiver-Diffuser," Sc.D. Thesis, Dept. of Mech. Engrg., Mass. Inst. of Tech., Cambridge, Mass., Sept. 1964.
2. Johnston, L. E., "Acoustic Study of the Interaction Between Two Receiver Ports Coupled by an Incident Fluid Jet," Sc.D. Thesis, Dept. of Mech. Engrg., Mass. Inst. of Tech., Cambridge, Mass., June 1965.
3. Brown, F. T., "Fluid Jet Modulators and Systems," Chapter 16 of Special Notes for a Two-Week Program on Instrumentation for Measurement and Control Held at the Mass. Inst. of Tech., Aug. 1963.
4. Shapiro, A. H., The Dynamics and Thermodynamics of Compressible Fluid Flow, Vol. I, The Ronald Press Co., New York, 1953.
5. Rule, J. T., and Coons, S. A., Graphics, McGraw-Hill Book Co., 1961. See also: Paynter, H. M., "Methods and Results from M.I.T. Studies in Unsteady Flow," Journal Boston Society of Civil Engrs., Vol. XXXIX, No. 2, April 1952.
6. Brown, F. T., "Hydraulic and Pneumatic Transmission Lines," Special Notes for a Two-Week Program on Fluid Power Control Held at the Mass. Inst. of Tech., June 1960.
7. Rohman, C. P., and Grogran, E. C., "On the Dynamics of Pneumatic Transmission Lines," Trans. ASME, May 1957.
8. Shapiro, A. H., Siegel, R., and Kline, S. J., "Friction Factor in the Laminar Entry Region of a Smooth Tube," Proceedings of the Second U. S. National Congress of Applied Mechanics, June 1954, pp. 733-741.
9. Brown, F. T., "Transient Response of Fluid Lines," Trans. ASME, Vol. 84, Series D, No. 4, Dec. 1962.

APPENDIX A

PROPAGATION OPERATOR AND CHARACTERISTIC IMPEDANCE DETERMINATION FOR A UNIFORM PNEUMATIC TRANSMISSION LINE

Constant R-L-C Model (Refs. 6 & 7) The series impedance and shunt admittance are given by

$$Z = ID + R$$

and

$$Y = CD$$

where

- I = inertance per unit length of line,
- C = capacitance per unit length of line,
- R = resistance to flow in line per unit length
- D = d/dt

Thus

$$\Gamma = \sqrt{IC D^2 + RCD} \cdot L$$

and

$$Z_c = \sqrt{Z/Y} = \sqrt{I/C} \cdot \sqrt{1 + R/ID}$$

where L = length of line.

But if R is sufficiently small (as it usually is), or if $R/I\omega \ll 1$, where ω is the lowest frequency component of interest, then

$$\Gamma = -\alpha + TD \approx \frac{LR}{2} \sqrt{\frac{C}{I}} + L \sqrt{CI} D$$

$$Z_c \approx \sqrt{\frac{I}{C}} \cdot \left(1 + \frac{R}{2ID}\right)$$

For sinusoidal excitation the following limiting forms are useful:

$$\frac{R}{\omega I} \ll 1$$

$$Z_c \approx \sqrt{\frac{I}{C}}$$

$$\Gamma \approx L \frac{R}{2} \sqrt{\frac{C}{I}} + jL \sqrt{IC} \omega$$

$$\frac{R}{\omega I} \gg 1$$

$$Z_c \approx \sqrt{\frac{R}{j\omega C}}$$

$$\Gamma \approx L \sqrt{\frac{RC\omega}{2}} + jL \sqrt{\frac{RC\omega}{2}}$$

Thus, for uniform attenuation, the attenuation constant is

$$\alpha = - \frac{LR}{2} \sqrt{\frac{C}{I}}$$

$$\text{for } \frac{R}{\omega I} \ll 1$$

and

$$\alpha = - L \sqrt{\frac{RC\omega}{2}}$$

$$\text{for } \frac{R}{\omega I} \gg 1$$

If it is assumed that the flow is fully developed and laminar and that the line friction is the same as for steady flow, the attenuation constant can be expressed in terms of line and fluid properties* as follows:

$$\alpha = - \frac{4Lv}{2a^2c_o} \quad \text{for} \quad \frac{8v}{2a\omega} \ll 1$$

$$\alpha = - \frac{2L}{ac_o} \sqrt{v\omega} \quad \text{for} \quad \frac{8v}{2a\omega} \gg 1$$

The assumption that the resistance is the same as for steady, fully-developed laminar flow, can be defended only for cases where the frequency is low and the line length-to-diameter ratio is large. At the higher frequencies unsteadiness of the flow results in an effectively higher value of the resistance. Rohmann and Grogran (Ref. 7) suggest that R be increased by 20 percent over the calculated value. Equally important is the fact that in many practical situations (and perhaps in the majority) the line length-to-diameter ratio is not large enough to discount the effect of increased resistance to developing flow, i.e., the apparent friction factor (and therefore the resistance) is significantly greater in the "entry length" of a tube than in the fully-developed region many diameters downstream. Resistance estimates based on the friction factor correlations summarized by Shapiro, et. al., (Ref. 8) should provide corrections which are adequate for most engineering purposes. These correlations allow computation of the integrated apparent friction factor in the laminar entry of a tube as a function of diameter Reynolds number and the tube L/D ratio. The resistance R is computed easily from friction factor information.

"Exact" Model. Derivations for the propagation operator and characteristic impedance are given by Brown (Ref. 9). The model assumes: cylindrical tube, one-dimensional flow, isothermal walls, small amplitude laminar disturbances, and continuous medium. Results pertinent to the present study have been extended in range and replotted in Figs. A.1 and A.2. Attenuation factors as a function of line and fluid properties may be obtained from Fig. A.1. Since dispersive effects are neglected in the present example, only the magnitude of the characteristic impedance need be considered. Figure A.2 may be used to obtain a correction to the nominal value of the characteristic impedance (i.e., $Z_{co} = c_o/A$).

APPENDIX B

If the solution sought in the example is assumed to start at $t = t_0$, a combination of Eqs. (8) and (9) yields

*
 v = kinematic viscosity
 a = line radius
 ω = frequency

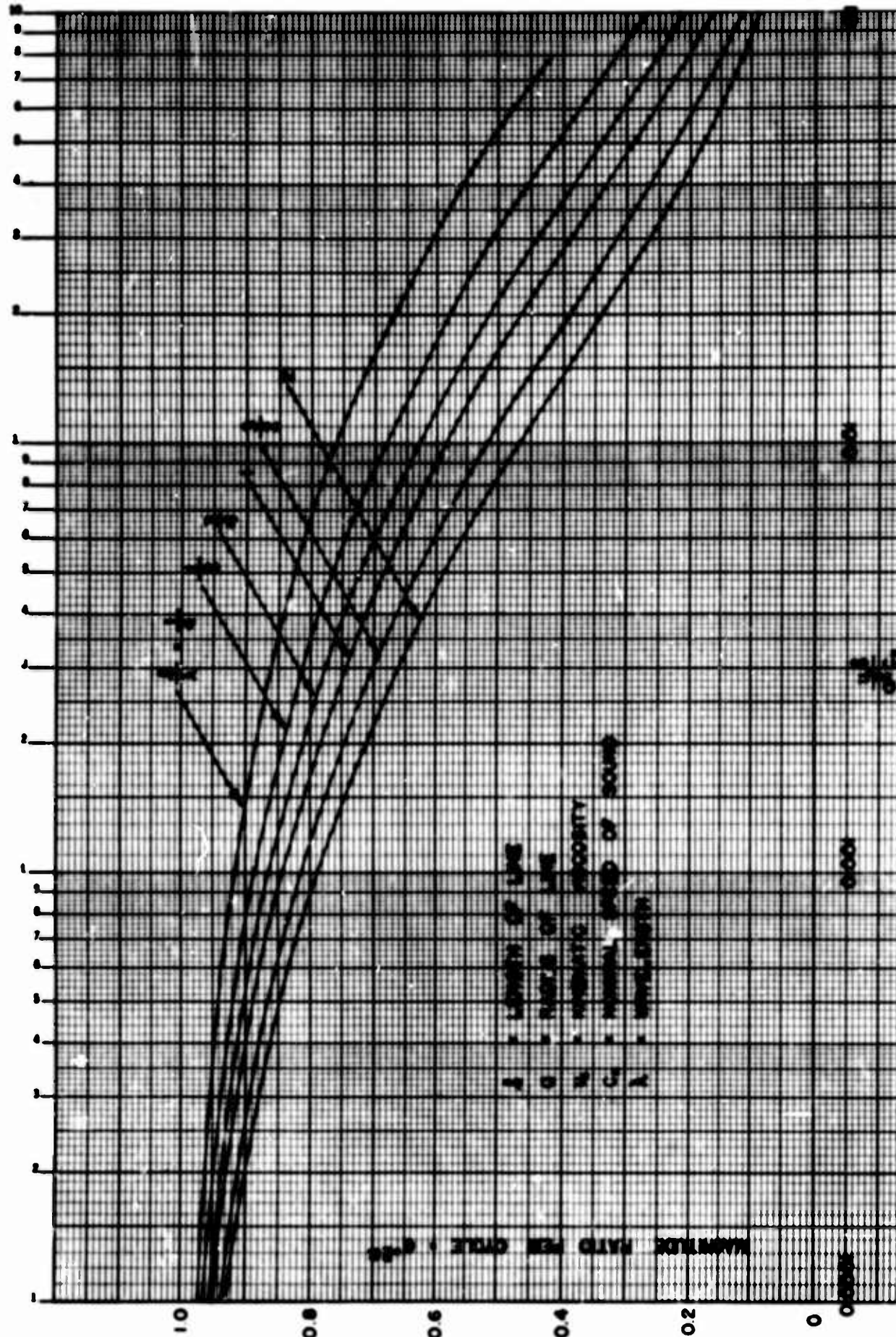


FIG. A.1 ATTENUATION PER CYCLE OF SMALL AMPLITUDE SINE WAVES
IN A RIGID, ISOTHERMAL - WALL, LAMINAR-FLOW,
CIRCULAR AIR LINE

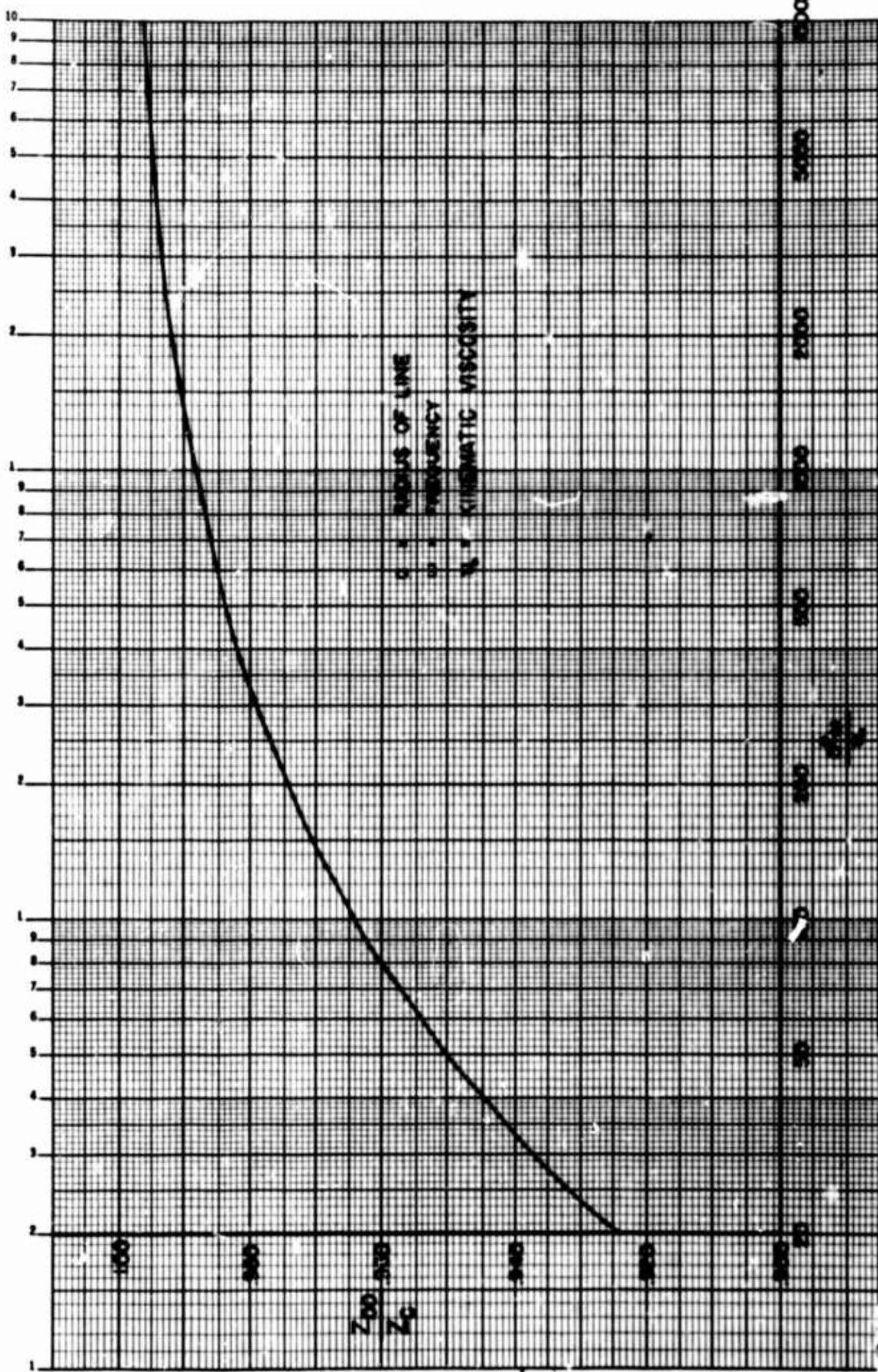


FIG. A.2 MAGNITUDE OF LINE CHARACTERISTIC IMPEDANCE

$$\delta \left(\frac{W_b}{W_s} \right) \equiv \frac{W_a(t+T)}{W_s} - \frac{W_b(t)}{W_s} = (1 - e^{-\alpha}) \frac{W_a(t+T)}{W_s} + \frac{1}{\bar{Z}_c} \left[\frac{e^{-\alpha} P_a(t+T)}{P_s} - \frac{P_b(t)}{P_s} \right] \quad (B-1)$$

for the time period $t = 0$ to $t = T$. Similarly, for the time period $t = T$ to $t = 2T$

$$\delta \left(\frac{W_b}{W_s} \right) \equiv \frac{W_b(t+2T)}{W_s} - \frac{W_a(t+T)}{W_s} = (e^{\alpha} - 1) \frac{W_a(t+T)}{W_s} + \frac{1}{\bar{Z}_c} \left[e^{\alpha} \frac{P_a(t+T)}{P_s} - \frac{P_b(t+2T)}{P_s} \right] \quad (B-2)$$

Equations (B 1) and (B 2) do not admit simple graphical interpretation. However, since the usual case is such that $\alpha \approx 0$, Eqs. (B-1) and (B-2) may be approximated by the following more tractable but approximate equations:

$$\delta \left(\frac{W_b}{W_s} \right) \approx \frac{1}{e^{\alpha} \bar{Z}_c} \left[\frac{P_a(t+T)}{P_s} - \frac{P_b(t)}{P_s} \right] \quad (B-3)$$

and

$$\delta \left(\frac{W_b}{W_s} \right) \approx \frac{1}{e^{-\alpha} \bar{Z}_c} \left[\frac{P_a(t+T)}{P_s} - \frac{P_b(t+2T)}{P_s} \right] \quad (B-4)$$

These relations are "exact" for the special case of a lossless line, i.e., $\alpha = 0$.

APPENDIX C

ANALYTICAL PREDICTION OF SURGE FREQUENCY FOR A LOSSLESS TRANSMISSION LINE TERMINATED BY A SIMPLE CLOSED CHAMBER

It is possible, without carrying out any graphical or numerical solutions, to predict the surge frequency of the system in Fig. 6 for two important special cases: 1) $R_L = \infty$, and 2) $R_L = 0$. The surge frequency is the lowest natural frequency of the system and is the frequency at which the limit cycle is most likely to exist. For $R_L = 0$ the surge frequency is merely the half-wave frequency of the line. The case of infinite load terminal impedance is more interesting. Two approaches are available, depending on the nature of the model for the line. Either the lumped or distributed parameter model may be used.

Distributed Parameter Solution. Assume that the line is lossless and that the effective bulk modulus of the fluid in the line is equal to that in the chamber. The governing equations for the lossless line are:

$$P_b = [\cosh TD]P_a - Z_c [\sinh TD]W_a \quad (C-1)$$

and

$$W_b = \frac{1}{Z_c} [\sinh TD]P_a + [\cosh TD]W_a \quad (C-2)$$

where $D \equiv d/dt$

Considering the terminating chamber as a "pure capacitance" gives

$$W_b = \frac{\rho V_c}{\beta} DP_b \quad (C-3)$$

Combining Eqs. (C-1) through (C-3) and assuming sinusoidal motion (i.e., setting $D = j\omega$)

$$\left(\frac{P_b}{P_a}\right)_{j\omega} = \frac{\beta(\cosh Tj\omega + \sinh^2 Tj\omega)}{\beta + \rho V_c Z_c(j\omega)(\tanh Tj\omega)} \quad (C-4)$$

where

ω = frequency

$j = \sqrt{-1}$

The surge frequency can be determined by setting the characteristic equation of the above transfer function equal to zero. Thus

$$\frac{\beta T}{\rho V_c Z_c} = \omega T \tan \omega T \quad (C-5)$$

Since

$$T = L \sqrt{\frac{\rho}{\beta}} \quad \text{and} \quad Z_c = \sqrt{\frac{\beta}{\rho A}}$$

we find that

$$\frac{V_l}{V_c} = \eta \tan \eta \quad (C-6)$$

where

V_l = volume of line $\equiv AL$

η = dimensionless surge frequency $= \omega T$

By noting that the fundamental natural frequency of the line with zero terminating volume is

$$\Omega_l = \frac{\text{speed of sound}}{4L} = \frac{1}{4T}$$

and setting $\omega = 2\pi\Omega_{cl}$, we obtain

$$\frac{\Omega_{cl}}{\Omega_l} = \frac{2}{\pi} \eta \quad (C-7)$$

Equations (C-6) and (C-7) relate the dimensionless surge frequency to the line-to-chamber volume ratio. The resulting relation for the fundamental is plotted in Fig. C.1. For the case when $R_l = 0$, it is necessary to consider the multi-valued character of Eq. (C-6).

Lumped Parameter Solution. When the surge frequency is small compared to the fundamental natural frequency of the line alone, a simple lumped parameter model of the line-tank system is adequate. For example, consider the line as a "pure inertance" (no capacitance),

$$P_a - P_b = \frac{L}{A} \frac{dW_b}{dt} \quad (C-8)$$

Combining Eqs. (C-3) and (C-8), and solving the resulting characteristic equation for the surge frequency gives

$$\Omega_{cl} = \frac{1}{2\pi} \sqrt{\frac{\beta A}{\rho L V_c}} \quad (C-9)$$

from which follows

$$\frac{\Omega_{cl}}{\Omega_l} = \frac{2}{\pi} \sqrt{\frac{V_l}{V_c}} \quad (C-10)$$

Alternatively, considering the line as a "pure inertance" followed by a "pure capacitance" (the volume of which may be lumped with the chamber volume), the following result is obtained:

$$\frac{\Omega_{cl}}{\Omega_l} = \frac{2}{\pi} \sqrt{\frac{1}{1 + \frac{V_c}{V_l}}}$$

The expressions in Eqs. (C-10) and (C-11) are compared to the distributed parameter solution in Fig. C.1.

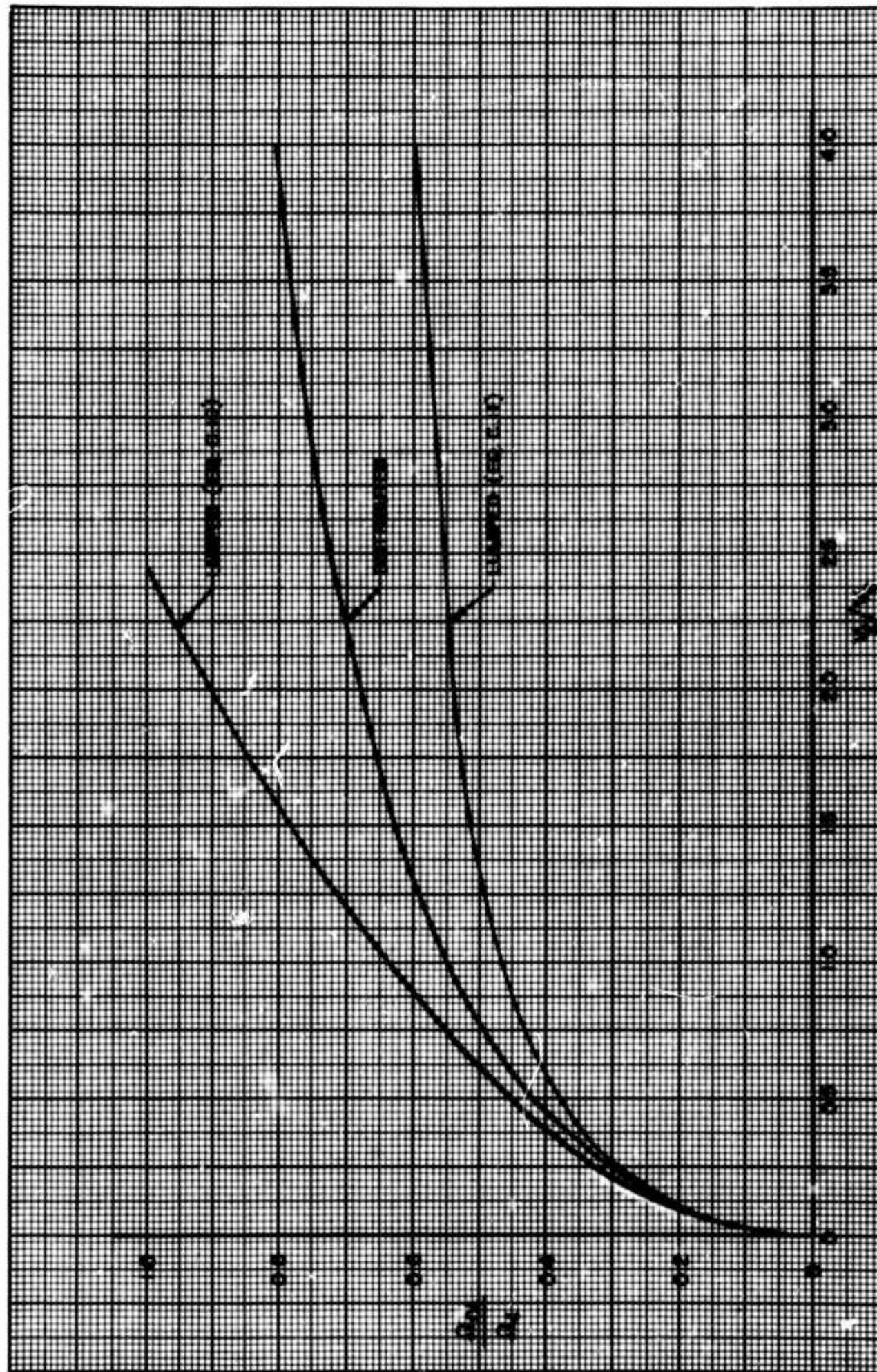


FIG. C.1 SURGE FREQUENCY OF A LOSSLESS TRANSMISSION LINE
TERMINATED BY A SIMPLE CHAMBER

TRANSIENT THEORY OF SWITCHING IN A BISTABLE VALVE

D. W. Harvey
Missile & Space Systems Division
Douglas Aircraft Company, Inc.

ABSTRACT

The basic equations are presented for one-dimensional unsteady flow of the control fluid in a bistable valve during switching. The effect of the induced pressure gradient is included, and a method is indicated for including friction. Solution of these equations by a modification of the method of characteristics is outlined, for the case of small control fluid bubble slope (so that the main stream can be assumed isentropic) and supersonic main stream velocity. It is shown how this solution may predict switching times.

CREDIT

Work presented herein was conducted by the Missile & Space Systems Division under company-sponsored Research and Development funds.

1.0 INTRODUCTION

Experiment (reference 1) seems to indicate that a bistable valve switches because of the growth of a bubble of control fluid along the wall downstream of the control port. Fluid is injected into the bubble at the port, not necessarily at a constant rate. The fluid in the bubble is forced downstream by the pressure gradient, and undergoes momentum transfer at both the wall and the bubble - main flow interface.

It is the purpose of this paper to analytically describe the transient behavior of the control bubble under these influences.

2.0 BASIC EQUATIONS

Geometry is assumed as shown in figure 1. Flow in the bubble is one-dimensional and unsteady. Consider the control volume; let $b = 1$ so that $dV = hdx$ and $A = h$.

Continuity Flow rate in = $(\rho uh)_x$
Flow rate out = $(\rho uh)_x + \frac{\partial}{\partial x} (\rho uh) dx$
Rate of storage = $\frac{\partial}{\partial t} \rho h dx$

$$\text{Flow in} - \text{storage} - \text{flow out} = 0$$

$$\frac{\partial \rho h}{\partial t} + \frac{\partial \rho uh}{\partial x} = 0 \quad (1)$$

Momentum

$$\frac{\partial \rho u}{\partial t} + \frac{\partial \rho u^2}{\partial x} + \frac{\partial P}{\partial x} = 0 \quad (2)$$

This implies inviscid flow but this is not essential; within the one-dimensional assumption friction is easily included by saying $p = p' - \tau$, where p is now the one-dimensional stress tensor, p' is the pressure, and τ includes shear at the wall and at the bubble-stream interface.

We now have two equations and four unknowns (ρ , u , h and p , all functions of x and t). The energy equation and a state equation such as $p = \rho RT$ are available; this gives a net decrease of one unknown. The other may be obtained from considering coupling with the main stream.

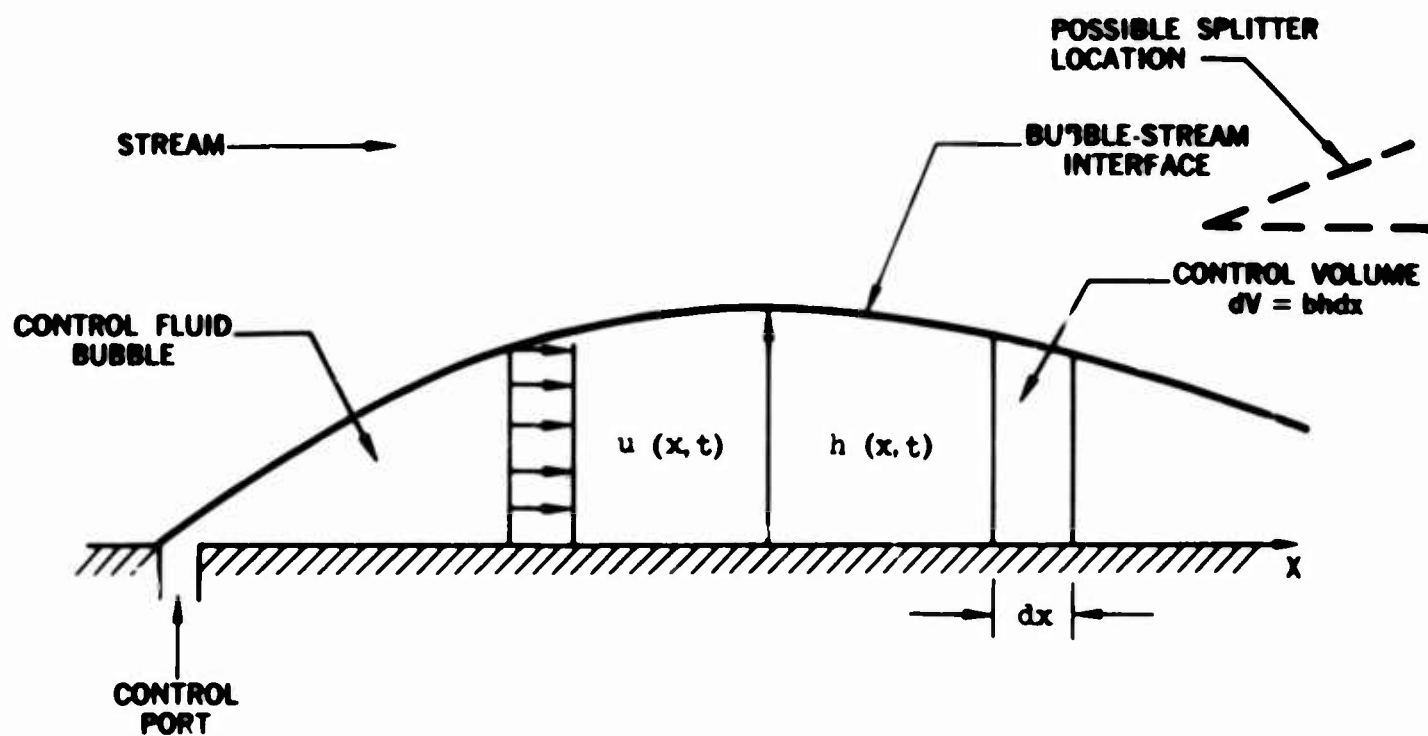


FIGURE 1

With some assumptions, a somewhat simpler scheme can be devised. Assuming the main stream to adjust much faster than h changes, $h(x)$ implies $p(x)$. Roughly speaking, this approximation will

be correct if $\frac{\partial h}{\partial t}$ is much less than the main stream x-direction velocity. Further, assuming flow in the bubble isentropic, p and ρ are related by $p\rho^{-\gamma} = \text{const.}$

The relation between h and p is to be found by solving the two-dimensional problem of a body (the bubble) in a jet (the main stream). This can often be done. If the body is slender, linearized methods can be used. If the main flow is supersonic, the method of characteristics may apply. In this case, even greater simplicity results if the main stream is assumed isentropic. Then

the change in boundary slope (i.e. $\frac{\partial h}{\partial x}$) can be set equal to the change in Prandtl-Meyer angle. This directly determines the local main stream Mach number and thus the local pressure p . (Note that since this last method implicitly assumes the main flow of infinite extent, it only applies downstream to the point at which the Mach wave from the leading edge of the bubble, reflected from the jet free surface, returns to the bubble-stream interface.)

3.0 METHOD OF SOLUTION

It appears possible to use the method of characteristics for solving (1) and (2). Modification is necessary in order to use the relation mentioned above between h and p without including it explicitly.

Characteristic Equation

Multiply (1) by λ and add to (2). This gives

$$\begin{aligned} \lambda \rho \frac{\partial h}{\partial t} + \lambda \rho u \frac{\partial h}{\partial x} + (\lambda h + u) \frac{\partial \rho}{\partial t} + (\lambda u h + u^2) \frac{\partial \rho}{\partial x} \\ + \rho \frac{\partial u}{\partial t} + (\lambda \rho h + 2\rho u) \frac{\partial u}{\partial x} + \frac{\partial p}{\partial x} = 0 \end{aligned} \quad (3)$$

It will be possible to combine partial derivatives to form total derivatives along the characteristic described by

$$\frac{dx}{dt} = \frac{\lambda \rho u}{\lambda \rho} = \frac{\lambda u h + u^2}{\lambda h + u} = \frac{\lambda \rho h + 2\rho u}{\rho}$$

This implies

$$\frac{dx}{dt} = u \text{ and } \lambda = -\frac{u}{h} \quad (4)$$

Compatibility Condition

Substitute for λ in (3), multiply by dt and where appropriate by

$$\frac{1}{u} \frac{dx}{dt} :$$

$$\begin{aligned} & - \frac{\rho u}{h} \frac{\partial h}{\partial t} dt - \frac{\rho u^2}{h} \frac{\partial h}{\partial x} \left(\frac{1}{u} \frac{dx}{dt} \right) dt + (u - u) \frac{\partial \rho}{\partial t} dt \\ & + (u^2 - u^2) \frac{\partial \rho}{\partial x} dt + \rho \frac{\partial u}{\partial t} dt + (2 \rho u - \rho u) \frac{\partial u}{\partial x} \left(\frac{1}{u} \frac{dx}{dt} \right) dt + \frac{\partial p}{\partial x} dt = 0 \end{aligned}$$

This reduces to

$$- \frac{\rho u}{h} dh + \rho du + \frac{\partial p}{\partial x} dt = 0$$

Integrating:

$$\ln \frac{h}{u} = \int \frac{1}{\rho u} \frac{\partial p}{\partial x} dt + C \quad (5)$$

This is the equation that holds along the characteristics.

Now in general another set of characteristics is needed, with equations like (5) holding along them. Here, since p is an implicit function of h and thus no longer an unknown in good standing, some other method must be used.

4.0 OUTLINE OF SOLUTION

Consider the $x - t$ plane. Conditions (i.e. h, u, p, ρ) must be known along the x axis (initial conditions) and the t axis (boundary conditions). Consider a time $t_1 > 0$. We can find $(h/u)^0$ along this line by (5) and (4), assuming initial conditions to hold on the interval $0 \leq t \leq t_1$ as is usual in the method of characteristics. The superscript is the level of approximation.

Knowing $(h/u)^0$, we can now assume $h^{0,0}(x, t_1) = h(x, 0)$ and calculate $u^{0,0}(x, t_1)$. This assumption implies $\rho^{0,0}(x, t_1) = \rho(x, 0)$. With these we can use (1) to calculate $(\frac{\partial h}{\partial t})^{0,0}$ and if t_1 is sufficiently small $h^{0,1}(x, t_1) = h^{0,0} + (\frac{\partial h}{\partial t})^{0,0} t_1$. Then $h^{0,1}(x, t_1)$ implies (by the assumed relationship between h and p) $p^{0,1}(x, t_1)$, and this in turn gives $\rho^{0,1}(x, t_1)$. Still using $(h/u)^0$ we can now find $u^{0,1}$ and $(\frac{\partial h}{\partial t})^{0,1}$. Then $h^{0,2}(x, t_1) = h^{0,1} + (\frac{\partial h}{\partial t})^{0,1} t_1$. Clearly iteration will give $h^{0,n}$ and $u^{0,n}$. These values can then be used to correct the characteristics to provide $(h/u)^1$. When $h^{m,n}(x, t_1)$ and $u^{m,n}(x, t_1)$ change sufficiently little between iterations, they are used as initial conditions to calculate values along t_2 .

5.0 APPLICATION

For the case of the bistable valve, it is conjectured that the time of interest is that at which h equals some fraction, perhaps one-half or greater, of the distance to the splitter. From here on the main flow may complete the process itself, by entraining fluid at the free surface and finally attaching to the opposite side. On the other hand, if the control flow is sustained at a high enough rate, the main flow may be driven over faster than it would move by itself. It may be expected then that for sufficiently high control flow rates the switching time will be proportional to the time required for h to equal some constant fraction of the distance to the splitter, as predicted by this analysis. For lower control flow rates the time will be less than the prediction. Note also that the considerations above neglect the inertia of the essentially stagnant fluid in the duct to which the main jet is to be switched. This will cause the switching time to increase, for ducts of sufficient length.

An experimental program intended to test this analysis has been started. An adjustable supersonic bistable valve is to be used. This will permit the bubble to generate only weak shocks in the main stream, allowing h and p to be related by the simple isentropic assumption, at least near the start of control flow. Direct measurements of bubble growth by flow visualization will be attempted.

6.0 CONCLUSIONS

A method of calculating control fluid bubble growth has been derived. The method is quite general for any case of a gas injected into a stream. In principle, the stream need not be uniform and the bubble need not be small, although these factors may complicate the relation between h and p . However, if the assumption of rapid adjustment is used, the stream must be of high velocity.

This method should accurately predict the rate of main stream deflection in the early stages of switching, and may be accurate to within a constant for sufficiently high control flow rates.

REFERENCES

1. Johnston, Richard Paul, "Dynamic Studies of Turbulent Reattachment Fluid Amplifiers," M.S. Thesis, University of Pittsburgh, 1963.

HARRY DIAMOND LABORATORIES
WASHINGTON, D. C. 20438

FLUERIC PRESSURE REGULATION
USING A RESISTANCE SET POINT

by

CAPT. HARRY N. WHITE

ARMY MATERIEL COMMAND

DEPARTMENT OF THE ARMY

ABSTRACT

A closed loop feedback control system is described that provides a stabilized pressure notwithstanding variations in the source pressure or the output loading. The system operates about a reference point at which the value of a linear and nonlinear resistor coincide.

PREFATORY NOTE

This paper discusses in simplified form portions of an analysis performed by Captain Harry N. White on the optimization of a fluoric pressure regulator. Because of the sudden reassignment of Captain White, this paper was written by Silas Katz and Gary Roffman.

The concept of the regulator is due to H. N. White and J. M. Kirshner.

1. A CONVENTIONAL PRESSURE CONTROL SYSTEM

The block diagram of a conventional pressure control system is shown in figure 1.* The objective of the system is to maintain the regulated pressure, P_R , at a value fixed by the reference pressure, P_S , for a wide range of unregulated pressure, P_U . In operation, the set point reference pressure and a feedback pressure signal are supplied to a summing junction whose output represents an error pressure. This error signal is in turn integrated and passed on to a control amplifier, which supplies the corrective action to reduce the error to zero. This corrective output plus the unregulated pressure supply are summed to produce the regulated pressure supply. With the loop closed the expression for the regulated pressure is

$$P_R(s) = \frac{P_S(s) K_A K_C}{s + H(s) K_A K_C} + \frac{s[P_U(s)]}{s + H(s) K_A K_C} \quad (1)$$

where s is the complex frequency,

K_A, K_C are the gains of amplifiers, and

$H(s)$ is the transfer function of the feedback circuit.

For a fixed reference pressure, the change in the regulated pressure due to a change in the unregulated pressure is obtained by differentiating equation (1) with respect to $P_U(s)$. The result is

$$\Delta P_R(s) = \frac{s[\Delta P_U(s)]}{s + H(s) K_A K_C} \quad (2)$$

where ΔP_R = change in regulated pressure, and

ΔP_U = change in unregulated pressure or the disturbance pressure signal.

Now if the disturbance is applied as a unit step change in the unregulated supply, $\Delta P_U(s) = 1/s$ and equation (2) becomes

$$\Delta P_R(s) = \frac{1}{s + H(s) K_A K_C} \quad (3)$$

Applying the final value theorem to equation (3) gives for the final steady-state change in regulated pressure

*Figures appear on pages 159 through 163.

$$\Delta P_R(t) = \lim_{t \rightarrow \infty} s \Delta P_R(s) = 0 \quad (4)$$

The steady-state value of the regulated pressure is therefore not changed by the change in the unregulated supply pressure. This is a consequence of the integration component. If the integration is imperfect, the regulated pressure does change.

2. FLUERIC PRESSURE CONTROL SYSTEM

An approximation to the pressure control system discussed in the previous section was constructed with flueric components. It will be shown that the flueric pressure control system is described by an equation of the same form as the conventional system.

A schematic drawing of the flueric pressure control system is shown in figure 2. The set point pressure is obtained by connecting the regulated pressure to the controls of a jet-deflection-type proportional fluid amplifier through a linear capillary resistor on one control and a nonlinear orifice resistor on the other. The values of these resistors are adjusted to provide a null output of the set point amplifier at the desired regulated pressure. The output of the set point amplifier is fed into a bootstrap integrator. This is a jet deflection amplifier with positive feedback resistors adjusted to provide an integrating operation. The output of the integrator is connected to the controls of a final control power jet deflection amplifier. The control amplifier supplies fluid to the regulated pressure source through one output aperture and dumps to atmosphere through the other. The power jet of the final control amplifier comes from the unregulated pressure source. The other amplifiers receive power jet pressure only from the regulated source.

The transfer functions of the flueric components of the system are considered in the following sections. Since the components presently available have relatively high output impedances, the transfer function is obtained with the component loaded by the succeeding component.

3. THE SET POINT

Unless moving parts are included, it is not feasible to use a fixed pressure reference. Rather the pressure set point must be a function of passive circuitry. This is easily accomplished with the push-pull jet-deflection-type amplifier by introducing a non-symmetry into the amplifier or the amplifier circuit. In

this case a linear capillary resistor R_A is connected to one control and a nonlinear orifice resistor^s of area A_S is connected to the other. This results in the bridge circuit shown in figure 3. The input resistances of the amplifier R_A are assumed to be linear. The control pressure on the linear side P_{cl} may be written as

$$P_{cl} = \frac{R_A}{R_A + R_S} P_R \quad (5)$$

The control pressure on the nonlinear side, assuming that the orifice has a discharge coefficient of unity, is

$$P_{cn} = - \frac{R_A^2 A_S^2}{\rho} + \frac{R_A^2 A_S^2}{\rho} \left[1 + \frac{2P_R}{R_A^2 A_S^2 / \rho} \right]^{1/2} \quad (6)$$

Using the binomial expansion, equation (6) becomes approximately

$$P_{cn} = P_R - \frac{1}{2} \frac{P_R^2}{R_A^2 A_S^2 / \rho} \quad (7)$$

The error pressure signal P_e applied across the controls of the set point amplifier is obtained from equations (5) and (7) as

$$P_e = P_{cl} - P_{cn} = \frac{-R_S}{R_A + R_S} P_R + \frac{1}{2} \frac{P_R^2}{R_A^2 A_S^2 / \rho} \quad (8)$$

When the error pressure is zero, the regulated pressure P_R equals the pressure set point P_S and equation (8) gives the set point as

$$P_S = \frac{2R_A^2 A_S^2 R_S}{(R_A + R_S) \rho} \quad (9)$$

The output of the set point amplifier is $k_1 P_e$, where k_1 is the gain of the set point amplifier when loaded with the bootstrap integrator circuit. This represents a resistive and capacitive load.

4. THE BOOTSTRAP INTEGRATOR

The quantity to be integrated is the product of the gain of the set point amplifier and the error pressure signal ($k_1 P_e$). Mathematically the perfect integral of this is written as $\frac{k_1 k_2 P_e}{s}$, where k_2 is the rate gain of the integrator.

To approximate this transfer function, the bootstrap integrating circuit (ref 1), shown schematically in figure 4, is used. The input is fed into a jet deflection amplifier through an RC circuit at each control. Each output is fed back to the controls in a positive sense. Following through the network equations yields the following relation between the output and input:

$$\frac{\text{Integrator output}}{\text{Integrator input}} = \frac{1}{\left[\frac{R_1 C s}{G} + \frac{1}{G} \left(1 + \frac{R_1}{R_F} + \frac{R_1}{R_B} \right) - \frac{R_1}{R_F} \right]} \quad (10)$$

where G = gain of the amplifier loaded with the controls of the final control amplifier R_c

R_1 = forward loop resistance of integrator

R_F = feedback loop resistance of integrator

R_B = input resistance of amplifier

C = capacitance of integrator tanks

Equation (10) shows that a perfect integration can be obtained by selecting the components so that the second and third terms in the denominator are equal. In practice this cannot be done perfectly, and the following function is obtained:

$$\frac{\text{Integrator output}}{\text{Integrator input}} = \frac{k_2}{s + \epsilon} \quad (11)$$

where ϵ is the error or deviation in the denominator that causes imperfect integration. For the integrator input $k_1 P_e$, the output of the integrator is

$$\frac{k_1 k_2 P_e}{s + \epsilon}$$

5. THE FINAL CONTROL CIRCUIT

The output of the integrator is applied across the controls of the final control amplifier (fig. 5). One of the output apertures of the final control amplifier supplies fluid to the regulated pressure source. The other aperture is dumped to atmosphere. The regulated supply pressure is a function of the control pressure difference across the amplifier, the power jet pressure of the amplifier, which is the unregulated supply pressure P_u and the load on the source. The final control amplifier provides the corrective action from the set point and integrator and is also the input for the unregulated supply pressure. The gain of the amplifier remains essentially constant over a large range of power jet pressure. Changing the unregulated supply pressure, however, does change the pressure recovered at the output aperture. This recovery pressure from the unregulated supply can be expressed as $k_4 P_u$, where k_4 , the recovery factor, is a function of the geometry of the unit and the load on the regulated supply.

Because the final control amplifier is not operated differentially, the gain k_2 is halved. The regulated pressure can be expressed in terms of the error signal of the set point, the integrator and final control amplifier gains, and the recovery pressure of the final control amplifier as

$$P_R = \frac{k_1 k_2 k_3 P_e}{2(s + \epsilon)} + k_4 P_u \quad (12)$$

The error pressure P_e is a function of the difference between the set point pressure P_S and the regulated pressure P_R . For small error pressure signals, P_e can be written as

$$P_e = \frac{R_S}{(R_A + R_S)} (P_R - P_S) \quad (13)$$

Thus in terms of the set pressure equation (12) becomes

$$P_R = \frac{-k_1 k_2 k_3 \left(\frac{R_S}{R_A + R_S} \right) P_S + 2(s + \epsilon) k_4 P_u}{2s + 2\epsilon - k_1 k_2 k_3 \left(\frac{R_S}{R_A + R_S} \right)} \quad (14)$$

Differentiating equation (14) with respect to P_u for a fixed reference pressure results in

$$\Delta P_R (S) = \frac{2(s + \epsilon) \Delta P_u (s) k_4}{2s + [2\epsilon - k_1 k_2 k_3 \left(\frac{R_S}{R_A + R_S} \right)]} \quad (15)$$

Now as in equation (2) a unit step disturbance is applied and equation (15) becomes

$$\Delta P_R (s) = \frac{2k_4 + 2\epsilon k_4/s}{2s + [2\epsilon - k_1 k_2 k_3 \left(\frac{R_S}{R_A + R_S} \right)]} \quad (16)$$

The steady-state value of the change in regulated pressure applying the final value theorem can then be written in the time domain as

$$P_R (\infty) = \frac{2\epsilon k_4}{2\epsilon - k_1 k_2 k_3 \left(\frac{R_S}{R_A + R_S} \right)} \quad (17)$$

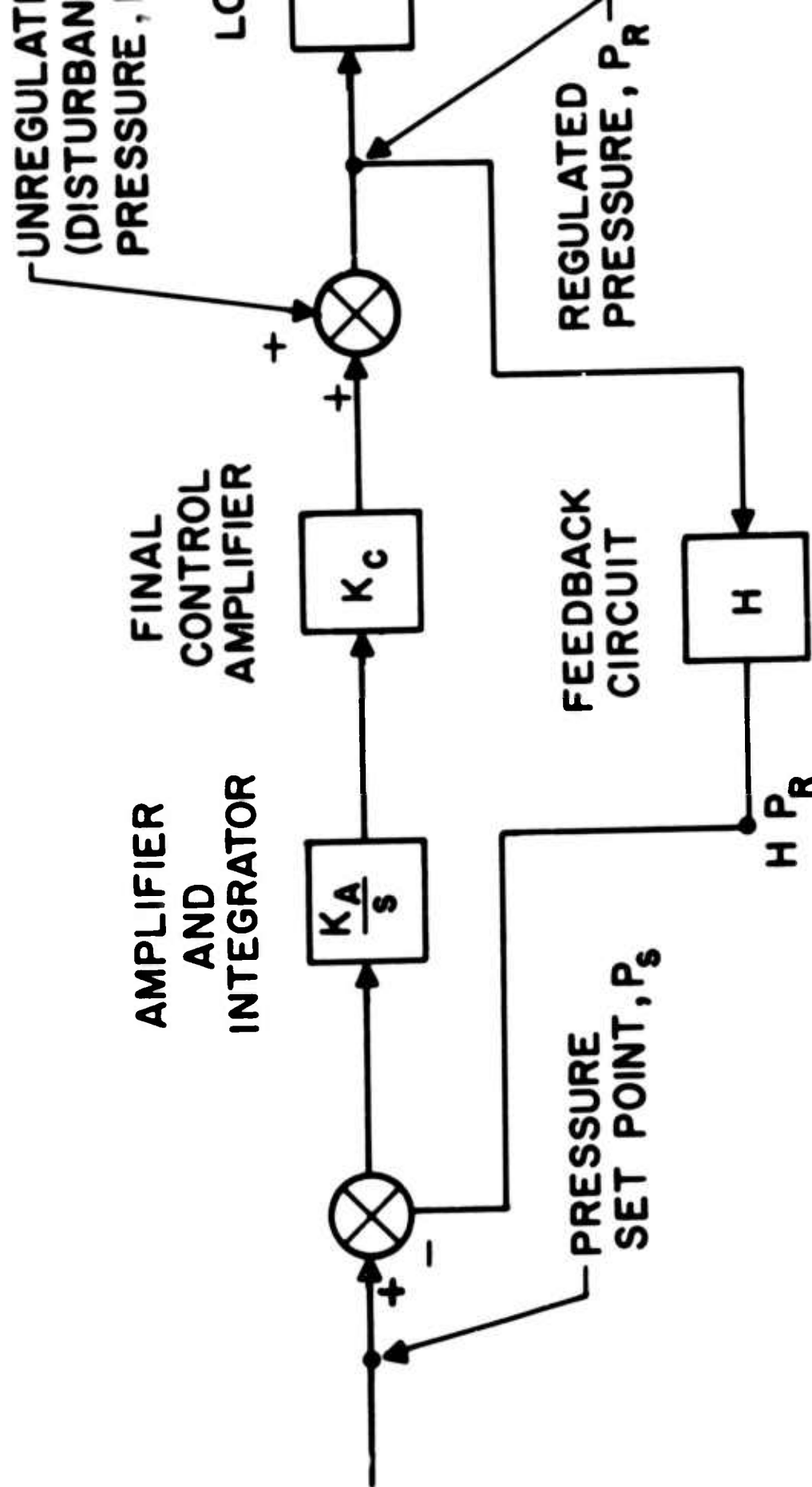
Thus the accuracy of maintaining a regulated pressure depends on the integrating error, the gain of the amplifiers, resistor values of the set point, and the pressure recovery factor for a unit input.

6. EXPERIMENTAL REGULATOR

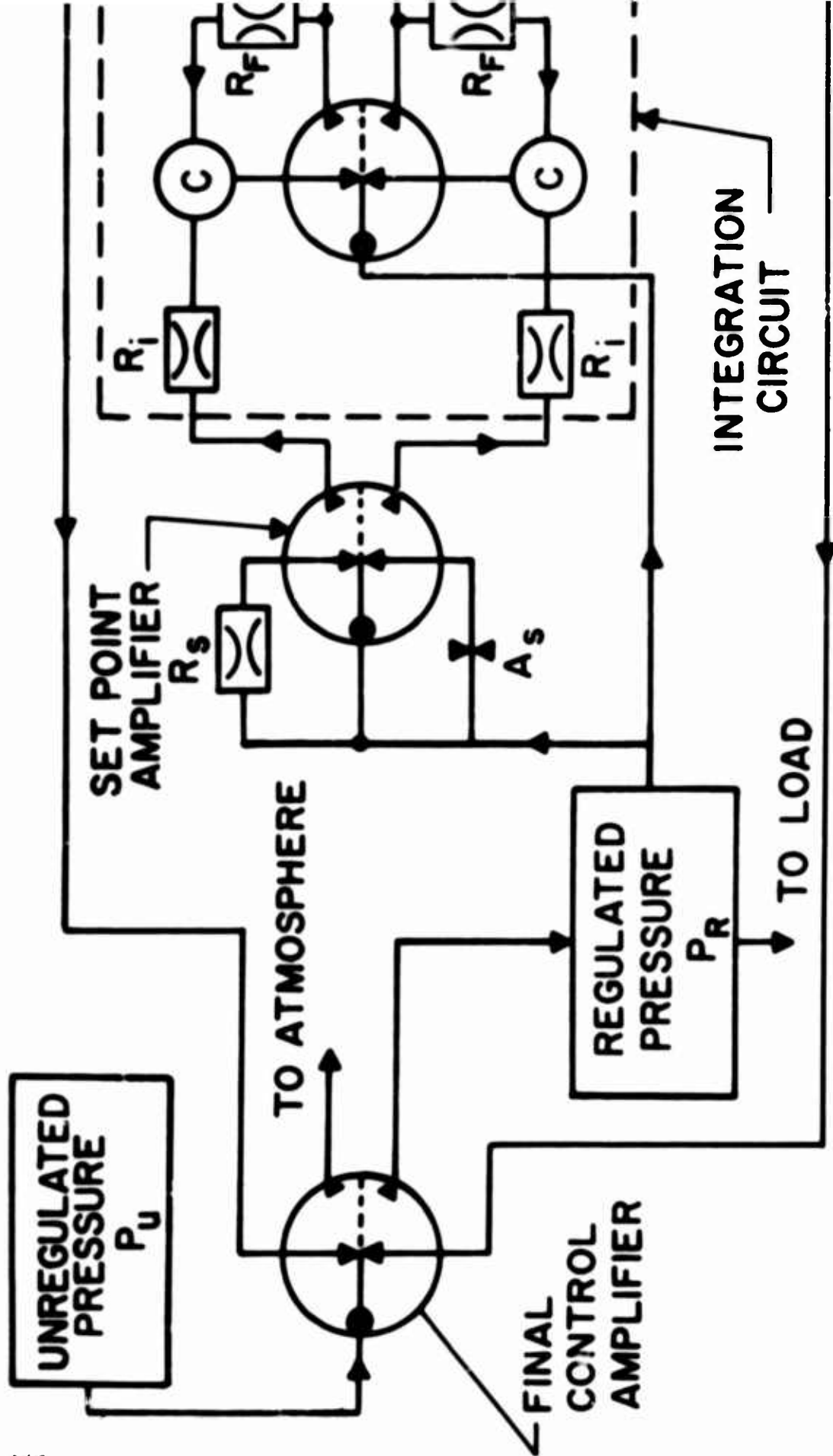
Several pressure regulators using the resistance set point were built by Captain White. These regulators were different from the pressure regulator described in this paper in that the set point resistors were introduced into the integrator stage to reduce the number of active components. Typical results are the maintaining of a regulated pressure of 16.4 kN/m^2 when the unregulated supply was operated between 60 and 100 kN/m^2 . Over this range of unregulated pressure the percentage change in the regulated pressure P_r was 1/17 the percentage change in the unregulated supply, P_u .

REFERENCE

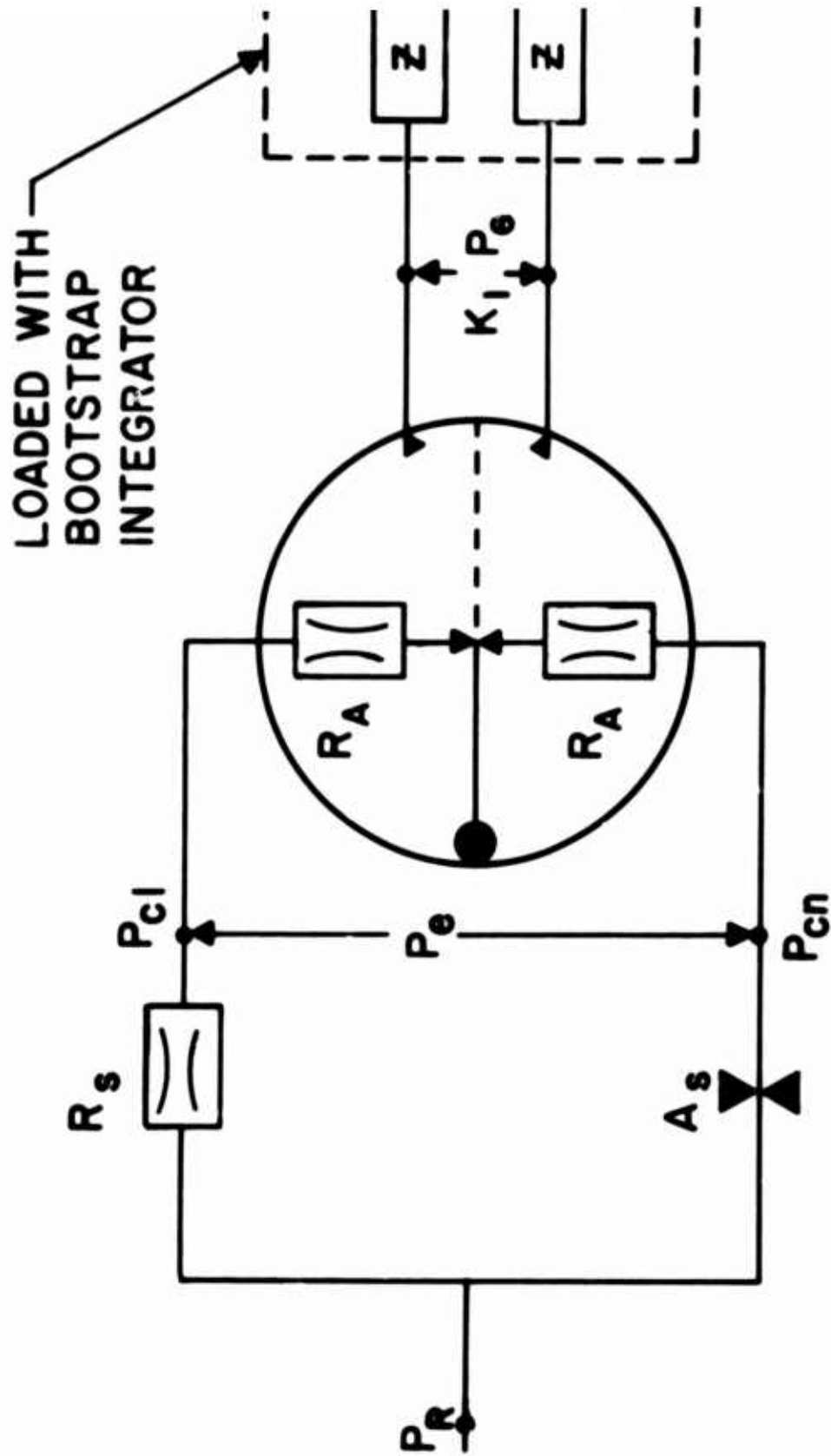
1. Roffman, G. L. and Katz, Silas, "Experimental Fluidic Analog Computation," Fluid Amplification No. 15, TR-1292, June 1965.



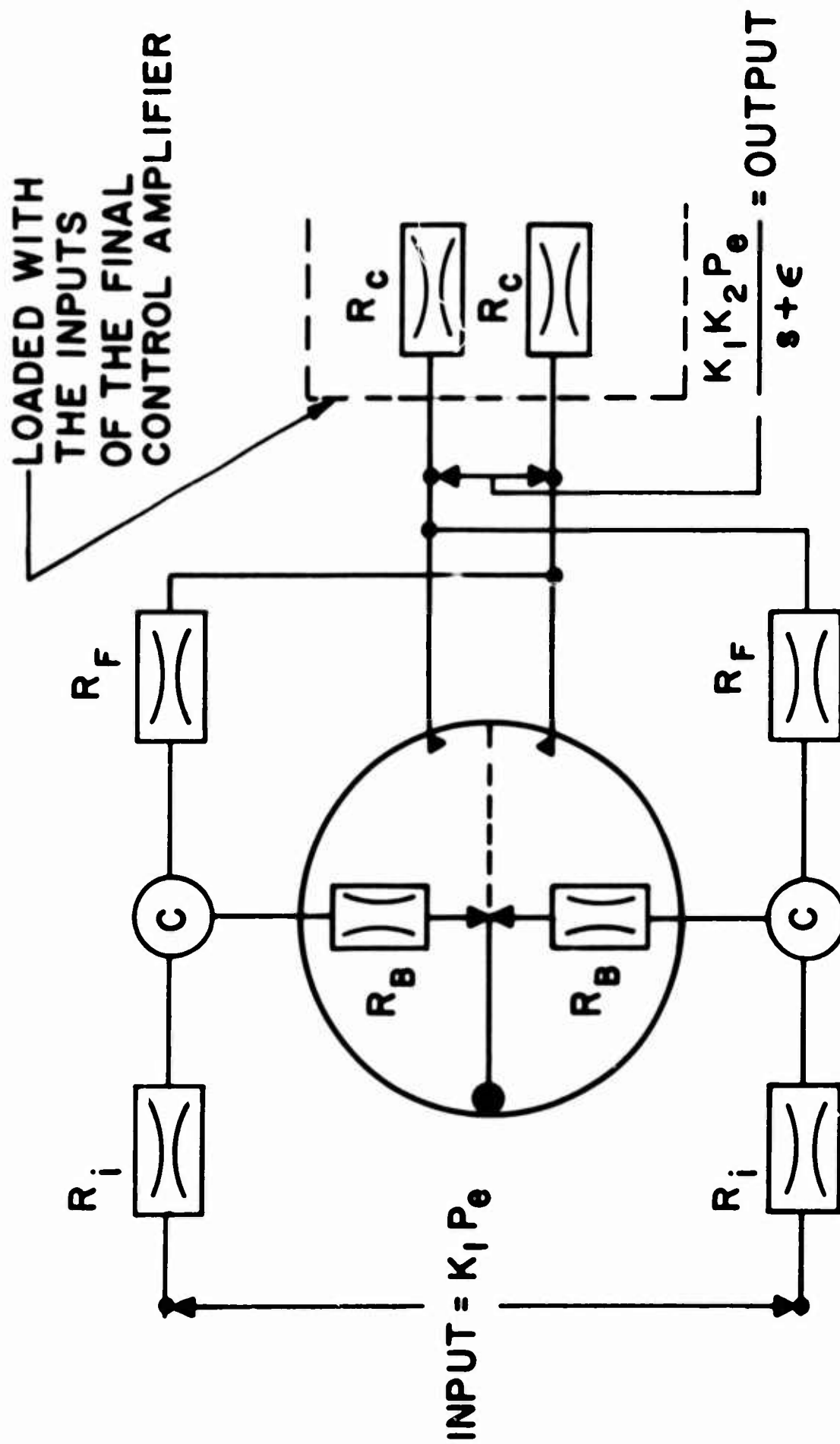
**BLOCK DIAGRAM OF PRESSURE
CONTROL SYSTEM
FIGURE 1**



**SCHEMATIC DRAWING OF FLUERIC PRESSURE
CONTROL SYSTEM
FIGURE 2**



THE SET POINT CIRCUIT
FIGURE 3



BOOTSTRAP INTEGRATOR CIRCUIT
FIGURE 4

A FLUERIC INDUCTION AND GATE

by

Elmer L. Swartz

Harry Diamond Laboratories

ABSTRACT

The characteristics of the fluid induction AND logic unit are discussed. The principle of operation of this empirically designed device and the impedance matching technique employed to adapt it to fluid circuits are discussed.

I. INTRODUCTION

Fluid logic circuits require an AND unit that functions even if there exists a considerable difference in amplitude between the two inputs. In addition, the AND unit should have a pressure recovery that is comparable to an average bistable amplifier and it must be capable of being impedance matched into circuits without difficulty. It is also desirable that it be an AND/NOT type of device. This device has three outputs in which there is flow in only one at a time. The outputs are designated by A not B, B not A, and A and B.

This report gives a short discussion on the behavior of an induction AND which meets these criteria and the principles of its operation. The use of a mutual control between the two input signals is the basic difference in principle from other units that perform logic functions.

II. THE PRINCIPLE OF SWITCHING

If the walls are close to the stream, lowering the pressure in the control of a fluid amplifier is as effective in switching the power stream as the use of a higher pressure, but this technique is not generally used

since higher pressures are more easily produced. The fluid induction AND, however, does operate as a result of a low pressure, but it generates its own reduced pressure from the input signals to produce the switching action.

The induction AND gate in the broadest sense is a combination of two fluid amplifiers. They are combined in such a way as to have a mutual control, a mutual output plus two individual outputs. Figure 1 shows the channels of the two input-three output network. The mutual control as indicated is the connecting channel in which the low pressure is generated by the entrainment of two simultaneous input signals. This is the pressure that causes both streams to switch to the inner walls. Both streams must be present to maintain any inner wall lock-on.

The operating characteristics of the AND/NOT device are as follows:

- a. With A input only, there is flow out of A output only (fig. 2a).
- b. With B input only, there is flow out of B output only (fig. 2c).
- c. With inputs A and B, there is flow out of A·B only. (fig. 2b).
- d. With flows into both A and B, if B suddenly ceases, A rapidly switches from A·B to A output only; a similar result occurs if A suddenly ceases.

The above action is accomplished by a unique biasing arrangement. This can be described by imagining a fluid signal being applied at one input. As the stream leaves the input nozzle it finds the pressure in the mutual control channel the same as in the entrainment passage which are just opposite one another. See figures 1 and 2. The flow path in this case will be determined by the physical construction of the unit.

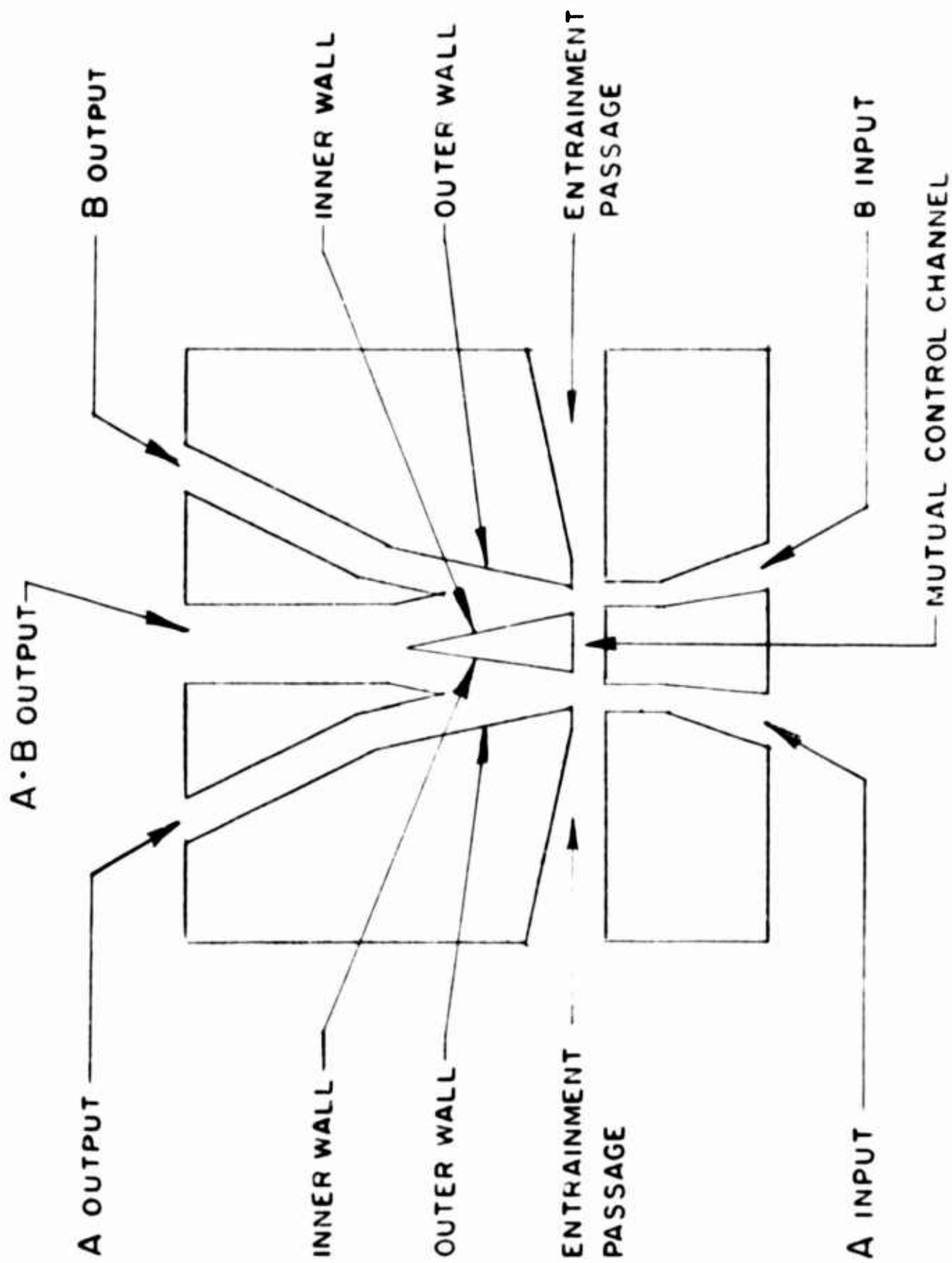
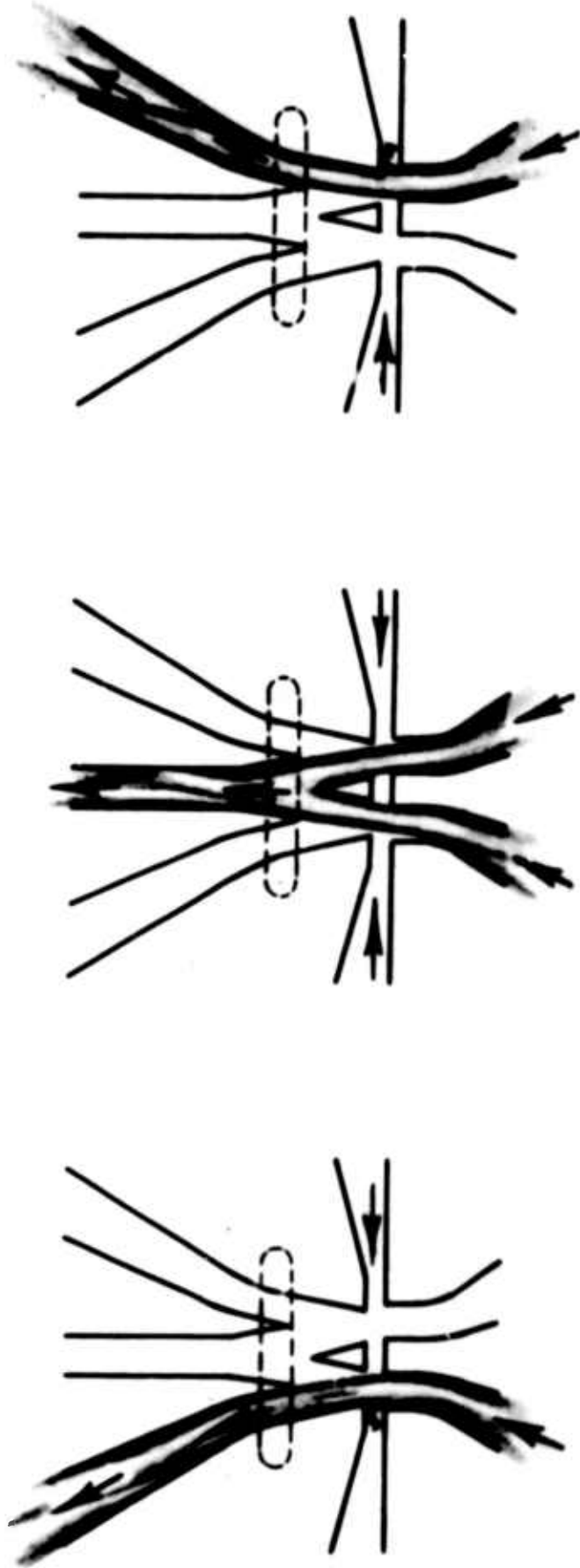


Figure 1. Channel network of the 'AND' gate.



c

b

a

990-65
Figure 2. Flow pattern in the induction 'AND' gate.

The outer wall which is on the entrainment passage side is much closer to the flow; in fact, the corner of the entrainment passage and outer wall slightly overlaps the input passage. The fluid will attach to this wall. A very small portion of the stream is peeled off by the corner causing a vortex to be formed in the entrainment passage. This configuration has a tendency to cause a stronger attachment to the wall than that in the average fluid amplifier. This accounts for its good pressure recovery. It should also be noted that in this condition, the mutual control channel is free to entrain from the atmosphere. This channel is small and as long as there is flow in an input there will be some pressure in this channel, which is lower than atmospheric pressure.

If at this point a fluid signal is applied to the second input, the second stream will immediately attach to the inner wall due to the slightly lower pressure in the mutual control created by the first stream. This flow will go out of the center as A·B output. It should be noted that a small pressure difference can readily override a bias created by the physical construction of the unit. The two streams upon passing on opposite ends of the mutual control channel will further decrease the pressure here in addition to not allowing entrainment from the atmosphere to satisfy this condition. The mutual control pressure quickly reaches the level to cause a rapid switch of the entire first stream to the inner wall. All flow is from the center port or A·B output as shown in figure 2b.

The negative pressure that these streams are inducing on one another through the mutual control enhances the attachment of the stream to the

inner wall. As the streams bend inward upon leaving the input channels they clear the overlapping corner on the outer walls. There should be no vortex in either entrainment channel at this time. In the average unit the amplitude of the static pressure at one input can be as great as eight times the other and the streams will still switch to the center.

Consider the action when there is an A·B output and B is suddenly switched off. The A signal loses its strong lock-on force. The attachment point is forced to move downstream, which decreases the bending of the stream in the control region until once again the outer wall corner has been contacted. The stream will then attach to the close or outer wall. The event takes place in a snap-action fashion and results in an A not B output.

The shape of the output signals and an indication of the switching time is shown in figures 3, 4, and 5, which are reproductions of the outputs of a two-pen recorder.

III. BLEEDS

It should be noted that these tests were made with a 1w load on each of the three outputs. The 1w indicates an orifice restrictor which has the same area as the input channel. This load cannot pass all the flow leaving the input nozzle because of the expansion of the gas and the entrained flow. Cover bleeds are provided to allow this excess gas to flow into the atmosphere rather than flow through the A or B outputs. The bleeds thus permit a low frequency impedance match; that is, any fluid which a given channel is unable to pass will be dumped from the system

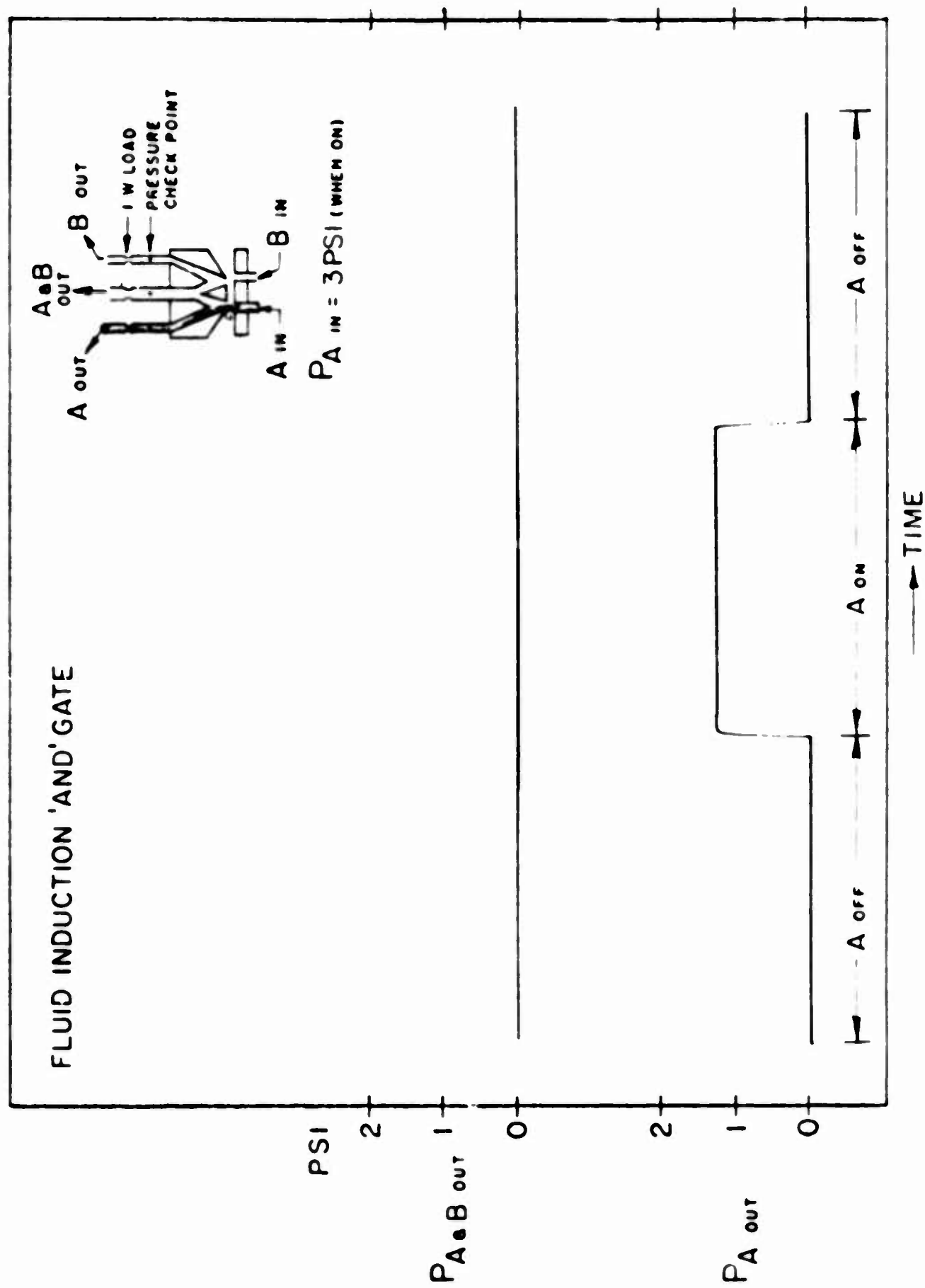


Figure 3.

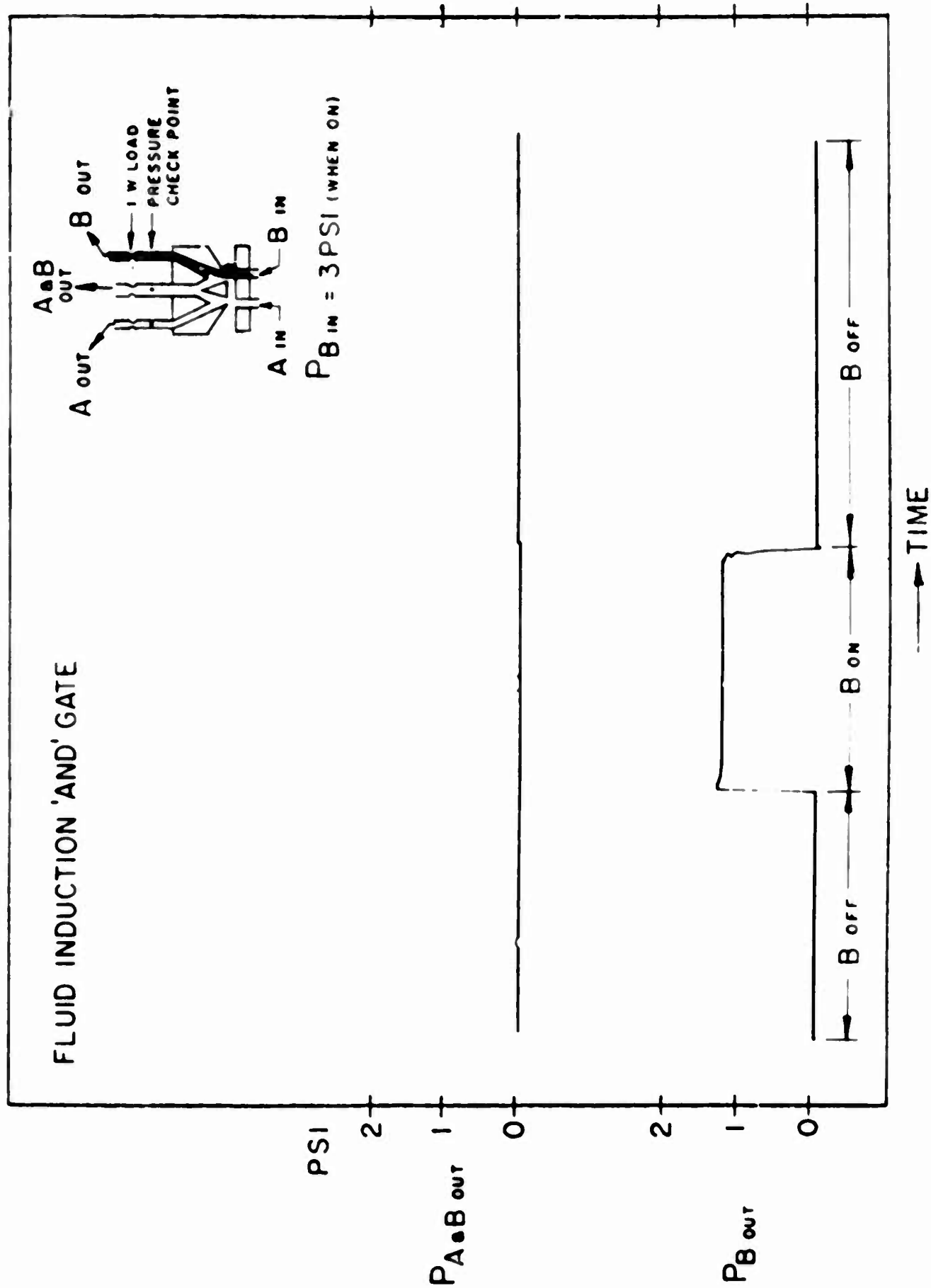


Figure 4.

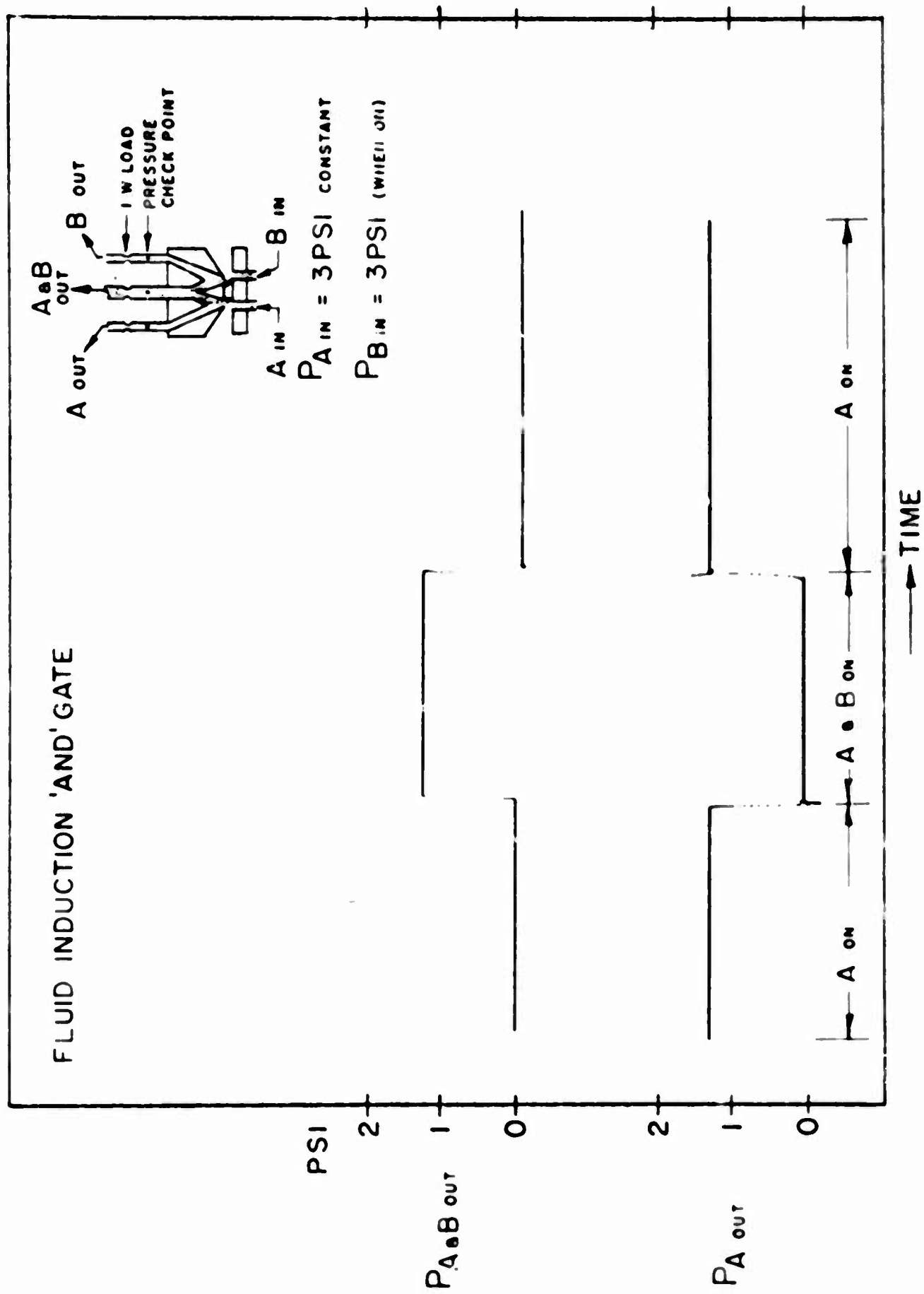
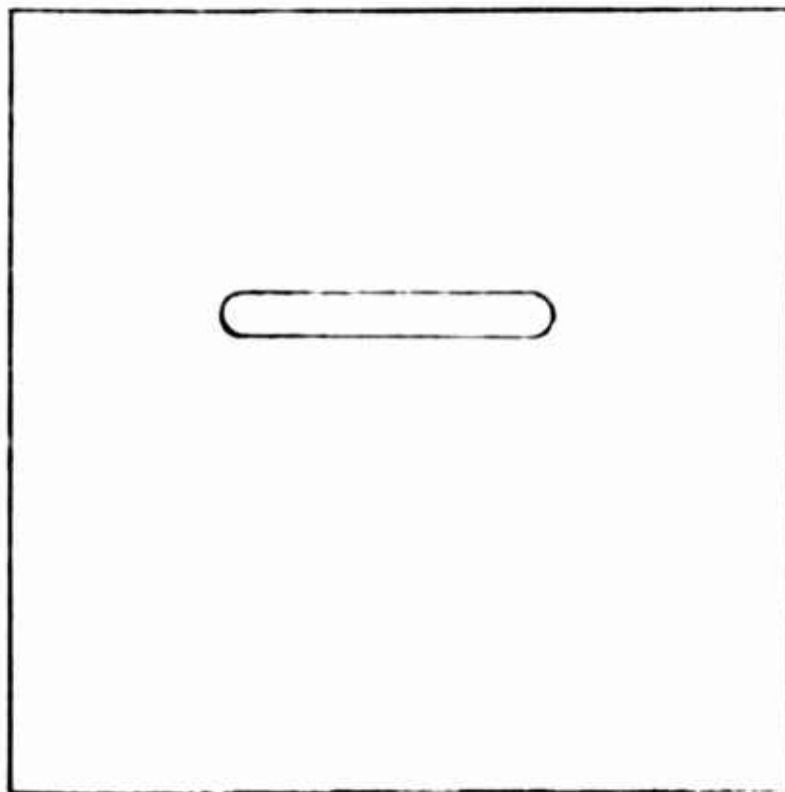
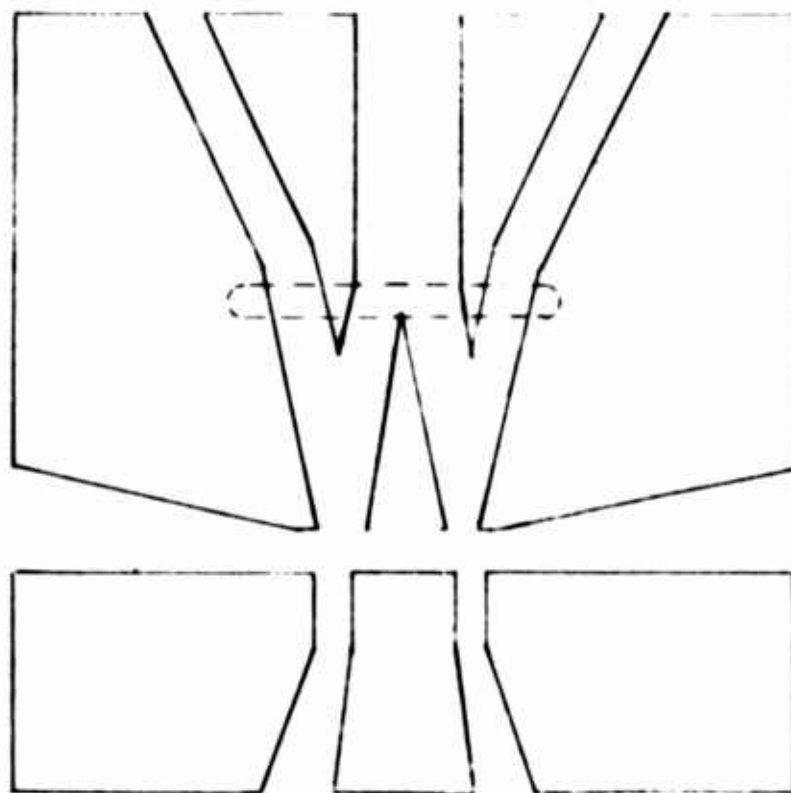


Figure 5.



COVER PLATE WITH BLEED SLOT



CHANNELED SECTION

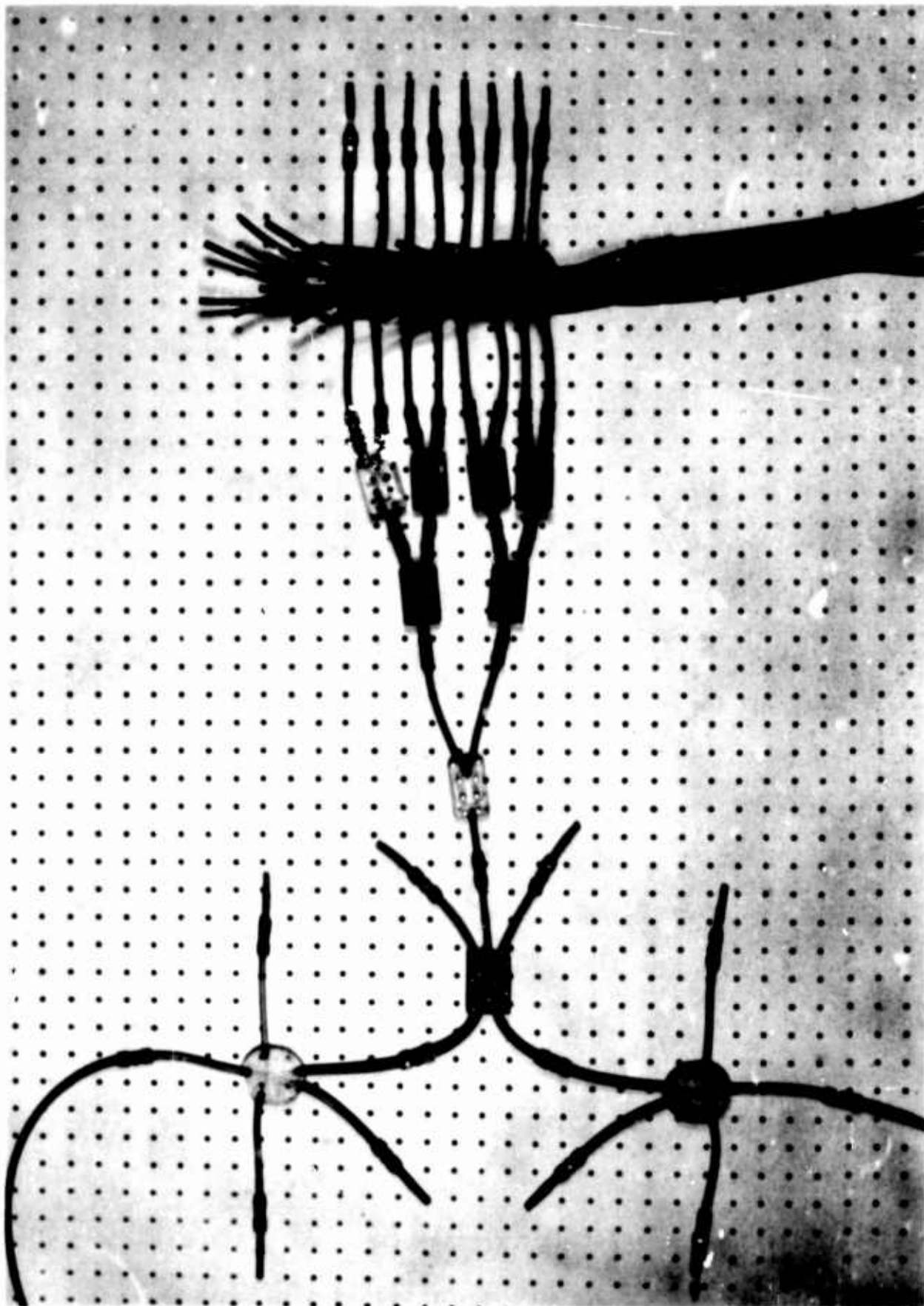
Figure 6. The induction 'AND' unit with the cover plate removed.

rather than spilled over into the adjacent channel. The cover bleed location is shown in figure 6. This AND unit is capable of working into the input of another similar AND. It can operate into the controls of a fluid amplifier or another passive device by utilizing the same size bleed.

Sometimes a bleed may require a change in size for the unit to operate properly. For example, there is the condition where a fluid unit feeds another unit with smaller inputs. This could require larger bleeds than normal if it is absolutely essential that there is no spillage into adjacent channels in the feeding unit. The second case, which seems the most practical, would have all units the same size requiring only one bleed of the proper size. The third case is when the bleeds are much larger than the minimum requirements. As a rule, the pressure recovery starts dropping somewhat as the bleed area is increased. In many cases there is much more power output than is required for the next stage so that a large bleed does not affect the operation. In general, bleed sizes are not too critical but care must be taken when certain channels require zero flow in the off position.

IV. CONCLUSION

The need for a more efficient AND gate led to the development of this device. There exists several devices that perform this same function but with a relatively lower gain and efficiency. They have the common disadvantage of turbulence losses and of occasional spurious signals as a result of the sharp turning of the streams after they interact with one



1144-65

Figure 7. The induction 'AND' gate operating into a fan-out of 8 Bl-stable amplifiers.

another to produce the output signal. There are no sharp turns in the induction AND but there is one disadvantage which should be noted. In the machining of the model there are several critical dimensions that must be maintained. The most critical is the set-back of the inner and outer walls. A change of one-thousandth of an inch there makes a noticeable difference in the operating characteristics. These critical dimensions were maintained, however, without difficulty when the model was reproduced with an epoxy material in a rubber mold. Figure 7 shows two amplifiers feeding into one of the molded 'AND' units. The output switches eight amplifiers in a fan-out circuit.

This device was specifically designed to operate in the low pressure region (1 to 5 psi). In this range the hydraulic analogy permits the use of the water table facility to its best advantage. This is a facility where large scale models are made of moveable or interchangeable metal blocks. These blocks are placed in the water to form the desired configuration. A change in configuration can be made in a matter of seconds, which is most useful since fluid interaction devices depend to a large extent on their geometry. Using the flow of water instead of air permits good visual observation of the flow. The use of dye to color the flowing water is required to obtain good results.

The patterns were set up for several models of the AND unit. The final pattern was carefully measured in the water table. After being sealed down to the normal lab size unit it was machined in brass metal

without modification. It is a good working model; however, the pattern has not been optimized.

MECHANICALLY ENTRAINED FLUIDIC OSCILLATOR

W. J. Westerman, Jr.
Martin Company
Orlando, Florida

A B S T R A C T

The paper presents the results of an analytical and experimental program aimed at achieving a temperature stable fluid oscillator which is insensitive to relatively low levels of accelerations. Mechanical entrainment of the oscillator frequency by means of a vibrating member is used much in the same manner as the crystal in a crystal controlled electronic oscillator. A mathematical model of the vibrator under the influence of a biaxial acceleration environment is presented. A mathematical model of the fluid control devices coupled with the frequency entrainment element is compared to experimental data. An explanation of the operation of the combined oscillator in its preferred configuration is included with photographs of the microminiature test model used in obtaining the data.

INTRODUCTION

Throughout scientific history men have been concerned with measuring time. From graduated candles, sundials, and hourglasses to Junghans escapements, crystal-controlled oscillators and atomic clocks, the technique of time measurement has been to count or measure some time-dependent phenomenon that occurs in a reasonably predictable manner. Essentially the quest has been to find such natural phenomena and then to control the disturbance variables such as temperature and acceleration so that their effect on the phenomena is minimized.

Unfortunately requirements exist and are still unsatisfied for a relatively stable time base where it is impossible to control the environment. Such an application is a fuze for artillery shells wherein the timing device is subjected to many thousand "g" acceleration for a very short period and then experiences accelerations that vary over $10g$ in a period of about 1 minute. Such timers must operate equally well at -60°F and at $+140^{\circ}\text{F}$. The shell will also be spinning at an unpredictable rate somewhere between 15,000 and 40,000 rpm with the distinct possibility of a slight wobble about the geometric axis of symmetry.

Throughout this environment, the need exists for a timing accuracy of 0.1 percent or one part in a thousand.

Since sundials and atomic clocks are equally ridiculous to consider, we start looking for a concept that falls between the two. Electronic oscillators have problems in surviving the initial firing but the real disadvantage is the cost of such a fuze. By a process of elimination, the mechanical escapement has been the concept most used. With frictionless bearings, a temperature-insensitive oil that will not oxidize, run, or gum up and a spring that has the same characteristics over a 200 degree temperature range, one has a fairly reliable time, but without the desired accuracy.

The restrictions on cost along with the severe inertial environment suggest the use of fluidics. The temperature environment, however, introduces some rather difficult problems to a pure fluid system. In addition, it is not clear that a sufficiently well regulated pressure can be provided using pure fluid techniques; likewise it would be equally difficult to mechanize a mechanical pressure regulator to operate successfully in the acceleration environment.

MECHANICAL ENTRAINMENT

From a standpoint of cost, reliability, and ruggedness, it is desirable to utilize pure fluid techniques in mechanizing a fuze timer. However, temperature and/or pressure variations present problems that can not be solved in a straightforward manner that is consistent with the simplicity of the basic fluid oscillator concept. Therefore, it seems that attention should be directed to harnessing some other time-dependent phenomenon with fluidic techniques. Mechanical timers have been made that will survive the severe environments although they generally do not perform satisfactorily with regard to accuracy.

Essentially mechanical timers utilize the principle of a spring and mass which are excited with a periodic, although nonlinear, force. The basic problem in such a device becomes one of eliminating friction in the spring mass system. Stated another way, one tries to eliminate the damping in the system as far as possible so that a sharp resonance peak is obtained for the oscillating system. In this way, the oscillator will quickly assume its natural frequency after having been excited by a nonlinear force. If the forcing function then approximates an impulse, it, in itself, will have little effect on the overall periodic nature of the oscillating spring-mass system. Due to the resonance phenomena and the very low damping, the impulsive force need only impart a very small amount of energy to the system over each cycle; in fact, it need only impart an energy equal to that lost through damping. The frequency of the periodic impulsive force is, of course, controlled by the amplitude (and hence the frequency) of the oscillating device.

One of the most effective methods of reducing the damping in a mechanical system is the elimination of the bearings and gear wheels associated with the Junghan's escapement device, which is commonly used in the type system described. This can be accomplished using fluidics if miniaturization techniques are available.

Figure 1* is a fluidic analog of a Junghan's escapement. A generalized mechanical vibrator, to be described later, forms the frequency reference just as a pallet wheel does in a Junghan's escapement. The vibrator must be of such a design that its resonant frequency is unaffected by temperature, gas pressure, or accelerations. The fluidic element is a monostable device whose stable configuration is shown in the figure as the bias leg. When the control port in the foreground is covered, the resulting low pressure will cause the power stream to flow down the curved output leg. The covering and later uncovering of this control port is accomplished by the "generalized mechanical vibrator" which oscillates back and forth in front of the control port at its resonant frequency, f_r , where in general:

$$f_r = \sqrt{\frac{k}{m} - \left(\frac{c}{2m}\right)^2}$$

c = damping

k = effective spring constant

m = effective mass.

*Figures appear on pages 195 through 203.

For most materials, the energy dissipated per cycle is independent of frequency over a wide range and is approximately proportional to the square of the amplitude. The minimization of the damping energy per cycle can thus be accomplished by minimizing the average strain per cycle.

From Figure 1 the amplitude of vibrator must be of the order of two control port widths. The actual configuration of the vibration is still to be selected and will affect the system damping in that its configuration will determine the average stress in the oscillating system.

General forms can be postulated for the mechanical vibrator. A vibrating wire or band could be used and, if it were mounted in a frame of the same material as the vibrator, would be temperature and acceleration insensitive over moderate ranges. A membrane could be used which would be acceleration insensitive so long as the acceleration vector were parallel to the plane of the membrane. A wheel or blade operating in conjunction with a torsional spring is another possibility.

A vibrating band or wire would be the most desirable device since it is the least complex of the several types of vibrators that might be postulated. A cantilever beam is quite acceleration-sensitive, being similar to a pendulum in some respects. Intuitively a vibrating beam, held at both ends, would be axially acceleration-insensitive. Since the overall oscillator should be small, a limit of 1 inch for the length of such a beam may be imposed. Due to manufacturing problems, the beam should be fixed at both ends as opposed to being hinged.

The natural frequency of such a clamped-clamped beam is:

$$\omega = 22.0 \sqrt{EI/\mu_1 l^4}$$

where

ω_n = natural frequency in rad/sec

E = Young's modulus

I = moment of inertia

μ_1 = density

l = length of beam.

If the control port width is on the order of 0.003 inch then the amplitude of the vibration of the beam must be at least 0.006 inch. If a small safety factor is introduced, a good approximation of the actual vibrator amplitude would approach 0.010 inch.

For a steel wire of 0.010 inch diameter, the natural frequency is $\omega_n = 1782$ cps. The kinetic energy for such a beam is:

$$KE = \frac{\mu_1}{2} Y_0^2 \omega l (1 + 1/2)$$

$$KE = 0.447 Y_0^2 \text{ in/lb}$$

where

KE = kinetic energy
 Y_0 = maximum amplitude.

If Y_0 is 0.010 inch, the kinetic energy is approximately 0.447×10^{-6} inch pounds, an approximate value for the expected material damping can be found from the maximum stresses expected in the beam (1). The maximum stress can be found from:

$$\sigma = \frac{Mc}{I}$$

where

σ = stress
M = the bending moment
c = distance from neutral axis to edge of cross section.

To a close approximation, $\sigma \approx 48,000$ psi (cycling stress).

The specific damping energy is approximately 0.002 in-lb/cu in. per cycle. The energy loss per cycle (only a small portion of the material is undergoing the maximum cycling stress) is approximately:

$$\text{Energy loss} = E_L = 0.039 \times 10^{-6} \text{ in-lb/cycle.}$$

These figures are in sufficient agreement with experimental results to warrant confidence.

The energy available per cycle is a function of the exciting gas stream and the drag coefficient of the beam. Again assuming a round wire for beam (the worst case) and assuming the gas to be nitrogen leaving the nozzle of the element at sonic velocity, the Reynold's number, N_R , is approximately

$$N_R = \frac{Vd\rho}{\mu} \approx 2500$$

where

V = velocity of gas
d = diameter of the stream
 ρ = density of the fluid
 μ = viscosity of the fluid.

The drag coefficient of a cylinder at this Reynolds number is (2):

$$\text{Drag coefficient} = C_D = 1.0.$$

The drag on the "beam" then becomes

$$\text{Drag} = D = C_D A \times \frac{\rho V^2}{2} = 3.12 \times 10^{-4} \text{ lb}$$

where

A = area

when it is assumed that the gas stream impinges on a length of the wire of about 0.012 inch. Since the velocity of the vibrating beam is never large compared to the velocity of the stream, the effects of relative velocities can be neglected.

For an amplitude of vibration of 0.012 inch, the energy available per cycle is approximately

$$\text{Energy} = E \approx 3.12 \times 10^{-6} \text{ in-lb/cycle.}$$

This is in the order of 100 times the energy lost to material damping. Thus a beam, as postulated, can be excited by the gas stream and that beam will reach a stable limit cycle operation where the amplitude (but not the frequency) of vibration will be dependent on the velocity of the gas stream, the drag coefficient, and the material damping present. The amplitude will undoubtedly be larger than the required 0.010 inch.

To investigate the effect of temperature on the device, it will first be necessary to obtain an expression for the fundamental frequency of a beam with both ends fixed and under tension. A clamped-clamped beam assumes a deflection curve that is approximately:

$$Y = Y_0 \left[1 - \cos \frac{2 \pi x}{\lambda} \right].$$

Since the tension effects will be small compared to the bending effects, it can be assumed that the effect of welding the vibrator to the frame while it is under a small amount of longitudinal tension will not alter the shape of the deflection curve but will alter the energy expressions.

It has been demonstrated (3) that the effect of this tension on the natural frequency of the vibrator is

$$\omega_n = \sqrt{\frac{T \pi^2}{\mu_1 l^2} + \frac{4 EI \pi^4}{\mu_1 l^4}}$$

where

T = tension
 μ = mass per unit length
 l = length of beam
 ω_n = natural frequency (undamped)
 E = Young's modulus
 I = moment of inertia.

If the vibrator is held in a "U" shaped frame made of the same material as the vibrator itself, any tension effects due to temperature will be as a result of a temperature gradient existing between the vibrator and the frame. This will give rise to a strain in the vibrator and hence an apparent tension. The tension can be expressed as

$$T = EA \epsilon = EA \frac{\Delta l}{l}$$

where

A = cross sectional area of vibrator
 ϵ = strain
 Δl = change in length of vibrator
 l = original length of vibrator.

If it is assumed that the frame holding the vibrator is very stiff in comparison to the modulus in tension of the vibrator (the term "EA" in the above equation), then the entire strain in the vibrator can be attributed to the thermal expansion of the frame. Thus

$$\Delta l = K l (\theta_F - \theta_V)$$

where

K = coefficient of thermal expansion
 θ_F = temperature of frame
 θ_V = temperature of vibrator.

Therefore, the tension in the vibrator can be expressed as:

$$T = EAK (\theta_F - \theta_V)$$

and

$$\omega_n = \sqrt{\frac{\pi^2 EAK (\theta_F - \theta_V)}{\mu l^2} + \frac{4 EI \pi^4}{\mu l^2}}.$$

Assuming, as before, that the vibrator is a 1 inch long, 0.010 inch diameter wire and that the vibrator and frame are made of 36 percent nickel steel (Invar), which has a very low coefficient of thermal expansion (0.9×10^{-6}), the maximum temperature difference that can be allowed for a frequency reference accurate to one part in 10^5 is:

$$(\theta_F - \theta_V) = 5.5 \text{ degrees C} = 9.8 \text{ degrees F.}$$

It should be recognized that the temperature of the frame and beam can vary considerably and the device will still operate at the expected frequency; however, the difference between the frame and beam must be kept small.

If the vibrator is accelerated along the axis of the beam, the maximum potential energy, which is a function of the tension and the shape of the deflected beam would remain constant since the tension in the front half of the beam would increase (while the shape would decrease) and the tension in the rear half of the beam would decrease (while the shape would increase). The integral:

$$\int_0^l y^2 dx$$

would remain the same as in the unaccelerated case and the kinetic energy expression would not change. This would, therefore, indicate the vibrating beam to be insensitive to acceleration along its axis. In fact it can be shown that the effects of accelerations in the 1 to 10g range are to be found in second order terms such that the shift in the natural frequency is less than one part in one thousand.

An important relationship exists relative to the phase relation between the excitation force and the oscillating vibrator. The oscillator that has been postulated here is not a linear system at all and is very difficult to describe in the frequency domain by the usual Laplace transform methods. A time plot of the vibrator amplitude is presented as Figure 2. T_1 and T_2 represent the time delays that occur between the nominal position of the vibrator at which the element switches and the position at which the change in jet force is felt at the vibrator itself.

The vibrator is considered initially at the null position with maximum velocity and is being powered by the jet stream. At some amplitude, X_s , the element begins to switch; after a delay, the element becomes fully switched; however, the trailing edge of the jet stream must still travel along the feedback path before the force on the vibrator is removed. The total time lag is represented at T_1 . The vibrator attains its maximum amplitude and begins to return to the opposite peak. At the same amplitude level, X_s , the element begins to switch. After sufficient time for the jet stream to entrain the necessary amount of gas in the control passage, the element switches. Again, however, the wave front must travel the length of the feedback path before the force of the jet stream is applied to the vibrator. This total time lag is represented by T_2 . The necessary lag can be provided in a number of ways. First, of course, the

feedback path can be made sufficiently long. Secondly, the volume of gas in the control port can be varied so that the lag due to the entrainment of the gas can be adjusted. Likewise, the "timing" of the point, X_S , can be changed by adjusting the position of the vibrator null position relative to the control port opening.

There are important aspects of the excitation function and its phase relations with the free vibrator that cannot be overlooked. The linear, slightly damped vibrator can be described by the following equations:

$$\frac{d^2x}{dt^2} + 2b \frac{dx}{dt} + a^2 x = 0$$

$$2b = \frac{r}{M}$$

$$a^2 = \frac{k}{M}$$

where

k = spring constant

r = damping

M = mass

x = amplitude of vibration along length of vibrator.

The general solution of characteristic equation of the vibrator is:

$$x = e^{-bt} (A \cos \omega t + B \sin \omega t)$$

$$\omega^2 = b^2 - a^2$$

where

ω = natural frequency of the damped vibrator.

For small amplitudes of a mechanical vibrator such as has been discussed:

$$\omega = \omega_n = \frac{k}{M}.$$

If the vibrator is now considered to be excited by some forcing function, $f(t)$, then:

$$\frac{d^2x}{dt^2} + 2b \frac{dx}{dt} + a^2 x = f(t).$$

Having the general solution, the particular integral can always be obtained. In the cases considered here, there will be a periodicity of the forcing function, $f(t)$. The cycle will have a period of:

$$T_f = \frac{2\pi}{\omega}.$$

Unfortunately, if the vibrator is being excited by a fluid stream which is, at the entrance to the transmitting channel, being turned on and then off with a period of T_f , the vibrator will not necessarily be excited at its natural frequency. Instead, in an incompressible fluid, for example, the excitation force as seen by the vibrator will be a square wave of force with period T_f , that is somewhat out of phase with the square wave at the tube entrance.

If the forcing function, $f(t)$, is a square wave, the higher modes of vibration of the vibrator will be inadvertently excited and will, therefore, tend to throw doubt on the validity of the predictions presented so far. There is, however, a factor in considering compressible fluids that can, if utilized properly, be of considerable advantage in minimizing the degradation of the first vibrating mode to be expected from the forcing function.

From a practical standpoint, the switching of a pure fluid logic element does not result in a square wave flow output even at a small distance from the interaction area. In fact, data presented by Keto (4) would seem to indicate a time constant in the order of 0.3 ms for an element having a power nozzle width of 0.0312 inch. Experiments carried out on smaller logic elements indicate much shorter time constants for the response of the elements to step inputs in the control ports. Collectively, these studies indicate that the dynamic response of a fluid amplifier can be tailored to give any flow profile as a function of time that is reasonably desired for exciting a mechanical vibrator such as that postulated above.

Care must be taken in that the transmission line carrying the flow from the logic element to the vibrator also alters the shape of the wave front as well as the "tail." Brown (5) as well as others has devoted considerable effort toward this problem so that it becomes a predictable, although involved, design procedure.

Techniques, such as described above, can be employed to shape the quasi square wave of period T (as described in the previous equation) until it very closely approximates a sine wave in a particular interval such that:

$$F = A \sin \omega_n t$$

where

$$\begin{aligned} A &= 0 & t_1 < t < t_2 \\ A &= \text{constant} & t_2 < t < t_1 \\ \omega_n &= \text{natural frequency of vibrator.} \end{aligned}$$

This would produce the desired particular integral associated with $f(t)$ describing the steady state performance of the vibrator.

Figure 3 is a block diagram representation of the oscillator system. The NOR element and the associated time lags can be represented collectively in the same block by enlarging the hysteresis of the nonlinear element as in "a." Conversely the two time lags T_1 and T_2 can be represented by separate terms having the form:

$$G_1(s) = e^{-T_1 s}$$

$$G_2(s) = e^{-T_2 s}.$$

These can be combined into one transport lag such that:

$$G(s) = e^{-Ts}$$

where

$$T = T_1 + T_2.$$

The block diagram can then be presented as in "b" by representing the nonlinear NOR gate by a relay of negligible hysteresis and including the time lag $G(s)$.

EXPERIMENTAL RESULTS

Several models of the oscillator utilizing the mechanical entrainment principle have been built and tested. The first model, made primarily to demonstrate the principle and to investigate the effects of damping on the mechanical vibrator, is illustrated in Figure 4. This device utilized a pendulum as the frequency reference and had provisions to change the damping (i.e., the friction). One provision altered the coulomb friction while another altered the viscous damping. The effect was, of course, quite dramatic. With no intentionally induced damping, a frequency stability of 0.5 percent was observed. Within supply pressure ranges of 3 to 12 psi, no observable change in frequency occurred. This was accomplished by properly designing the blade used to cover the control port so that an impulsive force could be realized.

Figure 5 illustrates a second mechanization of the principle. In this device a preferred mechanization was used in which a bistable element is incorporated in place of the NOR element. Rather than relying on the entrainment from a covered control port to accomplish switching, a jet is directed into each control port of the bistable element. One jet or the other is interrupted by a plate attached to the vibrator as shown in Figure 6. This rather crude model was observed to have a frequency stability of 1 percent over a pressure range of 3 to 28 psi. This instability was shown to be due to the effects of variable bearing friction as the vibrator amplitude increased. Above 28 psi the system degraded rapidly due to the excessive amplitude of the vibrator and the resultant nonlinear effects introduced. Temperature tests have shown that the device is independent of gas temperature effects over a wide range; no change was observed over a 120°F range. A plot of frequency versus input pressures is presented in Figure 7. Figure 8 shows two oscilloscope traces of the oscillator output. Figure 8a shows $P_g = 10$ and $P_I = 10$; Figure 8b shows $P_g = 14$ and $P_I = 10$. The mechanization shown is, of course, acceleration sensitive and the vibrator frequency is temperature sensitive inasmuch as the length and Young's modulus are affected. Materials are available, however, that can eliminate the temperature problems.

Figure 9 illustrates the miniaturization of the model presented in Figure 5. The fixture holding the oscillator is used to investigate the effect of vibrator positive relative to the control ports. Figure 10 is an oscilloscope trace of the output of this oscillator. As the frequency of the vibrator is on the order of 2000 cps, care must be taken to design the control port configuration in conjunction with the power leg so that the proper phase relations are obtained.

The time response of the complete circuit is 0.5 millisecond. The predominant effect is due to the delays associated with transportation lags and not with the element switching rate. In this manner, an impulsive force is still realized in spite of the large overall response to a step input.

CONCLUSION

Stabilizing the frequency of an oscillator by means of a vibrating mechanical member has been used in various electronic devices for some time. The accuracy

depends on the sharpness of the resonance peak of the vibrator or, stated another way, on the ability to minimize the damping in the vibrator. In nonfluidic systems, where a very small amplitude of vibration can be detected, the problem is not so difficult since the damping in the vibrator is a function of the average strain in the material.

The development of miniature, pure-fluid elements which have port sizes in the order of thousandths of an inch has made it possible to use the vibrator principle to stabilize fluid oscillations.

REFERENCES

1. B. J. Logan, "Proceedings of Meeting on Structural Damping at ASME," Atlantic City, New Jersey, December 1959.
2. J. K. Vannard, "Fluid Mechanics," New York; John Wiley & Sons, 1957.
3. W. J. Westerman, Jr., E. F. Richards, W. B. Depperman, "A Miniature Fluidic Oscillator and Pulse Counter," SAE Aerospace Fluid Power Systems and Equipment Conference, Los Angeles, California, May 1965.
4. Jorma R. Keto, "Transient Behavior of Bistable Fluid Elements," Proceedings of the Fluid Amplification Symposium," Vol. III, May 1964, Harry Diamond Laboratories, Washington, D. C.
5. Forbes T. Brown, "Pneumatic Pulse Transmission with Bistable Jet-Relay Reception and Amplification." Sc.D. thesis, M.I.T., Boston, Massachusetts, May 1962.

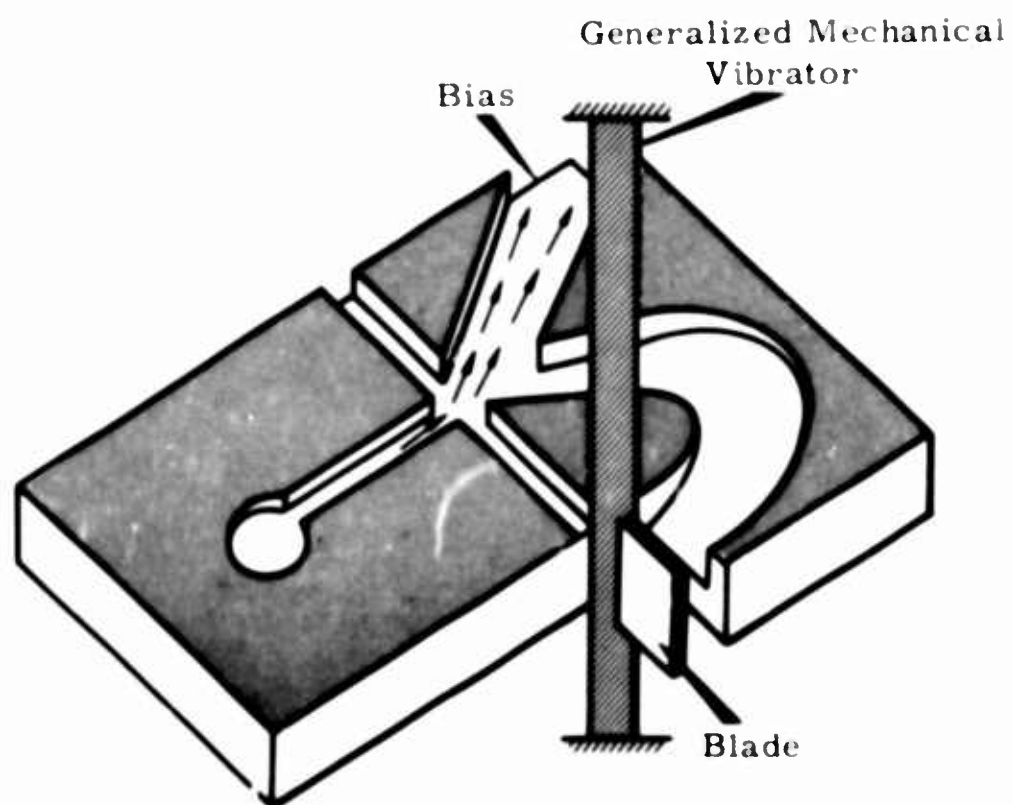


**FIGURE 1. GENERALIZED MECHANICALLY
ENTRAINED OSCILLATOR**

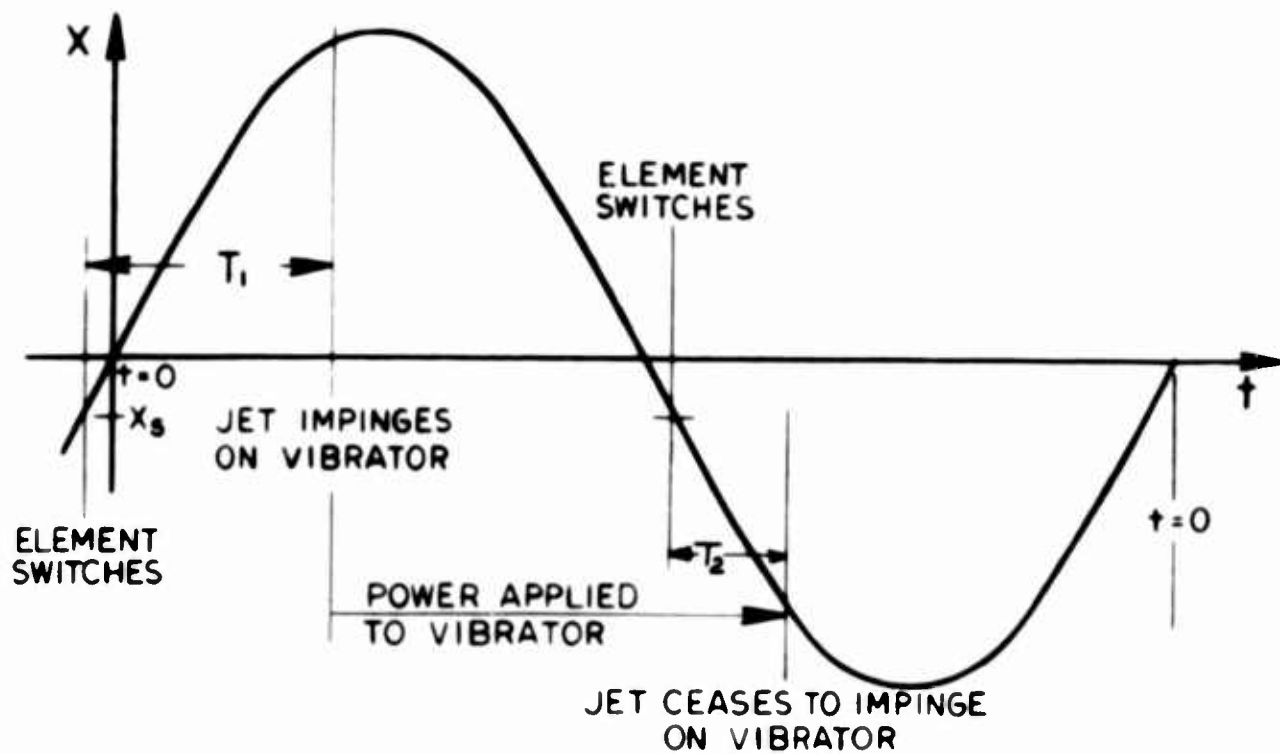


FIGURE 2. AMPLITUDE VERSUS TIME PLOT

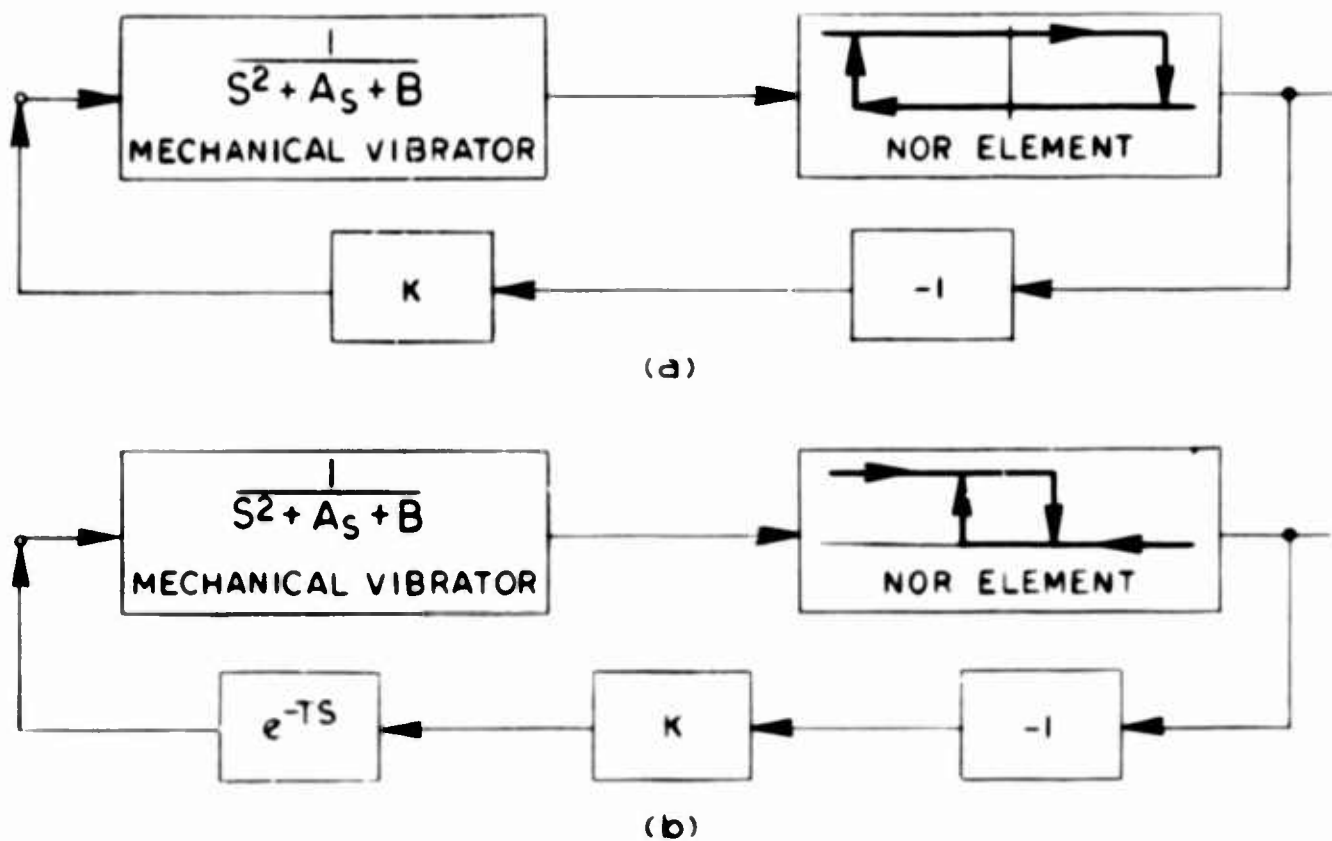


FIGURE 3. BLOCK DIAGRAM OF OSCILLATOR SYSTEM

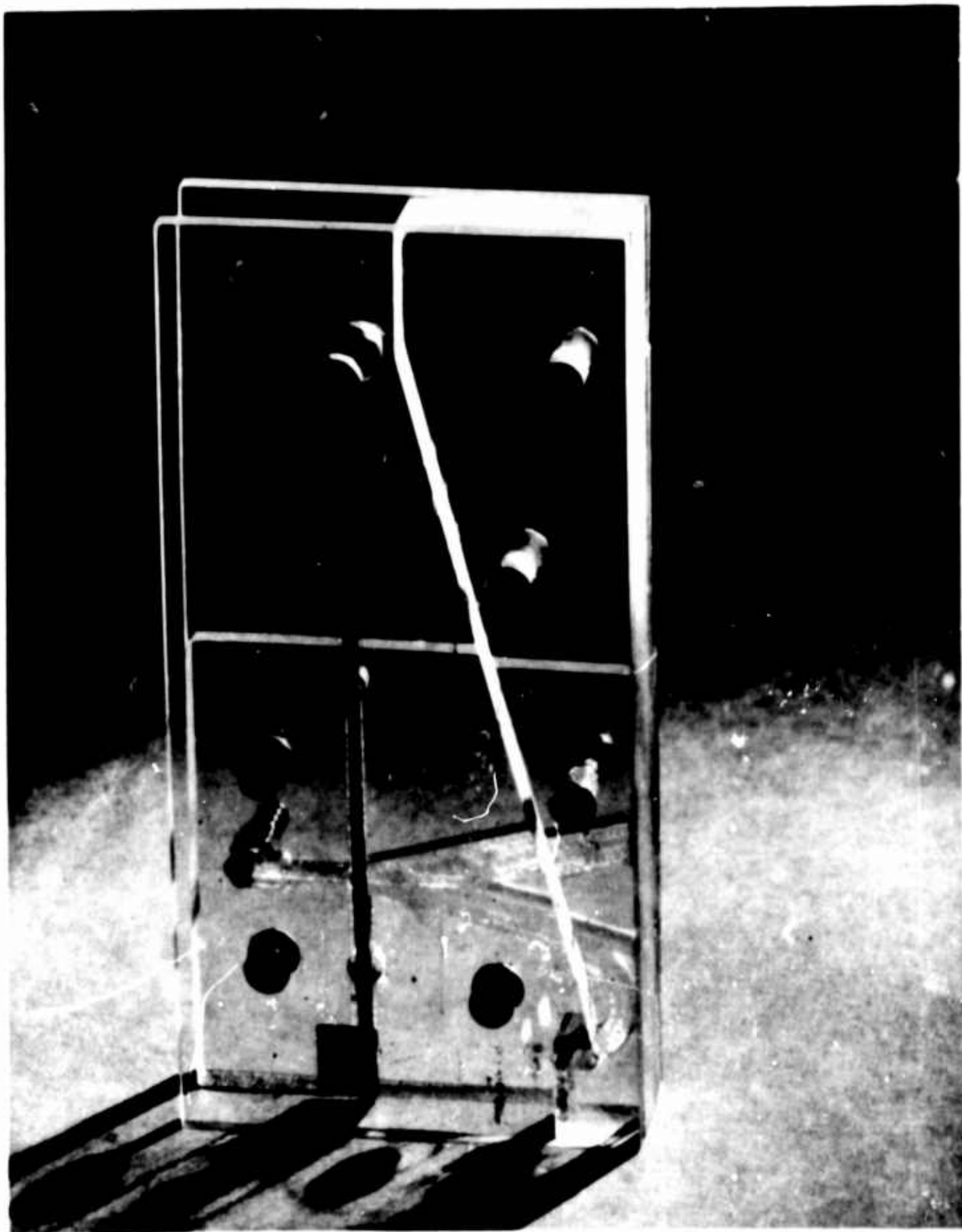


FIGURE 4. PENDULUM OSCILLATOR

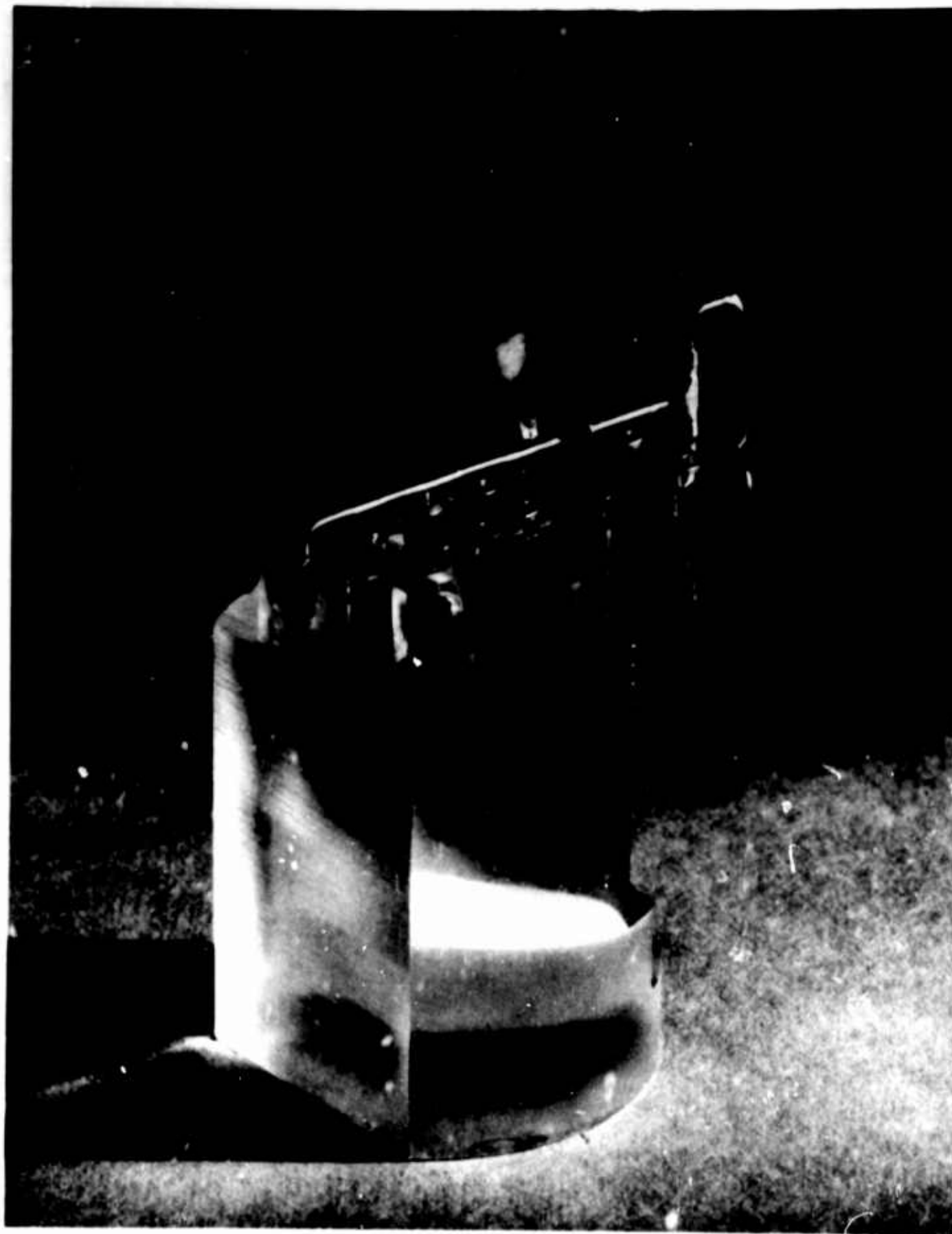


FIGURE 5. VIBRATOR ENTRAINED OSCILLATOR

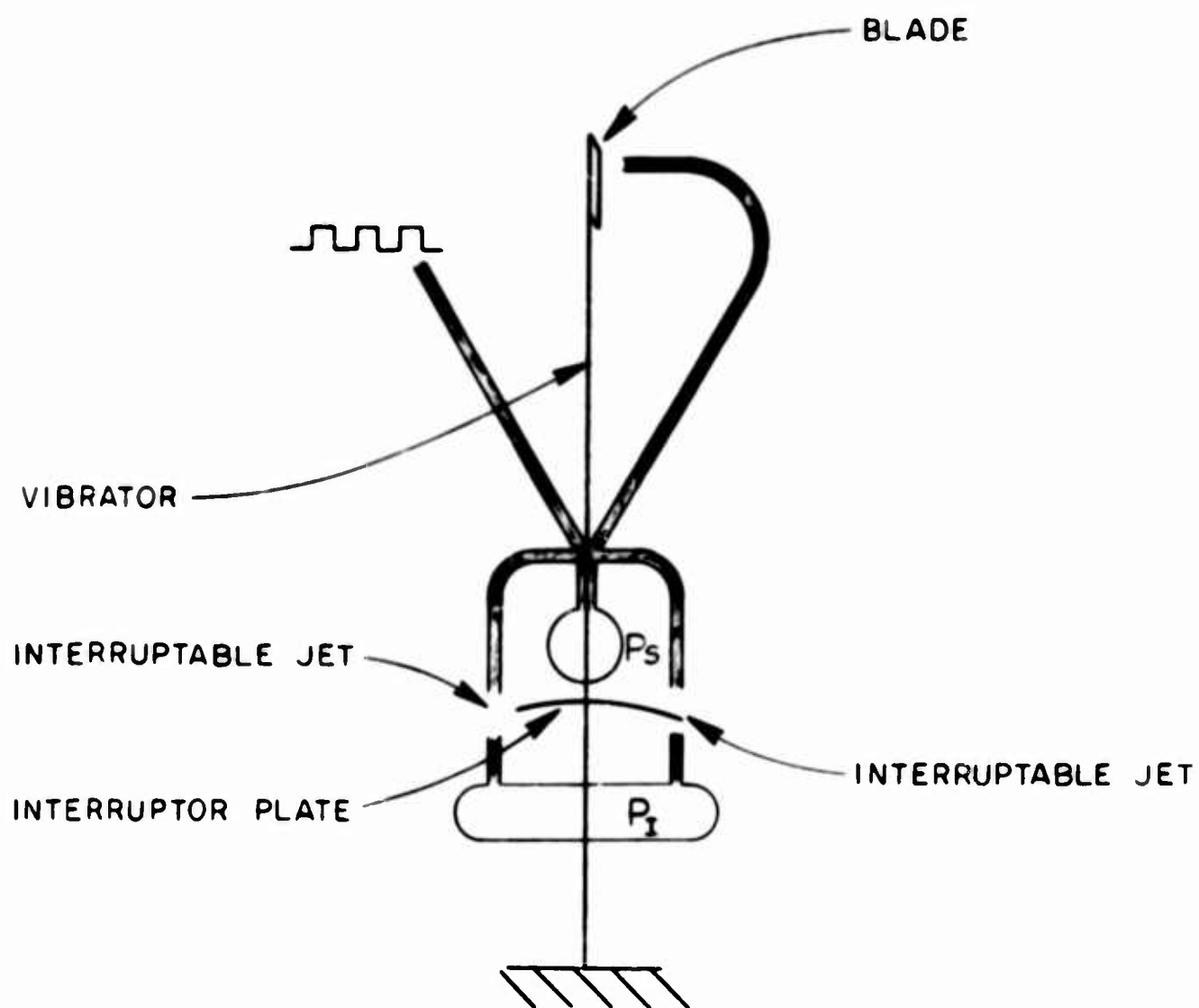


FIGURE 6. BISTABLE MECHANIZATION

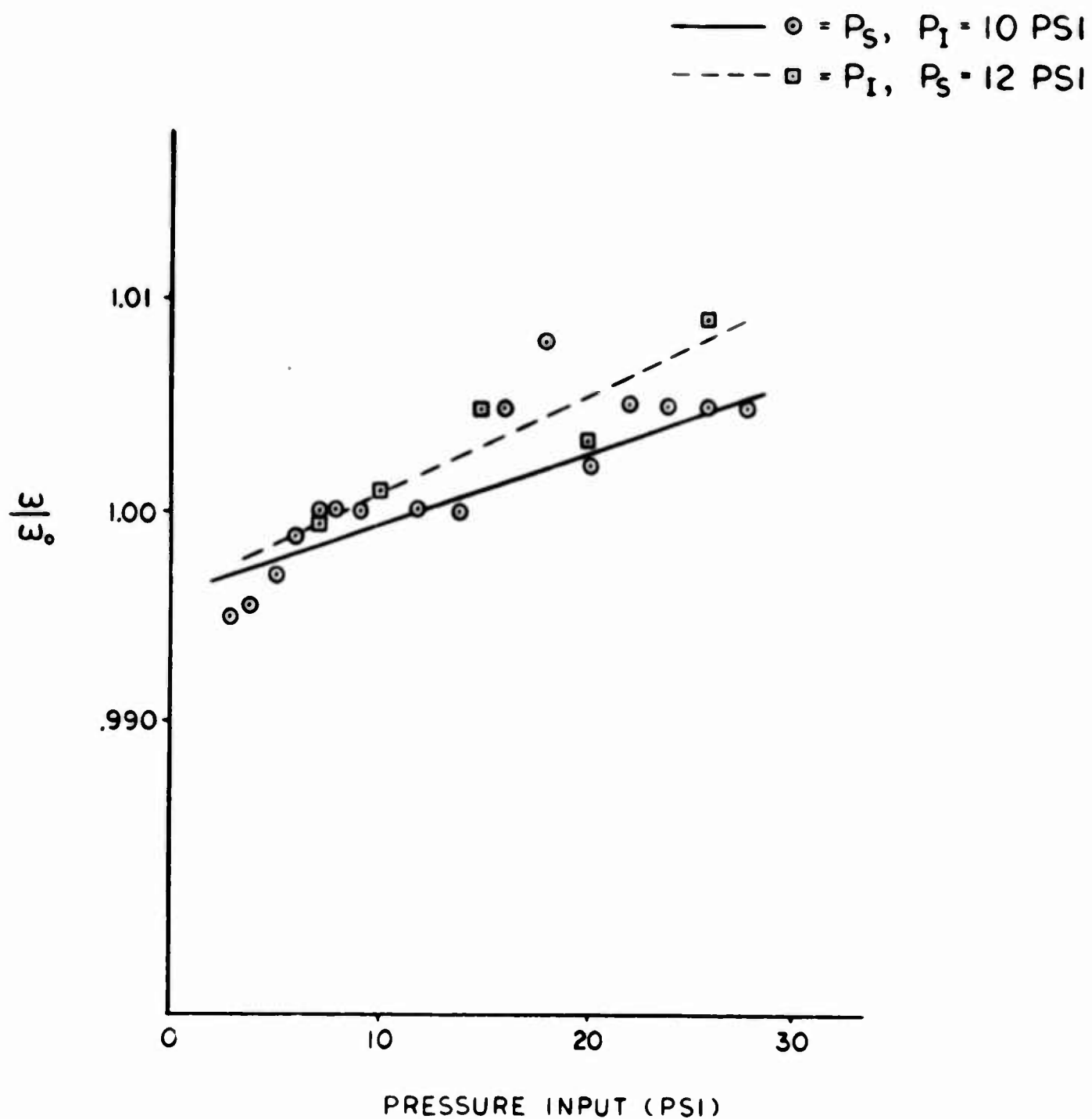


FIGURE 7. FREQUENCY VERSUS INPUT PRESSURE



a
 $P_S = 10 \text{ PSI}$
 $P_I = 10 \text{ PSI}$



b
 $P_S = 14 \text{ PSI}$
 $P_I = 10 \text{ PSI}$

FIGURE 8. OSCILLOSCOPE TRACES OF OSCILLATOR OUTPUT

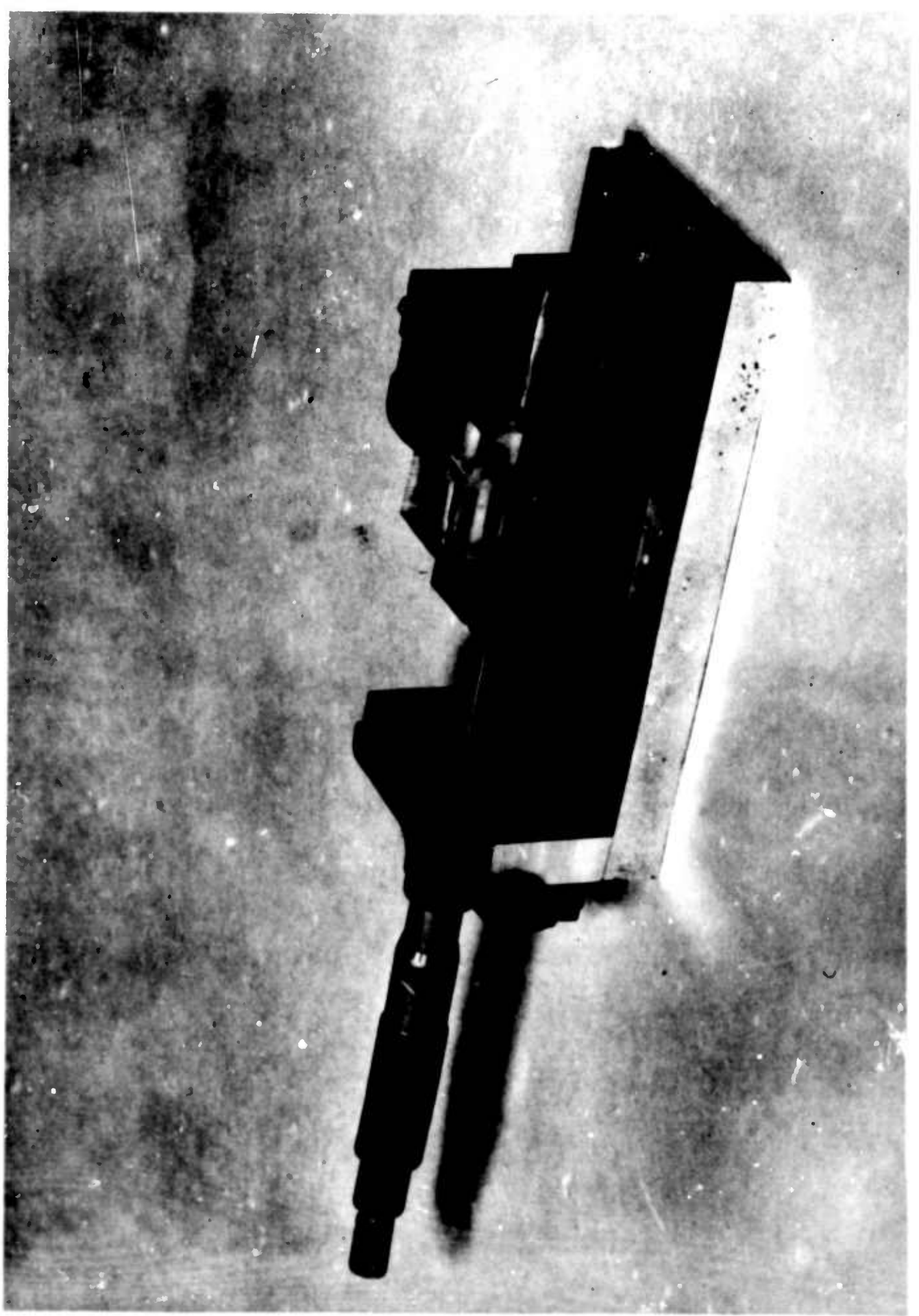


FIGURE 9. MINIATURIZED VIBRATOR ENTRAINED OSCILLATOR



FIGURE 10. OSCILLOSCOPE TRACE OF MINIATURIZED OSCILLATOR

STEADY FLOW IN A PURE FLUID VALVE TVC SYSTEM

D. W. Harvey and R. P. McRae
Missile & Space Systems Division
Douglas Aircraft Company, Inc.

ABSTRACT

A discussion of the application of bistable fluid-controlled valves to thrust vector control systems is presented, considering steady flow only. It is shown from pressure considerations that supersonic flow must exist in the valve body. From the effect of injectant total pressure on side force, it is also shown that the losses involved in decelerating this flow before injection may improve system performance.

CREDIT

Work presented herein was conducted by the Douglas Aircraft Company, Inc., Missile & Space Systems Division, under company-sponsored Research and Development funds.

1. INTRODUCTION

With the wider use of solid propellant rockets has come the need to steer them. An attractive way to do this is to inject a fluid into the nozzle divergent section. This partly blocks the main flow, and gives a side component of thrust that can be used for steering. A particularly light system results if the injected fluid is obtained from the combustion chamber. The principle problem in doing this is controlling the injectant, which is hot and usually carries abrasive particles. The pure fluid valve, since it has no moving parts, appears an ideal candidate for this purpose.

2. TYPE OF VALVE

The pure fluid devices that have been developed for pneumatic circuit applications have a common feature. This is control of a large flow by a small one. Of these devices, two appear promising for TVC application. These have been called the "proportional amplifier" and the "bistable element."

The geometry is about the same for both. It is shown somewhat schematically in Figure 1.* In the proportional amplifier, an incremental increase in control flow causes an increment of main stream deflection. The main stream, unless held all the way to one side or the other, divides on the splitter in proportion to the flow of control fluid. Thus in principle the entire main stream or none or any intermediate fraction can be channelled to the desired outlet. The number of outlets is not limited to the two shown in Figure 1.

The bistable element, or valve, is one in which one outlet or the other contains the entire main stream. To be truly bistable the main stream flow, when established in one leg, should stay there without a continuing flow of control fluid. A bistable valve is not always held to this requirement, often because the atmosphere serves as the control fluid so that continuous injection is no handicap. It is also possible that outside the atmosphere the vacuum of space may provide control, by suction instead of blowing. In this case too the bistable valve does not need to be strictly bistable. Note too that if the two dimensional layout of Figure 1 is not held to, a tristable valve is a possibility.

Both types of valve have advantages when applied to controlling combustion chamber bleed gases for thrust vector control. However, it has been found that in ducting solid propellant exhaust gases

*Figures appear on pages 213 through 216.

the greatest difficulty is found where the suspended particles of aluminum oxide impinge on the walls. Since in the proportional amplifier the main stream and its suspended particles impinge on the splitter, this difficulty has been considered to disqualify it, and only the bistable valve has been considered. But this conclusion is not final, and much of what follows refers with small modification to the proportional amplifier as well as to the bistable valve.

3. APPLICATIONS TO TVC

Consider the bistable valve then. It can direct the gas flow to one or the other outlet, but it cannot shut it off. This feature suggests the two system configurations shown in Figure 2.

In the two-sided system, fluid is injected into the nozzle continuously, whether or not steering is required. Unless the full available side force is needed, the thrust vector oscillates in a region enclosing the desired direction. The result is that more than the minimum injectant flow is used. This excess injectant is not completely wasted, since in most cases (depending on the main nozzle divergence angle at injection) the side force has an axial component; but neither is it used efficiently. The advantage of this system is that the back pressures seen by the valve do not vary with altitude. The back pressures appear to be equal but in reality are not so, since as flow is established in a leg a shock is formed in the main nozzle, increasing the back pressure. Even so, the back pressure inequality thus formed is less than that which can occur in the one-sided system.

The one-sided system (Figure 2b) eliminates the losses caused by constant injection into the nozzle. When no control is needed, this configuration exhausts the control fluid axially through what is essentially a smaller replica of the main nozzle. The resulting thrust per unit weight flow is the same, except for duct friction losses. The difficulty with this system is the large back pressure difference, especially at high altitudes; in addition, the outside leg back pressure varies with altitude.

We next consider in detail the operation of each of these systems, including the operation of the bistable valve.

4. STEADY FLOW IN A BISTABLE VALVE TVC SYSTEM

Figure 1 shows a schematic two-dimensional bistable valve in operation. The flow shown is inviscid; actually the "free surface" is the center of a mixing region, but at the moment this is not considered. For the flow to remain in leg II, the pressures on either

side of the free surface must be equal. In addition, if the streamlines are curved as shown, there must be a pressure gradient normal to the streamlines and to the free surface which is itself a streamline, with the pressure higher above the free surface than below it.

Now assume leg I leads to an injection port in the main nozzle located where the local undisturbed Mach number is M_N , and $M_N > 1$. Also neglect the back pressure in II. Then this model represents both the two-sided and one-sided systems; if the latter, the flow is exiting through the thrust nozzle.

Since the flow through this valve and the flow in the main nozzle both originate in the combustion chamber, they have the same total pressure (neglecting differential friction effects). If both the flow in I and the control flow are small, the pressure in I is that of the main nozzle, that corresponding to M_N . This is the pressure above the free surface; since the pressure below must be the same, we have the important result that at least part of the flow in the valve, that below the free surface, must be supersonic, at Mach number M_N .

The requirement of supersonic flow next to the free surface causes a revision of the valve design. The result is shown in Figure 3. The symmetry of Figure 3 indicates that it is applicable only to the two-sided system, since whichever leg the flow is in, the Mach number at the free surface is M_N . It is clear from the discussion above that in the one-sided configuration with flow into the nozzle, the pressure at the free surface is the ambient pressure P_∞ (or the base pressure, which is somewhat less). The resulting two-dimensional configuration resembles Figure 4. This valve is asymmetric so that the free surface Mach number is M_N when the flow is providing thrust and M_∞ (the Mach number at which the main nozzle flow is fully expanded to ambient pressure) when the flow is providing side force. In all cases of interest, $M_\infty > M_N$.

4.2 Flow in Outlet Ducts

Flow in the valve outlets has been shown to be supersonic. It is now necessary to deliver this flow to the injection port or thrust nozzle. In the two-sided system, outlet duct lengths are of the order of the main nozzle diameter. In the one-sided system they can be much shorter; with proper design, the thrust nozzle can be just an extension of the valve, while the duct to the injection port may perhaps be made sufficiently short to make frictional effects negligible. We now consider the problem of the relatively long ducts implied by the two-sided system.

The entering flow is supersonic. A boundary layer immediately starts to form where the flow attaches to the splitter; on the other three walls a boundary layer already exists. The flow is decelerated and turned slightly towards the duct center by the boundary layer growth. These effects cause oblique shocks to form. When a shock extends to the boundary layer, separation or boundary layer thickening occurs, since the higher downstream pressure is felt upstream of the shock through the subsonic part of the boundary layer. This separation or thickening produces more shocks.

The result of this process is that the originally supersonic flow decays to subsonic in a distance that for a straight tube is of the order of ten tube diameters. The end states of this process are related approximately by the normal shock equations. The difference is that wall friction occurs here and not in the normal shock; but since the boundary layer is thick or separated in the region where deceleration occurs, the wall friction is not very important.

In the configurations considered here some duct curvature will be necessary. The effect of this is to increase the rate of boundary layer growth and its tendency to separate in locations such as the inside wall of a bend. The net effect will be to decrease the length of tubing in which the transition from supersonic to subsonic flow takes place.

Thus it seems probable that in a TVC system using a bistable valve the injectant total pressure will be less than the main flow total pressure by a factor equal to the total pressure drop across a normal shock at a Mach number slightly greater than M_N (for the two-sided system) or M_{∞} (for the one-sided system).

4.3 Effects of Injectant Total Pressure on Side Force

It turns out, however, that the injectant total pressure loss may actually improve the performance of the system. A considerable body of experimental data exists to indicate that, for sonic injection and a constant injectant mass flow, the side force goes up as the injectant pressure goes down (References 1-3 are typical; 4 contains a summary). As P_{0i}/P_{0N} approaches one, the side force drops off again. This is shown in Reference 5, which seems to be the most complete work available in the range $1 \leq P_{0i}/P_{0N} \leq 50$. In this reference the most complete data are for CO_2 injectant. The results shown in Figures 5 and 6 should therefore be considered to indicate trends, rather than as absolute values. Figure 5 shows the effect on side force of injection of chamber bleed gas for a range of values of M_N . For $M_N > 2$, passing the injectant through a shock at M_N increases the side force. At $M_N = 3$, the increase

is about 25%.

These results are only strictly true for small injectant mass flows, compared with the main flow. It is found in Reference 5 that as the injection port diameter goes up, the side force goes down. This is shown in Figure 6. If the injectant total pressure has been lowered, the injection port diameter must be increased to pass the same mass flow. At large injectant mass flows the net result can be a drop in side force. As an example, consider the case tested in Reference 5, $M_N = 2.34$. After a normal shock at this Mach number, $P_{OJ}/P_{ON} \approx 1/2$; thus d_1/d^* is about twice the value required if no shock occurs. Neglecting the dependence of Figure 6 on P_{OJ}/P_N , Figure 7 results.

In view of the result that a maximum side specific impulse is achieved in the range of $1 \leq P_{OJ}/P_N \leq 10$, it may be a waste of time to consider the possibility of getting better pressure recovery than that through a normal shock at M_N . In case it does appear useful (see below), better pressure recovery seems possible by using the methods developed for supersonic air intakes to ramjets or turbojets. In these intakes, a system of weak oblique shocks slows the flow to low supersonic speed, where a normal shock is induced. The principal difficulty in using this method as a diffuser for a bistable valve outlet is that in the supersonic inlet the boundary layer generally starts at the inlet and is thin throughout. In the bistable valve a relatively thick boundary layer may exist on at least three sides of the outlet tube, at the diffuser inlet. Nevertheless, this type of deceleration shows promise if higher injectant total pressures appear useful.

This might happen if injection at Mach number greater than one is used. It is conjectured in Reference 4 that if higher than optimum injectant pressures are available, the best way to drop the pressure would be to have supersonic rather than sonic injection. Experimental data quoted in (4) does not seem to justify this, however.

5. CONCLUSIONS

1. A bistable valve for use in a TVC system must be designed for supersonic flow in the valve body and outlet legs.
2. The outlet flow will, in some cases, undergo deceleration by the equivalent of a normal shock before injection.
3. The losses involved in this process may act to increase the force per unit injectant mass flow.

REFERENCES

1. Strike, W. T., F. J. Schueler, and J. S. Deitering, Interactions Produced by Sonic Lateral Jets Located on Surfaces in a Supersonic Stream, AEDC Technical Documentary Report AEDC-TDR-63-22, dated April 1963.
2. Vinson, P. W., J. L. Amick and H. P. Liepmann, Interaction Effects Produced by Jet Exhausting Laterally Near Base of Ogive-Cylinder Model in Supersonic Main Stream, NASA Memo. 12-5-58W, dated February 1959.
3. Amick, J. L., G. F. Carvalho and H. P. Liepmann, Interaction Experiments of Lateral Jets with Supersonic Streams, University of Michigan, IP-361, March 1959.
4. Kallis, J. M., and M. Adelberg, Recent Advances in the Fluid Dynamics of Gas Injection for Thrust-Vector and Trajectory Control, Aerospace Corporation Report No. ATN-63 (3305)-3, July 1963.
5. Walker, R. E., A. R. Stone and M. Shandor, "Secondary Gas Injection in a Conical Rocket Nozzle," AIAA Journal, Vol. 1, No. 2, February 1963.

NOMENCLATURE

d_j	=	Injection port diameter
d^*	=	Main nozzle throat diameter
F_s	=	Side force
I_s	=	Side specific impulse, F_s/\dot{W}_j
I_s^*	=	Side specific impulse assuming a sonic jet exhausting into a vacuum
M_N	=	Mach number of the undisturbed flow in the main nozzle at the injection port
M_∞	=	Mach number at which main nozzle flow static pressure equals ambient, $P_N = P$
P_N	=	Pressure of the undisturbed flow in the main nozzle at the injection port
P_{oj}	=	Injectant total pressure
P_{on}	=	Main flow total pressure
P_∞	=	Ambient pressure
\dot{W}_j	=	Injectant weight flow
\dot{W}_{Main}	=	Main nozzle weight flow

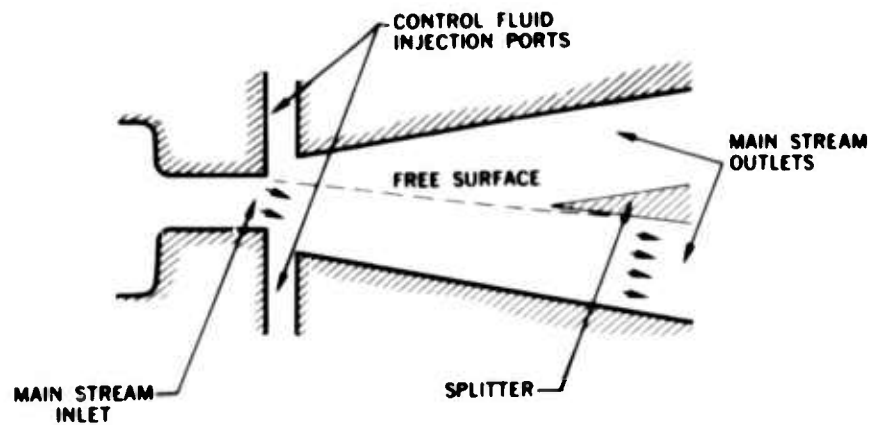


Figure 1. Schematic of a Pure Fluid Valve

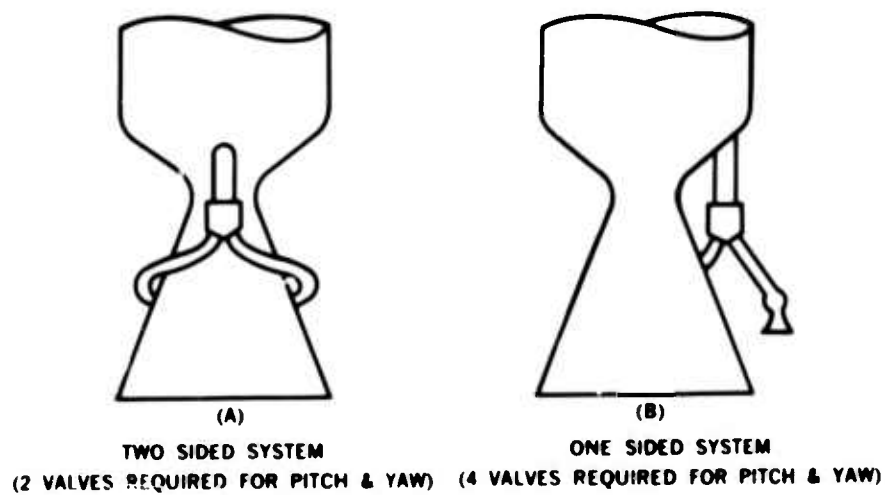


Figure 2. System Configurations Using a Bistable Valve

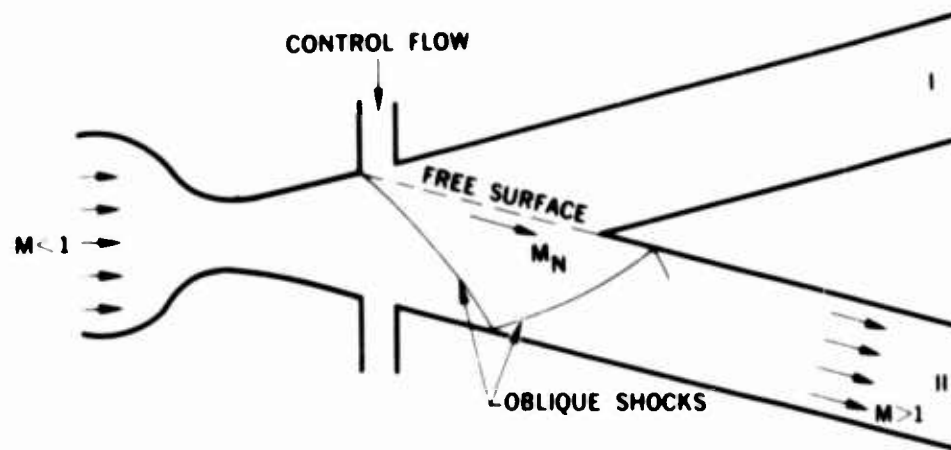


Figure 3. Supersonic Bistable Valve

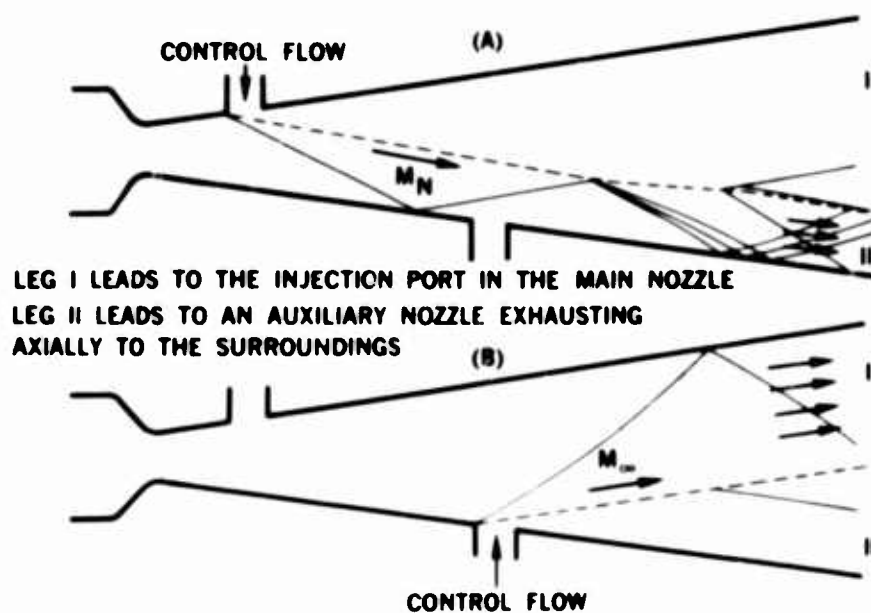


Figure 4. An Asymmetric Bistable Valve for use in a One-sided System

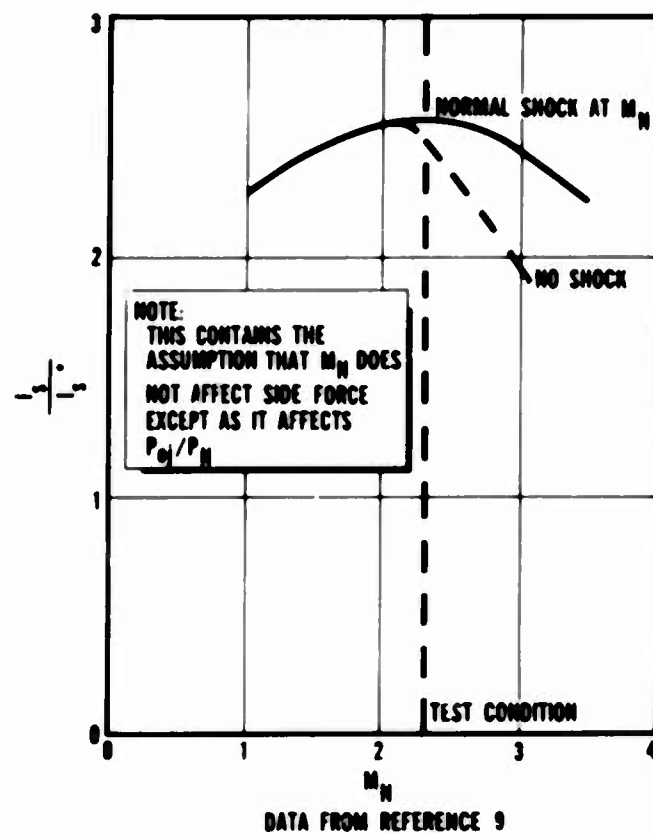


Figure 5. Effect on Side Force of Losses From a Normal Shock in Injectant

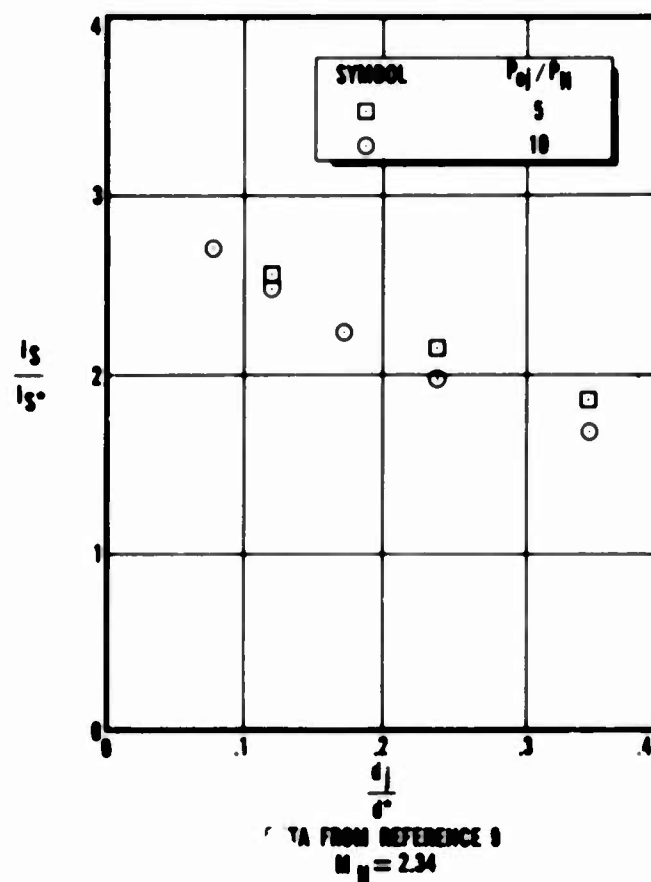


Figure 6. Effect on Side Force of Injection Port Diameter

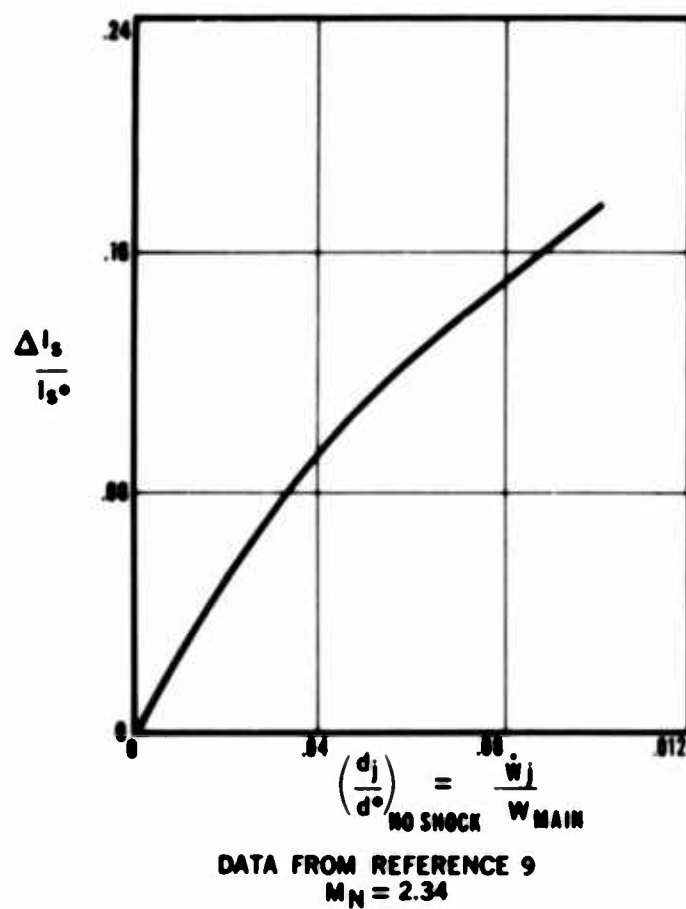


Figure 7. Effect on Side Force of Injection Port Diameter Increase Required if a Normal Shock Occurs in the Injectant

EXPERIMENTAL STUDY OF FLUID CONTROLLED VALVES

D. W. Harvey and R. P. McRae
Missile & Space Systems Division
Douglas Aircraft Company, Inc.

ABSTRACT

This report presents the results of a cold flow test program in which the flow in a supersonic bistable valve was investigated. Two different final valve configurations were developed that worked well under identical conditions, but the flow in one was quite different from the other.

Shadowgraphs of the flow are presented for most stages as the designs evolved. The effects of variation of valve design parameters are shown. Flow visualization and static pressure results are given for the two final valve configurations.

Some implications of these results are discussed, and future work is outlined.

CREDIT

Work presented herein was conducted by the Douglas Aircraft Company, Inc., Missile & Space Systems Division, under company-sponsored Research and Development funds.

1.0 INTRODUCTION

In recent years, the fluid amplifier principle developed at Diamond Ordnance Fuze Laboratories (now Harry Diamond Laboratories) has been considered for many applications (see e.g. References 1-4). This report considers the use of the fluid amplifier as a fluid controlled hot gas valve in a secondary injection TVC system using chamber bleed gas.

The operation of the fluid-controlled valve can be illustrated by considering the simplified valve shown in Figure 1.* Fluid from a high-pressure source flows through a nozzle throat and is expanded to a pressure lower than the back pressure in the outlet legs. At a downstream point where the main flow pressure is low enough, the main flow separates from one wall or the other. Now, because of the equality of pressure in the separated region and in the flow just above it, the flow on the separated side of the valve is raised to nearly the back pressure, while the flow at the wall on the attached side has been expanded to considerably below this. The resulting pressure gradient turns the main flow towards the attached side, where it is stable.

The introduction of a jet of control fluid on the attached side disturbs this pressure gradient, separates the main flow from the wall to which it was attached and impels it towards the opposite wall. If the control jet mass flow or momentum is large enough, the main flow will become attached to the wall opposite to the control jet, completing the switching process. This type of valve is called "bistable". In it the flow is always entirely in one leg or the other, except for the very short periods of actual switching. If the walls are cut away to prevent attachment, the main stream can also be deflected and held by control jet momentum alone. Such a valve is called a proportional amplifier. This paper considers only the bistable valve, first because it requires less control fluid, and second because in the proportional amplifier the nose of the splitter is almost constantly immersed in the stream of hot, particle-laden fluid.

Pressure considerations indicate that in TVC applications the flow within the valve must be supersonic at least upstream of the splitter (Reference 5). It also seems reasonable to hope that supersonic flow in the valve would decrease the sensitivity to back pressure found in subsonic valves. For the above reasons, only supersonic, bistable valve elements are considered in this report.

*Figures appear on pages 232 through 254.

2.0 OBJECTIVES

The objective of this experimental program is to develop sufficient knowledge about the flow in a bistable valve so that the feasibility of the use of such a valve in a chamber bleed TVC system can be evaluated and so that, as far as possible, design techniques can be established.

The present state of knowledge in this area is such as to require experimental attack. Some of the questions that require experimental answers are: What is the mechanism involved in switching? Can a satisfactory prediction of valve operation be obtained in terms of inviscid flow theory? In connection with fluid mechanical aspects of the TVC application, what are the effects of downstream influences, like varying back pressures and throats on the outlet legs, and what pressure recovery can be expected? And since in operation the valve must carry solid propellant exhaust gases, what particle impact and heat transfer rates can be expected, and what will the resulting erosion do to valve operation?

3.0 EXPERIMENTAL APPROACH

In order to approach these objectives, it was first necessary to obtain a working valve on which to experiment. This phase is the subject of this report.

The work done at Redstone Arsenal (Reference 1) was used as a starting point. Some of the first designs used in this report were based on those of Reference 1, except that control port location was determined somewhat differently. As the designs of Reference 1 evolved the control ports were moved to regions of lower pressure, until satisfactory operation was attained with the control ports located at a point where the main stream pressure (by a one-dimensional calculation) was 10 psia.

In the work reported here it was considered desirable (though not imperative) to evolve designs that could be switched by opening the control port to the atmosphere, instead of by introducing control fluid at some higher pressure. The control port was located at the point where the static pressure behind a shock sufficient to turn the main flow by twice the wall half-angle (i.e. parallel to the opposite wall) equals atmospheric, again by a one-dimensional calculation. The results of a typical calculation, this one for a main flow total pressure of 100 psia, are shown in Figure 2. (This method was not always followed exactly; in some cases a different location was used, for convenience or to follow Reference 1.)

3.1 Test Facility

All tests to date have been conducted at the Fluid Mechanics Facility of the Douglas Aerophysics Laboratory. The working fluid was air drawn from a 125 psia supply. In cases where the control pressure was greater than ambient pressure, air was drawn from the above supply and regulated to the desired pressure. Control fluid injection "on-off" control was provided by two solenoid valves. No attempt was made to closely control the duration of control fluid flow or the frequency of switching.

A schematic of the test setup is shown in Figure 3. As can be seen in the figure, the test model was mounted in a sound proof, dark room. All test operations, such as control fluid injection, pressure regulation, and data gathering, were controlled from outside the room. The use of the small room eliminated noise problems and also made it much easier to take shadowgraph pictures of the valve flow fields.

The high pressure air supply is piped from the source tanks to the Fluid Mechanics Facility in standard 4" pipe which is reduced to one inch tubing at the main control valve.

Initially, the control flow system used 0.50 inch tubing between the upstream supply and the solenoid control valves with 0.125 inch flexible tubing between the solenoid valves and the model. After some measurements were made of the pressure in the control ports with 60 psia control pressure, the 0.125 inch tubing was changed to 0.25 inch tubing. This was done between runs 63 and 64.

The 1" tubing upstream of the valve was about 32 inches long and was fitted with screens to straighten and smooth the flow at the model entrance. This apparatus was added between runs 39 and 40, when it had become apparent that flow entering the valve was neither smooth nor uniform.

3.2 Associated Equipment and Test Techniques

Data presented herein includes shadowgraphs of flow in the valve, wall flow visualization pictures, and pressure profiles.

Shadowgraph pictures were taken with a 4 x 5 Polaroid camera back, mounted into a remote-controlled shutter system. An Avco spark unit was used as a light source. The test model was mounted in the darkroom and the desired test conditions established. The shutter was then opened and the spark source triggered. The system is shown in Figure 3.

Pictures of the flow at the valve walls were obtained by coating the model inner walls with a mixture of fluorescent oil and vaseline. During air flow, the mixture assumes the flow pattern at the wall. The model is illuminated by ultraviolet light and photographed while the air is flowing. As was the case for the shadow-graph pictures, Polaroid film was used to give a quick look at the data.

All pressure measurements are of static pressure, taken at the wall of the two best valve designs. In both cases a total of forty pressure taps were fed into a fifty port Scanivalve which changed the pressure readings to an electrical output by means of a single 0-50 psia transducer. These electrical outputs were recorded on a Leeds-Northrup strip chart recorder.

3.3 Test Model Hardware

Two types of bistable valve designs have been considered, the two-dimensional valve and the valve with axisymmetric nozzle and two-dimensional body. The flow field of the two-dimensional valve will yield a much shorter and more compact design for any given chamber pressure, because of the greater increase in area per unit axial length.

A total of ten valve models have been tested with some variation of basic valve design parameters in each model. The design parameters were varied independently in each model to determine their influence on valve stability and switching. These parameters are defined in Figure 1. They are:

1. Nozzle half angle
2. Valve body and splitter half angle
3. Splitter location
4. Control port location
5. Control port dimension and shape
6. Setback

In most cases, the nozzle half angle, the body half angle, and splitter half angle were varied in combination rather than independently. Nozzle half angles less than, equal to, and greater than the body half angle were considered. In all cases the body half angle and splitter half angle were equal.

In all of the models tested, the nozzle convergent section was axisymmetric. Initially this convergent section was conical, with zero radius of curvature at the throat. Problems which arose

during testing of the first models seemed to be caused by a non-uniform flow field at the model entrance. Therefore, a longer section of straight pipe with screens was added upstream of the model and the nozzle convergent section was contoured to provide a better transition past the throat. The throat diameter for all models with two-dimensional nozzle divergent sections was 0.50 inch and for the axisymmetric nozzles was 0.60 inch. A half inch diameter throat was tried for the latter models but provided too great an expansion ratio to be used with the existing chamber pressure. Two injection port shapes, slots and circular holes, of various dimensions were tried.

All model parts, nozzles, valve bodies, splitters, and control fluid injection systems, were fabricated from plexiglass or aluminum. For visual observation of the flow field, the two-dimensional portion of each valve was sandwiched between two 0.50 inch thick sheets of plexiglass.

Sketches of the valve models tested are shown in Figures 4 through 13. The valve numbering system is defined in Appendix I.

The test results are presented and discussed in the next section.

4.0 EXPERIMENTAL RESULTS

Several parameters have been used to differentiate between designs and to grade valve operation. For each run, the nozzle half angle, valve body half angle, setback distance, splitter location, main flow total pressure (chamber pressure) and control pressure are given with the cited figure. Test success was based on a qualitative assessment of several factors: stability of flow in either outlet leg, division of flow between legs, switching ability, and reproducibility of results. The control pressure is the pressure at the control fluid regulator (see Figure 3) and not the pressure at the injection port.

4.1 Design Evolution Using Shadowgraph

The first design tested was 1113. In this design (Figure 4), the body blocks and splitter were contoured like the nozzle. Several nozzle-body half angle combinations (15° - 15° , 10° - 10° , and 10° - 15°), splitter locations, and setback distances were tried. A few partially successful runs were made with this design in which approximately 90% of the main flow could be made to flow in either outlet leg and could be switched from leg to leg. In most runs, though, the main flow either attached itself to one of the outlet leg walls (almost always the top leg) and could not be separated or was about

equally divided between the outlet legs. The test results were not reproducible from one assembly of the test model to another.

During testing of this model, it was noticed that somewhat better results were obtained with the splitter nose dropped about 0.100 inch below the valve centerline. It was therefore thought that at least part of the problems with this design were due to asymmetry and some bluntness of the contoured splitter. Two methods were used in an attempt to overcome this problem. First, a new set of wedge shaped splitters with sharp pointed nose and flat walls were fabricated (design 1213); second, the nose of the contoured splitters were ground sharp and the walls faired back into the contoured cross section (design 11B13).

Design 1213 was clearly an improvement since switching was satisfactory except for the farthest downstream splitter location. However, still on the order of 10% of the main flow was in the supposed non-flow leg. When the flow could not be switched, it again favored the top leg.

Design 11B13 was not a noticeable improvement over 1113. Again the top leg was favored. In an effort to explain this the nozzle blocks and control ports were reversed. Now the bottom leg was favored.

The design of the control ports on all valves tested so far was such that some asymmetry in assembly could hardly be avoided. It was observed that separation and a shock induced by it occurred at the control port on both sides. This was somewhat unexpected, since the operation of a bistable valve is often discussed in terms of the flow attaching to one wall. It was therefore thought that improving the control port design might both improve switching performance and decrease the flow asymmetry mentioned above.

Valve design 1222 used circular instead of slot injection ports to decrease disturbance of the main flow by the control ports and to provide a comparison of the two types of ports. Test results for valve design 1222 were similar to those for the previous models in that the flow attached itself to one outlet leg wall (again the top) and could not be switched.

At this point the straight section described in Section 2.1 was added upstream of the valve. This upstream section was used in all successive runs.

In the next runs flat-faced body walls and splitter were used with slot and circular (13C22) ports. In both cases the flow chose upper and lower legs more nearly at random, indicating that the

straight upstream section was an improvement. The flow could be switched but a high control pressure was required.

At this point a longer convergent section was added. The wall was smoothly contoured to axial at the throat. This convergent section was used in all successive runs, and the valves using it are numbered 1AXXX and 2XXX. Several reruns of previous runs were made but no improvement was noted.

When greater care was taken to minimize the size of joints in the walls, the flow did not separate as soon on the "attached" side. For this reason one-piece sides were built. These valves were numbered 1A4XX.

The first runs were made with no control ports at all (1A430). Separation occurs on the "attached" side, but far enough downstream so that it can probably be said to be caused by the effect on the wall boundary layer of the main deflection shock. Flow visualization studies done later show that the separated region terminates a short distance downstream. This lends credibility to the conjecture that it is caused by the main deflection shock.

After these tests, circular 1/8 in. diameter control ports were drilled into the walls. This gave design 1A422. The main stream could be started in either outlet leg by prior application of control flow, but once started could not be switched. When a partial blockage was introduced at the outer walls of each outlet port the flow could be switched from leg to leg. This blockage was caused by plates at the outlet exits which protruded into the stream. The effect was apparently to raise the pressure along the outlet leg walls and increase separation of the main stream.

At this point it was decided to measure the control pressure at the control ports. The results cast considerable light on the switching problem. It was found that with no control flow the static pressure in the control port was 5 psia. When control flow measuring 60 psia at the regulator was turned on, the static pressure in the control port rose to 7 psia. As a result, the control system was reworked and all 1/8 in. tubing was replaced with 1/4 inch. All subsequent tests used this reworked control system and all previous models were retested with this system. The test results with the first five valve designs were not greatly affected by this increased control flow rate, but it did cause a reduction in control pressure for design 1A422.

In order to study the effect of control port shape, the circular 1/8 in. diameter control port on one side of 1A422 was cut out to form a 1/8 in. wide slot. The circular port was left on the other side of the valve. This configuration was 1A4(21)2. When the control pressure was lowered to 25 psia the valve would only switch towards the circular port, never towards the slot.

After this result, a similar slot was cut in the other side. This was design 1A412. This valve switched well at a control pressure of 25 psia, and the internal flow seemed fairly well-behaved, with the exception of the shock and apparent separation on the attached side, Figures 14 and 15.

At this point the direction to take for further improvement was not evident. It was decided to test a design (200X) that was somewhat different. This was based on a design with which success had been obtained at AMC (Reference 1). Valve design 2513 had an axisymmetric nozzle and a two-dimensional valve body. The body wall sections were contoured by cutting a one-half inch radius semi-circle at the inner surface. The splitter was a sharp pointed, flat walled wedge. Slot injection ports of various widths (one-quarter, one-eighth, and one-sixteenth inch) were tried. Successful bistable operation and switching were obtained with this valve design. Best switching was obtained with a control port width of one-eighth inch. Here the atmosphere was used as control fluid. Switching was not possible with the smaller width slot and the larger width seemed to cause a large flow disturbance even without control flow.

From the shadowgraphs of the flow field of this valve design (Figures 16 and 17) it was seen that a normal shock exists across the center of the flow downstream of the nozzle exit. The distance from the nozzle exit to this normal shock was dependent upon the splitter location. To provide better visual observation of the valve flow field, model design 2612 was built with flat body walls and the best port width. Successful bistable operation and switching were obtained with valve design 2112, although higher than ambient pressure control flow was required. The flow is shown in Figures 16 and 17.

4.2 Flow Visualization

Work to date had resulted in two fairly satisfactory valve designs, 1A412 and 2612. The flows inside them, as shown in shadowgraphs, are quite different. While 1A412 was evolved by trying to keep the flow attached on one side as far downstream as possible, the flow in 2612 seemed by the shadowgraphs to be separated all around. This

made it seem desirable to find out more about the flow next to the wall. This was done using a mixture of vaseline and fluorescein dye, which was painted on the inner wall of the valve. The results can be seen in Figures 18-21.

Wall flow patterns in design 1A412 can be seen best in Figures 20 and 21, which show respectively conditions without and with control flow. These tests used the models with which pressures were measured. The taps are clearly visible and make it easy to compare pressures with wall flow. It should be remembered in looking at these figures that the presence of the side walls makes the flow truly three-dimensional, and also that the patterns seen are not in the free stream but in the side wall boundary layer. This is what allows the main deflection shock to show up in Figure 20. The main deflection shock causes a local separation or thickening of the side wall boundary layer, and the indicating fluid collects there. (That this is really the main deflection shock is shown both by comparison with shadowgraphs and by pressure measurements, of which more later).

Both figures show clearly the separated region on the "attached" side. By comparison with the location of the main deflection shock, it is evident that this region is caused by impingement of the main shock. Both figures show also that the main shock turns the flow too far; its reflection from the wall turns the flow back to parallel the wall. This is expected.

It is not known why the main deflection shock shows up only in Figure 20, but it may be because it moves downstream in the absence of control flow and thus becomes stronger, and so has more effect on the side wall boundary layer. The jog shown just downstream of the valve centerline is not easily explained. The horseshoe-shaped region is apparently caused by the interaction between the main deflection shock and the shock off the separated region. In Figures 14 and 15, shadowgraphs for the same configuration are shown with and without control flow. With control flow (Figure 15) the shocks cross cleanly and there is probably no slip surface from the point of crossing. Without control flow an approximately normal shock region seems to exist where the main and separation shocks interact. Strong vortex sheets extend downstream of the edges of the normal shock region, with quite different velocities on either side (subsonic behind the normal shock, supersonic behind the oblique). The arms of the horseshoe are probably the regions of interaction between the vortex sheet and the side wall boundary layer. They do not extend far downstream because the velocity discontinuity is quickly broken down by viscosity.

The wall flow in design 2612 is not as enlightening, as the main flow is separated from the side walls. The flow is so strongly three-dimensional that attachment is not easy to locate. In the critical region between the control ports and the splitter, very little light is shed on the deflection mechanism.

4.3 Static Pressure Surveys

Static pressure measurements were made in both valve designs. The results are shown in Figures 22-29. The approximate location of the beginning of the shock structure is also shown in these figures.

An interesting feature can be seen in the surveys of design 1A412 without control flow. Following the pressures along the valve centerline, the fifth tap (reading downstream) reads considerably lower than the fourth or sixth. This result was reproducible. The position of the shock as shown by the shadowgraph would lead one to expect a sharp rise in pressure at or near the fifth tap but no sharp drop in front of it. However, recall that in the corresponding wall flow (Figure 20) there is a jog in the main deflection shock indication just downstream of the fourth tap. It is conjectured that the same thing that causes this jog also causes the pressure to behave as it does. It is not clear what this cause might be, especially since nothing shows up on the shadowgraphs in that region.

The surveys of design 2112 show no corresponding anomaly, but one indication may need some explanation. In all cases the tap above (not in) the control port indicates a pressure approximately equal to that in the control port. There is a temptation to believe this means the flow is separated that far out from the control port, and that this in turn means the flow is separated upstream almost to the throat. This is probably not the case. This tap is just downstream of the abrupt transition from circular to rectangular cross section and, since it is not on the centerline of the side where the circle is tangent to the rectangle, it is behind a downstream-facing step. It is thus in a separated region, but one which remains near the wall and does not extend upstream beyond the cross-section transition.

5.0 CONCLUSIONS

An experimental study of the flow in a bistable fluid controlled valve is outlined. Data including shadowgraphs, wall flow visualization pictures, and pressure surveys for two workable designs are presented. Shadowgraphs for all the valve designs which were tried during this study are available in Reference 6.

Two quite different valve configurations have been developed experimentally that work well under substantially identical conditions.

This implies the probability that neither configuration is near optimum, and so the conclusions that follow are only tentative.

It was found to be helpful for the entering flow to be smooth. The amount of smoothness required was not found. This question will be important in TVC applications. It can be conjectured that symmetry of the entering flow about the plane of the outlet legs is not as important as symmetry about the plane that intersects the plane of the outlet legs at right angles along the valve centerline.

Slot type injection ports were found to work better than circular ports. Slot widths smaller than those used successfully elsewhere (References 1 and 4) were found to work quite well. The injection ports were initially located so that the pressure downstream of the main deflection shock would be ambient when the flow is turned through an angle equal to twice the nozzle half angle. As can be seen by comparing shadowgraph pictures of valve design 1A412 with and without control flow, the main deflection shock moves downstream when the control flow is turned off. It is not clear what this indicates about port location.

Nozzle half angle seemed to affect valve operation only in that it controls the nozzle length necessary to obtain a given expansion ratio. The combination of nozzle and body half angles proved quite important, with best results obtained with body angle larger than nozzle angle. This was true in the models which were fabricated in several parts and did not hold for the model with one piece construction. This difference in angle may tend to cause local boundary layer thickening and thus partially eliminate the effect of wall irregularities due to the multi-piece construction. Design 1A512 which had one piece walls seemed to bear this out.

Setback had a similar effect. It improved operation with the multi-piece walls in the two-dimensional design, but was clearly not essential with the one-piece walls. The local separation induced by setback probably decreases the effect of irregularities in the wall.

For each valve design tested, the range of splitter locations for which successful operation was obtained proved to be quite limited. This was especially true in the 2XXX designs, where movement of the splitter upstream or downstream greater than one-tenth inch from optimum caused the flow to divide on the splitter or lock into one outlet leg. The thinner, two-dimensional models were not as sensitive to splitter location but proved to be much more sensitive to wall irregularities.

6.0 PLANS FOR FUTURE WORK

Many important aspects of bistable valve operation have been left out of consideration in the work of this report. Tentative plans for future work include a systematic investigation of the switching process, including the effects of control pulse duration and frequency, control mass flow and momentum, and port location. It is also planned to investigate conditions imposed by the TVC application, including the effects of back pressure asymmetry and variation with time and flow rate, and the effects of putting throats in the outlet legs. Finally, the environmental aspects of TVC usage will be studied, by using the methods presented in Reference 7 to predict erosion by convection and particle impact. This erosion will be added to the valve dimensions and the resulting configuration tested.

REFERENCES

1. "Experimental Design of a Fluid-Controlled Hot Gas Valve", U.S. Army Missile Command Report RE-TR-62-9, 13 December 1962.
2. Clayton, B. J., J. G. Williams and J. L. Byrd, "Development of Pure Fluid Missile Control System", U.S. Army Missile Command Report RG-TR-62-7 (Second Edition), 28 October 1963.
3. Byrd, J. L., W. A. Griffith, T. G. Wetheral, and J. G. Williams, "Development of a Pure Fluid Missile Control System", U.S. Army Missile Command Report RG-TR-63-31, 31 December 1963. Confidential.
4. Proceedings of the Fluid Amplification Symposium, Volume 1, Diamond Ordnance Fuze Laboratories, October 1962 (AD 297-935).
5. Harvey, D. W., Steady Flow in a Pure Fluid Valve TVC System, Douglas Report SM-45873, March 1964.
6. Harvey, D. W., and R. P. McRae, Experimental Evolution of Two Supersonic Bistable Valve Designs, Douglas Report SM-47668, July 1964.
7. Harvey, D. W., and R. P. McRae, Flow Studies in Propulsion System Ducting, Douglas Paper No. 2085, April 1964.

APPENDIX I

VALVE NUMBERING SYSTEM

A valve design is defined by four parameters. Numbers (sometimes followed by letters) designating these are combined as follows:

()₁ ()₂ ()₃ ()₄.

()₁ : Nozzle configuration

- 1 - Axisymmetric convergent section, two-dimensional divergent section
- 1A - New axisymmetric convergent section, two-dimensional divergent section
- 2 - Axisymmetric nozzle, two-dimensional body

()₂ : Internal configuration

- 1 - Contoured nozzle divergent section, control ports, body walls, and splitter
- 1B - Identical to 1, except that splitter nose is ground sharp
- 2 - Contoured nozzle divergent section, control ports, and body walls; flat-faced splitter
- 3 - Contoured nozzle divergent section; flat-faced control ports, body walls, and splitter
- 3C - Contoured nozzle faired to flat at ports
- 4 - Flat-faced one piece walls
- 5 - Contoured body walls; flat-faced splitter
- 6 - Flat-faced walls and splitter

()₃ : Control port configuration

- 1 - Slot
- 2 - Circular
- 3 - No ports

()₄ : Control port characteristic dimension (width of slot or diameter of circle)

- 0 - No ports
- 1 - .0625 in.
- 2 - .125 in.
- 3 - .250 in.

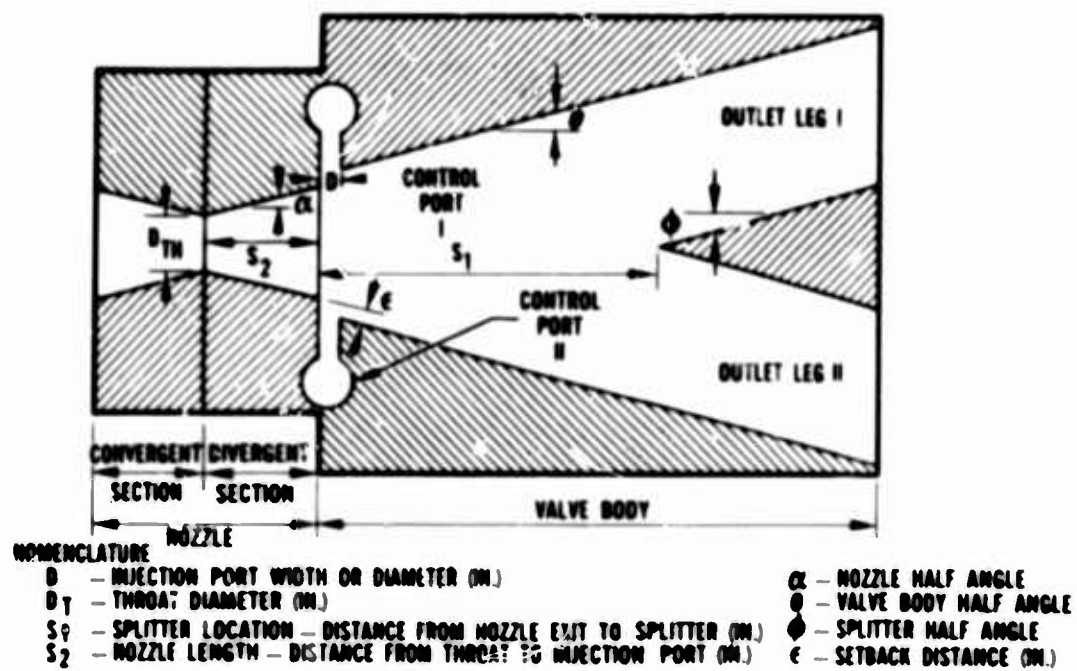


Figure 1. Valve Design Nomenclature

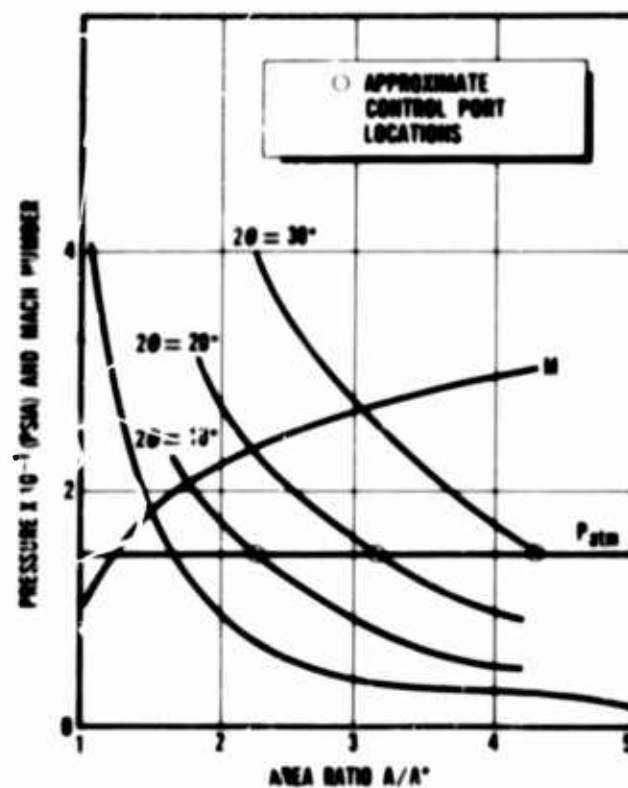


Figure 2. Method of Determining Control Port Location

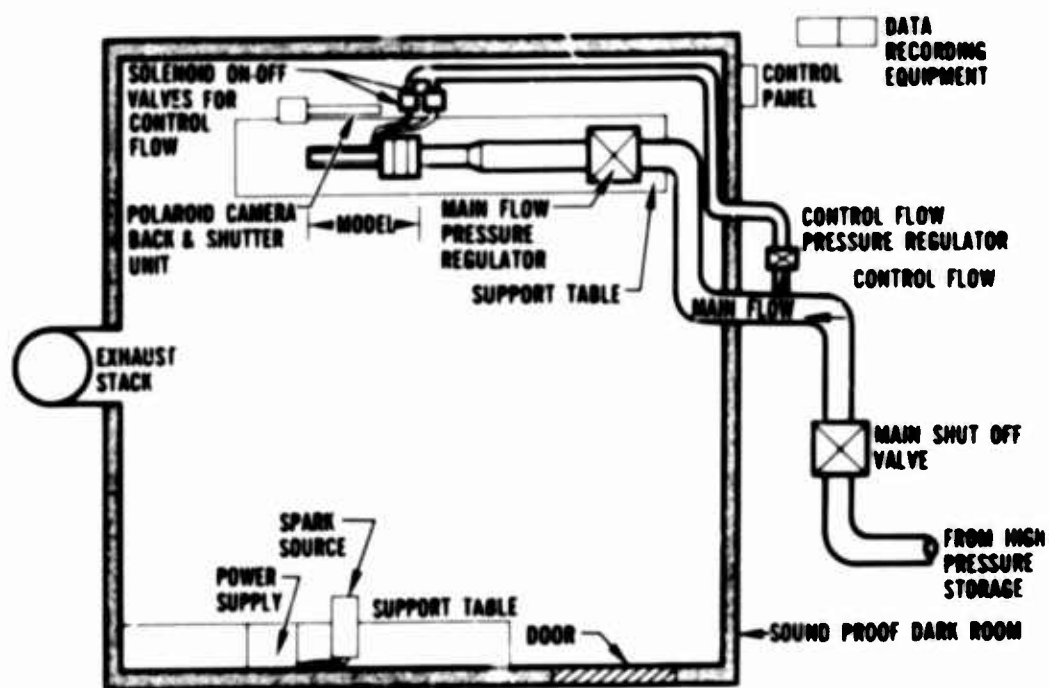
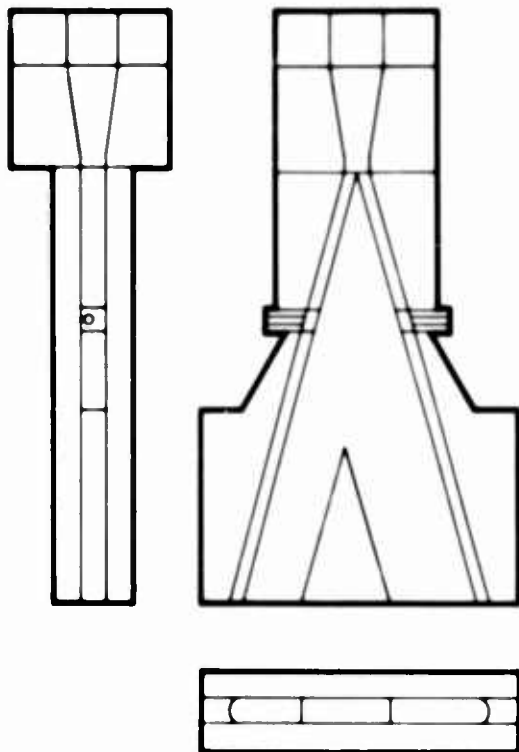
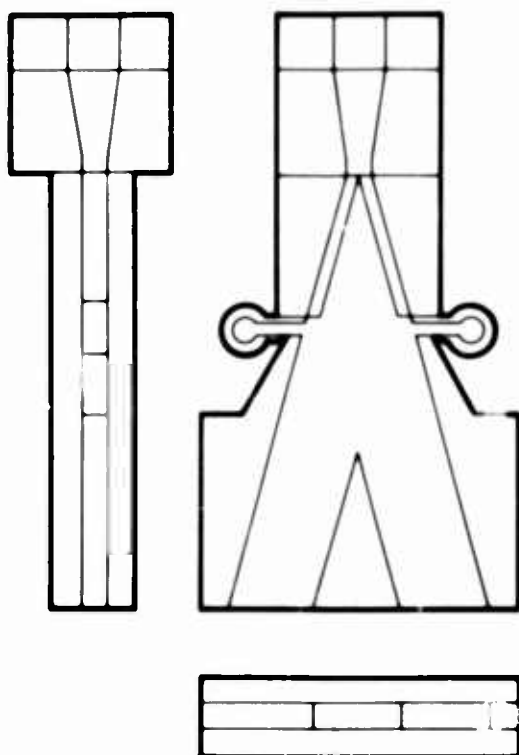


Figure 3. Test Setup



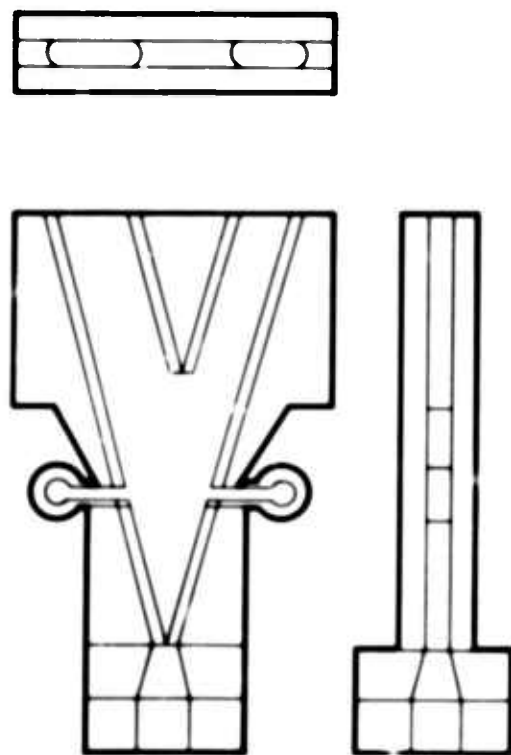
$D_T = 0.50$ IN.
 $\alpha = 10^\circ$
 $\theta = 15^\circ$
 $\phi = \theta$
 $S_1 = 3.625$ IN.
 $\epsilon = 0.100$ IN.
 $S_2 = 2.2$ IN.

Figure 6. Valve Configurations – Valve Design 1A222



$D_T = 0.50$ IN.
 $\alpha = 10^\circ$
 $\theta = 15^\circ$
 $S_1 = 3.875$ IN.
 ϵ WAS VARIED FROM 0 TO 0.090 IN.
 $S_2 = 2.2$ IN.

Figure 7. Valve Configurations – Valve Design 1A313



$D_T = 0.50$ IN.

$\alpha = 10^\circ$ AND 15°

$\theta = 10^\circ$ AND 15°

$\phi = \theta$

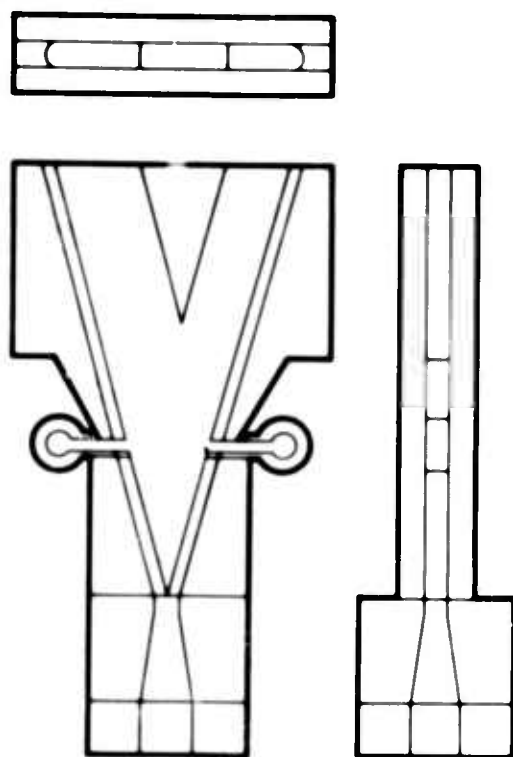
S_1 WAS VARIED FROM 2.875 IN. TO 4.125 IN.

ϵ WAS VARIED FROM 0 TO 0.150 IN.

$S_2 = 2.2$ IN. FOR 10° NOZZLE

$S_2 = 2.6$ IN. FOR 15° NOZZLE

Figure 4. Valve Configurations – Valve Design 1113



$D_T = 0.50$ IN.

$\alpha = 10^\circ$

$\theta = 15^\circ$

$\phi = \theta$

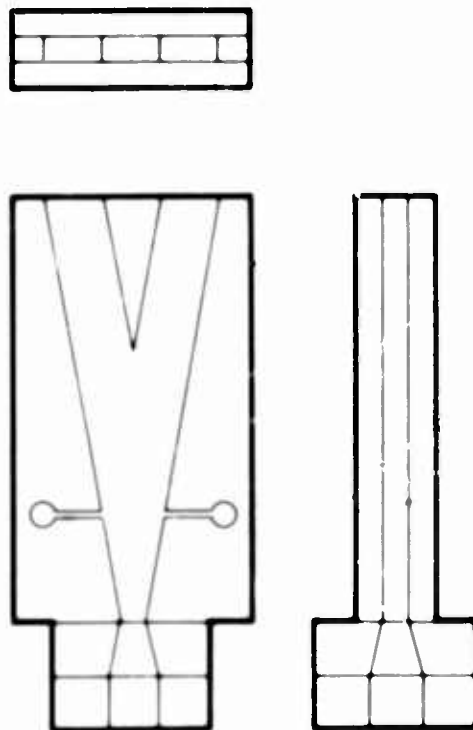
S_1 WAS VARIED FROM 3.625 IN. TO 4.625 IN.

ϵ WAS VARIED FROM 0 TO 0.120 IN.

$S_2 = 2.2$ IN.

THE LONGER CONTOURED NOZZLE CONVERGENT SECTION IS SHOWN IN THIS FIGURE AND FIGURES 5 AND 6.

Figure 5. Valve Configurations – Valve Design 1A213



$D_T = 0.50$ IN.

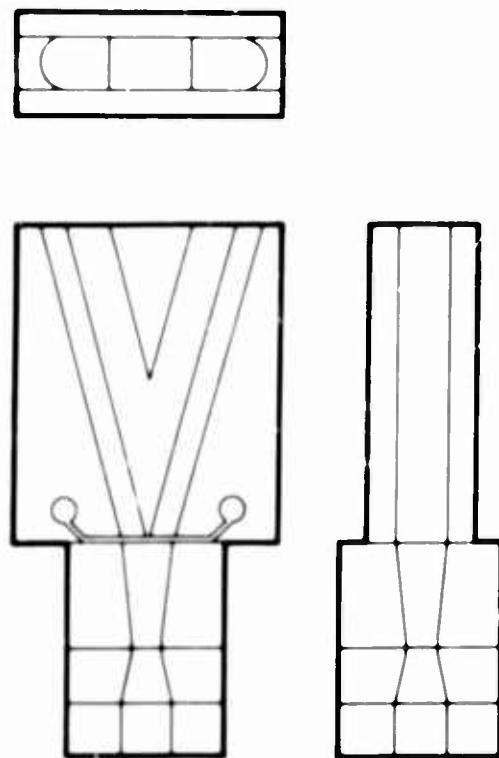
$\alpha = \theta \quad \phi = 10^\circ$

S_1 WAS VARIED FROM 3.00 IN. TO 4.00 IN.

$\epsilon = 0$

$S_2 = 2.00$ IN.

Figure 8. Valve Configurations – Valve Design 1412



$D_T = 0.60$ IN.

$\alpha = 11.3^\circ$

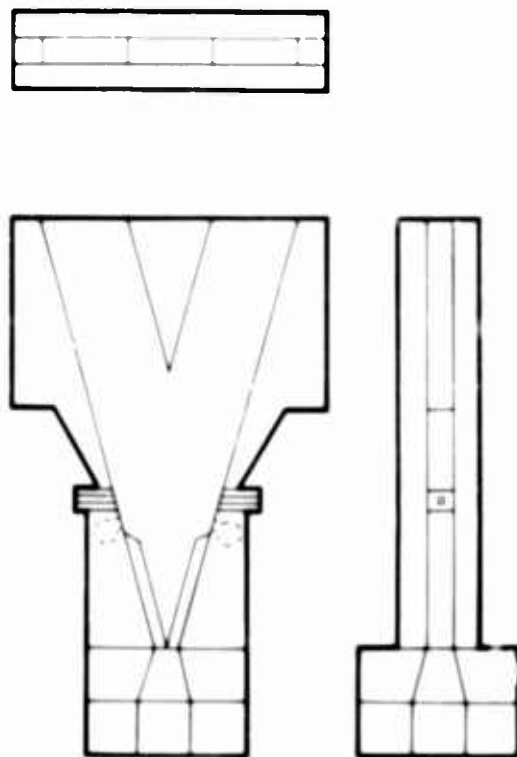
$\theta = \phi = 15^\circ$

S_1 WAS VARIED FROM 2.1 IN. TO 3.0 IN.

ϵ WAS VARIED FROM 0 TO 0.100 IN.

$S_2 = 2.00$ IN.

Figure 9. Valve Configurations – Valve Design 2511, 2512, 2513



$D_T = 0.50$ IN.

$\alpha = 10^\circ$

$\theta = 8^\circ, 10^\circ, \text{ AND } 15^\circ$

$\phi = \theta$

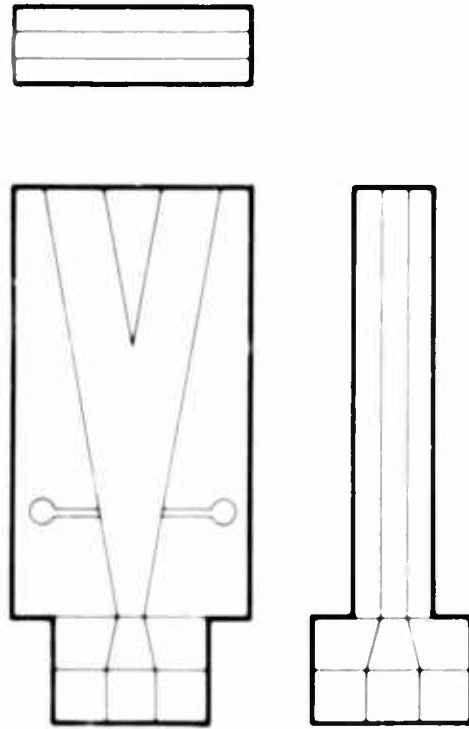
S_1 WAS VARIED FROM 2.375 IN. TO 3.075 IN.

ϵ WAS VARIED FROM 0 TO 0.060 IN.

$S_2 = 2.2$ IN. AND 1.7 IN.

LAST 0.50 IN. OF NOZZLE BLOCKS WERE FLATTENED AND FOR SOME RUNS THE INJECTION PORTS WERE LOCATED IN THIS PORTION OF THE NOZZLE SECTION.

Figure 10. Valve Configurations – Valve Design 13C22,
Dotted Lines 13C23



$D_T = 0.50$ IN.

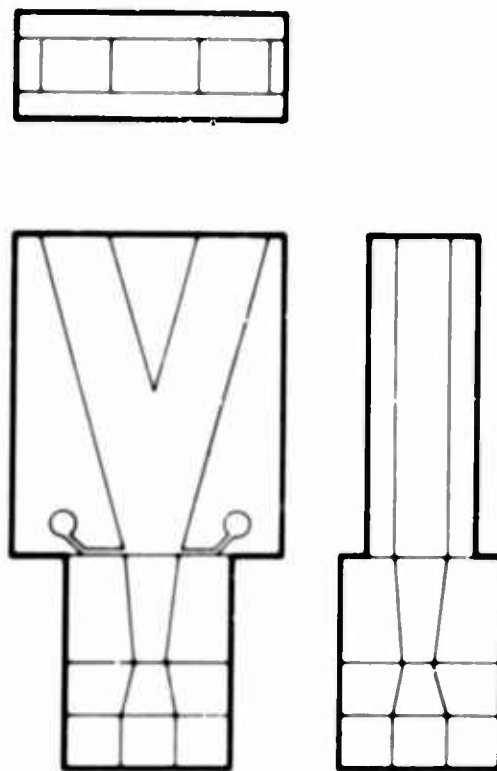
$\alpha = \theta \quad \phi = 10^\circ$

S_1 WAS VARIED FROM 2.80 IN. TO 3.50 IN.

$\epsilon = 0$

$S_2 = 2.00$ IN.

Figure 11. Valve Configurations – Valve Design 1422



$D_T = 0.60$ IN.

$\alpha = 11.3^\circ$

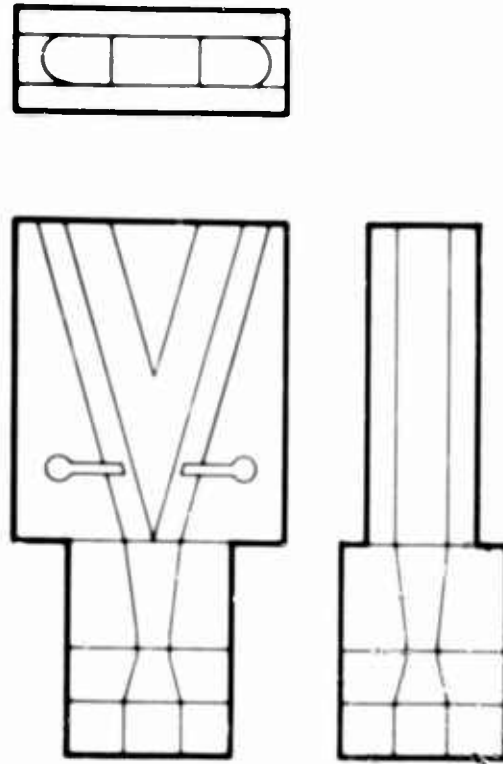
$\theta = \phi = 15^\circ$

S_1 WAS VARIED FROM 2.00 IN. TO 2.65 IN.

$\epsilon = 0$

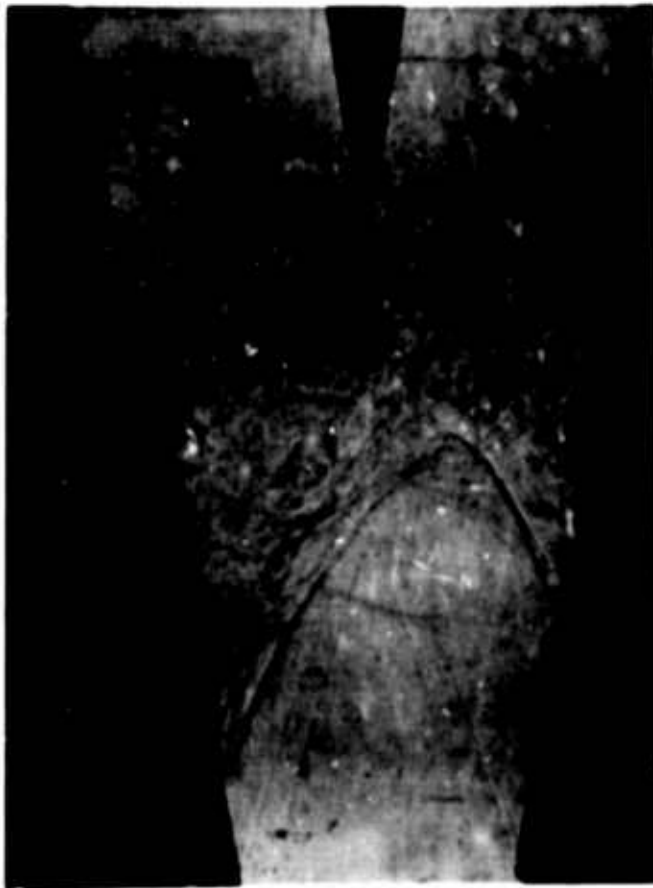
$S_2 = 2.00$ IN.

Figure 12. Valve Configurations - Valve Design 2612



VALVE DESIGN 2523 WAS VALVE DESIGN 2513 WITH CIRCULAR INJECTION PORTS LOCATED IN THE VALVE BODY SECTION.

Figure 13. Valve Configurations - Valve Design 2523



RUN NO. 66A

MODEL CONFIGURATION: 1A412

BODY HALF ANGLE 10°
SPLITTER LOCATION 3.00 IN.

NOZZLE HALF ANGLE 10°
SETBACK

CONTROL FLUID PRESSURE 25 PSIA

CHAMBER PRESSURE 115 PSIA
CONTROL FLUID OFF



RUN NO 66 B

MODEL CONFIGURATION: 1A412

BODY HALF ANGLE 10°
SPLITTER LOCATION 3.00 IN.

NOZZLE HALF ANGLE 10°
SETBACK

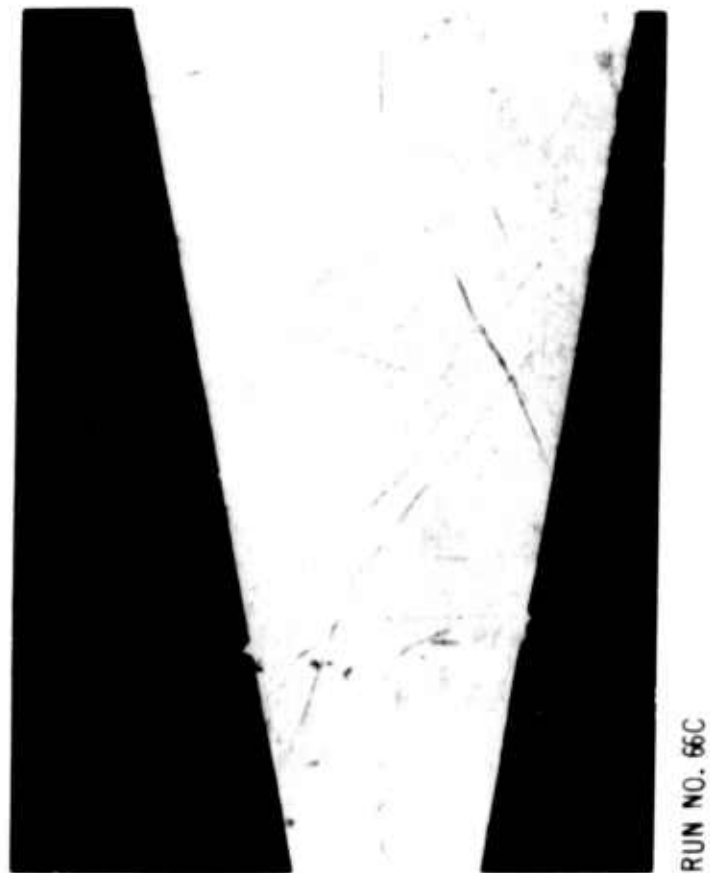
CONTROL FLUID PRESSURE 25 PSIA

CHAMBER PRESSURE 115 PSIA
CONTROL FLUID OFF

REMARKS: FLOW WAS STABLE IN EITHER LEG AND COULD BE SWITCHED.

REMARKS: RUN 66B SHOWS THE FLOW IN THE OTHER OUTLET LEG.

Figure 14.



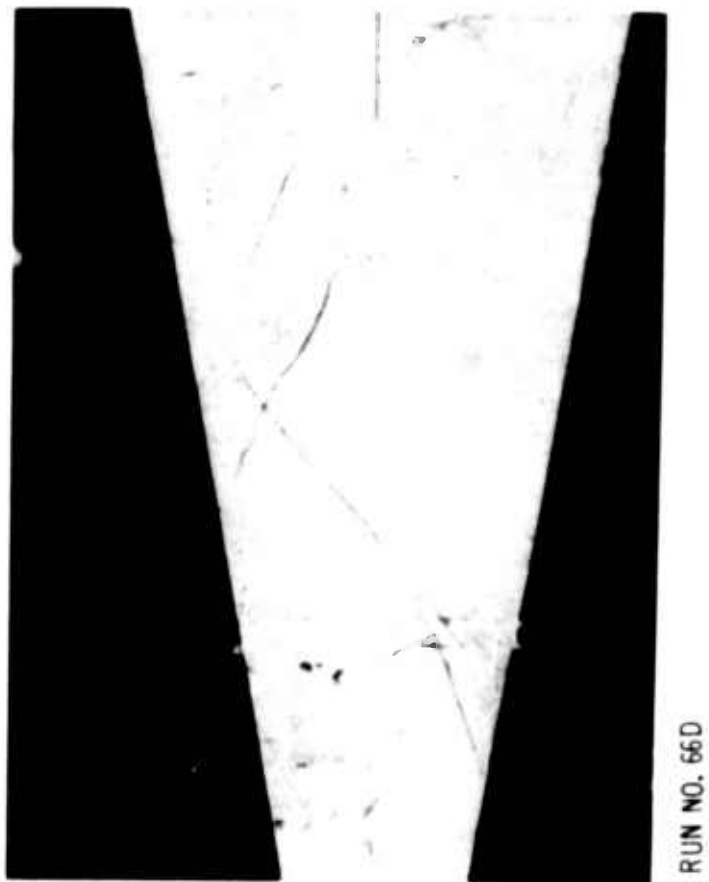
MODEL CONFIGURATION: 1A412

NOZZLE HALF ANGLE 10°
SETBACK

BODY HALF ANGLE 10°
SPLITTER LOCATION 3.00 IN.

CHAMBER PRESSURE 115 PSIA
CONTROL FLUID IN TOP

CONTROL FLUID PRESSURE 25 PSIA



MODEL CONFIGURATION: 1A412

NOZZLE HALF ANGLE 10°
SETBACK

BODY HALF ANGLE 10°
SPLITTER LOCATION 3.00 IN.

CHAMBER PRESSURE 115 PSIA
CONTROL FLUID IN BOTTOM

CONTROL FLUID PRESSURE 25 PSIA

REMARKS: RUN 66C WAS A RERUN OF RUN 66A WITH CONTROL FLUID ON.

REMARKS: RUN 66D WAS A RERUN OF RUN 66B WITH CONTROL FLUID ON.

Figure 15.



RUN NO. 83A

MODEL CONFIGURATION: 83A

NOZZLE HALF ANGLE 11.3°
SETBACK 0.0 IN.

CHAMBER PRESSURE 115 PSIA
CONTROL FLUID IN TOP

BODY HALF ANGLE 15°
SPLITTER LOCATION 2.65 IN.

CONTROL FLUID PRESSURE 60 PSIA

REMARKS:

THE FLOW WAS STABLE IN EITHER LEG AND COULD BE SWITCHED. THE CONTROL FLOW DID NOT SEEM TO HAVE AS GREAT AN EFFECT ON THE FLOW OF THIS MODEL AS IN THE PREVIOUS THINNER MODELS (CONFIGURATIONS 1XXX AND 1AXXX).



RUN NO. 83B

MODEL CONFIGURATION: 2612

NOZZLE HALF ANGLE 11.3°
SETBACK 0.0 IN.

CHAMBER PRESSURE 115 PSIA
CONTROL FLUID IN BOTTOM

BODY HALF ANGLE 15°
SPLITTER LOCATION 2.65 IN.

CONTROL FLUID PRESSURE 60 PSIA

REMARKS: RUN 83B SHOWS THE FLOW IN THE OTHER OUTLET LEG.



RUN NO. 84A

MODEL CONFIGURATION: 2612

NOZZLE HALF ANGLE 11.3°
SETBACK 0.0 IN.CHAMBER PRESSURE 115 PSIA
CONTROL FLUID OFFBODY HALF ANGLE 15°
SPLITTER LOCATION 2.3 IN.

CONTROL FLUID PRESSURE 50 PSIA

REMARKS:

THE FLOW WAS STABLE IN EITHER LEG AND COULD BE SWITCHED. A REVERSE FLOW EXISTED IN THE NON-FLOW OUTLET LEG.



RUN NO. 84B

MODEL CONFIGURATION: 2612

NOZZLE HALF ANGLE 11.3°
SETBACK 0.0 IN.CHAMBER PRESSURE 115 PSIA
CONTROL FLUID OFFBODY HALF ANGLE 15°
SPLITTER LOCATION 2.3 IN.

CONTROL FLUID PRESSURE 50 PSIA

REMARKS: RUN 84B SHOWS THE FLOW IN THE OTHER OUTLET LEG.

Figure 17.



RUN NO. 92A

MODEL CONFIGURATION: 2612

NOZZLE HALF ANGLE 11.3°
SETBACK 0.0 IN.

CHAMBER PRESSURE 115 PSIA
CONTROL FLUID OFF

BODY HALF ANGLE 15°
SPLITTER LOCATION 2.65 IN.

CONTROL FLUID PRESSURE 50 PSIA

REMARKS:

RUN 92 WAS A WALL FLOW VISUALIZATION STUDY OF THE CONFIGURATION OF RUN 91. THE MAIN FLOW IS IN THE UPPER LEG. NOTICE THE REVERSE FLOW IN THE NON-FLOW LEG.



RUN NO. 92B

MODEL CONFIGURATION: 2612

NOZZLE HALF ANGLE 11.3°
SETBACK 0.0 IN.

CHAMBER PRESSURE 115 PSIA
CONTROL FLUID OFF

BODY HALF ANGLE 15°
SPLITTER LOCATION 2.65 IN.

CONTROL FLUID PRESSURE 50 PSIA

REMARKS: THE MAIN FLOW IS IN THE LOWER LEG

Figure 18.



RUN NO. 93A

MODEL CONFIGURATION: 2612

NOZZLE HALF ANGLE 11.3°
SETBACK 0.0 IN.

CHAMBER PRESSURE 115 PSIA
CONTROL FLUID IN BOTTOM

BODY HALF ANGLE 15°
SPLITTER LOCATION 2.65 IN.

CONTROL FLUID PRESSURE 50 PSIA

REMARKS:

RUN 93 WAS A RERUN OF RUN 92 WITH CONTROL FLOW ON. THE MAIN FLOW IS IN THE UPPER LEG.



RUN NO. 93B

MODEL CONFIGURATION: 2612

NOZZLE HALF ANGLE 11.3°
SETBACK 0.0 IN.

CHAMBER PRESSURE 115 PSIA
CONTROL FLUID IN TOP

BODY HALF 15°
SPLITTER LOCATION 2.65 IN.

CONTROL FLUID PRESSURE 50 PSIA

REMARKS: THE MAIN FLOW IS IN THE LOWER LEG.

Figure 19



RUN NO. 110A

MODEL CONFIGURATION: 1A412

NOZZLE HALF ANGLE 10°
SET BACK - - -
BODY HALF ANGLE 10°
SPLITTER LOCATION 4.00 IN.

CHAMBER PRESSURE 115 PSIA
CONTROL FLOW OFF
CONTROL FLUID PRESSURE
25 PSIA

REMARKS: RUN 110 WAS A RERUN OF RUN 70 WITH A DIFFERENT
CAMERA FOCUS. THE FLOW IS IN THE UPPER LEG



RUN NO. 110B

MODEL CONFIGURATION: 1A412

NOZZLE HALF ANGLE 10°
SETBACK - - -
BODY HALF ANGLE 10°
SPLITTER LOCATION 4.00 IN.

CHAMBER PRESSURE 115 PSIA
CONTROL FLOW OFF
CONTROL FLUID PRESSURE
25 PSIA

REMARKS: THE FLOW IS IN THE LOWER LEG.

Figure 20.



RUN NO. 111A

MODEL CONFIGURATION: 1A412

NOZZLE HALF ANGLE 10°
SETBACK - - -

BODY HALF ANGLE 10°
SPLITTER LOCATION 4.00 IN.

CHAMBER PRESSURE 115 PSIA
CONTROL FLUID IN BOTTOM

CONTROL FLUID PRESSURE 25 PSIA

REMARKS: RUN 111 WAS A RERUN OF RUN 110 WITH CONTROL FLOW ON.
THE MAIN FLOW IS IN THE UPPER LEG



RUN NO. 111B

MODEL CONFIGURATION: 1A412

NOZZLE HALF ANGLE 10°
SETBACK - - -

BODY HALF ANGLE 10°
SPLITTER LOCATION 4.00 IN.

CHAMBER PRESSURE 115 PSIA
CONTROL FLUID IN TOP

CONTROL FLUID PRESSURE 25 PSIA

REMARKS: THE MAIN FLOW IS IN THE LOWER LEG.

Figure 21.

RUN NO. 94
VALVE DESIGN 1A412

FLOW IN LOWER LEG
CONTROL FLOW OFF
ALL PRESSURES ARE PSIA
FLOW CONDITIONS ARE THE
SAME AS RUN 88B

LINE A SHOWS BEGINNING OF SHOCK STRUCTURE, FROM FIGURE 14

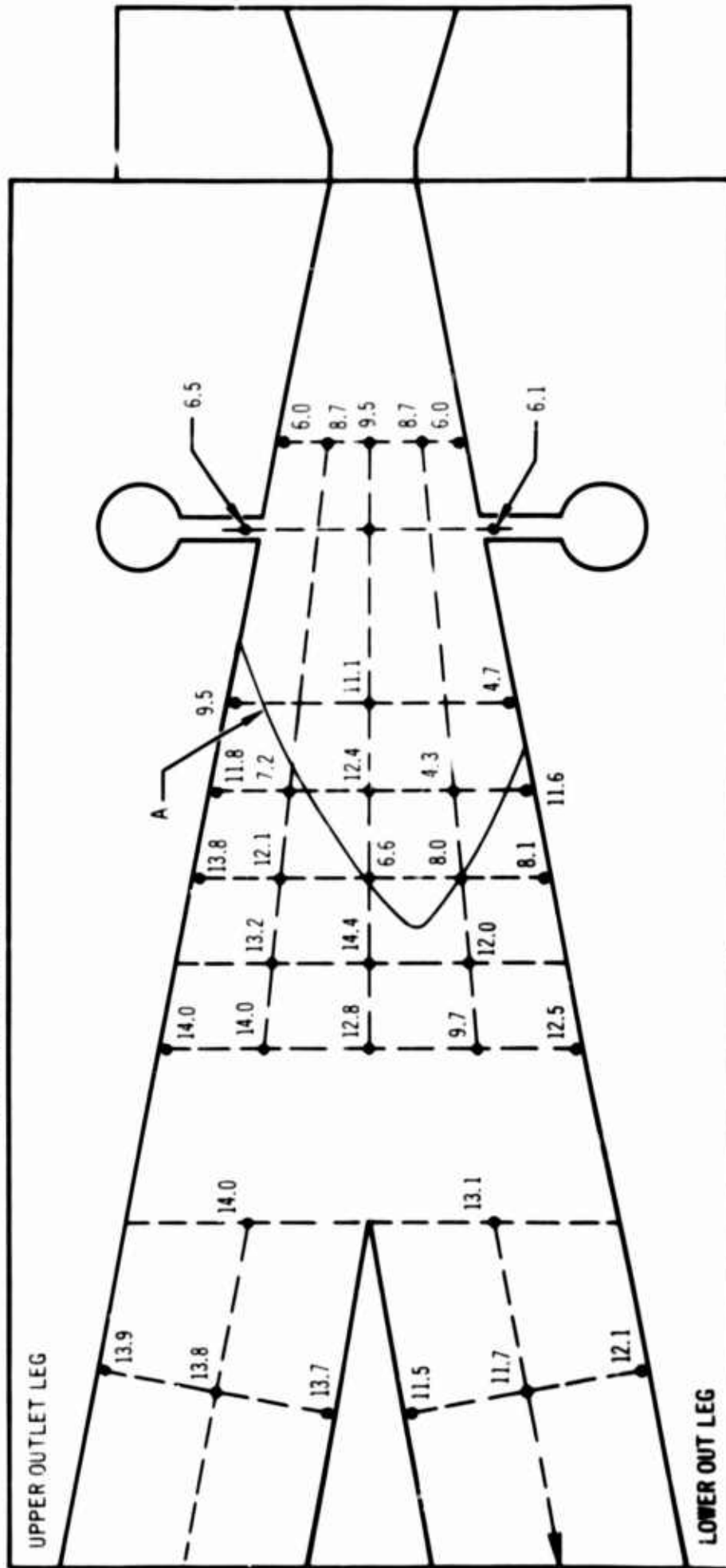


Figure 22. Static Pressure Survey

FLOW IN UPPER LEG
CONTROL FLOW OFF
ALL PRESSURES ARE PSIA
FLOW CONDITIONS ARE THE
SAME AS RUN 88A

LINE A SHOWS BEGINNING OF SHOCK STRUCTURE, FROM FIGURE 14

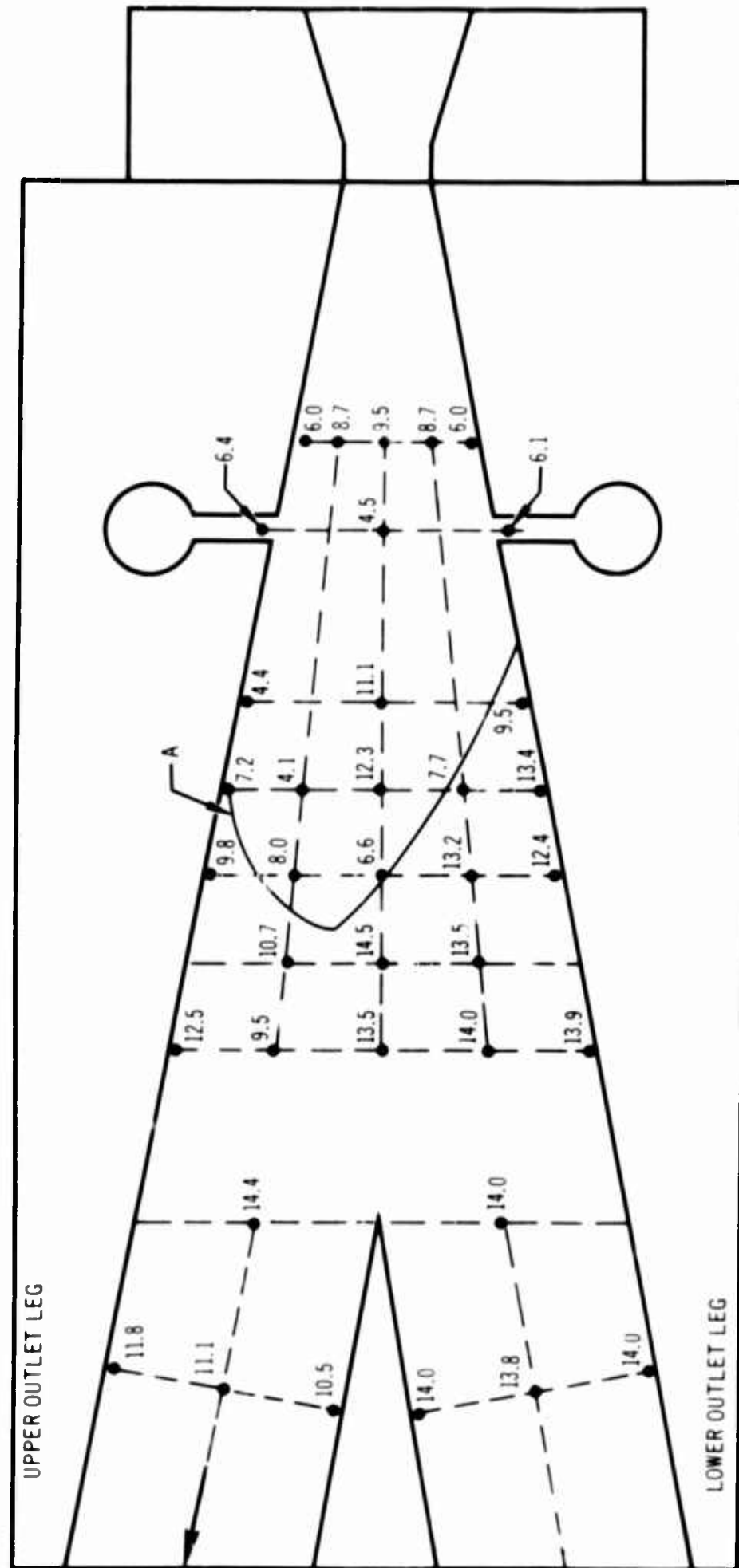


Figure 23. Static Pressure Survey

RUN NO. 96
VALVE DESIGN 1A412

FLOW IN LOWER LEG
CONTROL FLOW IN UPPER PORT
ALL PRESSURES ARE PSIA
FLOW CONDITIONS ARE THE
SAME AS RUN 66C

LINE A SHOWS BEGINNING OF SHOCK STRUCTURE, FROM FIGURE 15

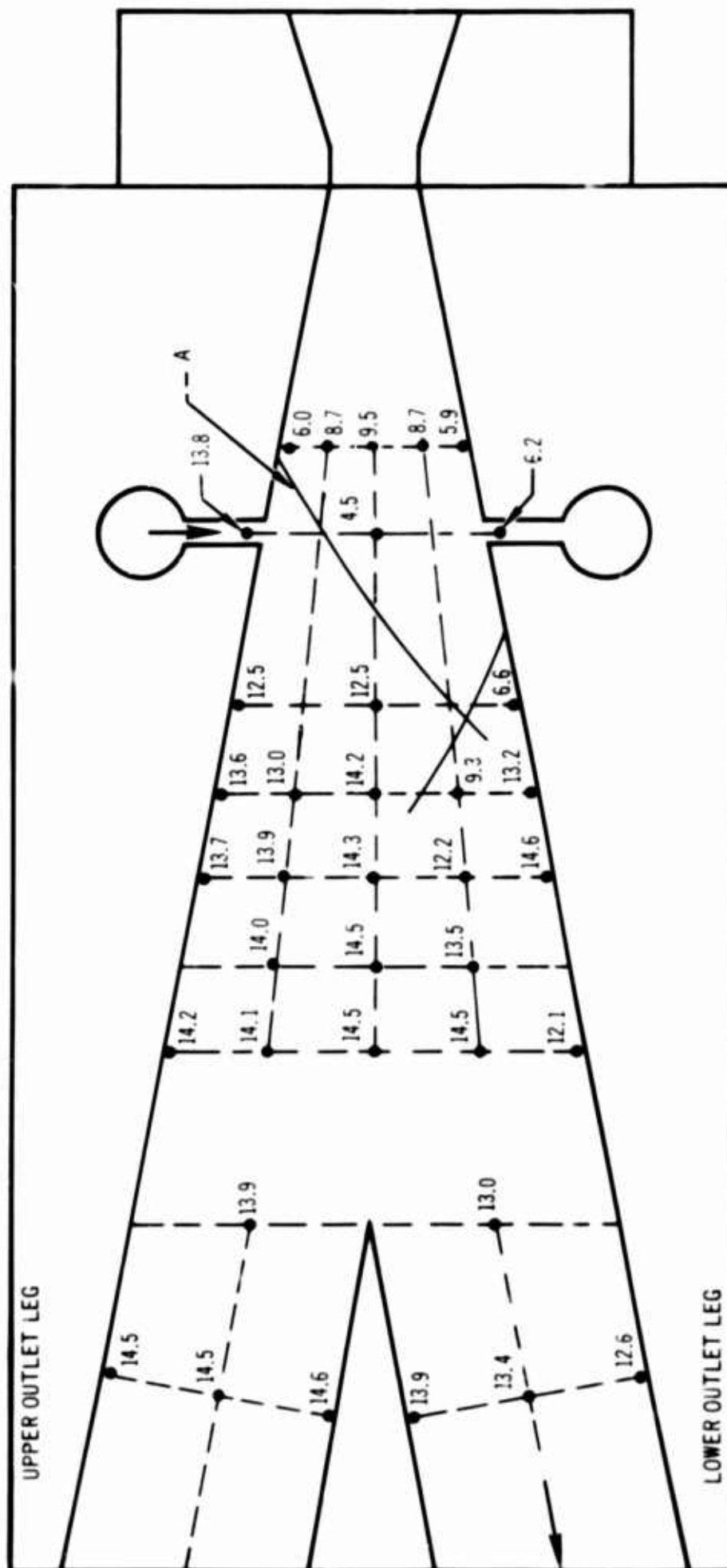


Figure 24. Static Pressure Survey

RUN NO. 97
VALVE DESIGN 1A412

FLOW IN UPPER LEG
CONTROL FLOW IN LOWER PORT
ALL PRESSURES ARE PSIA
FLOW CONDITIONS ARE THE
SAME AS RUN 66D

LINE A SHOWS BEGINNING OF SHOCK STRUCTURE, FROM FIGURE 15

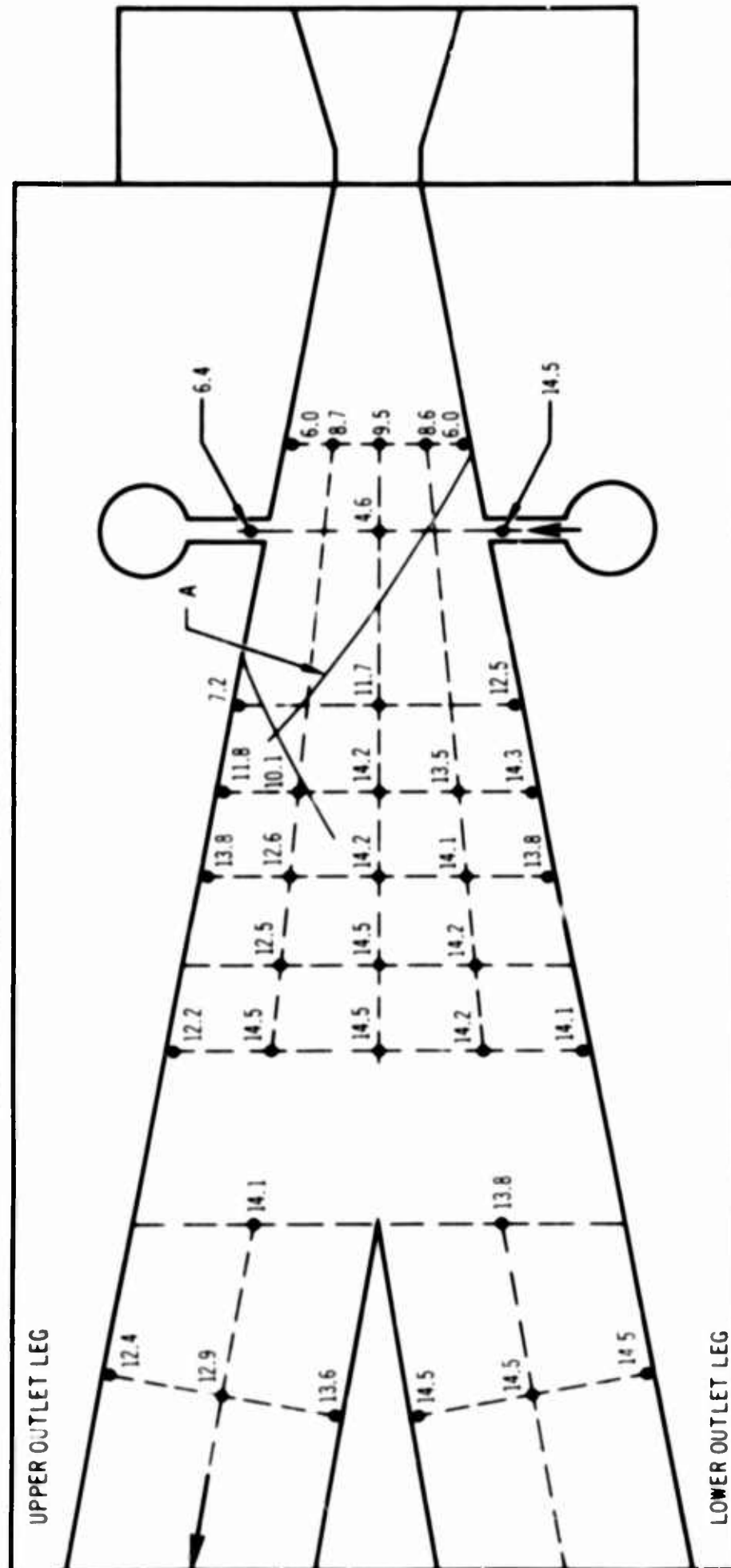


Figure 25. Static Pressure Survey

RUN NO. 102
VALVE DESIGN 2612

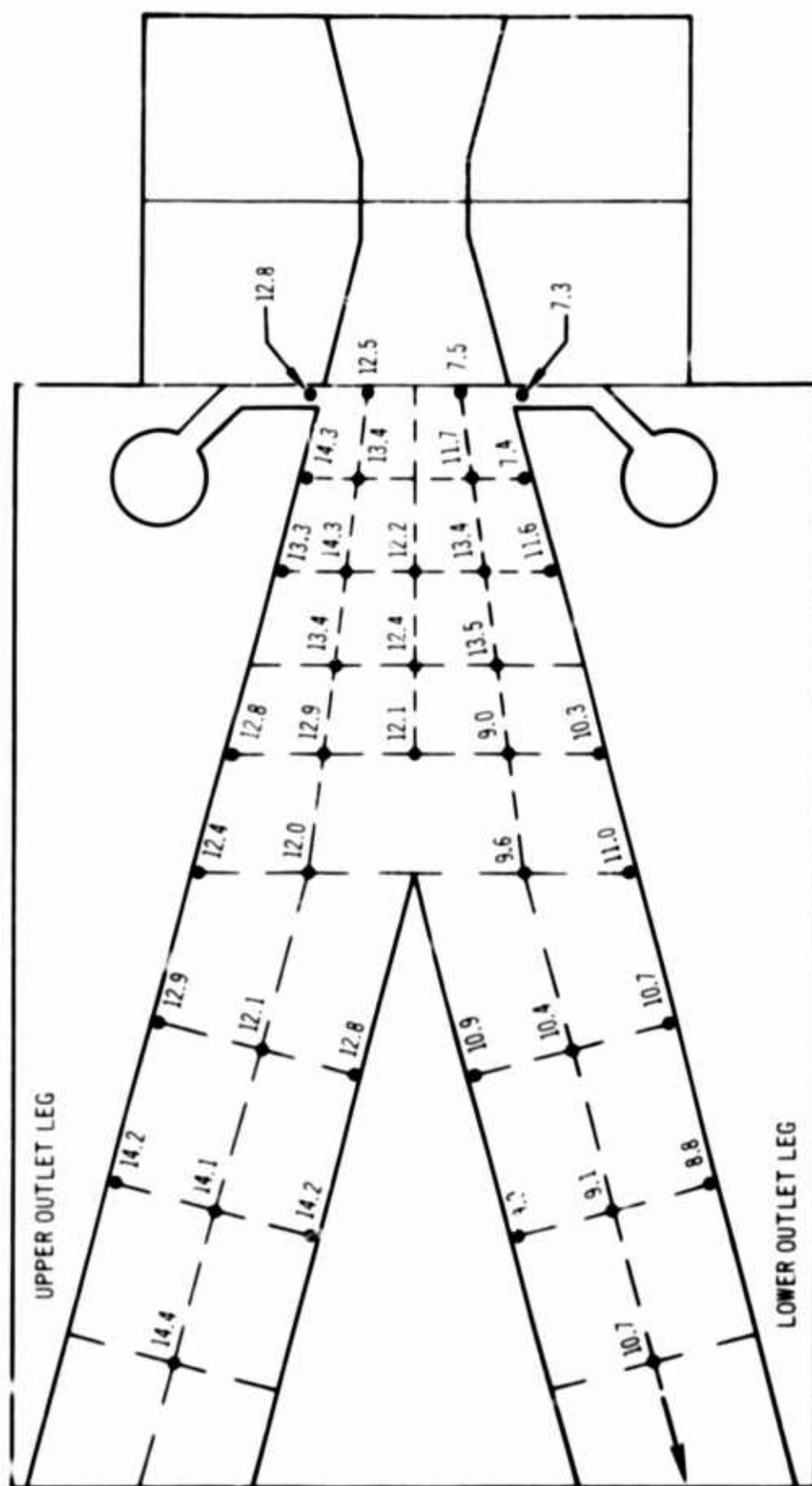


Figure 26. Static Pressure Survey

RUN NO. 103
VALVE DESIGN 2612

FLOW IN UPPER LEG
CONTROL FLOW OFF
ALL PRESSURES ARE PSIA
FLOW CONDITIONS ARE THE
SAME AS RUN 91B

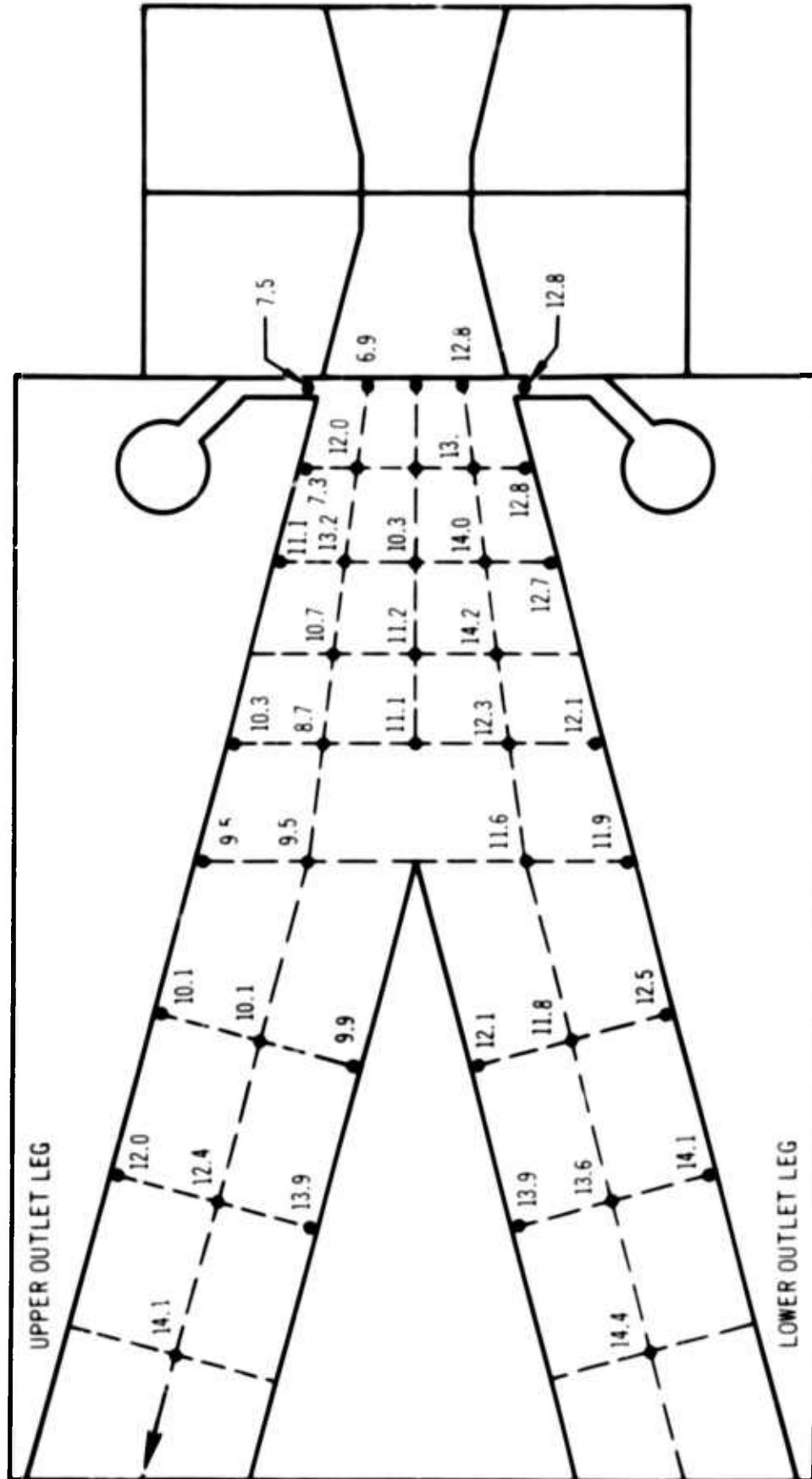


Figure 27. Static Pressure Survey

RUN NO. 104
VALVE DESIGN 2612

FLOW IN LOWER LEG
CONTROL FLOW IN UPPER PORT
ALL PRESSURES ARE PSIA
FLOW CONDITIONS ARE THE SAME AS RUN 83A

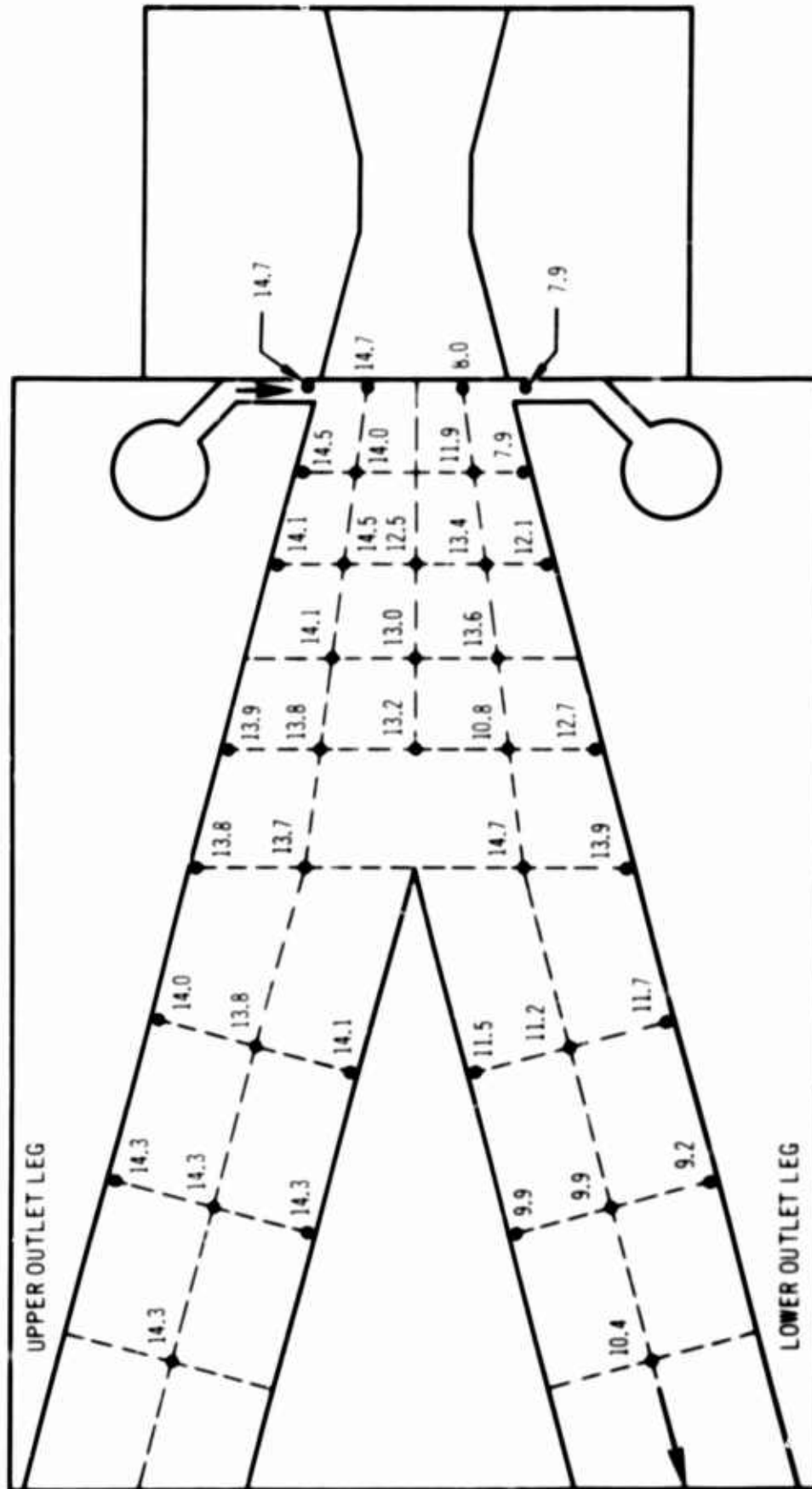


Figure 28. Static Pressure Survey

RUN NO. 105
VALVE DESIGN 2612

FLOW IN UPPER LEG
CONTROL FLOW IN LOWER PORT
ALL PRESSURES ARE PSIA
FLOW CONDITIONS ARE THE
SAME AS RUN 838

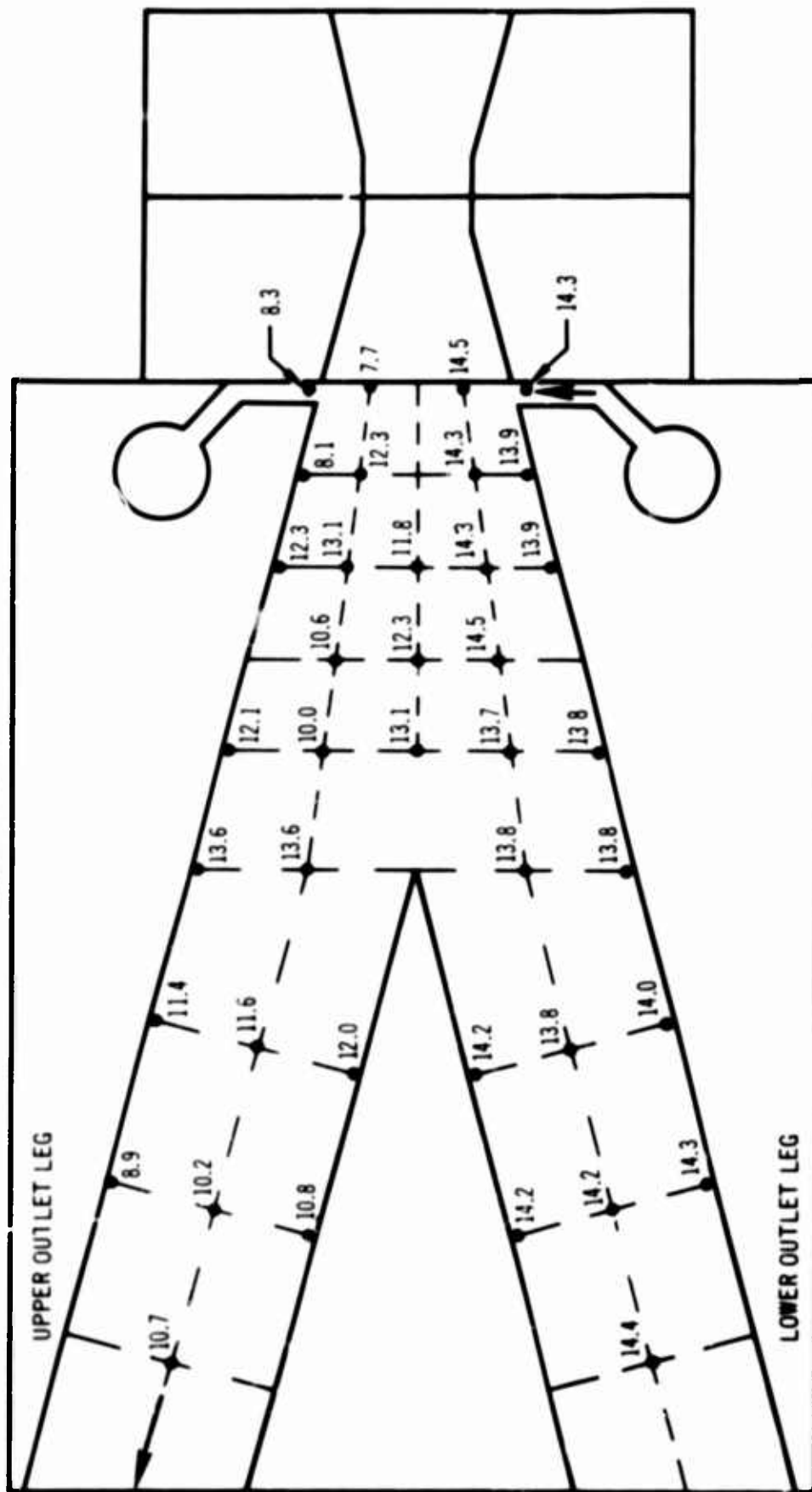


Figure 29. Static Pressure Survey



CORNELL AERONAUTICAL LABORATORY, INC.
BUFFALO, NEW YORK 14221

EXPERIMENTAL INVESTIGATION OF THE
PERFORMANCE CHARACTERISTICS OF A FLOW-
INSTABILITY SENSING DEVICE

By
E. F. Schroeder
Transportation Research Department

Prepared for Inclusion in the Third Fluid Amplification
Symposium Proceedings to be Conducted
26-28 October 1965

ABSTRACT

Research performed for the U. S. Air Force Aero-Propulsion Laboratory (Contract AF33(615)-1240) included an investigation of fluid state devices potentially capable of sensing the flow instabilities characteristic of rotating stall in axial-flow jet-engine compressors. The sensing system investigated consists of three interrelated components: (1) control circuit, (2) fluid amplifier, and (3) load. Static and dynamic tests were performed with several control circuit configurations and a range of bistable amplifier geometric parameters defining the mixing region. The input signal, consisting of periodic pressure pulses applied to a total pressure probe, is modified by the control circuit transmission characteristics (filtering, time delay, reflections, etc.). This modified signal is applied at the fluid amplifier control ports to produce a switching action. The resulting output, which consists of alternating pressure pulses from the two receiver ports, could be used with a signal processing device to initiate an appropriate compressor control action. Test results indicate that switching is possible with some configurations over the frequency range of 50-1000 cps with input pressure pulses of magnitude less than .05 times the absolute nozzle pressure, at a nozzle pressure ratio down to .70, using a power nozzle area of .010 sq. in. A description of the test equipment, a discussion of the sensor performance, and an evaluation of the test results are given in the paper.

INTRODUCTION

Rotating stall and surge have been continuing problems for the designers of gas turbines since the inception of their use in aircraft. For the compressor designer, a major problem associated with rotating stall has been how to limit blade stresses resulting from blade resonance with the passage of stall zones. From a performance point of view, stall and surge can place severe limits on transient performance of a gas turbine. At present, rotating stall and surge are circumvented in axial-flow jet engines by means of pre-scheduled control programs. Because of unavoidable variations between engines of a given model, this approach may result in serious compromise of engine performance. If some means could be devised for sensing the inception of stall or surge in time to allow corrective action by the control system before the instability can cause deterioration in performance, a gas turbine could then be operated at its peak performance without regard to control scheduling. Research currently being performed for the U. S. Air Force Aero-Propulsion Laboratory includes an investigation of fluid state devices potentially capable of sensing the flow instabilities characteristic of incipient stall in axial-flow jet-engine compressors.

The flow-instability sensor investigated (Figure 1) can be considered to be made up of three basic interconnected components: (1) control circuit, (2) bistable fluid amplifier, and (3) load. The control circuit consists of one or two total pressure probes, signal modifying elements (filters, delays, junctions, etc.), and connections to the two control ports of a bistable fluid amplifier. The variable geometry bistable fluid amplifier (Figure 3) utilizes the wall-attachment principle. Provisions are made for varying the power nozzle width, control port width and lateral offset, and the splitter distance. The sensor load, which includes the fluid amplifier receiver channels, could consist of some kind of signal processing device to initiate an appropriate compressor control action. In the tests performed, the fluid amplifier outlet tubes were simply connected to a reference tank held at a constant pressure.

*Figures appear on pages 273 through 298.

SENSOR PERFORMANCE CRITERIA

The flow-instability sensor performance characteristics (i. e., relationship between input and output) can be considered to be the combined effect of the performance of the three basic components which make up the sensing system, namely, control circuit, fluid amplifier, and load. In an experimental investigation of a sensor arrangement, it is extremely difficult to separate the contribution of the individual components to the total measured performance because the performance of each component influences, and is influenced by, the characteristics of the other components. Some of these functional relationships are shown qualitatively in Figure 2.

The input signal p_i , applied to the control circuit probe during the onset of unstable flow conditions is assumed to consist of fluctuations in total pressure resulting from the passage of stall cells. For simplicity, it is assumed that this probe input signal can be represented by a train of periodic, rectangular negative pressure pulses characterized by period (or frequency), duty cycle (pulse duration as a fraction of the period), and magnitude. For a dual-probe configuration, the space separation between the two probes is also required to characterize the input signal.

The output signal of the control circuit configuration, which is also the input signal to the fluid amplifier, is a difference signal across the fluid amplifier control ports, which can be called simply the control port signal, p_c . The control port signal is designated as that quantity which is effective in switching the fluid amplifier; it may be the static pressure difference, the flow rate difference, the power difference, the flow momentum difference, or a combination of these quantities, depending on fluid amplifier geometry. It is apparent that the performance characteristic of a control circuit configuration, defined by the output/input signal relationship, depends on the definition of the control port signal, which in turn is a function of the fluid amplifier geometry. In the dynamic tests performed, the static pressures were measured at the two control ports and the pressure difference is assumed to represent the control port signal.

The input signal applied to the bistable fluid amplifier is the control port signal, p_c . The power nozzle supply is operated on by the control port signal to produce an amplified output signal. The bistable fluid amplifier output signal is designated as that quantity which is the effective input to the load element; it may be the static or total pressure difference across the receiver ports, the flow rate difference,

the power difference, the momentum difference, or some combination of these quantities, depending on the nature of the load. In the dynamic tests performed, the static pressures were measured at the end of the two receiver channels, and the pressure difference is assumed to represent the fluid amplifier output signal, p_r . The performance characteristic of a bistable fluid amplifier configuration, defined by the output/input signal relationship, depends on the definition of the input signal, which is a function of the fluid amplifier geometry, and also on the definition of the output signal, which depends on the nature of the load.

For a complete flow-instability sensor configuration, the requirement for a definition of the control port signal at the interface between the control circuit and the fluid amplifier can be eliminated and the output/input signal relationship (or transfer function if it is linear) can be expressed in terms of the probe input signal, p_i (total pressure fluctuation) and the fluid amplifier output signal, p_r .

To evaluate and compare the performance of different sensor configurations, it is necessary to define pertinent performance factors, including power gain, shape of output signal vs shape of input signal, stability, efficiency, etc. The relative importance of any of these performance factors depends on the sensor application. Performance measures used in this investigation include the input signal amplitude required to obtain reliable switching, and the resulting receiver pressure amplitude and shape, at a given set of operating conditions.

TEST APPARATUS AND PROCEDURE

A schematic of the dynamic test apparatus is shown in Figure 4. The input signal consists of total pressure pulses that are produced in a flow modulator by interrupting a jet of air, directed against the probe opening, with a flow-interrupter disc having evenly spaced holes. The magnitude of the pressure pulses and the average pressure level are adjusted by means of two valves controlling the flow into and out of the flow modulator. Duty cycle is changed by using different discs, each with a different ratio of hole diameter to hole spacing. The pulse frequency is continuously adjustable over the range 0-1100 cps, using a 16-hole disc, by means of a variable speed dc motor.

The probe pressure signal, p_p , contains substantial contributions from reflected signals and, in general, does not represent the effective sensor input signal, p_i , in magnitude or shape. For calibrating the sensor input signal, a 100-foot long tube, with the same internal diameter as the probe, was connected to the probe to eliminate downstream reflections as shown in Figure 7(a). The probe pressure signal, p_p , obtained with this arrangement was assumed to represent the effective input signal, p_i , for all sensor arrangements. The shape of the signals obtained at various frequencies is shown in Figure 7(c). The source of the noise component (approximately 2000 cps) that is present in all the signals has not been determined. However, any performance effects resulting from its presence should be small. It was observed that there is a proportional relationship between the input signal pulse amplitude and the pressure difference across the flow modulator measured at the locations shown in Figure 7(a). Accordingly, this pressure difference was measured and used to define the input signal pulse amplitude for all of the dynamic tests.

Dynamic tests were performed using the four basic control circuit configurations shown in Figure 5. With configuration I, the right control port was connected to an independent regulated pressure source using a very long connecting tube to eliminate reflected signals. The input signal from the flow modulator was applied to the left control port only. This simple research configuration was selected to determine the effects of pressure unbalance across the control ports, to investigate control port crosstalk characteristics, and to measure the static and dynamic switching characteristics. The other three control circuit configurations (II, III and IV) consist of a single total pressure sensing probe with two branches leading to the left and right control ports of the fluid amplifier. One branch, arbitrarily chosen to be the right branch, is longer than the other branch by a

suitable amount. The resulting fixed time delay in the right control port signal produces a difference signal across the control ports to switch the fluid amplifier. Configurations III and IV have a filtering volume in the right branch in addition to the time delay to improve the sensor switching performance at low frequency. The table in Figure 5 lists the geometric parameters (lengths and areas) that characterize the control circuit configurations tested.

The bistable fluid amplifier configuration and the load configuration tested are shown in Figure 6. The values of the geometric parameters used in the tests are indicated in the accompanying table.

The operating conditions of the flow-instability sensor are defined by the power nozzle supply pressure, the load pressure level, and the input signal properties (frequency, duty cycle, amplitude, and average pressure level). The values of the operating parameters used in the tests are listed in Table I.

Wideband pressure transducers were used to measure the instantaneous static pressures at the locations shown in Figures 3 and 4. Any two of the individual signals, or their difference, could be displayed simultaneously on a dual-beam oscilloscope. The following instantaneous static pressures and pressure differences were measured:

Probe pressure (generally not equal to the input pressure, P_i)	P_p
Left control pressure	P_{cl}
Right control pressure	P_{cr}
Pressure difference across control ports	$P_{cl} - P_{cr}$
Left receiver pressure	P_{rl}

Because it was determined early in the test program that the right receiver pressure was generally a mirror image of the left receiver pressure, it was not measured in most of the tests and is not shown in any of the oscilloscope photographs.

Separate static pressure taps were provided to measure the average static pressures at the locations shown in Figures 3 and 4. A sensitive differential pressure gauge was used with the pressure manifolding arrangement shown in Figure 4 to enable an accurate measurement of the difference between any pressure connected to the

left manifold and any pressure connected to the right manifold. Several other pressure gauges were also provided to measure pressures outside the range of the differential pressure gauge. The following pressure differences were usually measured during the static and/or dynamic tests:

Reference pressure level above atmospheric pressure	$P_o - P_a$
Power nozzle supply pressure above reference pressure	$P_n - P_o$
Left control pressure level above reference pressure	$P_{cl} - P_o$
Pressure difference across control ports	$P_{cl} - P_{cr}$
Left receiver pressure level above reference pressure (static tests)	$P_{rl} - P_o$
Pressure difference across receiver channels (static tests)	$P_{rl} - P_{rr}$
Mixing region pressure level above reference pressure (static tests)	$P_m - P_o$
Pressure difference across flow modulator (proportional to sensor input signal pulse amplitude for dynamic tests)	$P_{FM1} - P_{FM2}$

Flowmeters of the float/tapered tube type were installed at the locations shown in Figures 4 and 5(a). With the rapidly fluctuating flow conditions existing during the dynamic tests, the two receiver flowmeters do not indicate the true average flow rates and the readings were regarded as only qualitative indications of the average flow rates. The following average flow rates (indicated) were measured:

Power nozzle mass flow rate	\dot{m}_n
Average right control mass flow rate (Configuration I)	$\bar{\dot{m}}_{cr}$
Average left receiver mass flow rate (indicated)	$\bar{\dot{m}}_{rl}$
Average right receiver mass flow rate (indicated)	$\bar{\dot{m}}_{rr}$

DISCUSSION OF TEST RESULTS

The oscilloscope photographs shown in Figures 8 to 17 have been selected to illustrate the influence of the input signal properties and the system physical parameters on the performance of the sensor configurations tested. The pressure signal traces, in most of the photographs, are in the following order:

- Trace 1. Probe pressure, P_p - in general not equal to the assumed effective input signal, P_i , which is shown in Figure 7(c).
- Trace 2. Left control port pressure, P_{cl} . Traces 1 and 2 were recorded simultaneously.
- Trace 3. Left control port pressure, P_{cl} - repeated to obtain a common time reference for P_{cr} .
- Trace 4. Right control port pressure, P_{cr} . Traces 3 and 4 were recorded simultaneously.
- Trace 5. Pressure difference across control ports, $P_{cl} - P_{cr}$
- Trace 6. Left receiver pressure, P_{rl} - assumed to represent one-half the magnitude of the fluid amplifier output signal, i. e., one-half the pressure difference across the receiver channels. Traces 5 and 6 were recorded simultaneously.

The input signal pulse train can be represented by a Fourier cosine series, i. e., the sum of a series of cosine waves of frequencies which are integral multiples of the fundamental input frequency. A train of rectangular pulses with a duty cycle of 0.33, which is approximately equivalent to the sensor input signal shown in Figure 7(c), contains harmonic components at 1, 2, 4, 5, 7, 8 ... times the fundamental frequency. The third and sixth harmonics are absent or of very small magnitude. The magnitude of each harmonic present is inversely proportional to the harmonic number, e. g., the magnitude of the fourth harmonic is one-fourth the magnitude of the fundamental. However, the

effective control port signal, in general, will not have the same amplitude and phase distribution of the harmonic frequency components as the input signal. The various frequency components of the left and right control port signals are attenuated and shifted in phase by different amounts depending on the delay times and on their proximity to the many resonant frequencies inherent in any control circuit geometric arrangement. The pressure difference signal across the control ports contains the same frequency components as the individual control port pressure signals but a completely different amplitude and phase distribution. As discussed above under Performance Criteria, the effective control port signal could be a combination of the pressure difference and, say, the momentum difference. In that event, perhaps the control port signal could be represented as a constant times the pressure difference signal plus a constant times the pressure difference signal squared. Another possible nonlinear effect could be amplitude-dependent reflection coefficients at the control ports. These nonlinear effects would create different harmonics at frequencies consisting of sums and differences of the frequencies contained in the input pressure signal, e. g. , the third and/or sixth harmonics could be present in the effective control port signal, although absent in the input signal.

With control circuit configuration I-2, the shape of the control port pressure difference signal, $P_{CL} - P_{CR}$ (upper row of Figures 8 to 14) bears a general resemblance to the input signal pulse train, although modified considerably at some frequencies because of reflections originating at the control port and at the junction between the probe and left control branch.

With control circuit configuration II-2 (split probe with time delay), the shape of both the left and right control port pressure signals, P_{CL} and P_{CR} , as can be seen in Figure 15 and position (d) of Figures 8 to 14, resembles the shape of the input signal pulse train, modified according to the control circuit transmission characteristics (reflections and control port crosstalk). The right control port signal, P_{CR} , is delayed with respect to P_{CL} by a fixed amount (0.6 msec) producing a phase shift proportional to frequency (180° at 833 cps). The control port pressure difference signal, $P_{CL} - P_{CR}$, resulting from the time delay, bears no resemblance to the shape of the input signal pulse train, but, in general, approximates a train of alternating positive and negative pulses, with the duration and separation interval varying as a function of frequency and input duty cycle.

With the two split probe control circuits incorporating a filter and time delay (configurations III and IV), the right control port signal is considerably different from the left control port signal, as can be seen in positions (e) and (f) of Figures 8 to 14. The different frequency components of the input signal are attenuated and shifted in phase by various amounts to produce a complex control port difference signal. The larger magnitude of the control port pressure difference signal at 50 cps illustrates the improvement of the low frequency performance produced by the filters (compare Figures 8(e) and 8(f) with 8(d)). At 500 cps where the wavelength is four times the length of the filter elements in both configurations III-2 and IV-1, the power transmission to the right control port is at a minimum and the right control port signal is attenuated considerably (see Figures 12(e) and 12(f)). At 1000 and 2000 cps, where the wave lengths are approximately two and one times the filter length, the filter elements permit 100% power transmission of the fundamental and second harmonic signal components to the right control port, and the performance of the three split probe control circuits is nearly identical (see Figure 12(d) (e) (f)). There is a slight difference in the performance of configuration IV-1, indicated by the different probe pressure trace in Figure 12(f), owing to the fact that, with this configuration, the sum of the two control port branch lengths is different from that with the other configurations, whereas the branch length difference is the same.

With the split probe/time delay control circuit configuration II-2, it appears that harmonic frequency components of the left and right control port signals and the difference control port signal in the vicinity of 100, 310, and 550 cps are augmented to some degree. The augmentation of the fundamental frequency components at 100, 310 and 550 cps may be seen in Figures 15(b), 15(i) and 15(l) respectively and the pronounced second harmonic components at 50 and 275 cps may be noted in Figures 15(a) and 15(g). This 1-3-5 relationship between the resonance frequencies bears a resemblance to the resonance characteristics of a closed organ pipe. However, even with this relatively simple control circuit configuration, the manner in which the three basic lengths contribute towards any resonance condition is very complex. Listed below are the frequencies at which the various length combinations make their largest contribution towards resonance at room temperature.

Characteristic Dimension	$f_n = \frac{(2n+1)c}{4L}$ cps $n = 0, 1, 2, \dots$
$L_P = 7.4''$	452, 1355, 2260, ...
$L_L = 18.1''$	185, 555, 925, ...
$L_R = 26.1''$	128, 384, 640, 895, ...
$L_P + L_L = 25.5''$	131, 393, 655, 917, ...
$L_P + L_R = 33.5''$	100, 300, 500, 700, 900, 1100, ...
$L_L + L_R = 44.2''$	76, 228, 380, 532, 684, ...
$L_P + L_L + L_R = 51.6''$	65, 195, 325, 455, 585, ...
$L_P + \frac{1}{2}(L_L + L_R) = 29.5''$	114, 342, 570, 800, 1025, ...

The relative contribution of each of the above characteristic dimensions to any resonance condition depends on the branch cross-section areas and the reflection and crosstalk coefficients at the control ports.

The reflection and crosstalk coefficients may be defined as the ratios of the magnitudes of the signal reflected at the control port, and the signal transmitted to the opposite control port, respectively, to the magnitude of the incident signal. It is possible to estimate the magnitudes of the control port reflection and crosstalk coefficients from the data obtained with control circuit configuration I-2 (see the upper row of Figures 8 to 14). However, because the probe area is different from the left control branch area, reflections at the junction complicate the shape of the incident signal traveling towards the left control port. As a result, it is difficult to obtain accurate reflection and crosstalk coefficients from these particular data. The task would be simplified immensely by using a probe of the same cross-sectional area as the left control branch. As a rough estimate, both the reflection and crosstalk coefficients are in the range 0 to +0.3, varying with frequency, overall pressure ratio,

P_o/P_n , and probably also with the average control pressure level, P_c/P_n . Comparing the probe pressure traces in Figure 7(d), obtained with the test arrangement shown in Figure 7(b), with the probe pressure traces obtained with control circuit configuration I-2 shown in the upper row of Figures 8 to 14, it is seen that they are not greatly different at any frequency. This is an indication that the control port reflection coefficient is small.

When a periodic input signal is applied, the output signal of an ideal bistable amplifier would be a train of periodic, rectangular pulses characterized by period (or frequency), duty cycle, and magnitude. However, because the output signal of an actual bistable fluid amplifier is usually not a perfect train of rectangular pulses, it can be represented, more generally, in terms of the magnitudes and phases of the frequency components. This latter representation also includes a rectangular pulse train, which can be expressed as a Fourier cosine series.

In Figures 15(c) (d) (f) (h) (j) (n), it is seen that if any frequency component of the control port signal is in the range 850 - 900 cps, there is always some degree of output response at that component frequency superimposed on the response to the fundamental signal frequency. The following relationship exists between the fundamental input frequency and the resonant frequency of the harmonic component of the left receiver pressure signal, P_{RL} :

<u>Fundamental Input Frequency, cps</u>	<u>Resonant Frequency of Output Harmonic, cps</u>
145	870 6th harmonic
170	850 5th harmonic (intermittent)
220	880 4th harmonic
285	860 3rd harmonic (more pronounced in Fig. 11(f))
445	890 2nd harmonic
870	870 fundamental

This indicates that there is a fluid amplifier resonant frequency in the range 850-900 cps. The output harmonic obtained at some other frequencies, e. g., the 2nd harmonic at 50 cps and 275 cps (Figures 15(a) and 15(g)), are considered to represent the normal response to the augmented 2nd harmonic in the control signal and are not thought to be associated with a fluid amplifier resonance condition. The fluid amplifier resonance is believed to be caused by the influence of the load on switching referred to in Figure 2 as output impedance feedback. It is determined by the load geometric parameters such as receiver channel dimensions, load connecting tube dimensions, and load impedance.

With the two different sets of load geometric parameters tested, it was observed that fluid amplifier resonance occurs at approximately 70-80% of the computed frequency at which the input impedance of the receiver channels (at the splitter) is a minimum. A possible explanation for this may be that the crossflow between the receivers resulting from load reflections would have the maximum influence on switching when the power jet is in an intermediate position (partially switched).

Another type of fluid amplifier feedback effect is that caused by the influence of switching on the control port signal. As seen in Figure 2, this effect differs from the output impedance feedback effect, which does not influence the control port signal (except indirectly as a result of switching). Because the fluid amplifier is an active element (i. e., connected to an independent power supply), it can generate an input signal to the control circuit as a result of switching. This input signal is modified by the control circuit (reflections, time delays, etc.) and the resulting control port signal is a modified input signal to the fluid amplifier. Because this modified fluid amplifier input signal is created by the fluid amplifier output signal (i. e., switching), this effect can be referred to as switching feedback. As a result, the control port signal and the resulting fluid amplifier response are augmented at some frequencies (regenerative or positive feedback) and are diminished at other frequencies (degenerative or negative feedback). If the positive feedback is of sufficient magnitude at any one of the control circuit resonant frequencies, a self-sustaining oscillation is possible. With the fluid amplifier geometric configuration selected for most of the dynamic tests, the tendency towards oscillation is small because the switching has a minimal effect on the control port signal (Figures 8-16). However, the geometric configuration with a larger lateral offset distance shows a marked tendency towards oscillation (Figure 17). The low frequency oscillation at approximately 100 cps is not self-sustaining, but is reinforced periodically by the input signal when the input signal is nearly an odd multiple of the oscillation frequency.

The third and sixth harmonics are presumed to be absent, or of very small magnitude, in the input signal. However, there are substantial third and sixth harmonics in the output signal shown in Figures 11(f) and 15(c), respectively, with no evidence of these harmonics in the control port pressure difference signal. This is some indication that the effective control port signal may be some nonlinear function of the pressure difference signal, as discussed earlier.

In a qualitative interpretation of the test data, it may be concluded that the output response of the sensor to any of the input signal frequency components depends on the amplitude and phase of the component in the effective control port signal and the proximity of the component frequency to the fluid amplifier resonant frequency. The maximum amplitude of the response is limited by the saturation characteristics of the fluid amplifier.

The response of the different sensor configurations to an input signal approximating a series of alternating positive and negative steps is shown in Figure 16. It should be noted, however, that the rise time of the steps (approximately 2-3 milliseconds at 10 cps) is long compared to the fluid amplifier response time (less than one millisecond) and compared to some of the faster control circuit transients. This is an inherent limitation of the test apparatus used and is determined by the ratio of the sensing probe diameter to the width of the disc holes. A disc with two blades (the minimum possible for dynamic balance) was installed in the flow modulator. The low value of the input pulse frequency (10 cps) was selected to allow the transient pressure fluctuations in the control circuit to decay between pulses. Despite the uncertainty about the validity of the input signal, the data obtained illustrate, qualitatively, the effects of multiple reflections, from various locations, on the control circuit dynamic response.

In the quantitative switching performance data shown in Figures 18 to 25, the performance measure used is the input signal pulse amplitude required to obtain reliable switching. The figures show some of the effects of the operating conditions on the switching performance of the sensor with different control circuit configurations.

The sensor switching performance, as a function of frequency, with the four different control circuit configurations is compared in Figure 18 for a specific set of operating conditions (nozzle supply pressure, $P_n = 25$ psia; load pressure ratio, $P_L = .7$; average control pressure ratio, $\bar{P}_c = .7$; duty cycle, $d = .33$). For these operating conditions, the typical input signal amplitude required for switching, $|P_i|$, is generally in the range of .02 to .04, over the frequency range of 50 to 1000 cps. Larger values are required with configuration II-2 at low frequency and with configuration IV-1 at 670 and 1000 cps.

Although the definition of "good switching" is somewhat subjective, the relatively small partial switching range, shown in Figure 19, indicates that any errors in the switching performance data are quite small.

The effect of the average input pressure ratio, \bar{P}_i , (approximately equal to the average control pressure ratio, \bar{P}_c) on the switching performance of configuration II-2 may be seen in Figures 20 and 21. In Figure 21, it is seen that the required input signal amplitude generally has a pronounced minimum in the range $\bar{P}_c = .8$ to .9. At this optimum pressure ratio, switching is obtained over most of the frequency range 50-1000 cps with an input signal pulse amplitude of $.025 P_n$. With an input signal amplitude of $.04 P_n$, switching is obtained over most of the frequency range 50-1000 cps for a wide range of average control pressure ratios extending from .6 to nearly unity.

The effect of the load pressure ratio, P'_L , on the switching performance is shown in Figure 22. It appears that the input signal amplitude required for switching is roughly proportional to $(1 - P'_L)$. The decreased input signal amplitude required as the load pressure ratio, P'_L , approaches unity does not necessarily result in increased gain of the sensor, because, as seen in the upper row of Figures 8 to 14, the magnitude of the sensor output signal also decreases in approximately the same proportion as P'_L approaches unity.

The sensitivity of the sensor to pressure unbalance across the fluid amplifier control ports is illustrated in Figure 23. It is seen that the optimum average pressure difference across the control ports is not zero but some positive quantity increasing with the minimum value of the input signal amplitude. This would be predicted when an input signal pulse train of duty cycle less than 0.5 is applied to one control port only, as was the case in the tests with configuration I-2. Also, as expected, the input signal amplitude required for switching increases, with a positive or negative change in the control port pressure difference, by an amount that is greater than the incremental change in the control port pressure unbalance.

Some switching performance data at different power nozzle supply pressures (25, 50 and 75 psia) are shown in Figure 24. These data provide an indication that the performance of the sensor is nearly identical at all pressures in the range 25 to 75 psia if all pressure parameters are nondimensionalized ratios of the power nozzle supply pressure. The same would be expected to be true if all pressures and pressure differences were nondimensionalized in terms of the dynamic pressure of the power jet or any other suitable reference pressure. Slight differences in the sensor performance could be expected over the supply pressure range 25 to 75 psia because of the 3 to 1 variation in flow Reynolds number, in direct proportion to the absolute pressure.

Some qualitative effects of fluid amplifier geometry on the sensor switching performance and stability are shown in Figure 25. It was observed that the configurations with a control port lateral offset from the centerline greater than one-half the power nozzle width had a pronounced tendency towards self-sustained oscillations. This instability is believed to be caused by the generation of an effective control signal by the fluid amplifier switching action, referred to previously as the switching feedback effect. At this point in the experimental program, special emphasis was placed on reducing the number of fluid amplifier configurations by selecting, for further tests, only those few arrangements which appeared to provide suitable performance. The many geometric combinations investigated for static switching performance

were reduced to a single configuration which exhibited switching capability and stability across the complete frequency band. Any tendency towards oscillation was arbitrarily judged to be unsatisfactory and the control port lateral offset, $b' = 0.5$, was selected on this basis. The control port width, $d_c' = 1$, was selected in preference to a smaller value because it was believed to provide a better terminal impedance match for the control port inlet passages. The splitter distance, $L' = 6.5$, was selected in preference to higher values because it exhibited less hysteresis and better pressure recovery during the static switching tests. The wall angle, θ , was increased from 10° to 12° to improve the bistability or the division of flow between the receiver channels. Although this configuration is not necessarily optimal, it provided a suitable arrangement to investigate the several control circuit configurations and the many combinations of operating conditions of interest.

Some of the static switching characteristics of the fluid amplifier configuration selected are shown in Figure 26. It is seen that the hysteresis, or the increment in the control pressure difference required to complete the switching action, is small (of the order of $.004 p_n$). The discontinuity in the control port flow/pressure characteristic curve resulting from switching is small. This is believed to be the characteristic responsible for the absence of any switching feedback effect. The pressure recoveries in the active and inactive receiver channels are approximately 50% and 25% of the power jet dynamic pressure, resulting in a pressure difference across the receiver channels of approximately 25% of the power jet dynamic pressure. The static pressure gain, defined as the change in the receiver pressure difference divided by the change in the control port pressure difference required for switching, is of the order of 50. All of these data are for an overall pressure ratio, $p_o' = .7$.

The results obtained with the sensor configurations tested indicate that good switching performance is possible with input pressure pulses of magnitude less than $.05 p_n$ over a fairly wide range of operating conditions ($p_n = 25$ to 75 psia; $p_o/p_n = .7$ to $.9$; $\bar{p}_r/p_n = .6$ to $.95$; $f = 50$ to 1000 cps). All tests to date were performed at room temperature. A series of tests is planned at high temperatures (up to $1280^\circ R$) simulating the environmental conditions in a jet engine compressor.

Table I Sensor Operating Conditions

Operating Parameter	Symbol	Values Tested	Values for Scope Photographs	
			Figs. 8 to 15	Fig. 17
Power nozzle supply pressure	p_n	25, 50, 75 psia = 1.0*	25 psia	20 psia
Load pressure level	p'_o	.7, .8, .9	Noted	.72
Average control pressure (approx. equal to average input pressure level)	$\overline{p'_c}$.6, .7, .8, .9, .95, 1.0	Noted	.76
Average pressure difference across control ports (Configuration I)	$\overline{p'_{el} - p'_{ea}}$	-.01 to .03	0	0
Input signal pulse amplitude	$ p'_i $	0 to .10	.05	.025
Input signal duty cycle	d	.33, .55	.33	.55
Input signal frequency	f	0 and 50-1100 cps	50-1100	50-1000
Temperature		Room Temperature		

* Note: Pressures are nondimensionalized in terms of power nozzle supply pressure.

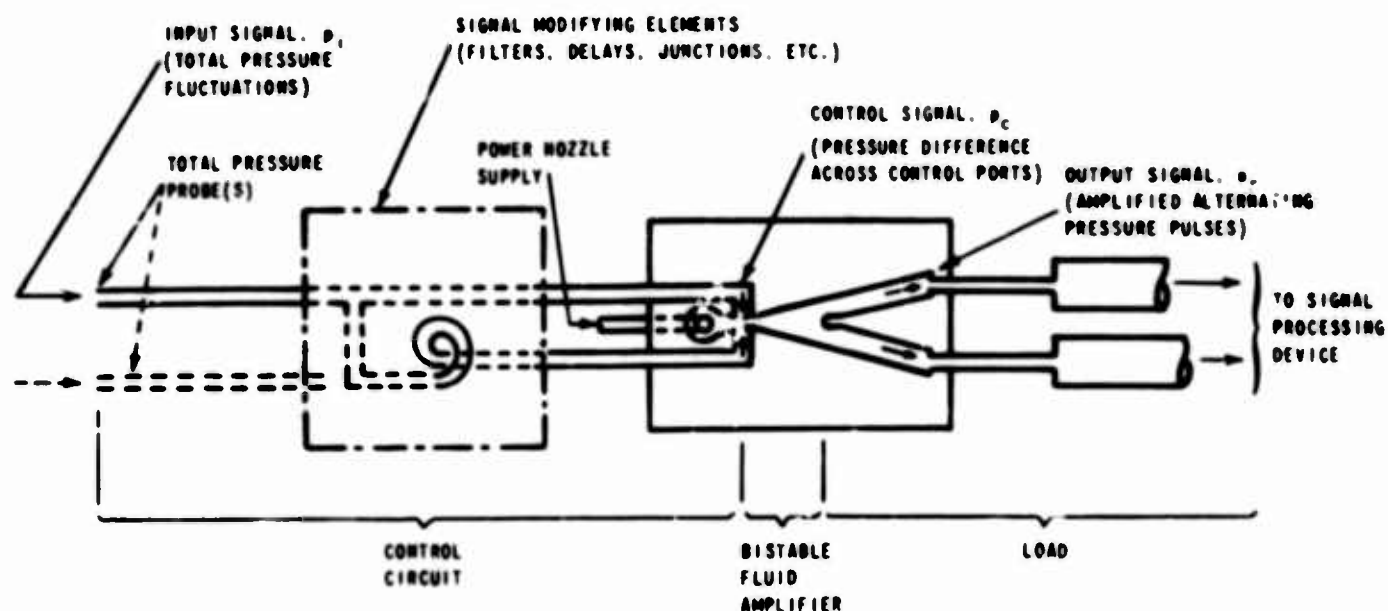


Figure 1 FLOW-INSTABILITY SENSOR

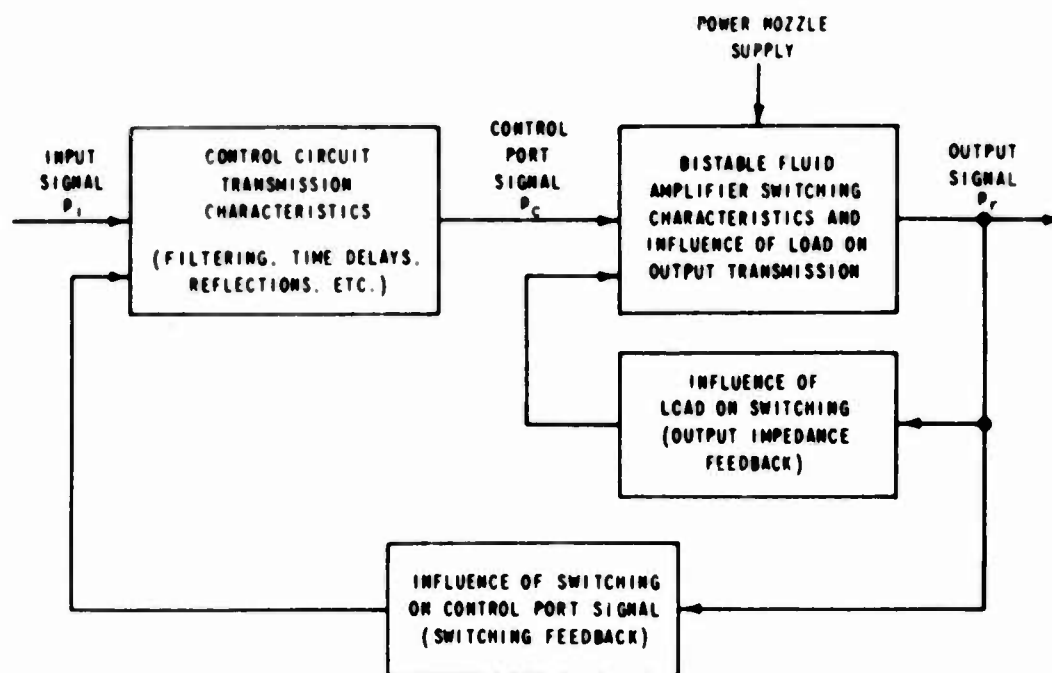


Figure 2 FLOW-INSTABILITY SENSOR FUNCTIONAL SCHEMATIC

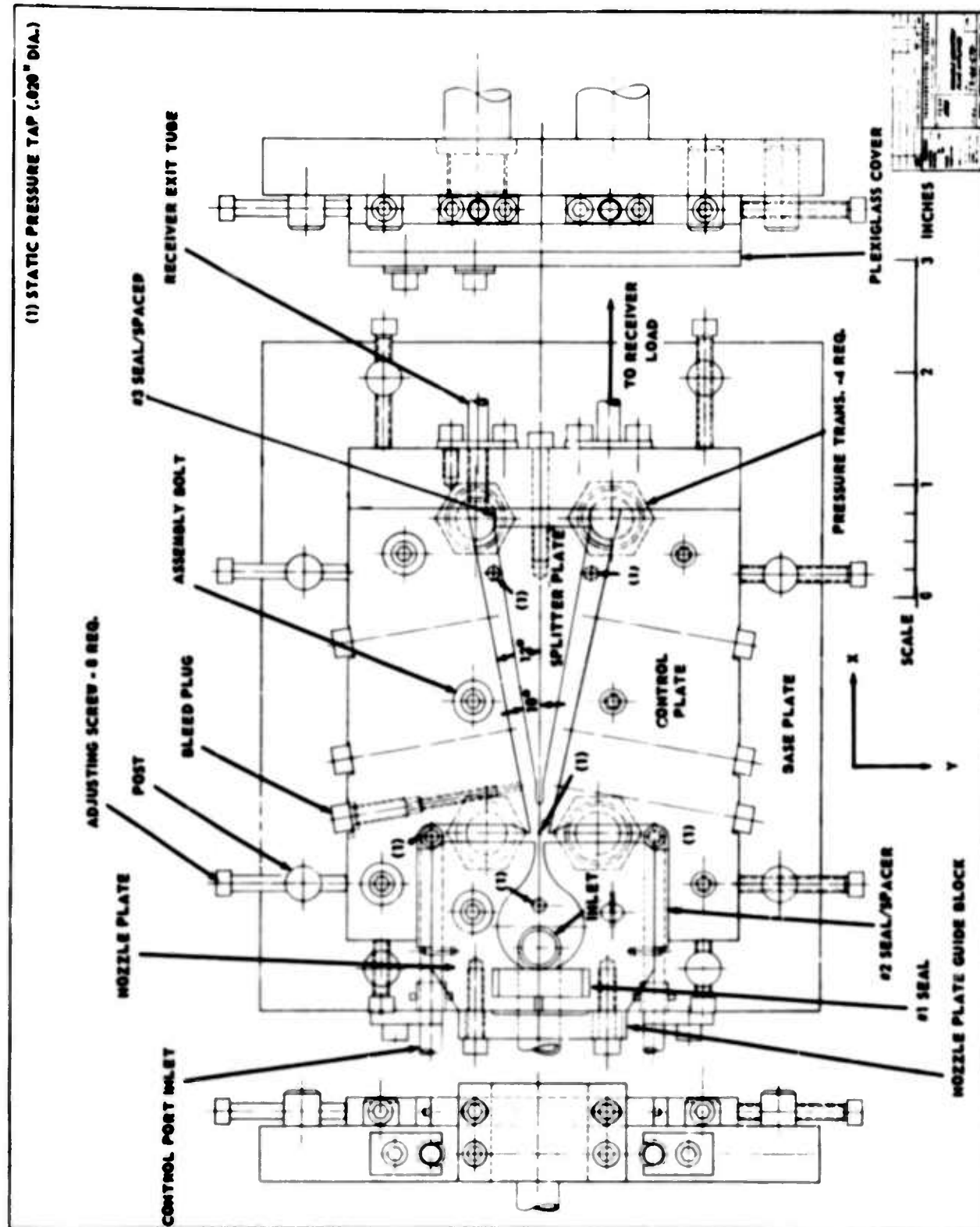
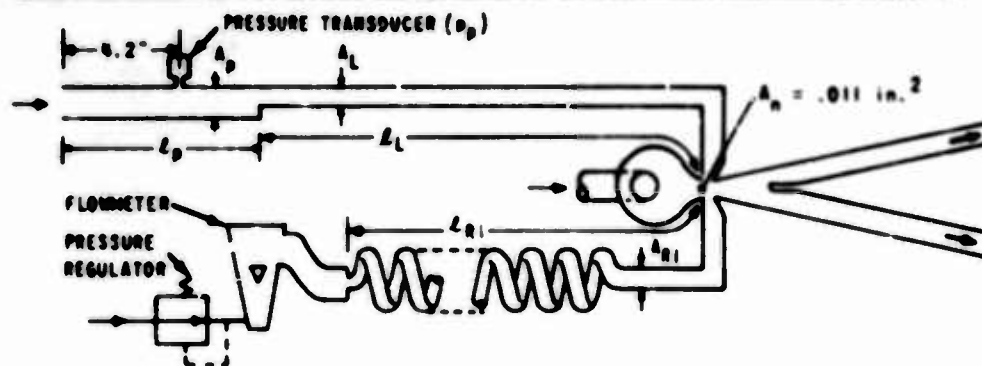


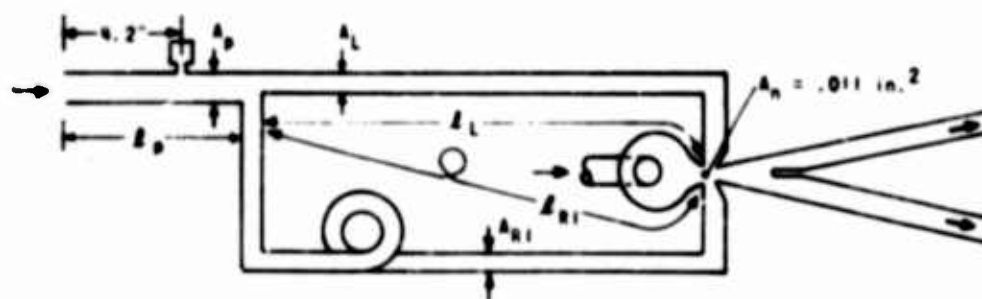
Figure 3 VARIABLE GEOMETRY BISTABLE FLUID AMPLIFIER



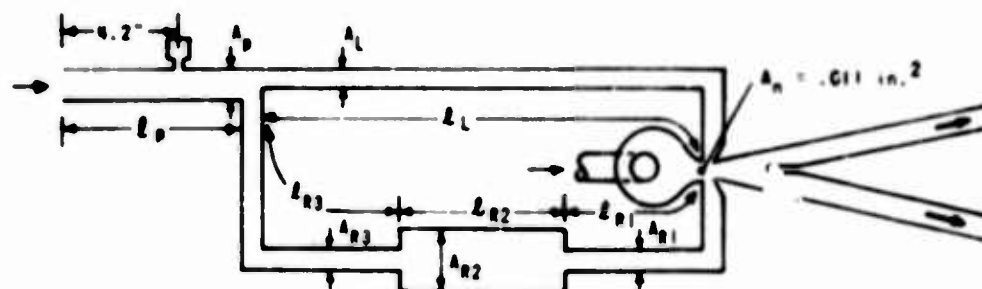
GEOMETRIC CONFIGURATION	L_p in.	L_L in.	L_{R1} in.	L_{R2} in.	L_{R3} in.	$\frac{A_p}{A_n}$	$\frac{A_L}{A_n}$	$\frac{A_{R1}}{A_n}$	$\frac{A_{R2}}{A_n}$	$\frac{A_{R3}}{A_n}$
I-1	6.5	17.5	4.0	-	-	2.55	2.4	2.4	-	-
I-2	7.4	10.1	12.00	-	-	4.55	2.10	2.10	-	-
II-1	8.0	10.0	26.0	-	-	2.55	1.03	1.03	-	-
II-2	7.4	10.1	26.1	-	-	4.55	2.10	2.10	-	-
III-1	8.0	26.0	10.0	3.0	14.0	2.55	1.03	1.03	100	1.03
III-2	7.4	10.1	5.3	7.0	14.0	4.55	2.10	2.10	10.3	2.10
IV-1	7.4	12.1	13.4	6.7	6.7	4.55	2.10	2.10	10.3	2.10



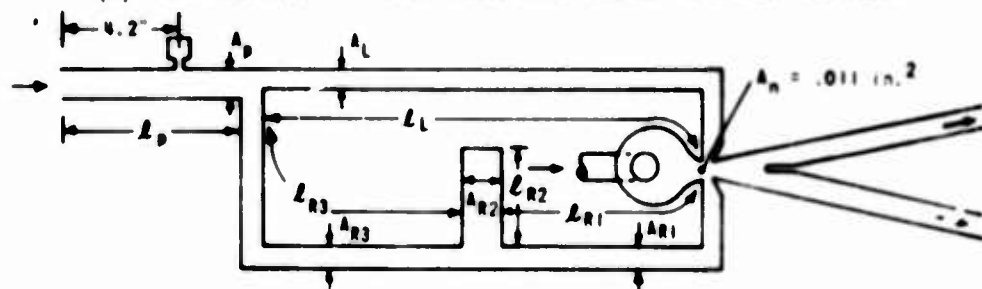
(a) CONFIGURATION I - INDEPENDENT CONTROL BIAS (RESEARCH CONFIGURATION)



(b) CONFIGURATION II - SPLIT PROBE WITH TIME DELAY



(c) CONFIGURATION III - SPLIT PROBE WITH IN-LINE FILTER AND TIME DELAY



(d) CONFIGURATION IV - SPLIT PROBE WITH BRANCH FILTER AND TIME DELAY

Figure 5 CONTROL CIRCUIT CONFIGURATIONS TESTED

GEOMETRIC PARAMETER	SYMBOL	VALUES TESTED	VALUES FOR TEST DATA PRESENTED	
			FIGURES 8 TO 16	FIGURE 17
FLUID AMPLIFIER PARAMETERS				
POWER NOZZLE WIDTH	d_n	.043 IN. = 1.00°	1.00	1.00
POWER NOZZLE AREA	A_n	.011 IN. ² = 1.00°	1.00	1.00
CONTROL NOZZLE WIDTH	d_c^1	.25, .50, 1.00, 1.50, 2.00	1.00	1.00
CONTROL NOZZLE LATERAL OFFSET FROM CENTERLINE	b^1	.50, .75, 1.00, 1.25, 1.50, 2.00	.50	1.00
SPLITTER DISTANCE FROM EDGE OF CONTROL NOZZLE	L^*	6.5, 10, 13.5	6.5	10
WALL ANGLE FROM CENTERLINE	θ	10°, 12°	12°	10°
LOAD PARAMETERS				
RECEIVER LENGTH	l_r		2.60 IN.	2.44 IN.
CONNECTING TUBE LENGTH	l_t		2.8 IN.	5.5 IN.
RECEIVER AREAS (DEPENDENT ON FLUID AMPLIFIER GEOMETRY)	A_{r1}^1		0.1	-
	A_{r2}^1		4.6	-
CONNECTING TUBE AREA	A_t^1		2.0	2.0
OUTLET TUBE AREA	A_o^1		10.0	10.0

*NOTE: LINEAR DIMENSIONS AND AREAS WITH PRIMED SYMBOLS ARE NONDIMENSIONALIZED IN TERMS OF THE POWER NOZZLE WIDTH AND AREA e.g., $b^1 = \frac{b}{d_n}$.

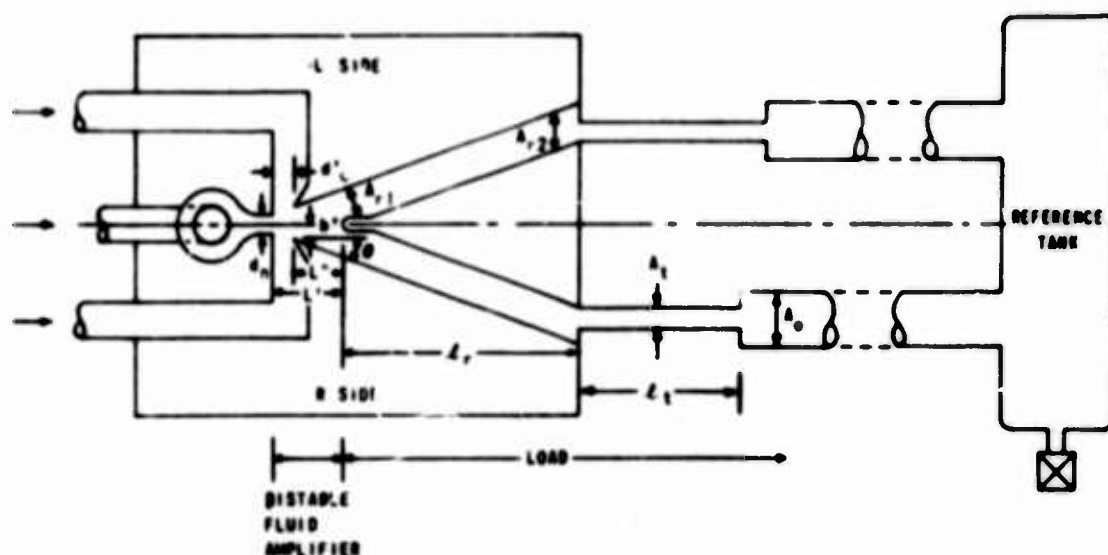
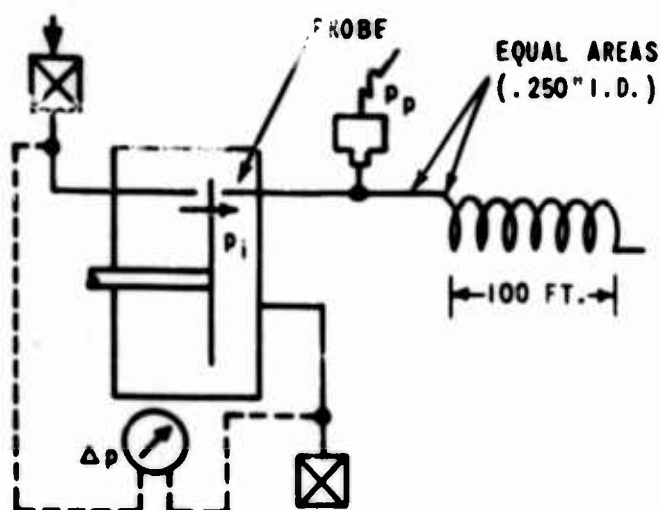
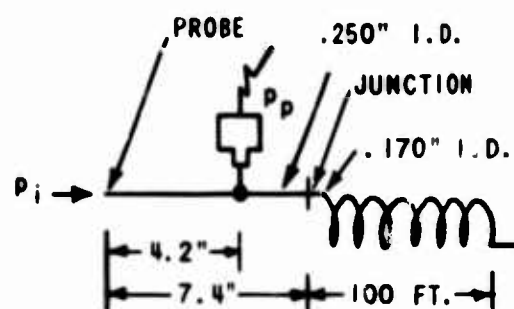


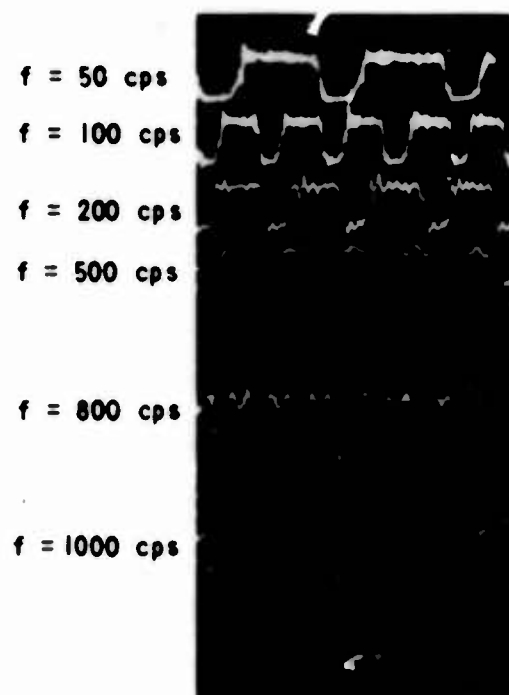
Figure 6 BISTABLE FLUID AMPLIFIER AND LOAD CONFIGURATION TESTED



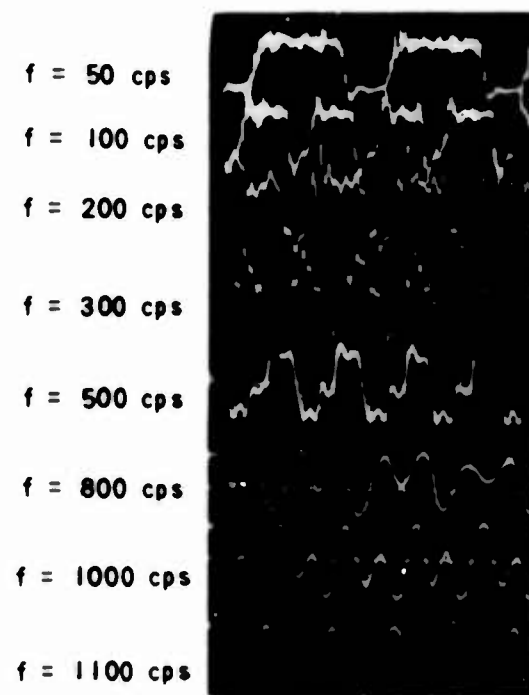
(a) SIGNAL CALIBRATION ARRANGEMENT



(b) ARRANGEMENT FOR PHOTO (d)



(c) SENSOR INPUT SIGNAL FOR FIGURES 8 TO 15
(PROBE PRESSURE WITH NO DOWNSTREAM
REFLECTIONS)



(d) PROBE PRESSURE WITH REFLECTION
DUE TO JUNCTION ONLY

OPERATING CONDITIONS FOR SCOPE PHOTOGRAPHS OF SENSOR PERFORMANCE

$$p_n = 25 \text{ PSIA}$$

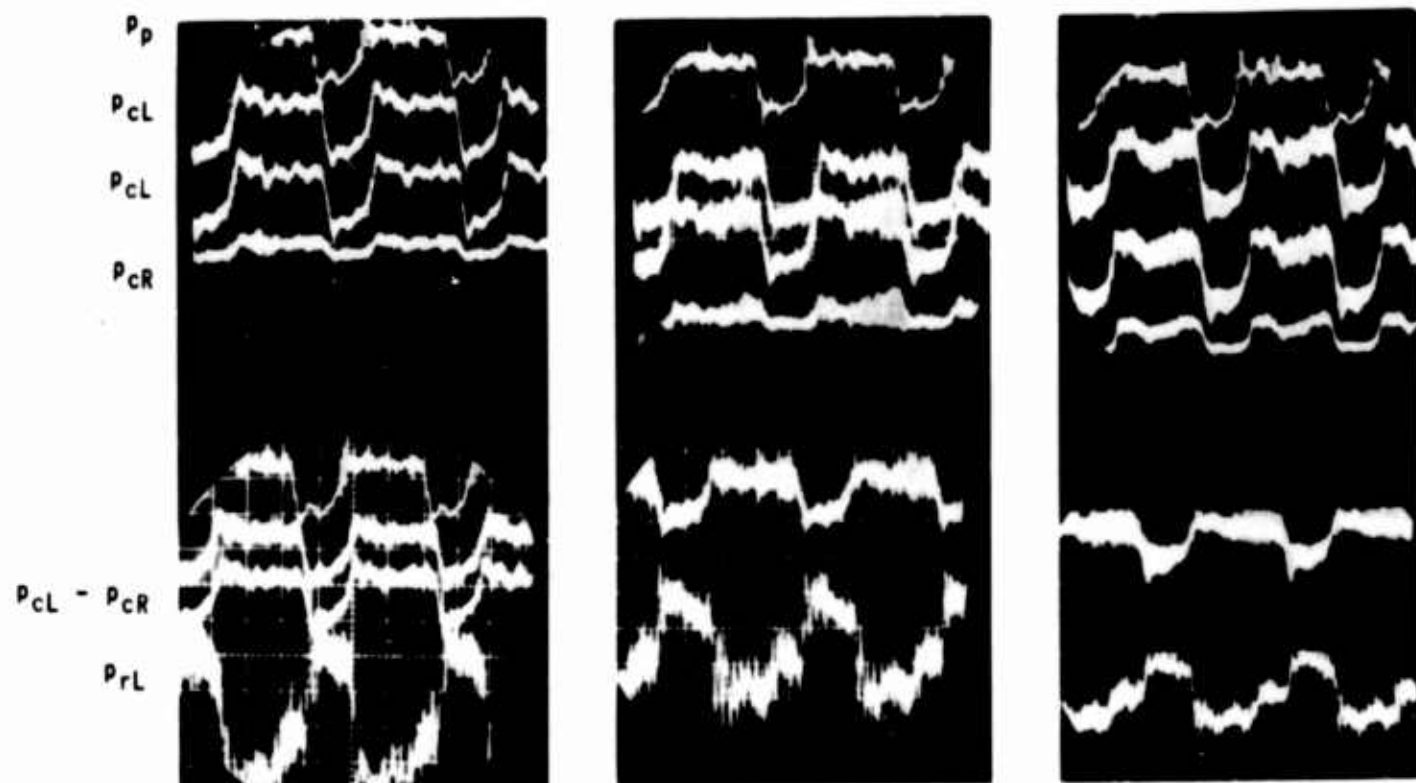
$$p_o' = .7 \text{ (EXCEPT AS NOTED)}$$

$$\overline{p_c'} = p_o'$$

$$\overline{p_{CL}} - p_{CR} = 0 \text{ (C.C.C. I-2)}$$

$$d = .33 \text{ (EXCEPT AS NOTED)}$$

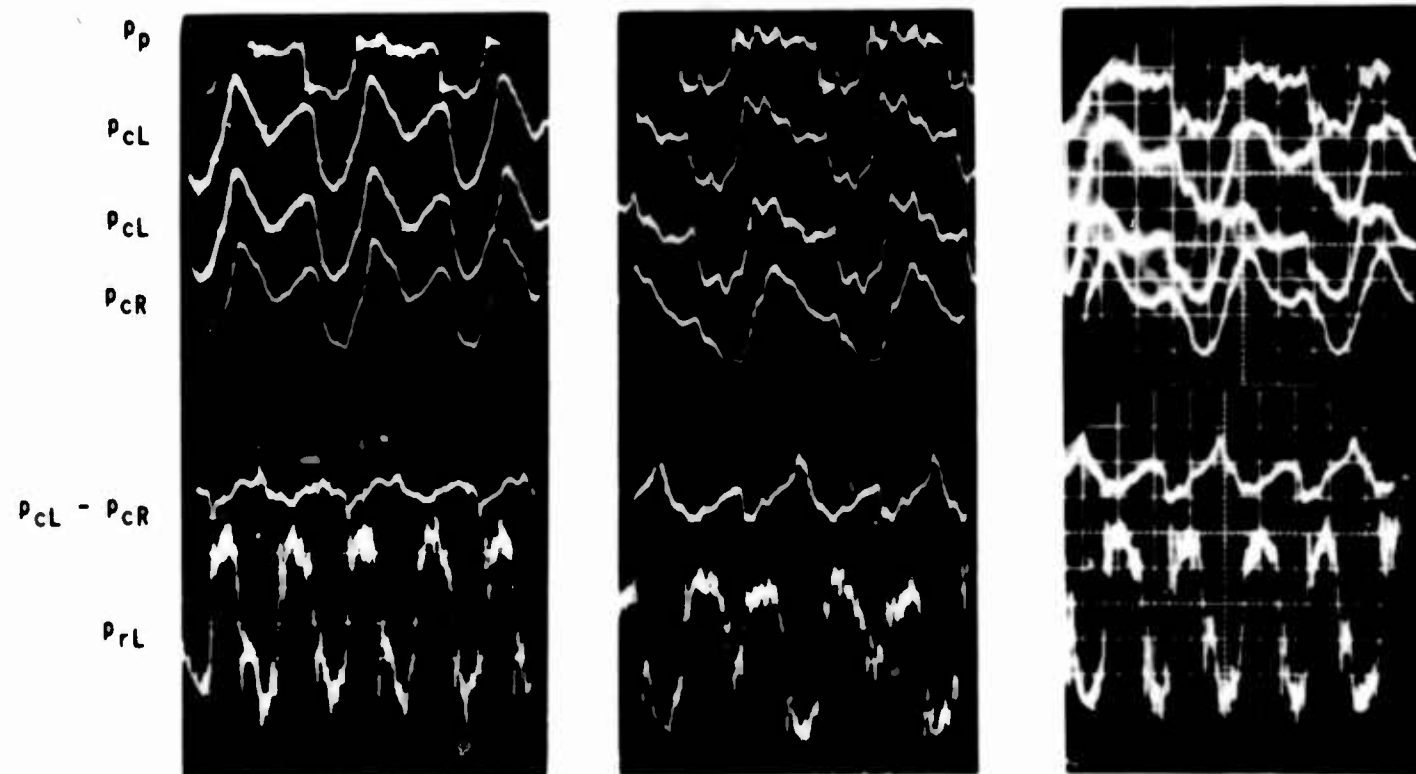
Figure 7 OPERATING CONDITIONS AND INPUT SIGNAL CALIBRATION
FOR SENSOR PERFORMANCE SCOPE PHOTOGRAPHS



(a) C.C. CONFIG. I-2
 $P'_0 = \overline{P'_{CL}} = \overline{P'_{CR}} = .7$

(b) C.C. CONFIG. I-2
 $P'_0 = \overline{P'_{CL}} = \overline{P'_{CR}} = .8$

(c) C.C. CONFIG. I-2
 $P'_0 = \overline{P'_{CL}} = \overline{P'_{CR}} = .9$



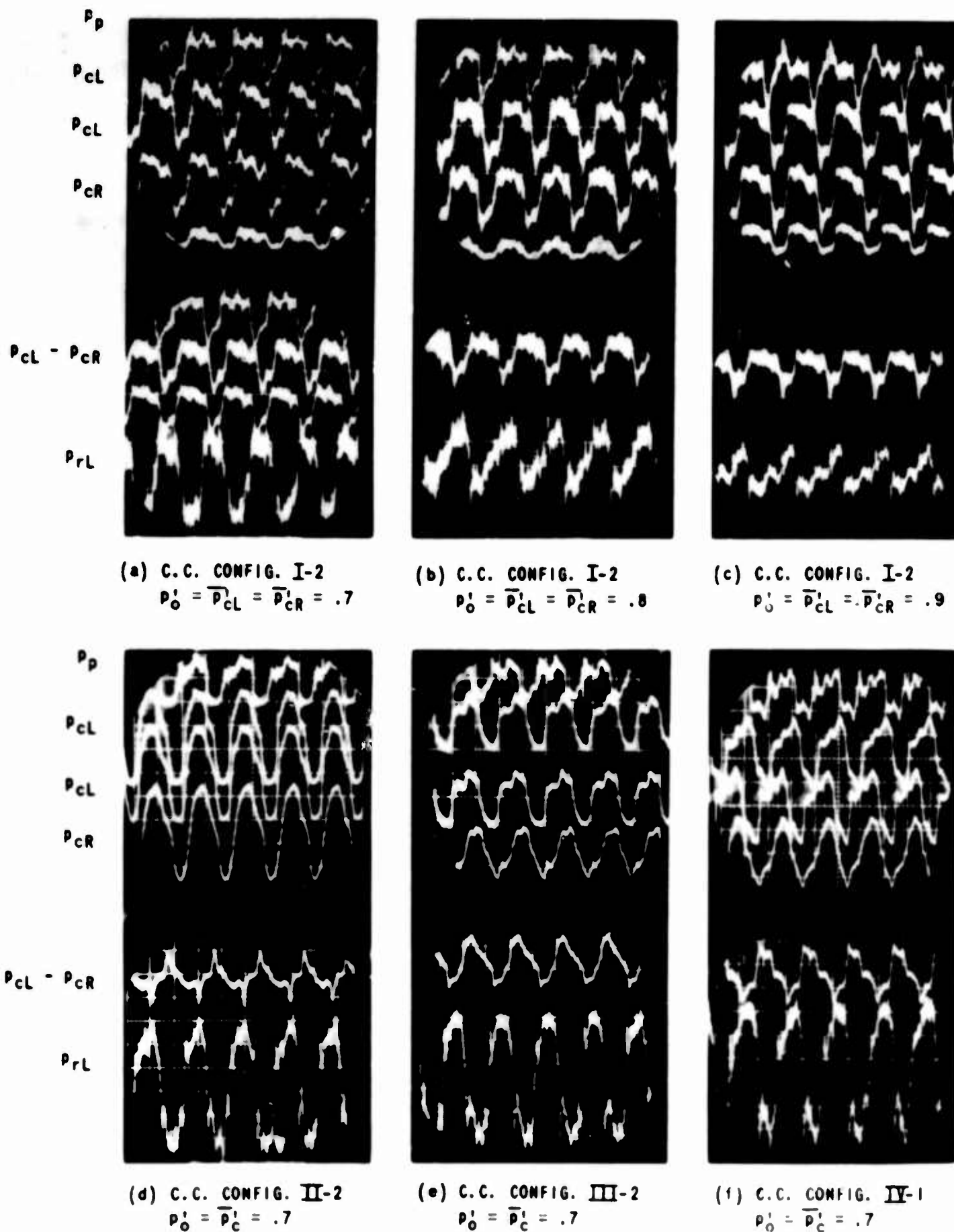
(d) C.C. CONFIG. II-2
 $P'_0 = \overline{P'_C} = .7$

(e) C.C. CONFIG. III-2
 $P'_0 = \overline{P'_C} = .7$

(f) C.C. CONFIG. IV-1
 $P'_0 = \overline{P'_C} = .7$

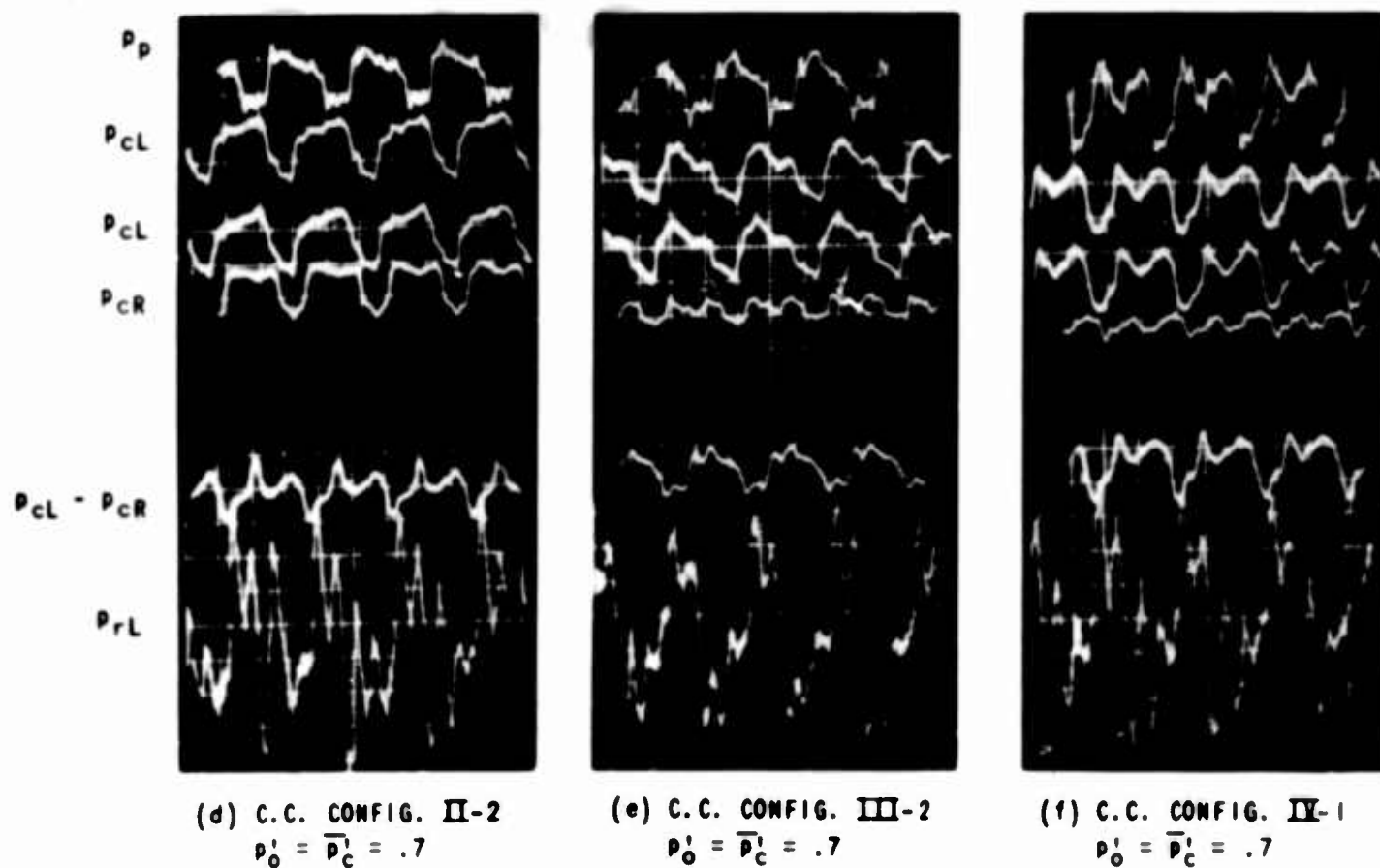
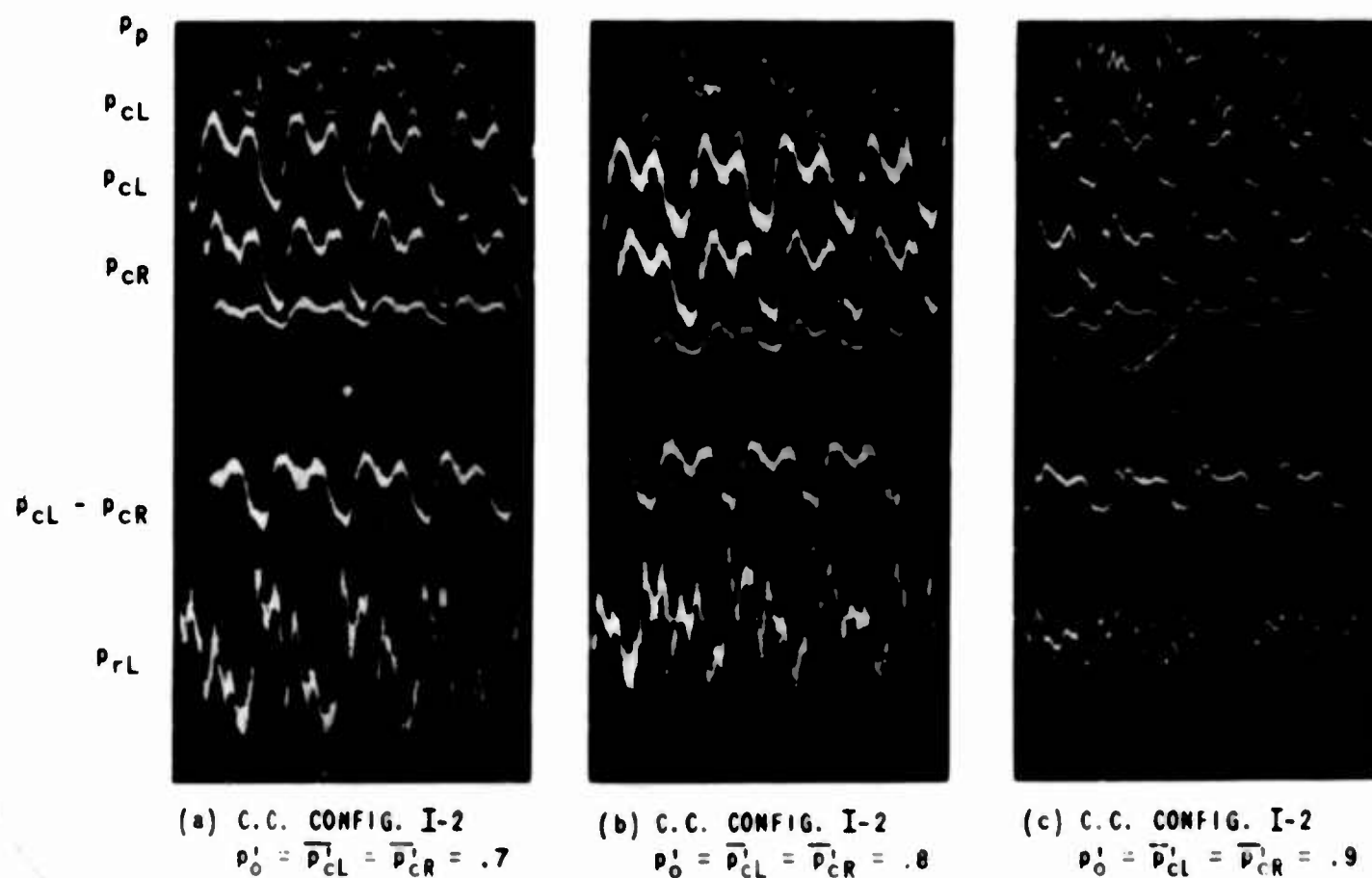
VERTICAL SCALE: 1 cm = 1 psi = .04 P_n

Figure 8 PERFORMANCE COMPARISON OF SENSOR CONFIGURATIONS AT 50 cps



VERTICAL SCALE: 1 cm = 1 psi = .04 p_n

Figure 9 PERFORMANCE COMPARISON OF SENSOR CONFIGURATIONS AT 100 cps



VERTICAL SCALE: 1 cm = 1 psi = .04 p_n

Figure 10 PERFORMANCE COMPARISON OF SENSOR CONFIGURATIONS AT 200 cps

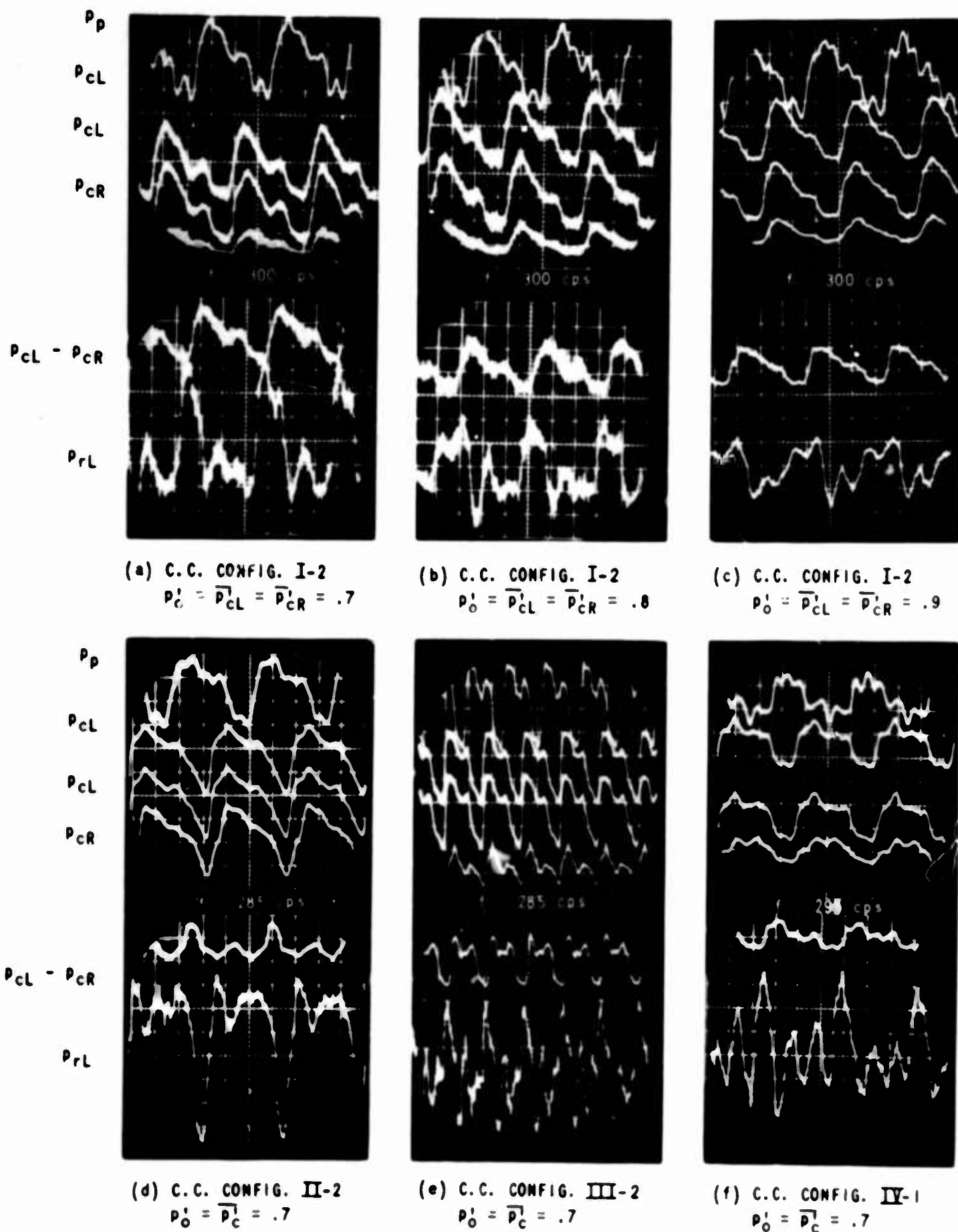
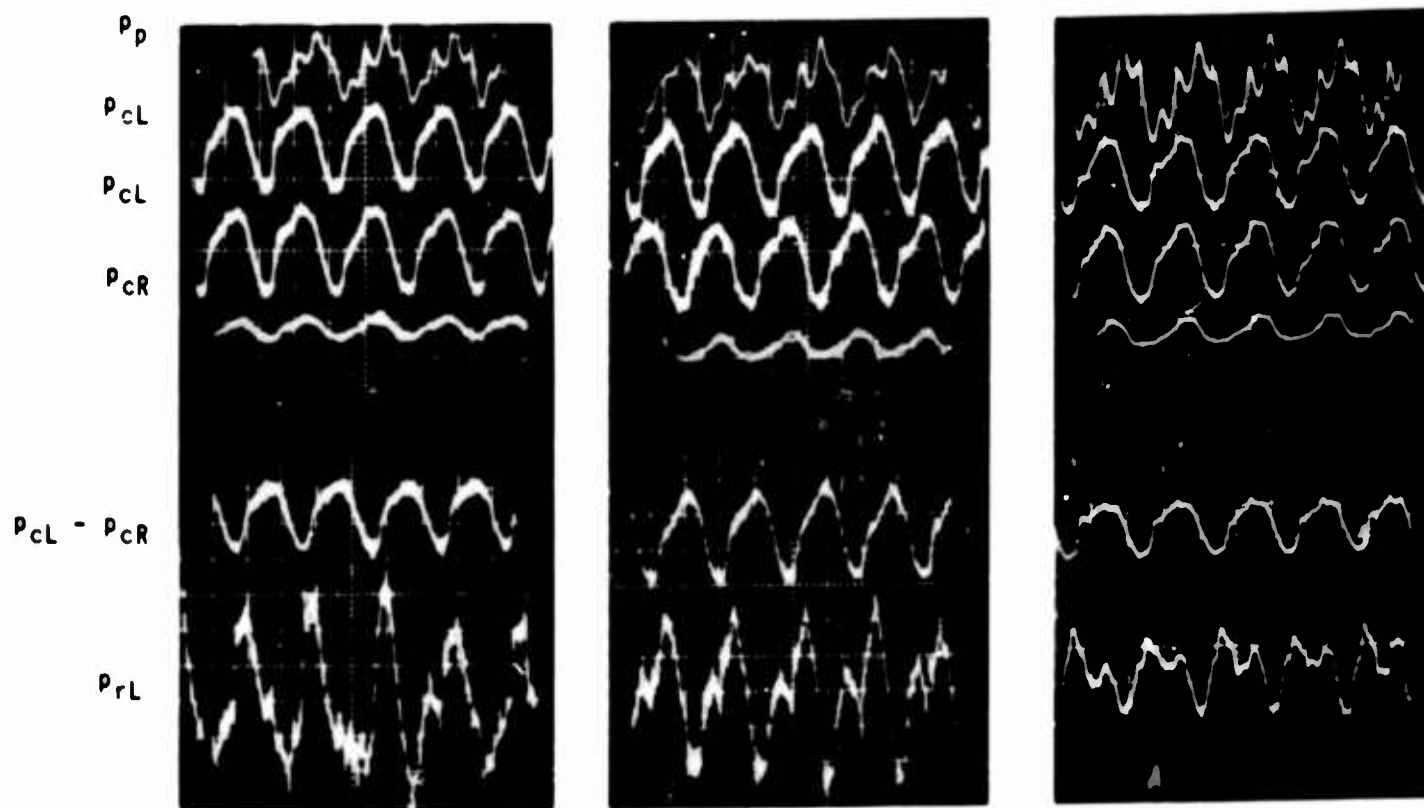


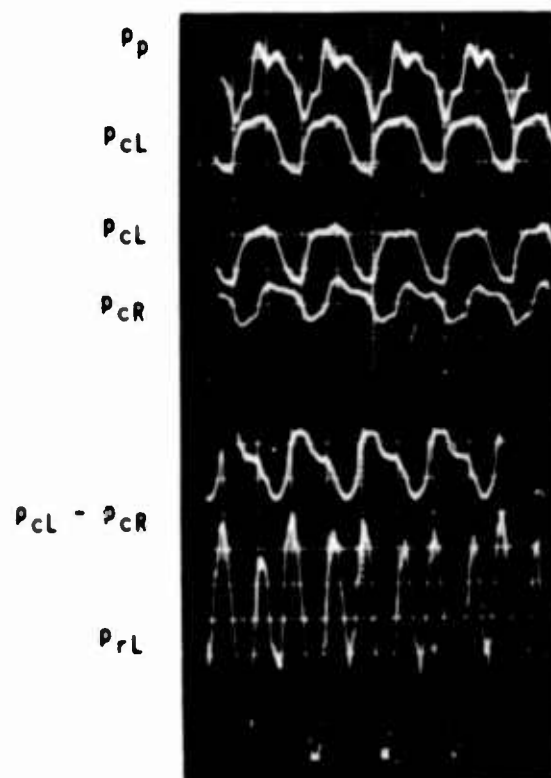
Figure 11 PERFORMANCE COMPARISON OF SENSOR CONFIGURATIONS AT 285 - 300 cps



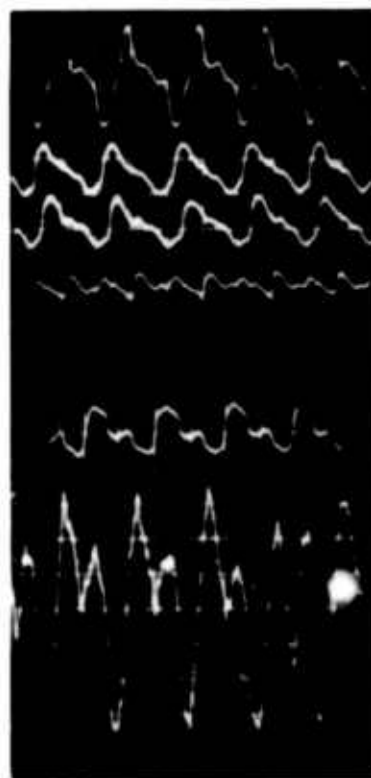
(a) C.C. CONFIG. I-2
 $p'_0 = \overline{p'_{cL}} = \overline{p'_{cR}} = .7$

(b) C.C. CONFIG. I-2
 $p'_0 = \overline{p'_{cL}} = \overline{p'_{cR}} = .8$

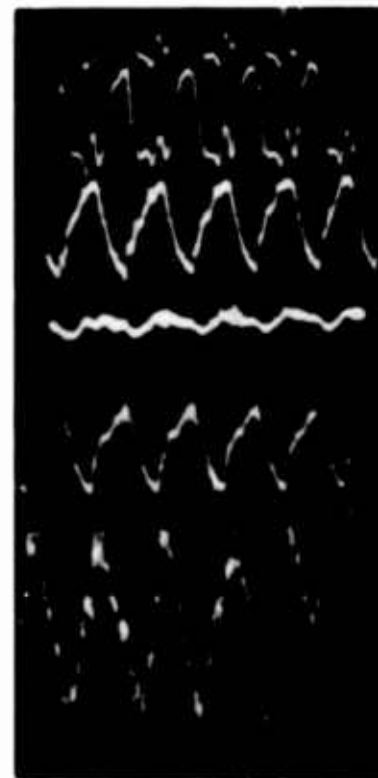
(c) C.C. CONFIG. I-2
 $p'_0 = \overline{p'_{cL}} = \overline{p'_{cR}} = .9$



(d) C.C. CONFIG. II-2
 $p'_0 = \overline{p'_c} = .7$



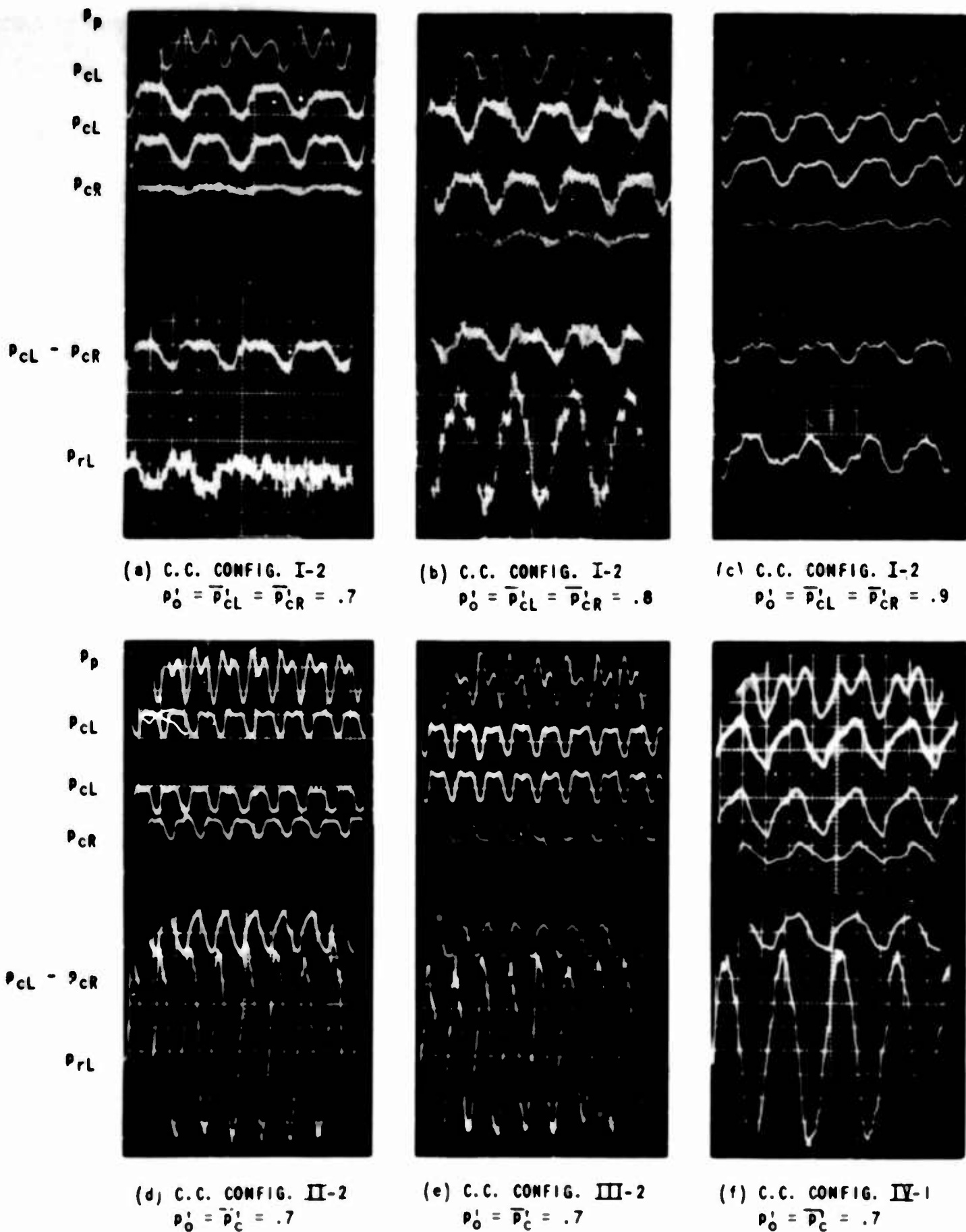
(e) C.C. CONFIG. III-2
 $p'_0 = \overline{p'_c} = .7$



(f) C.C. CONFIG. IV-1
 $p'_0 = \overline{p'_c} = .7$

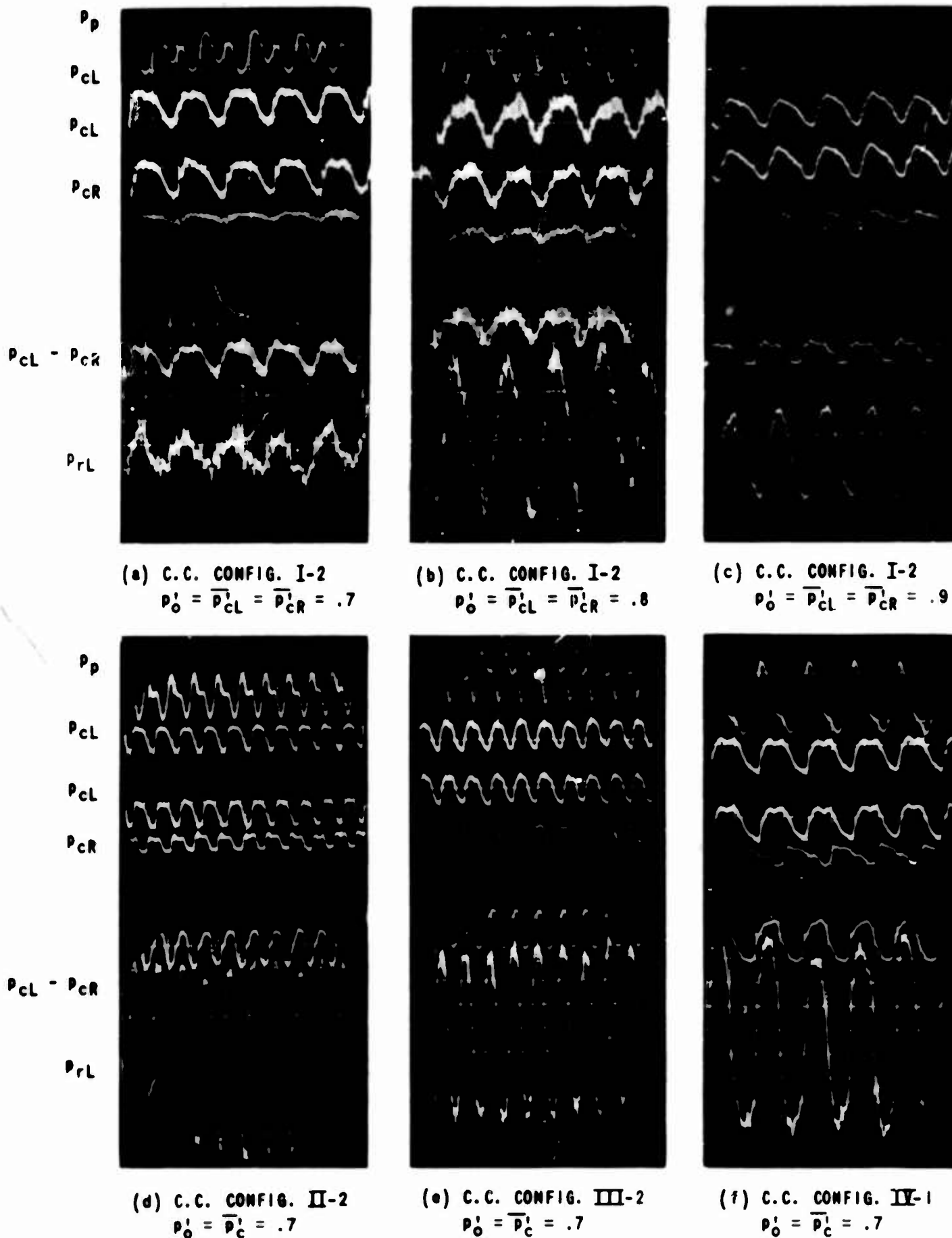
VERTICAL SCALE: 1 cm = 1 psi = .04 p_n

Figure 12 PERFORMANCE COMPARISON OF SENSOR CONFIGURATIONS AT 500 cps



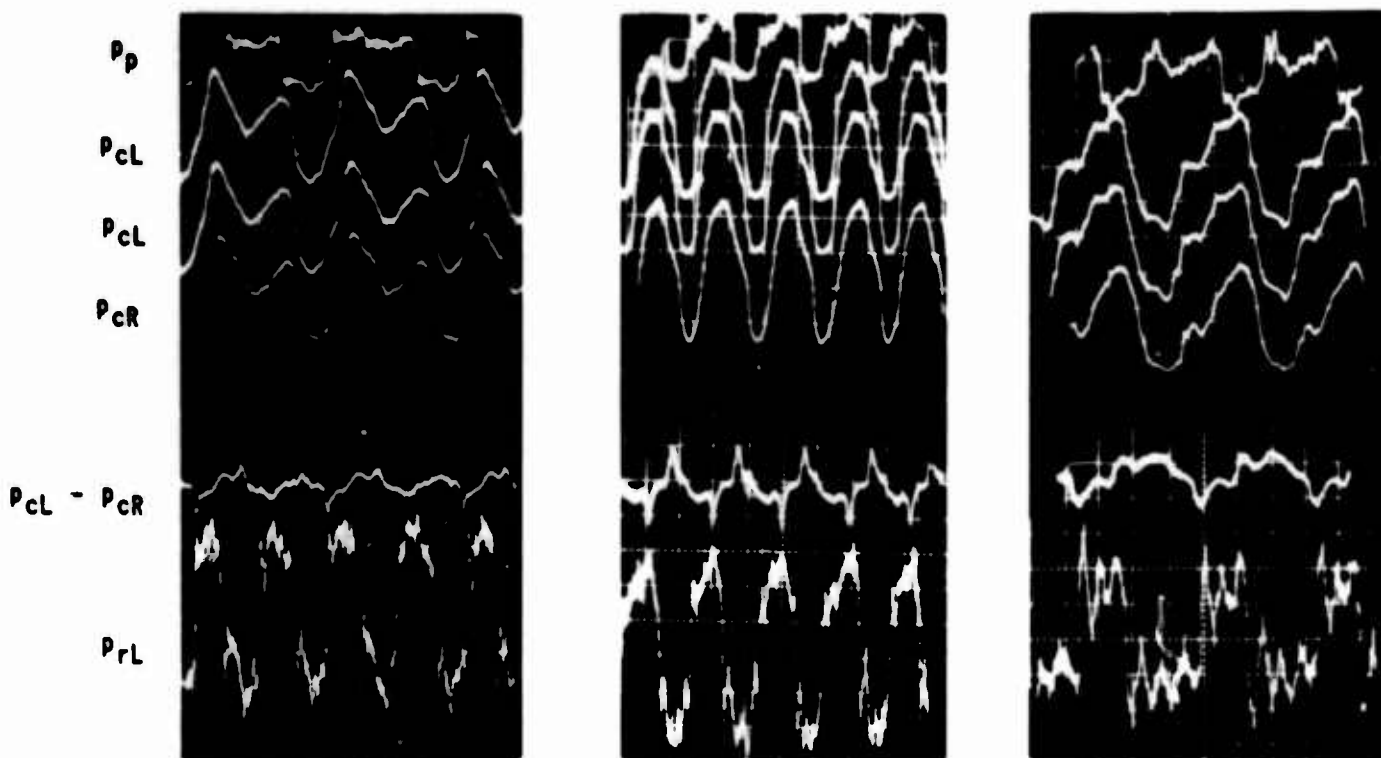
VERTICAL SCALE: 1 cm = 1 ; si = .04 P_n

Figure 13 PERFORMANCE COMPARISON OF SENSOR CONFIGURATIONS AT 800 cps



VERTICAL SCALE: 1 cm = 1 psi = .04 p_n

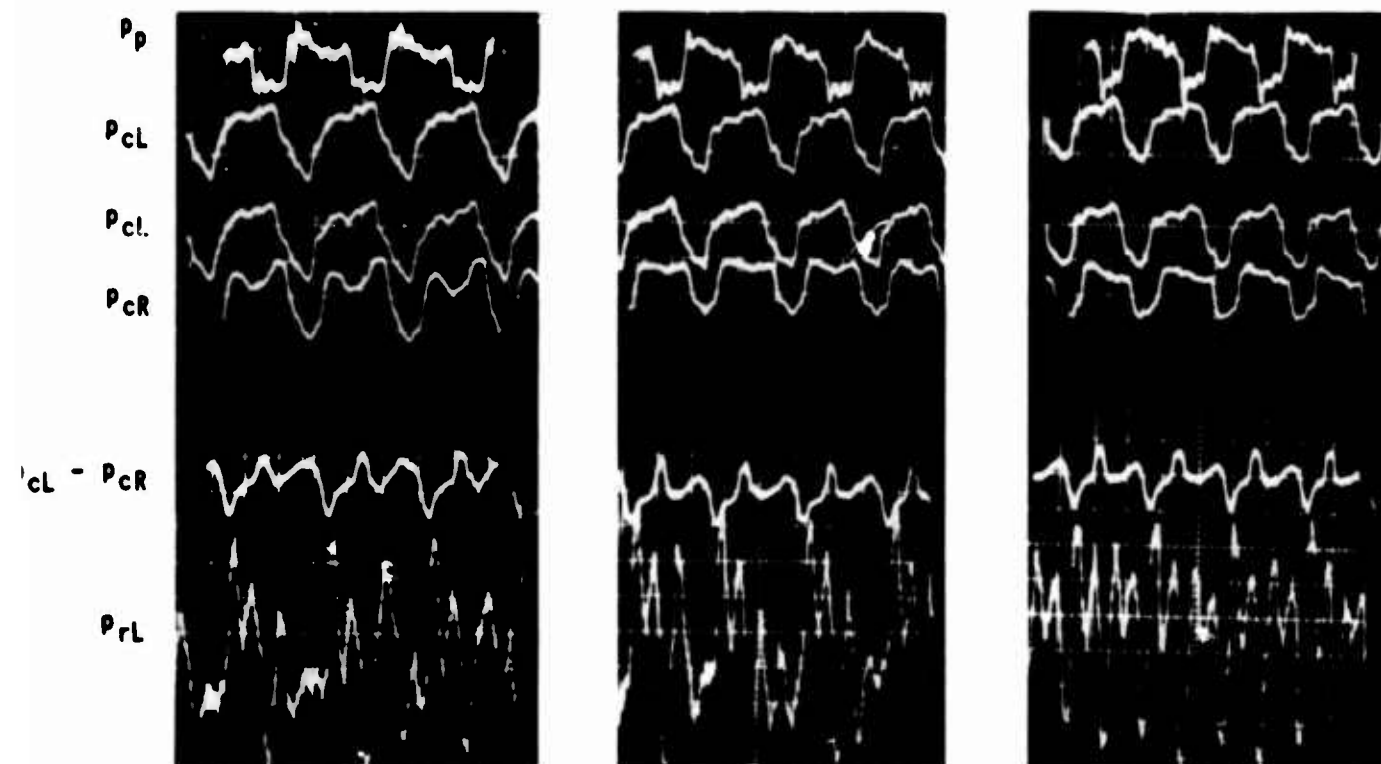
Figure 14 PERFORMANCE COMPARISON OF SENSOR CONFIGURATIONS AT 1000 cps



(a) $f = 50$ cps

(b) $f = 100$ cps

(c) $f = 145$ cps



(d) $f = 170$ cps

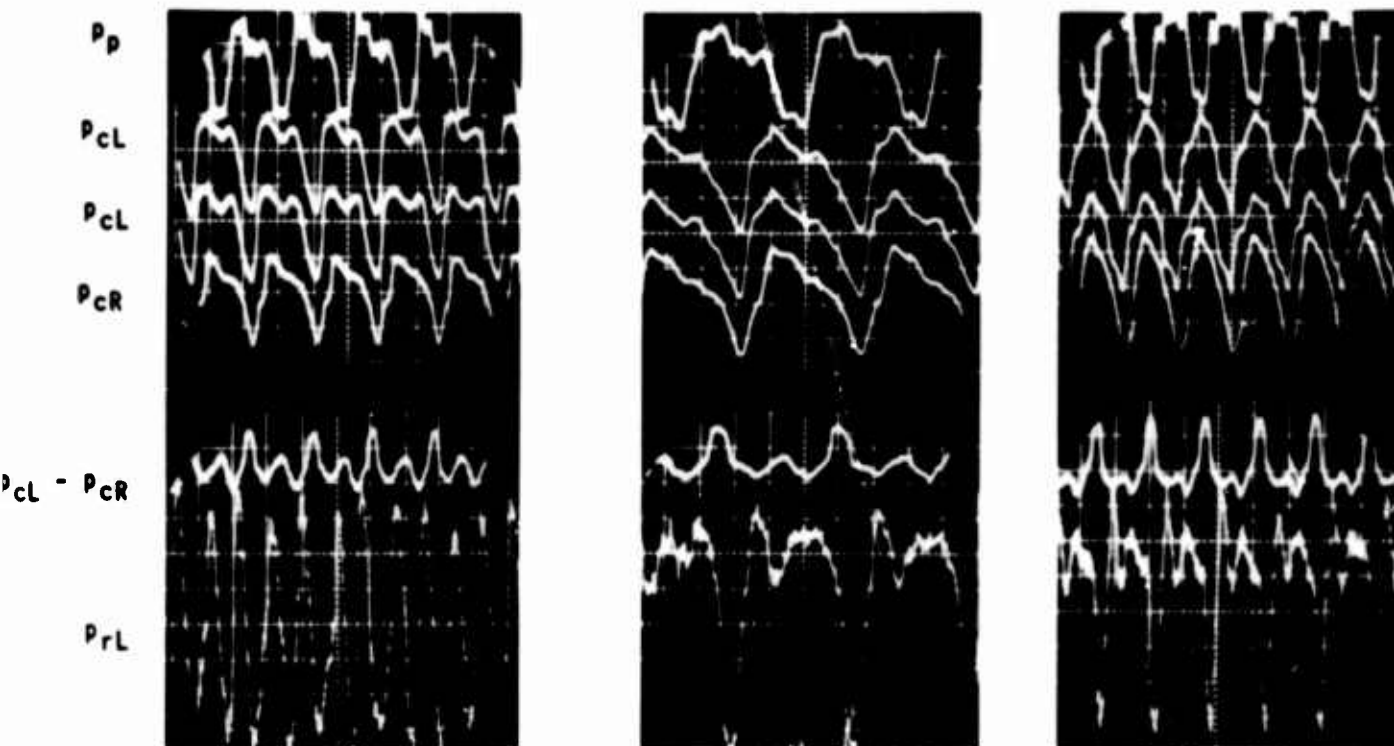
(e) $f = 200$ cps

(f) $f = 220$ cps

VERTICAL SCALE: $1 \text{ cm} = 1 \text{ psi} = .04 p_n$

$$p'_0 = \overline{p'_c} = .7$$

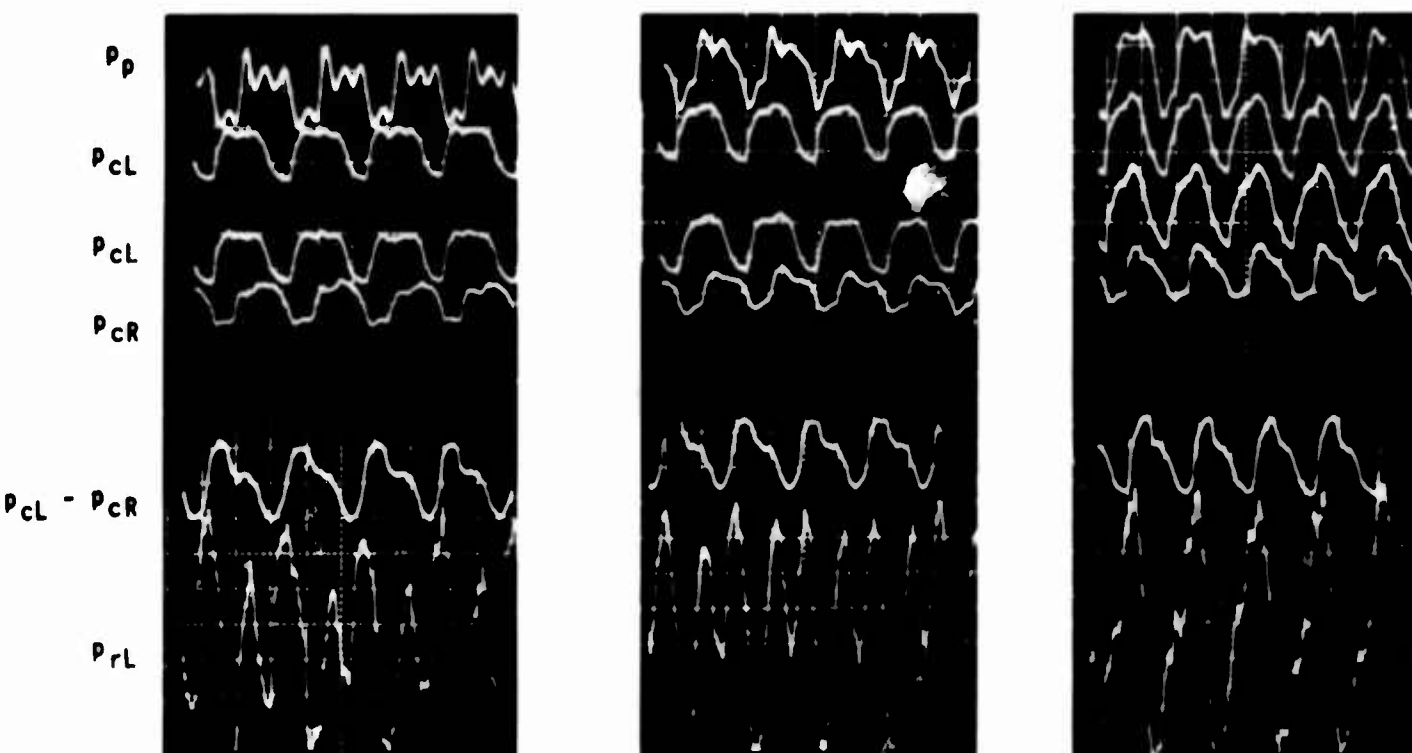
Figure 15 EFFECT OF FREQUENCY ON SENSOR PERFORMANCE WITH
CONTROL CIRCUIT CONFIGURATION 11-2



(g) $f = 275$ cps

(h) $f = 285$ cps

(i) $f = 310$ cps



(j) $f = 445$ cps

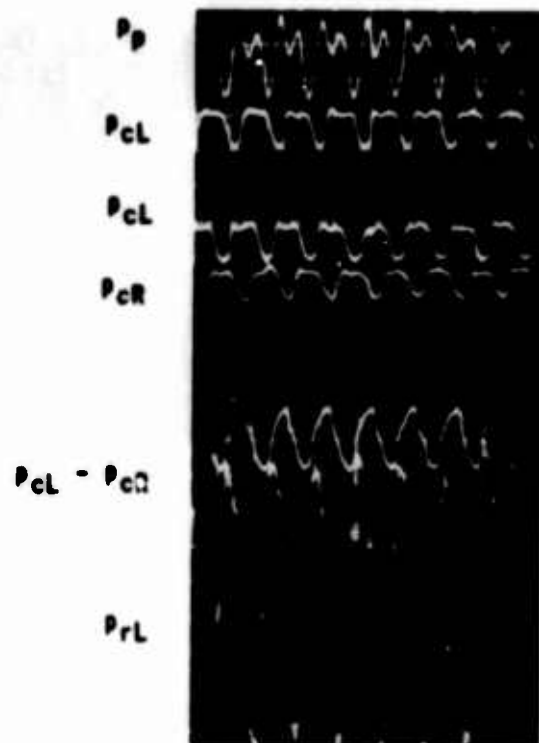
(k) $f = 500$ cps

(l) $f = 550$ cps

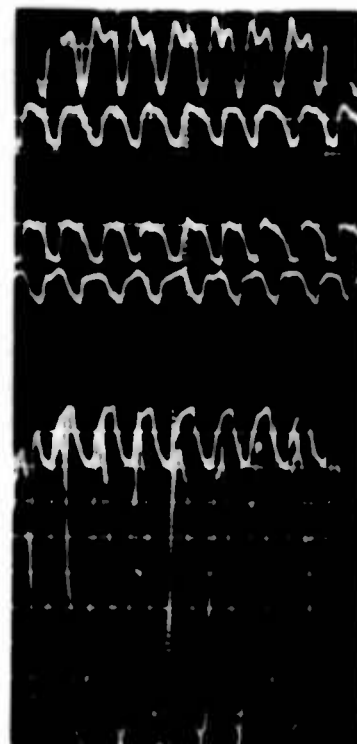
VERTICAL SCALE: $1 \text{ cm} = 1 \text{ psi} = .04 P_n$

$$P'_0 = \overline{P'_c} = .7$$

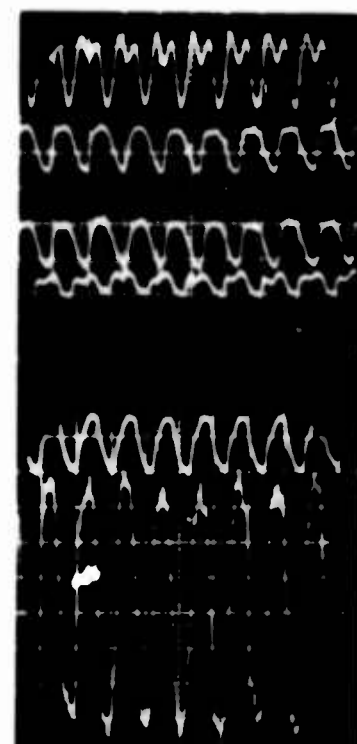
Figure 15 EFFECT OF FREQUENCY ON SENSOR PERFORMANCE WITH
CONTROL CIRCUIT CONFIGURATION 11-2 (CONT.)



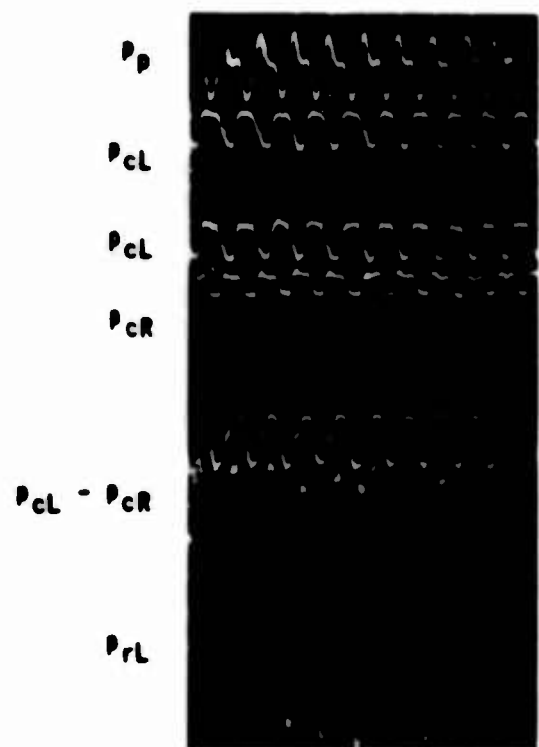
(m) $f = 800$ cps



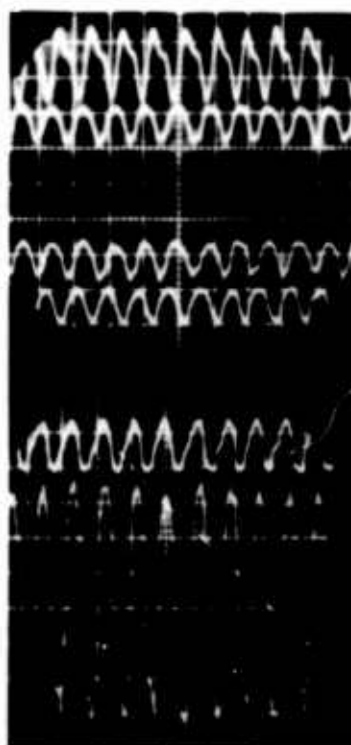
(n) $f = 870$ cps



(o) $f = 900$ cps



(p) $f = 1000$ cps

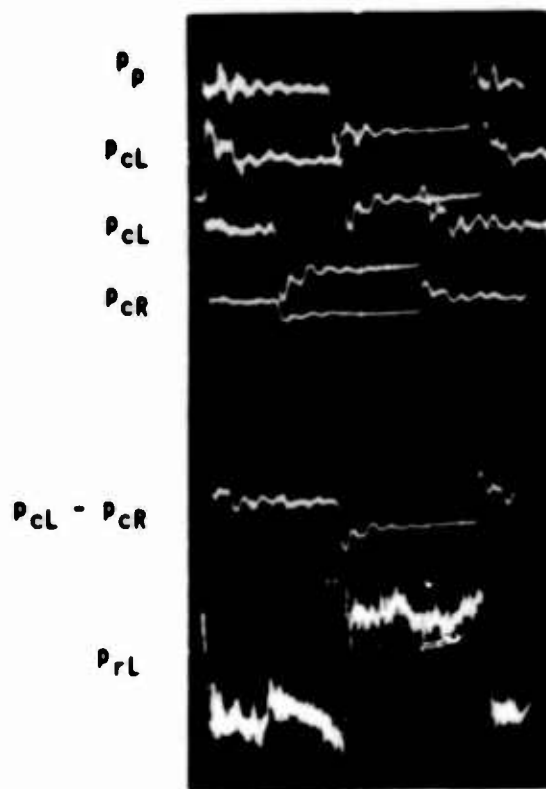


(q) $f = 1100$ cps

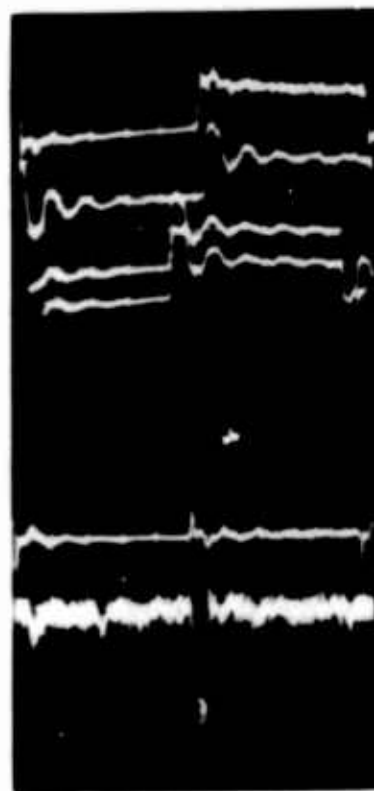
VERTICAL SCALE: $1 \text{ cm} = 1 \text{ psi} = .04 p_n$

$$p'_0 = \overline{p'_c} = .7$$

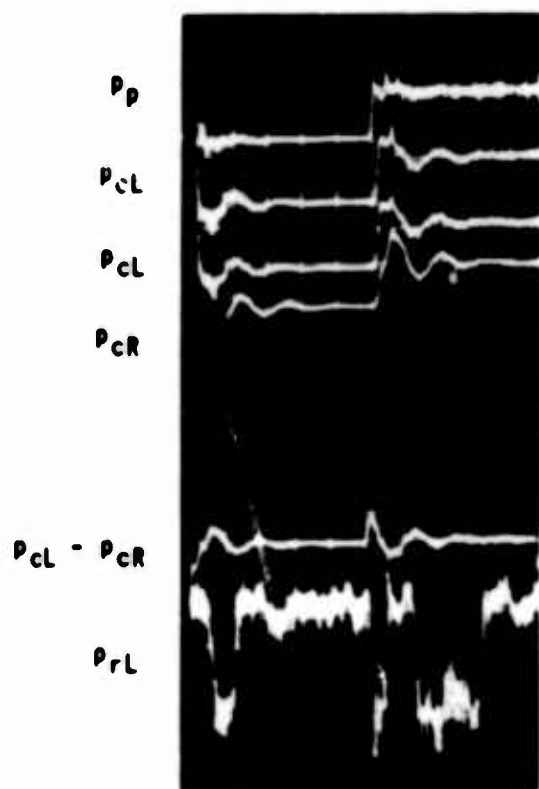
Figure 15 EFFECT OF FREQUENCY ON SENSOR PERFORMANCE WITH CONTROL CIRCUIT CONFIGURATION 11-2 (CONT.)



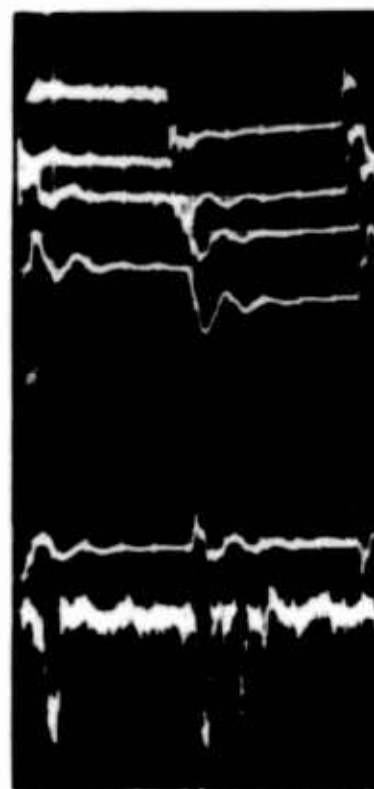
(a) C.C. CONFIG. I-2
 $f = 25 \text{ cps}$
 $p'_0 = \overline{p'_{cL}} = \overline{p'_{cR}} = .7$



(b) C.C. CONFIG. II-2
 $f = 10 \text{ cps}$
 $p'_0 = \overline{p'_c} = .7$



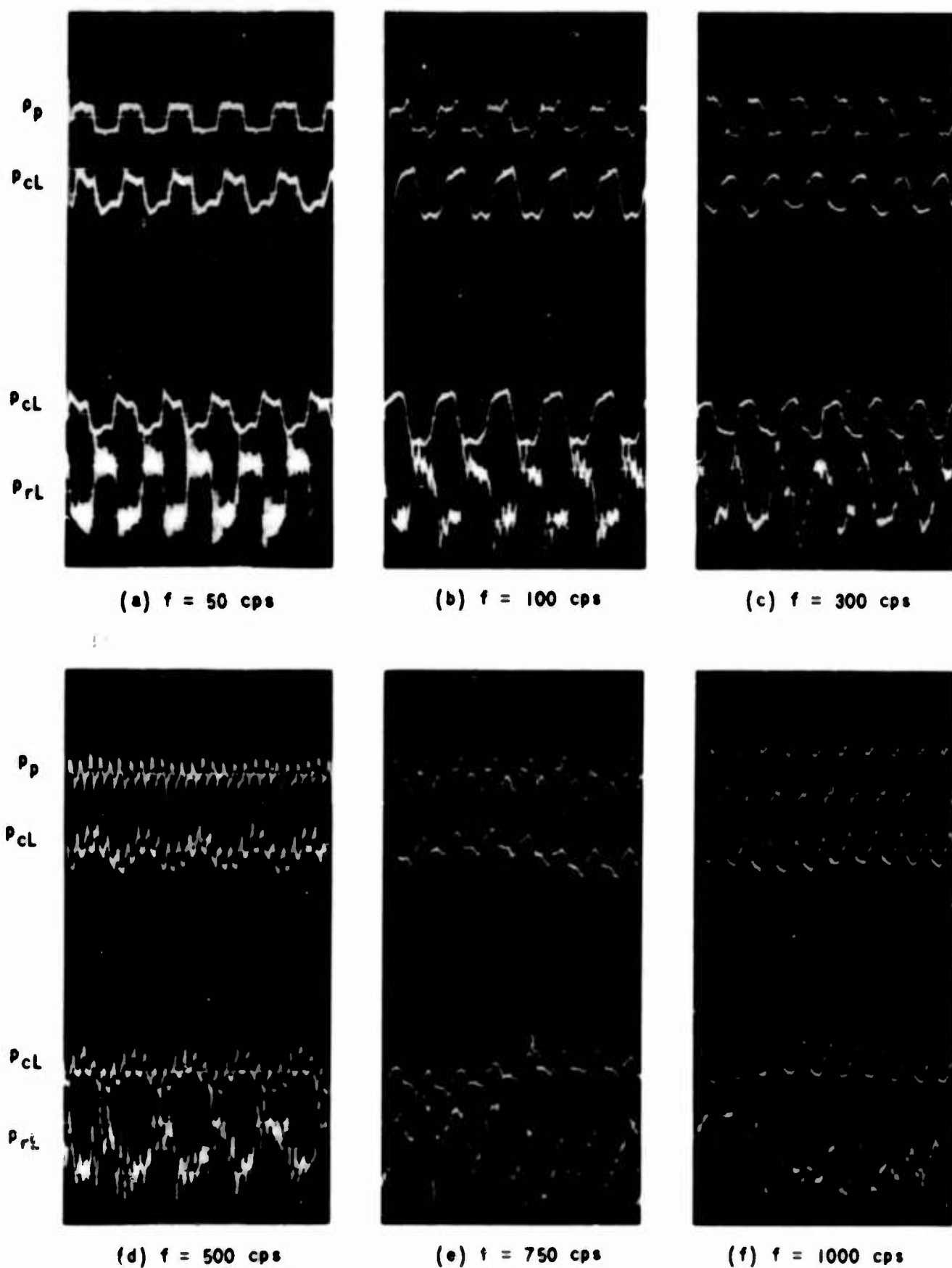
(c) C.C. CONFIG. III-2
 $f = 10 \text{ cps}$
 $p'_0 = \overline{p'_c} = .7$



(d) C.C. CONFIG. IV-1
 $f = 10 \text{ cps}$
 $p'_0 = \overline{p'_c} = .7$

VERTICAL SCALE: 1 cm = 1 psi = .04 p_n

Figure 16 SENSOR RESPONSE TO ALTERNATING STEP INPUT (SLOW RECTANGULAR PULSES)



C.C. CONFIG. I-1
 F.A. CONFIG. (SEE FIG. 6)
 $P_o' = .76$
 $\overline{P_{cL}} = \overline{P_{cR}} = .72$

VERTICAL SCALE: 1 cm = .5 psi = .025 P_n

Figure 17 SENSOR PERFORMANCE DATA ILLUSTRATING SWITCHING FEEDBACK EFFECT

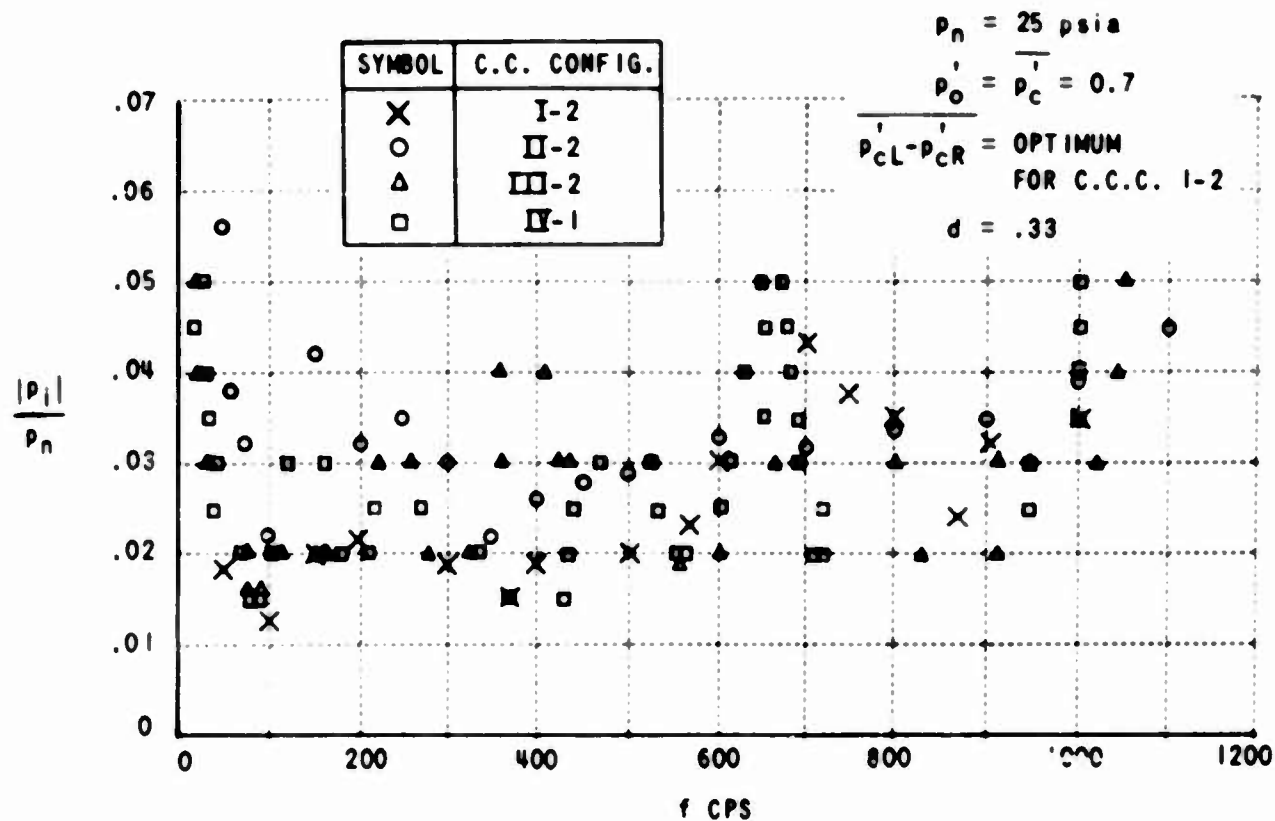


Figure 18 EFFECT OF FREQUENCY ON INPUT SIGNAL AMPLITUDE REQUIRED FOR SWITCHING WITH DIFFERENT CONTROL CIRCUIT CONFIGURATION

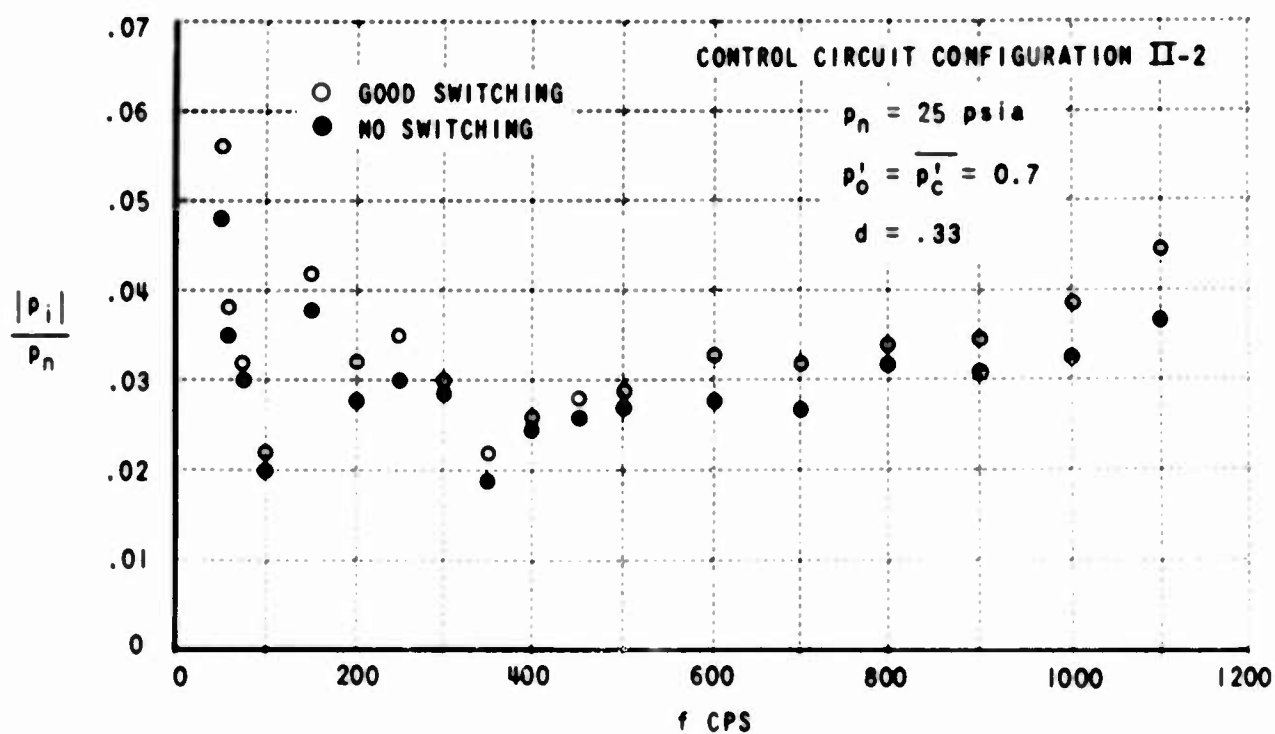


Figure 19 INPUT SIGNAL AMPLITUDE RANGE OF PARTIAL SWITCHING

CONTROL CIRCUIT CONFIGURATION II-2

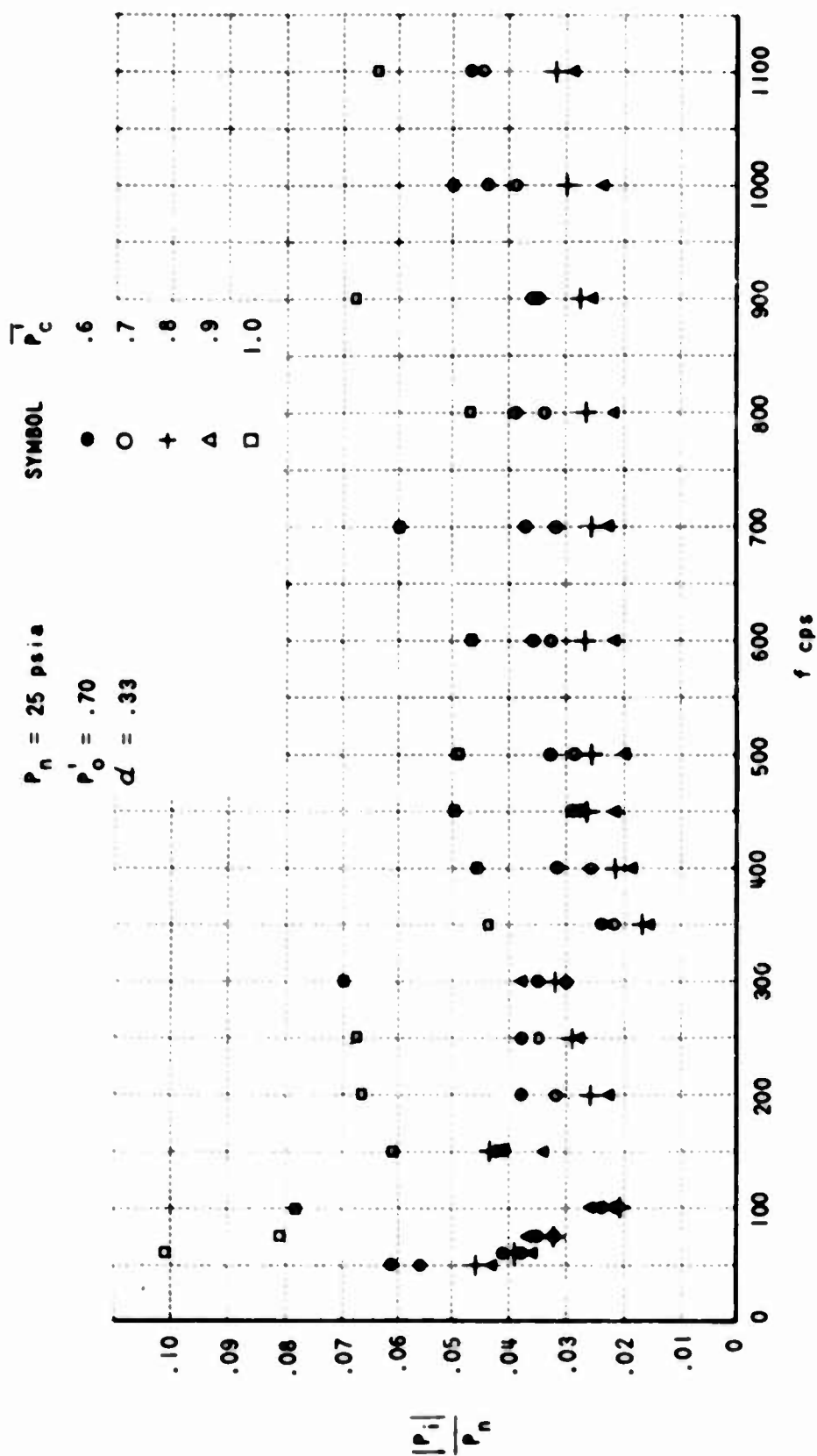
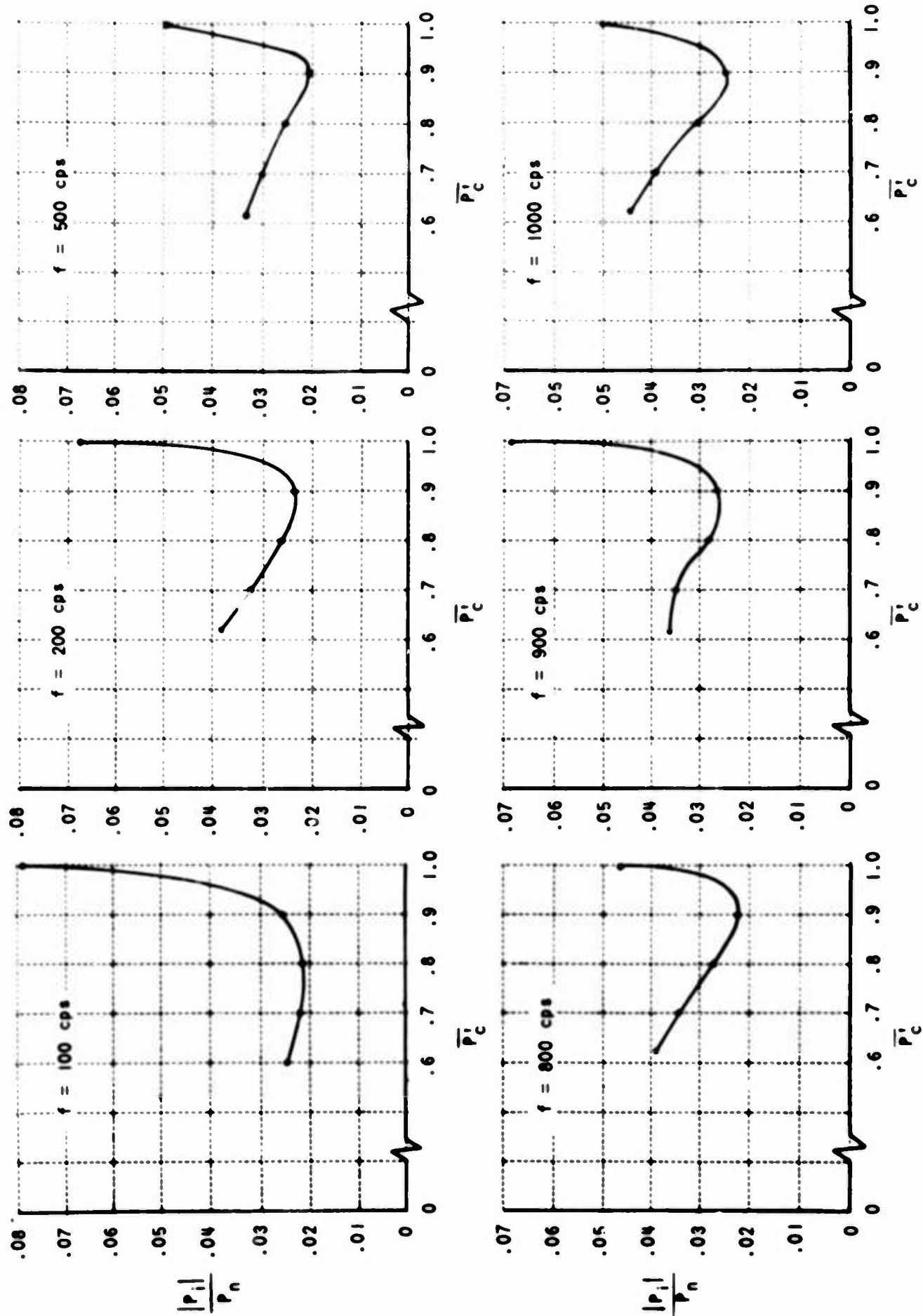


Figure 20 INPUT SIGNAL AMPLITUDE REQUIRED FOR SWITCHING AS A FUNCTION OF FREQUENCY AND AVERAGE CONTROL PRESSURE LEVEL



CONTROL CIRCUIT CONFIGURATION II-2

$p_n = 25$ psia $p'_0 = .7$

Figure 21 EFFECT OF AVERAGE CONTROL PRESSURE LEVEL ON INPUT SIGNAL AMPLITUDE REQUIRED FOR SWITCHING

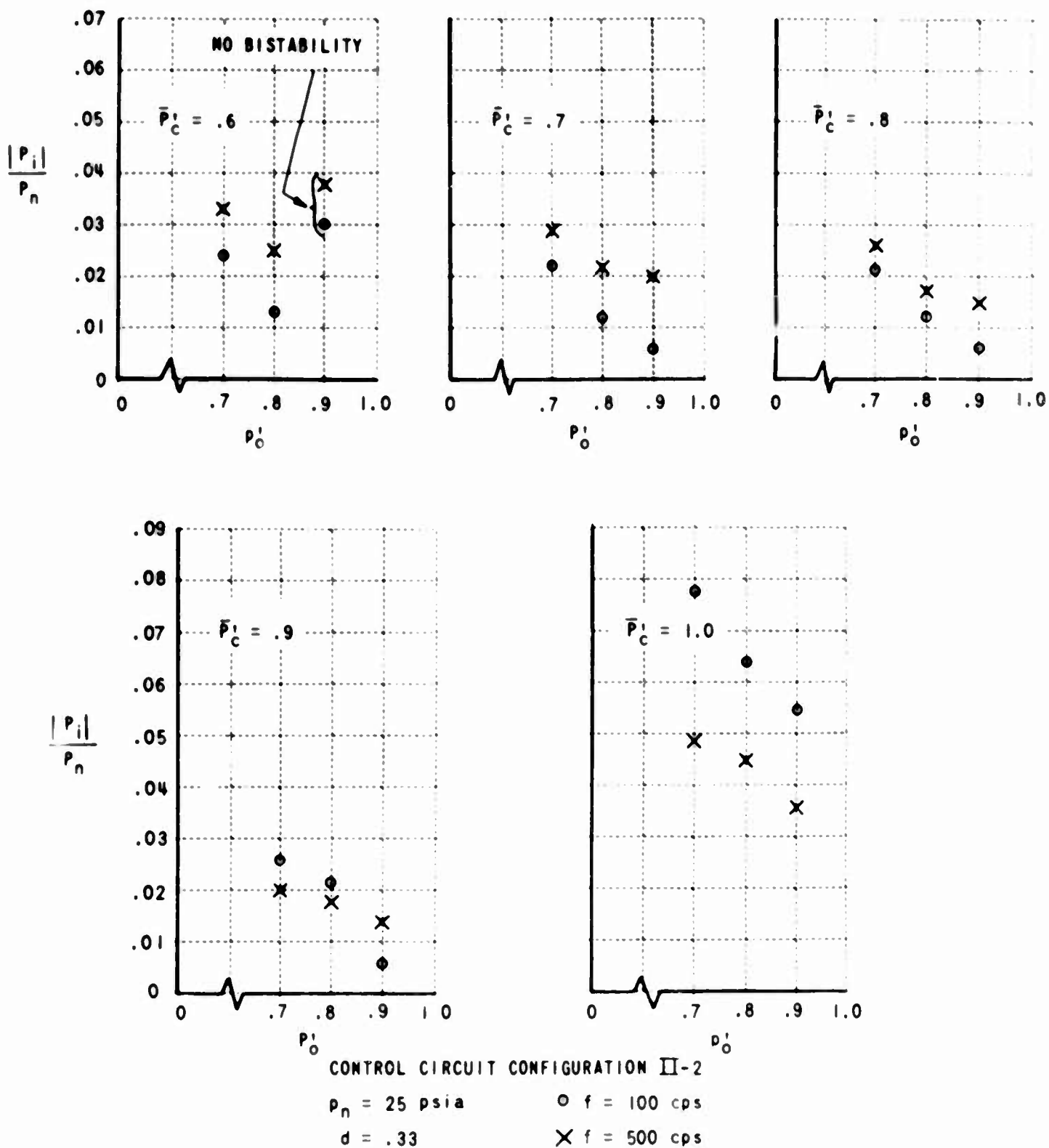


Figure 22 EFFECT OF LOAD PRESSURE LEVEL ON INPUT SIGNAL AMPLITUDE REQUIRED FOR SWITCHING

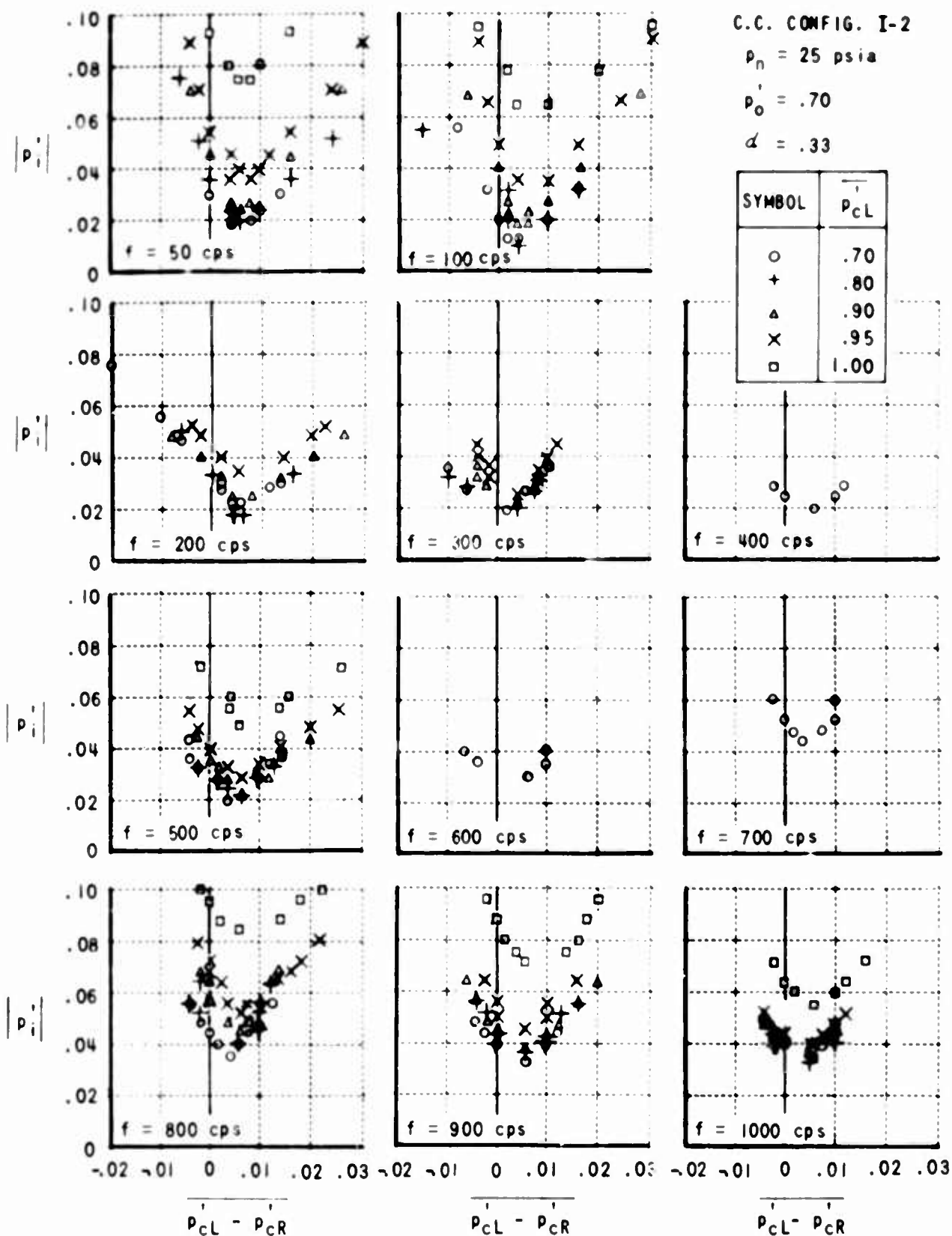
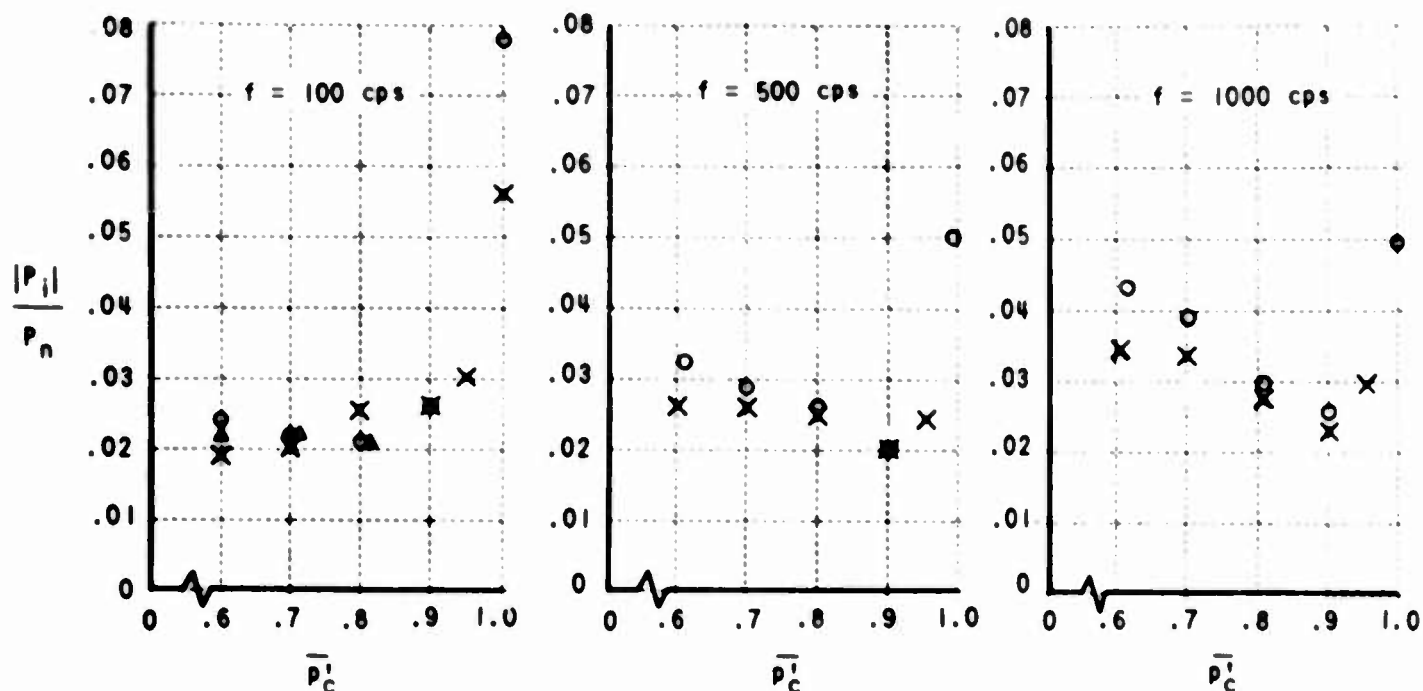


Figure 23 EFFECT OF AVERAGE PRESSURE DIFFERENCE ACROSS CONTROL PORTS ON INPUT SIGNAL AMPLITUDE REQUIRED FOR SWITCHING



CONTROL CIRCUIT CONFIGURATION II-2

$\bar{p}'_O = .7$
 $d = .33$

○ $P_n = 25$ psia
 × $P_n = 50$ psia
 △ $P_n = 75$ psia

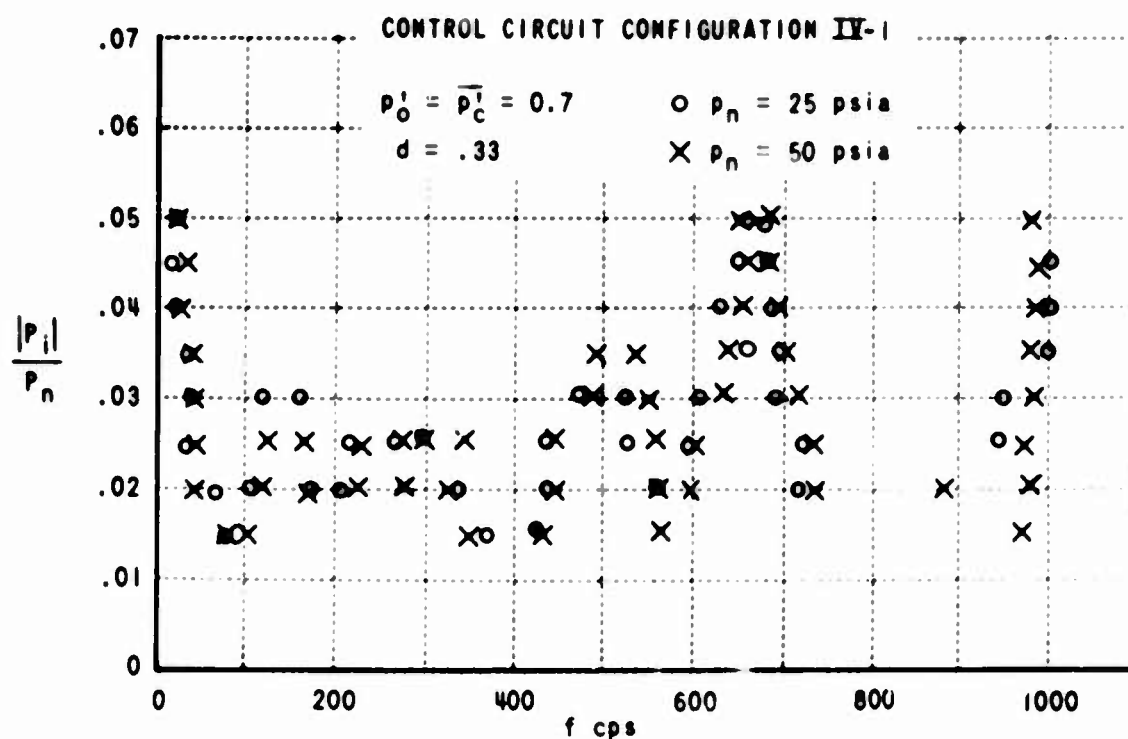


Figure 24 SWITCHING PERFORMANCE DATA AT DIFFERENT POWER NOZZLE SUPPLY PRESSURES INDICATING SUITABILITY OF METHOD CHOSEN TO NONDIMENSIONALIZE PRESSURE PARAMETERS.

SWITCHING PERFORMANCE			OSCILLATION FREQUENCY, CPS
NO SWITCH	MARGINAL	SWITCH	
○	◉	●	NO OSCILLATION
△	▲	▲	80 - 100
□	◻	■	100 AND 800
▽	▼	▼	700 AND 3000
◇	◊	◆	30000

C.C. CONFIG. I-1

$$p_n = 25 \text{ psia}$$

$$p_o' = p_c' = .7$$

$$|p_i'| = .03$$

$$f = 50 - 1000 \text{ cps}$$

$$d = .50$$

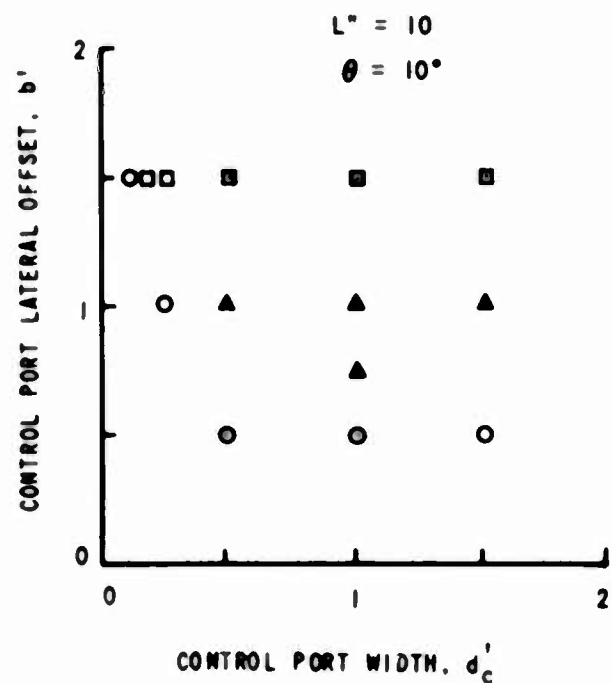
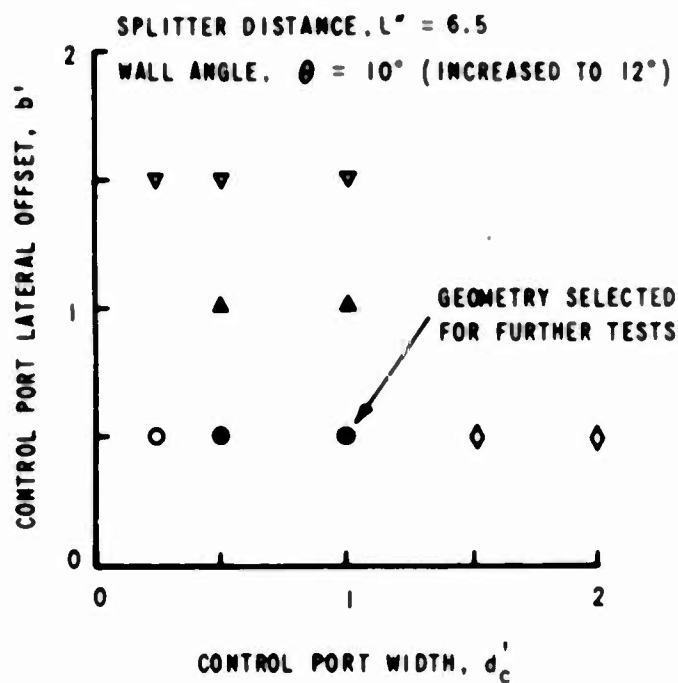
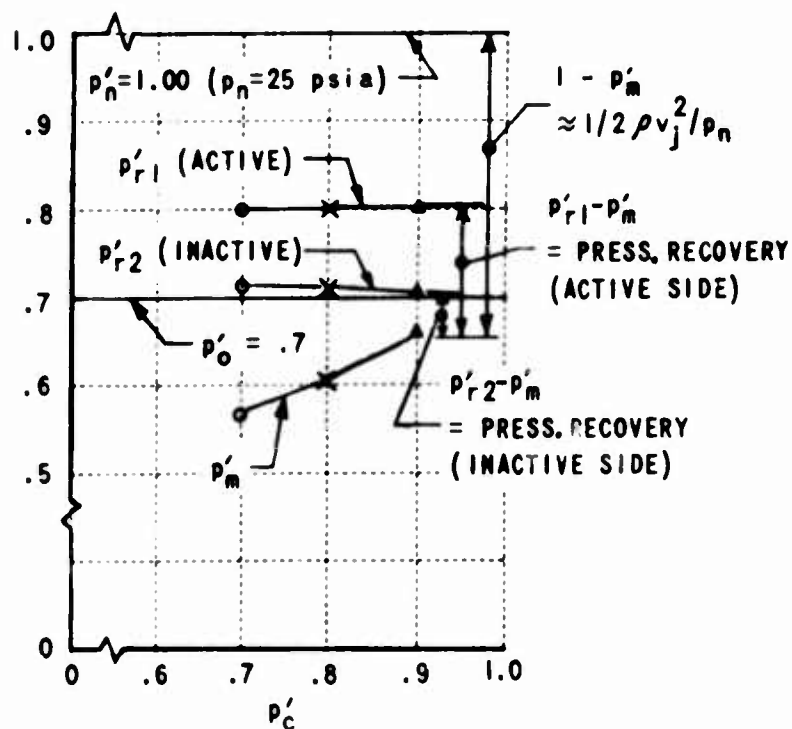
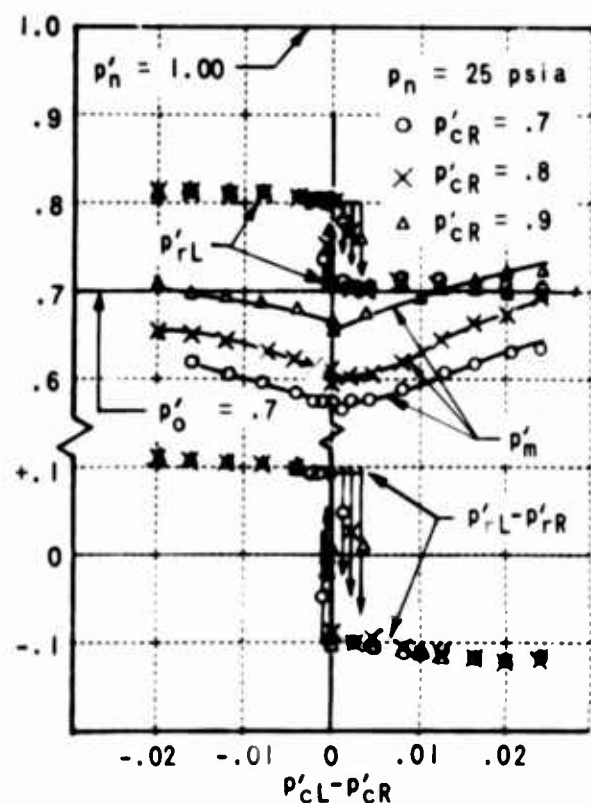


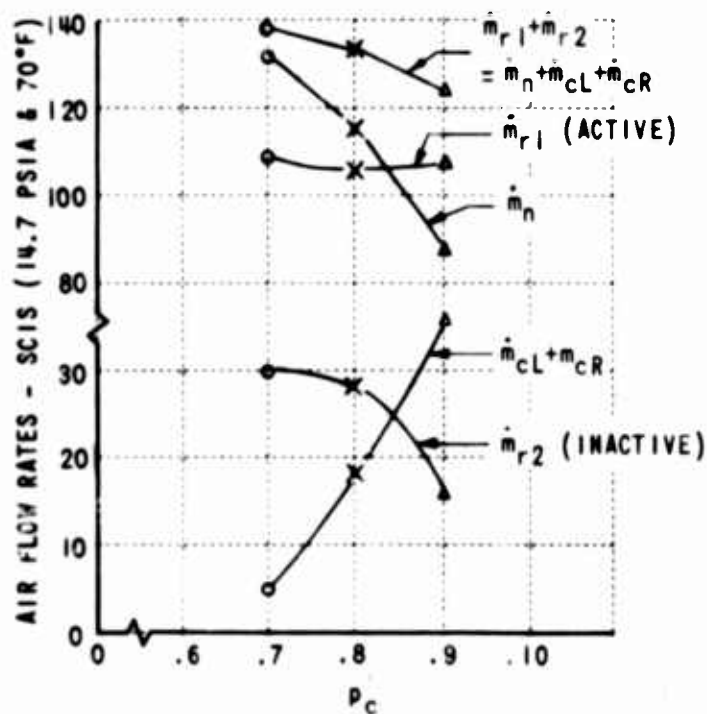
Figure 25 SOME QUALITATIVE EFFECTS OF FLUID AMPLIFIER GEOMETRY ON SWITCHING PERFORMANCE AND STABILITY



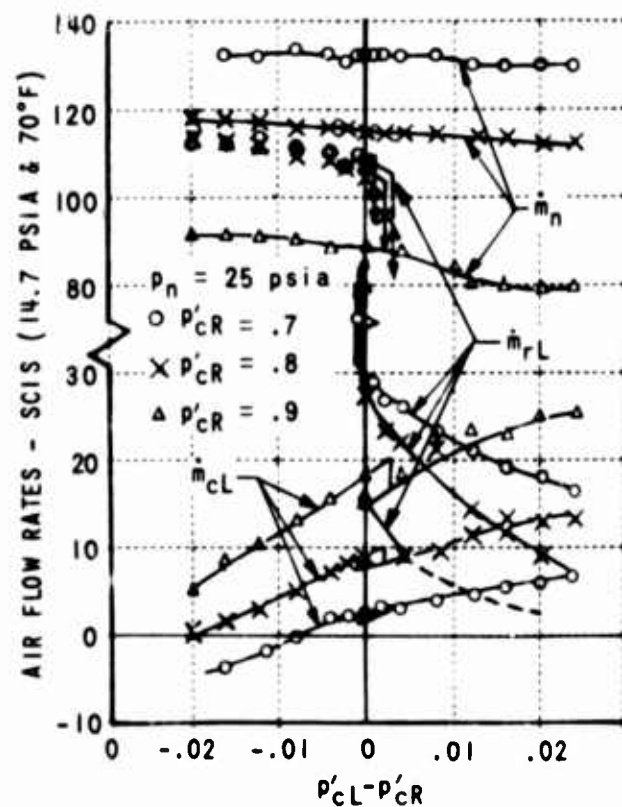
(a) PRESSURES AT SWITCHING POINTS



(b) PRESSURE VARIATION WITH CONTROL PRESSURE DIFFERENCE



(c) FLOW RATES AT SWITCHING POINTS



(d) FLOW VARIATION WITH CONTROL PRESSURE DIFFERENCE

Figure 26 BISTABLE FLUID AMPLIFIER STATIC SWITCHING CHARACTERISTICS